
Fabrication of methylammonium lead iodide thin films via sequential closed space sublimation

**Herstellung von Methylammonium Bleiodid Dünnschichten mittels
sequentieller Closed Space Sublimation**

Zur Erlangung des akademischen Grades Doktor-Ingenieur (Dr.-Ing.)
genehmigte Dissertation von Ralph Dachauer aus Lich

Tag der Einreichung: 20.08.2019, Tag der Prüfung: 05.11.2019

Darmstadt – D 17

1. Gutachten: Prof. Dr. Wolfram Jaegermann
2. Gutachten: Prof. Dr. Oliver Clemens



TECHNISCHE
UNIVERSITÄT
DARMSTADT

Surface Science Division
Materials Science Department

Fabrication of methylammonium lead iodide thin films via sequential closed space sublimation

Herstellung von Methylammonium Bleiodid Dünnschichten mittels sequentieller Closed Space Sublimation

Genehmigte Dissertation von Ralph Dachauer aus Lich

1. Gutachten: Prof. Dr. Wolfram Jaegermann
2. Gutachten: Prof. Dr. Oliver Clemens

Tag der Einreichung: 20.08.2019

Tag der Prüfung: 05.11.2019

Darmstadt – D 17

Bitte zitieren Sie dieses Dokument als:

URN: urn:nbn:de:tuda-tuprints-94923

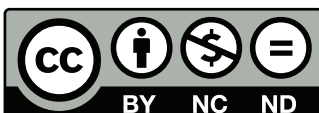
URL: <https://tuprints.ulb.tu-darmstadt.de/id/eprint/9492>

Dieses Dokument wird bereitgestellt von tuprints,

E-Publishing-Service der TU Darmstadt

<https://tuprints.ulb.tu-darmstadt.de>

tuprints@ulb.tu-darmstadt.de



Die Veröffentlichung steht unter folgender Creative Commons Lizenz:
Namensnennung – Keine kommerzielle Nutzung – Keine Bearbeitung
4.0 International

<https://creativecommons.org/licenses/by-nc-nd/4.0/deed.de>

Erklärung zur Dissertation

Hiermit versichere ich, die vorliegende Dissertation ohne Hilfe Dritter nur mit den angegebenen Quellen und Hilfsmitteln angefertigt zu haben. Alle Stellen, die aus Quellen entnommen wurden, sind als solche kenntlich gemacht. Diese Arbeit hat in gleicher oder ähnlicher Form noch keiner Prüfungsbehörde vorgelegen.

Darmstadt, den

(Ralph Dachauer)



“Die Wissenschaft fängt eigentlich erst da an interessant zu werden, wo sie aufhört.”

Justus von Liebig (1803-1873)



Abstract

In this work, the characterization of methylammonium lead iodide (MAPI) layers, which were fabricated from PbI_2 and PbCl_2 via a sequential (2step) closed space sublimation (CSS) route under high vacuum, is presented. The characterization was carried out by means of scanning electron microscopy (SEM), X-ray diffraction (XRD), UV/VIS absorption spectroscopy, photoluminescence (PL) spectroscopy and in vacuo photoelectron spectroscopy (PES). In addition, the 2step CSS MAPI layers were incorporated into planar solar cells which were subsequently analyzed. For the transformation of the lead salt layers in the CSS, four substrate temperatures (75 °C, 90 °C, 130 °C, 150 °C) were chosen. The crucible temperatures and transformation times were adjusted to obtain most complete transformations. A high phase purity for the 2step CSS MAPI fabricated from PbI_2 and from PbCl_2 can be derived from the XRD measurements in the whole substrate temperature range. The SEM measurements show that the morphology of the MAPI layers undergoes significant changes which become more pronounced with increasing substrate temperature and can be separated into three distinct processes taking place simultaneously: the formation of the perovskite by incorporation of MAI into the lead salt grains, the recrystallization of the perovskite grains and an Ostwald ripening like growth of the recrystallized grains [1]. From UV/VIS spectroscopy experiments a band gap of MAPI around 1.58 eV could be derived. The in vacuo PES experiments show the Fermi level pinned to the conduction band minimum. The UV/VIS and PE spectroscopy results appear to be independent on the substrate temperature. Combining the UV/VIS and the PES results, band energy diagrams for PbI_2 , PbCl_2 , MAI and MAPI could be created. Those band energy diagrams highlight the importance of a complete reaction of the lead salt on one hand and the avoidance of a MAI capping layer on top of the MAPI absorber, on the other hand. Working solar cells incorporating MAPI layers derived from PbI_2 and from PbCl_2 could be fabricated for all examined substrate temperatures. However, the efficiencies of the fabricated solar cells were mostly limited to the range of 2-3 %, with few solar cells exceeding 4%. The reason for this is probably the combination of a hindered charge extraction due to a thin PbI_2 interface layer between the MAPI absorber and the FTO/ TiO_2 electrode with the recombination of photoexcited charge carriers in the MAPI layers. Nevertheless, the relatively large size and the narrow efficiency distribution of the solar cells on one substrate indicate the potential of the 2step CSS process to fabricate solar cells with active areas in the square centimeter regime. Thereby, the unique property of the CSS, the combination of high processing temperatures and a high vacuum environment, is expected to open promising opportunities, especially for research on inorganic perovskite absorber materials.

Zusammenfassung

Das Thema dieser Arbeit ist die Charakterisierung von Methylammonium Bleiodid (MAPI) Dünnschichten, welche mittels sequentieller Closed Space Sublimation (CSS) aus PbI_2 und PbCl_2 Schichten unter Hochvakuumbedingungen hergestellt wurden. Die so hergestellten Schichten wurden mittels Rasterelektronenmikroskopie (REM), Röntgenbeugungsexperimenten (XRD), UV/VIS Absorptionsspektroskopie, Photolumineszenzspektroskopie (PL) und in vacuo Photoelektronenspektroskopie (PES) untersucht. Zudem wurden Dünnschichtsolarzellen mit den CSS MAPI Schichten als Absorbermaterial hergestellt. Für die Umwandlung der Bleisalzschichten in der CSS wurden Substrattemperaturen von 75 °C, 90 °C, 130 °C und 150 °C gewählt. Die Tiegeltemperatur und die Umwandlungszeit wurden so angepasst, dass sie eine möglichst vollständige Umwandlung der Bleisalzschichten gewährleisten. Die durchgeführten XRD Experimente zeigen, dass bei allen untersuchten Substrattemperaturen MAPI Schichten mit einer hohen Phasenreinheit hergestellt werden können. Der Vergleich der REM Bilder zeigt, dass sich die Morphologie der Schichten im Zuge der Umwandlung vom Bleisalz zum Perowskiten deutlich verändert und diese Veränderung durch eine höhere Substrattemperatur begünstigt wird. Dabei kann die Entwicklung der Morphologie der Perowskiteschicht in drei simultan ablaufende Prozesse unterteilt werden: Die Bildung des Perowskiten durch Einlagerung von MAI in die Bleisalze, eine Rekristallisation der Perowskitkörner und ein Kornwachstum der rekristallisierten Perowskitkörner in einem Ostwaldreifung ähnlichen Prozess. Aus UV/VIS Absorptionsexperimenten kann eine Bandlücke im Bereich von 1.58 eV für MAPI abgeleitet werden. In vacuo PES Experimente zeigen, dass das Fermi-niveau für alle untersuchten Proben am Leitungsbandminimum liegt. Durch die Kombination der UV/VIS und der PE Spektroskopie Ergebnisse konnten Banddiagramme für PbI_2 , PbCl_2 , MAI und MAPI erstellt werden, welche die Notwendigkeit einer vollständigen Umwandlung der Bleisalzschrift zum Perowskiten bei gleichzeitiger Vermeidung einer MAI Schicht auf der MAPI Schicht hervorheben. Aus den von PbI_2 und PbCl_2 abgeleiteten MAPI Schichten konnten für alle untersuchten Substrattemperaturen funktionierende Solarzellen hergestellt werden. Allerdings blieb die Effizienz dieser Solarzellen meistens auf den Bereich von 2-3 % limitiert. Nur wenige Solarzellen erreichten Effizienzen welche größer als 4 % waren. Der Grund für die niedrigen Effizienzen ist vermutlich die Kombination aus einer dünnen PbI_2 Schicht, welche die Ladungsträgerextraktion aus dem MAPI Absorber in die FTO/ TiO_2 Elektrode behindert, und der Rekombination der photogenerierten Ladungsträger in der Perowskiteschicht. Nichtsdestotrotz, weisen die relativ große aktive Fläche der einzelnen Solarzellen und die enge Verteilung der Effizienzen der Solarzellen auf einem Substrat auf das Potential der sequentiellen CSS hin, Solarzellen mit aktiven Flächen im Quadratzentimeterbereich herzustellen. Dabei erscheint die einzigartige Eigenschaft des CSS Prozesses, die Kombination aus hohen Prozesstemperaturen und einer Hochvakuumumgebung, besonders vielversprechende Möglichkeiten für die Herstellung von anorganischen Perowskitabsorbern zu eröffnen.

Contents

1. Important abbreviations	9
2. Introduction	11
3. Basic informations	17
3.1. Semiconductors	17
3.2. Solar cells	20
3.2.1. The p/n-contact	21
3.2.2. The Schottky contact	27
3.2.3. The equivalent circuit in the dark	29
3.2.4. IV characteristics under light	29
3.2.5. Solar spectrum and Shockley-Queisser limit	33
3.3. Thin film deposition under high vacuum conditions	35
3.3.1. Adsorption on solid surfaces and layer growth	35
3.3.2. Temperature dependence of the sublimation pressure	36
3.3.3. Transformation - inward diffusion and reaction	37
3.4. Analysis techniques	40
3.4.1. Photoelectron Spectroscopy	40
3.4.2. X-ray diffraction	44
3.4.3. Scanning electron spectroscopy	47
3.4.4. UV/VIS absorption spectroscopy	48
3.4.5. Photoluminescence spectroscopy	50
4. Experimental	53
4.1. Materials	53
4.2. Synthesis	54
4.2.1. Substrate preparation	54
4.2.2. Vacuum deposition	56
4.2.3. Solar cell finishing	62
4.3. Analysis	65
4.3.1. Photoemission spectroscopy (PES)	65
4.3.2. X-ray diffraction (XRD)	68
4.3.3. Scanning electron spectroscopy (SEM)	69
4.3.4. UV/VIS absorption spectroscopy	69
4.3.5. Photoluminescence spectroscopy	70
4.3.6. IV measurements on solar cells	70

5. Results and discussion	71
5.1. Prerequisites	71
5.1.1. The glass/FTO/titanium dioxide substrate	71
5.1.2. MAPI layer fabrication protocols	79
5.1.3. Relevant measurement effects	84
5.1.4. Most important facts	88
5.2. MAPI fabricated from lead iodide	89
5.2.1. Morphology	89
5.2.2. Crystal structure	92
5.2.3. Optoelectronic structure	98
5.2.4. The titanium dioxide/lead iodide interface	110
5.2.5. Most important facts	115
5.3. MAPI synthesized from lead chloride	117
5.3.1. Optoelectronic structure	117
5.3.2. Morphology and crystal structure	124
5.3.3. Evolution of MAPI from lead chloride	130
5.3.4. Most important facts	142
5.4. Photoactivity	143
5.4.1. Photoluminescence	143
5.4.2. Solar cells incorporating MAPI derived from lead iodide	147
5.4.3. Most important facts	155
6. Summary and Conclusions	157
7. Outlook	161
8. Acknowledgments	167
9. List of Figures	169
10. List of Tables	175
Bibliography	177
A. Appendix	193
B. Publications, conference contributions and student theses	203
C. Résumé	205

1 Important abbreviations

AM	air mass
ASF	atomic sensitivity factor
BE	binding energy
CBM/ E_{CBM}	conduction band maximum
(2step) CSS	(sequential) closed space sublimation
CVD	chemical vapor deposition
d	thickness or distance which is specified by a subscript
DAISY-SOL	DArmstadt Integrated SYstem for SOLar cell research
E_{F}	Fermi level
E_{g}	band gap
E_{ph}	photon energy
ETL	electron transport layer
E_{vac}	vacuum level
FWHM	full width half maximum
FTO	fluorine doped tin oxide
FF	fill factor
HOMO	highest occupied molecular orbital
HTL	hole transport layer
I	current
I_{MPP}	current at maximum power point
I_{p}	ionization potential
I_{sc}	short circuit current
ITO	indium tin oxide
IV	general indication for measures related to current-voltage characteristics
J	current density
J_{MPP}	current density at maximum power point
J_{sc}	short circuit current density
LUMO	lowest unoccupied molecular orbital
MACl	methylammonium chloride
MAI	methylammonium iodide
MA^+	methylammonium ion
MAPI	methylammonium lead iodide
$\text{MAPI}_{\text{PbI}_2}$	methylammonium lead iodide derived from lead iodide
$\text{MAPI}_{\text{PbCl}_2}$	methylammonium lead iodide derived from lead chloride
MASI	methylammonium tin iodide
MPP	maximum power point
n/n	denotes a contact between two n-type semiconductors

P_{el}	electrical power
PCE	power conversion efficiency
PES	photoelectron spectroscopy
PL	photoluminescence
p/i/n	denotes a contact between a p-type, an intrinsic and an n-type semiconductor
p/n	denotes a contact between a p-type and an n-type semiconductor
PVD	physical vapor deposition (used for a deposition process involving an open sublimation of the precursor material, in contrast to a CSS process)
P_{rad}	radiation power
$R_{h\nu}$	photon energy dependent directed reflection
R_p	parallel resistance
R_s	series resistance
SCR	space charge region
SE	secondary electron
SEE/ E_{SEE}	secondary electron edge
SEM	scanning electron microscopy
Spiro-MeOTAD	2,2',7,7'-tetrakis-(N,N-di-4-methoxyphenylamino)-9,9'-spirobifluorene
t_a	annealing time
T_c	crucible temperature
TCO	transparent conductive oxide
$T_{h\nu}$	photon energy dependent transmission
T_s	substrate temperature
t_t	transformation time
UPS	ultraviolet photoelectron spectroscopy
UV/VIS	denotes absorption experiments with radiation in the ultraviolet and the visible regime
VBM/ E_{VBM}	valence band maximum
V_{MPP}	voltage at maximum power point
V_{oc}	open circuit voltage
XPS	X-ray photoelectron spectroscopy
XRD	X-ray diffraction
$\alpha_{h\nu}$	photon energy dependent absorption coefficient
χ	electron affinity
ΔE_{CBM}	conduction band offset
ΔE_{VBM}	valence band offset
ϕ	work function
Φ_B	equilibrium barrier height
η	power conversion efficiency of a solar cell
λ	wavelength
θ	diffraction angle
ψ_b	band bending

2 Introduction

One of the most severe challenges of today's society is global warming. Compared to the pre-industrial level, the current global warming caused by humanity is about 1 °C and still increasing [2]. Thereby, the effects of a further temperature increase are dependent on the global region and range from extreme heat, missing rain and drought to down-pour [2]. In addition, the oceans are likely to warm up and the sea level to rise [2]. All those effects will occur for a global temperature increase of 2 °C and even of 1.5 °C, compared to the pre-industrial level [2]. However, most of them will be less severe if the global warming can be limited to 1.5 °C [2]. To achieve this goal, the global CO₂ emissions have to be reduced for 45 % compared to 2010 till 2030 and the net CO₂ emission has to be zero till 2050 [2]. One way to reduce the global CO₂ emissions is the substitution of the energy production based on fossil fuels by renewable energies. In 2017, 36.2 % of electric energy consumed in Germany were produced by renewable energies, and 18.3 % of those by solar cells [3]. Concerning, the solar cell technology, on a global scale, wafer based silicon technologies, monocrystalline or multicrystalline, are dominant compared to thin film technologies like CdTe or CIGS [4].¹ However, with laboratory efficiencies of up to 22.9 % for CIGS and 21.0 % for CdTe compared to 26.7 % for mono-Si and 22.3 % for poly-Si, the thin film technologies play in the same league as the wafer based Si technologies [4]. Even more, when the recent module efficiencies of 17 % for common silicon solar cells (21 % for Super-mono cells) and 16.6 % for CdTe solar cells are compared [4]. In addition, compared to wafer based Si solar cells, thin film technologies possess several advantages. For example, their module price per Watt peak is lower and the energy payback time is smaller compared to wafer based Si technologies [4]. Thereby, CdTe solar cells have an energy payback time of about 1.1 years in Germany and 0.6 years in Sicily [4]. However, with energy payback times of about 3.2 years in northern Europe and about 1.75 years on Sicily, even monocrystalline silicon solar cells can provide a multiple of the energy needed for their production [4]. Besides their fast energy payback time and lower production costs, thin film solar cells possess other advantages like the possibility to use large area and high throughput production techniques [5]. In addition, the size and shape of a module is not limited to the the size and shape of a Si wafer. Some years ago, a new type of solar cell absorber entered the stage: organic-inorganic hybrid perovskites. Although, research on those hybrid perovskites was carried out already in the late 1990s, the first solar cells were reported by Kojima et al. in 2009 [6,7]. Organic-inorganic hybrid perovskite absorbers are materials with the chemical composition ABX₃ and a perovskite

¹ The term thin film solar cells refers to the thickness of the solar cell absorber which is typically in the range of 200 μm for silicon solar cells but only in the range of several hundredth nanometers to few micrometers for thin film technologies [4,5].

crystal structure. Thereby, a central A cation is surrounded by eight octahedra including the B cations and X anions. Since organic molecules are often used on the A position while the ions in the octahedra are inorganic, the description as organic-inorganic hybrid material is derived. One of the first reported perovskite solar cell absorber, and till now the most investigated one, was methylammonium lead iodide $\text{CH}_3\text{NH}_3\text{PbI}_3$ [7]. This absorber material is also subject to this work and will be referred to as MAPI in the following. At first, the perovskite absorbers were implemented in dye-sensitized solar cells [7]. However, the stability of those cells was limited due to degradation of the perovskite dye by the liquid electrolyte [8,9]. With the use of solid electrolytes, the stability of the perovskite solar cells became reasonable and the field of research on perovskite solar cells was launched and is still emerging rapidly [8,9]. In the dye sensitized solar cells, the perovskite was incorporated in a mesoporous metal oxide scaffold (for example Al_2O_3 or TiO_2) [7, 10]. The scaffold is supposed to provide the separation of photoinduced charge carriers and the charge carrier transport. With emerging development, it became apparent that both, charge separation and charge transport, are possible in a sufficient manner in the perovskite absorber itself and the scaffold layers became thinner. Nowadays, state of the art solar cells, still possess the scaffold layers. However, they are rather thin and covered by a dense perovskite capping layer [11]. Furthermore, high efficient solar cells without any scaffold layer and even without metal oxide layers are presented in literature [12, 13]. Hence, perovskite solar cells can be considered as thin film technology. With laboratory efficiencies above 22 % for solar cells incorporating the mesoporous scaffold and still over 20 % for planar configurations, the perovskite solar cells are in the same efficiency range as the other thin film technologies and even close to wafer based silicon solar cells, after only 9 years of intensive research [12, 14, 15]. Besides their high PCE, perovskite solar cells possess several other advantages. Some important ones are described in the following. In the perovskite itself, only abundant, inexpensive elements are incorporated. However, often at least one organic charge transport layer is used in perovskite solar cells which can be quite expensive. Hence, the replacement of expensive organic charge transport materials by more cost effective alternatives is topic to current research [16, 17]. The fabrication of perovskite layers does not require high temperatures. Accordingly, a broad range of suited substrates, including polymer foils, is available [17, 18]. Last but not least, perovskite absorbers possess a band gap which can easily be varied, for example by halide or cation substitution, from around 1.6 eV to above 2 eV, making them interesting for single junction and for tandem solar cells [11, 14, 19–25]. However, in spite of their advantages, perovskite solar cells possess also some drawbacks. Their stability, to heat, oxygen and moisture is poor without encapsulation, in the range of tenth to hundredth of hours compared to ten thousands of hours estimated as the life time of a solar module [25]. However, the stability of perovskites could be drastically improved during the last years and with proper encapsulation operating times of thousands of hours can be achieved [25]. Besides the stability issues, another problem is the toxicity of lead. Most of the highly efficient perovskite absorbers include Pb^{2+} ions on their B site. In spite

of intensive research, no lead free perovskite could be found with a photovoltaic performance comparable to those of its lead containing counterpart [26, 27]. Still, promising efficiencies around 9% are reported in literature for FASnI_3 [26, 27]. The proposed lead replacements, for example tin or germanium, are significantly more sensitive to oxidation and their processing is difficult [26, 27]. Accordingly, an oxygen free fabrication environment appears to be crucial for research on lead free perovskites for solar cell applications. One of the most common fabrication techniques for perovskite solar cells, is spin coating [11, 14, 28]. However, spin coating does not belong to the upscalable fabrication techniques [28]. Therefore, several upscalable fabrication techniques are currently examined in literature, for example blade coating, ink jet printing, spray coating, physical and chemical vapor deposition techniques, to name just a few [28]. However, with increasing size, the efficiency of perovskite solar modules decreases dramatically to around 12% for a 703 cm^2 module, highlighting the need for further research in that direction [4, 14, 28]. Thereby, the vapor deposition methods provide several advantages, for example good process control, uniform large area films and precise control of the layer thickness and layer properties [13, 28–38]. Furthermore, multilayer stacks can feasibly be fabricated since vapor based deposition methods are not restricted to orthogonal solvents and are applicable to a wide range of substrates [28, 32]. Among the gas phase deposition techniques, the vacuum deposition processes possess the advantage that even oxygen sensitive materials can be used [1, 39]. As mentioned above, this feature may become important for the research on lead free perovskites, using oxygen sensitive compounds like SnI_2 , or for research on purely inorganic perovskites with moisture sensitive precursors like CsBr . Furthermore, vacuum deposition processes provide the possibility of in line production of all layers needed in a thin film solar cell, ease the fabrication of tandem solar cells and allow the tuning of the interface properties by the deposition of thin interface layers [1, 13, 21, 33, 38]. Vacuum fabrication techniques for perovskite absorbers can be divided into two groups, the co-evaporation and the sequential processes. Sequential processes decouple the deposition parameters of the metal salt from those of the organic halide, leading to additional possibilities to tune the properties of the perovskite, like the band gap [33, 34]. Furthermore, if the sequential depositions are carried out in separate chambers, cross-contaminations between the evaporated species can be reduced [30]. A subgroup of the sequential vacuum processes are those, which work in confined reaction spaces with small distances between the predeposited metal halide layer and the organic halide precursor. Those processes have the advantage of a simplified design and the reduction of the material consumption during the process and have already shown promising results [1, 34, 36, 40].

In this work, a sequential closed space sublimation (2step CSS) under high vacuum conditions is used for the fabrication of the MAPI layers. Thereby, lead halide layers are deposited in a conventional PVD process under high vacuum conditions in a first step and transformed to MAPI layers by exposure to methylammonium iodide (MAI) vapor in the second, closed space sublimation, step. The sequential nature of the process allows to fea-

sibly vary the used lead salts. In addition, since the process is carried out in a high vacuum environment, it is also suited for water or oxygen sensitive materials. The unique feature of the CSS transformation step is that the reaction volume is limited to the CSS crucible. Thus, although the CSS chamber is kept at high vacuum, high methylammonium partial pressures can be established in the CSS crucible, allowing high substrate temperatures and an extended fabrication window for the perovskite layers. From a surface scientific point of view, the feature that the sequential CSS is carried out in a high vacuum environment is interesting since it allows to perform photoemission spectroscopy experiments directly after the the perovskite layer fabrication, without breaking the vacuum conditions. Thus, surface contaminations will be reduced and the electronic structure of the perovskite layers, at least at the surface, can be decently probed. Knowing this structure, suited materials for the charge transport layers can be found for the different photoactive perovskites, possibly even alternatives to cost intensive materials which are currently used. Last but not least, vapor deposition processes in general and also specifically CSS type processes are already established fabrication routes for other thin film systems like CdTe and have already proved their upscalability [28, 41]. Besides those general properties, the CSS might provide some specific advantages for the transformation of lead halide layers to MAPI. Methylammonium iodide has a low sticking coefficient, especially at elevated temperatures, and deposits rather from a background pressure than in a directed deposition [42]. Accordingly, the small reaction volume of the CSS crucible combined with the high deposition pressure might be advantageous for the transformation of lead salts to MAPI, possibly making the process more effective [42].

Based on those promising features of the CSS transformation step, the aim of this work is to apply and evaluate a closed space sublimation process under high vacuum conditions for the transformation of lead halide layers to perovskite absorbers. Thereby, the unique features of the CSS, the high substrate temperatures for a high vacuum environment process, and their effect on the properties of the resulting perovskite will be the main subject of this work. To work on this subject, $\text{CH}_3\text{NH}_3\text{PbI}_3$ (MAPI) was used, which is the archetype of the perovskite solar cell absorbers and can be considered as a model system for the organic-inorganic hybrid perovskites [7, 43–45]. The transformation of PbI_2 and PbCl_2 to MAPI with a systematic variation of the substrate temperature during the CSS process from 75 °C to 150 °C was examined. The source materials, lead iodide, lead chloride and methylammonium iodide, were used as powders. The fabricated MAPI layers were characterized with scanning electron microscopy (SEM), X-ray diffraction (XRD), UV/VIS spectroscopy, photoluminescence spectroscopy and in vacuo photoelectron spectroscopy. Furthermore, IV measurements on solar cells in a planar configuration were carried out.

In the following chapters, the basic informations relevant for this work will be discussed first, followed by a description of the experimental procedures. Thereafter, the properties of MAPI derived from PbI_2 with the 2step CSS will be presented in dependence on the substrate temperature during the CSS step and compared to those of MAPI derived from

PbCl₂. Based on the analytical results, the photoactivity of the fabricated MAPI layers and the performance of the fabricated solar cells will be discussed. Finally the obtained insights will be summarized and commented in form of a conclusion, leading to an outlook on the future perspectives for the use of a 2step CSS process as fabrication technique for perovskite solar cells.



3 Basic informations

The following chapter provides the theoretical background for this work. Summaries of the information considered most important are given.

3.1 Semiconductors

This section is based on the book “Festkörperphysik” by S. Hunklinger which is recommended for further reading [46].

Numerous important electrical and optical properties of a solid, like the conductivity or the radiation absorption are determined by the band structure of the solid. In inorganic solids, a band is the broadening of an atomic state (atomic orbital) due to interatomic interactions (overlapping of atomic orbitals). Hence, for a solid consisting of N atoms, every atomic state which contributes to the interatomic interactions will form a band consisting of N energy states. Taking an s orbital as example: Under consideration of the Pauli principle, which says that every energy state can only be occupied by two electrons (spin up and down), an s band can be occupied by $2N$ electrons. In dependence on the amount of electrons occupying a band, it is possible to differentiate between metals on one hand and semiconductors and insulators on the other. Charge transport is only possible in partially filled bands. Neither completely full nor completely empty bands can contribute to the charge transport. Metals provide partially filled bands and accordingly show a good conductivity. Intrinsic semiconductors and insulators have only completely filled and completely empty bands. Hence, no charge transport is possible at 0 K . The highest occupied band is called the valence band, its band edge the valence band maximum VBM. The lowest unoccupied band is called the conduction band, its band edge the conduction band minimum CBM. However, in dependence on the energetic difference between the VBM and the CBM (the band gap E_g), at temperatures above 0 K , charge carriers will be thermally excited from the valence band to the conduction band. Hence, both bands are partially filled and charge transport is possible. If an electron is excited from the valence band to the conduction band, its vacancy can be described as positively charged particle, as hole. The dependence of the amount of thermally excited charge carriers on the band gap can be used as a differentiation between a semiconductor and an insulator. Materials showing a not too large band gap are considered as semiconductors, materials with a large band gap as insulators. Figure 3.1 illustrates the differentiation between a metal, a semiconductor and an insulator.

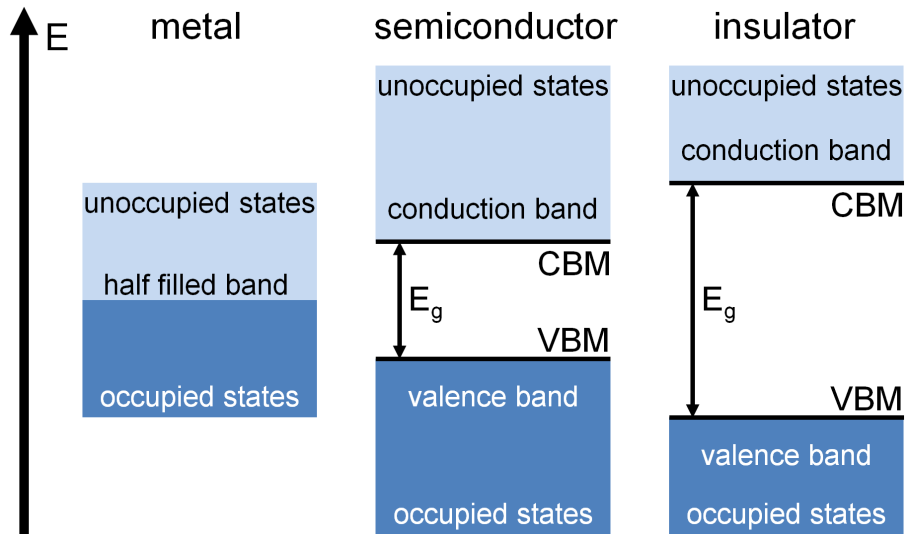


Figure 3.1.: Schematic depiction of the band edge region of a metal, a semiconductor and an insulator.

As mentioned above, a band consists of N energy states, available for electrons, but not all of them are occupied. The superposition of all available states provided by the different energy bands, independent on whether they are occupied or not is described by the density of states (DOS). The probability that an energetic state is occupied is given by the Fermi-Dirac distribution in equation 3.1.

$$f(E) = \frac{1}{e^{\frac{E-\mu}{k_B T}} + 1} \quad (3.1)$$

In equation 3.1, $f(E)$ is the probability that a state at the energy E is occupied, k_B is Boltzmann's constant and μ is the chemical potential of the electrons. At 0 K, $f(E)$ is 1 for $E < \mu$, 1/2 for $E = \mu$ and 0 for $E > \mu$. In addition, at 0 K, μ matches E_F . E_F is the Fermi energy which is the energy below which all energy states are occupied at 0 K. At temperatures higher the 0 K, E_F is only approximately equal to μ . Nevertheless, E_F will serve as a measure for the chemical potential of the electrons and holes. Since electrons and holes are charged particles, they are influenced by electric fields. To account for that, the Fermi level will be used as measure for the electrochemical potential of the electrons and holes. As mentioned above, at temperatures > 0 K electrons will be excited from the valence band to the conduction band and the Fermi-Dirac distribution will not be a step function anymore, reflecting that the probability that an energy state above E_F (μ) is occupied and that energy states below E_F are unoccupied is > 0 . The Fermi-Dirac distribution is schematically shown in figure 3.2 b.

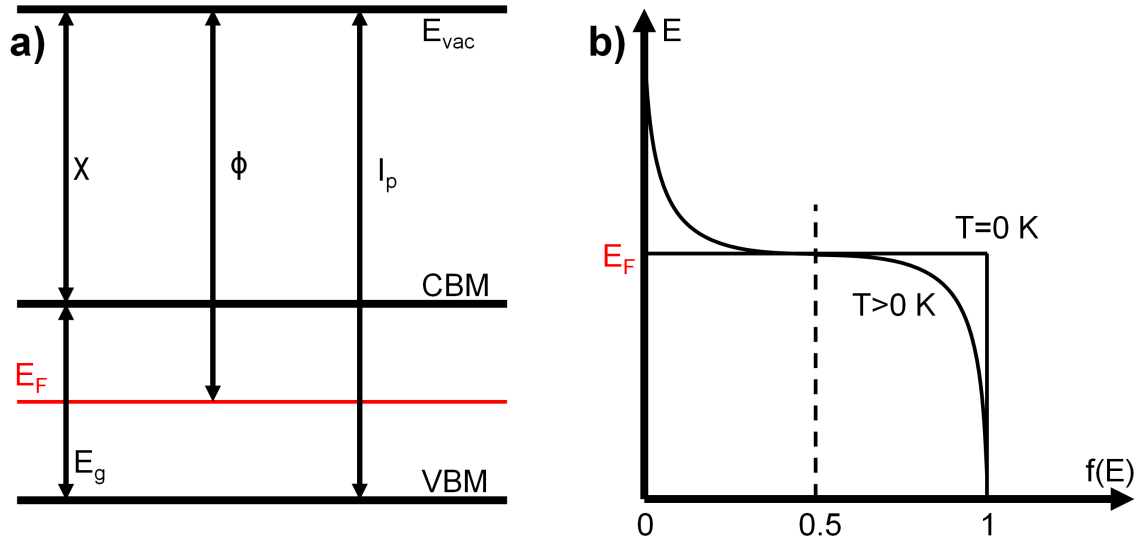


Figure 3.2.: Schematic depiction of the electron affinity χ , the work function ϕ , the ionization potential I_p , the band gap E_g and the Fermi level E_F of a semiconductor (a). Fermi-Dirac distribution for $T=0$ K and $T>0$ K (b).

Besides the Fermi level and the band gap, other measures are commonly used for the description of a semiconductor. The vacuum level E_{vac} is the energy level at which an electron is considered free from the influence of the solid it originates from. Accordingly, the electron affinity χ is the energy which is released if a free electron occupies the lowest unoccupied state (the conduction band minimum at 0 K), the ionization potential I_p is the energy needed to release an electron from the highest occupied state of the solid (the valence band maximum at 0 K) and the work function is the energetic difference between the Fermi level and the vacuum level and thus the minimum energy necessary to release an electron from a solid. The electron affinity, the work function and the ionization potential are illustrated in figure 3.2 a.

Bands are described by the dispersion relation of the energy E in dependence on the wave vector \vec{k} [47]. This description allows to categorize semiconductors in direct and indirect semiconductors. Direct semiconductors are those with the valence band maximum and the conduction band minimum at the same wave vector \vec{k} . Here, electrons can be excited directly from the valence band maximum to the conduction band minimum by the absorption of a photon. Indirect semiconductors have the VBM and the CBM at different wave vectors \vec{k} and need phonons and a photon for the excitation of an electron from the VBM to the CBM.

3.2 Solar cells

A thin film solar cell usually consists of at least five different layers, two electrodes, two charge transport layers and the absorber layer. These five layers form Schottky contacts between the (metal) electrodes and the semiconducting charge transport layers and semiconductor hetero contacts between the absorber and the charge transport layers (see figure 3.3).

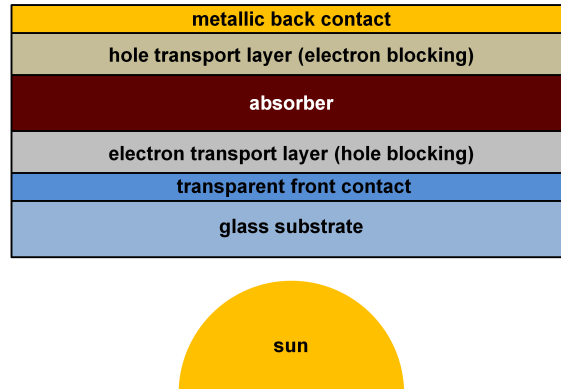


Figure 3.3.: Schematic illustration of a thin film solar cell consisting of a transparent front contact an electron transport layer, an absorber, a hole transport layer and a metallic back contact.

The radiation absorption and photoexcitation of charge carriers in the thin film solar cell shown in figure 3.3 takes place in the absorber layer. Accordingly, the absorber layer needs a high radiation absorption coefficient corresponding to the solar spectrum and a band gap which considers the trade off between the number of photoexcited charge carriers and their energy. This trade off is described by Shockley and Queisser and will be discussed below [48]. Besides the absorption coefficient and the band gap, the charge transport properties of the absorber layer are important. The mean free path and the life time of photoexcited electrons and holes need to be sufficiently large to let them reach the charge transport layers. Accordingly, the thickness of the absorber layer is determined by the trade off between being thick enough for a sufficient radiation absorption and thin enough to let the photoexcited charge carriers reach the HTL and the ETL, respectively. The hole (electron) transport layers shown in figure 3.3 have two requirements, they need to be hole (electron) conducting but they need also to form an electron (hole) blocking contact with the absorber. From the charge transport layers, the separated charges are transferred to the contact layers. Since the solar cell is illuminated through the front contact, the front contact needs to be transparent but also conductive. Those requirements are fulfilled by transparent conductive oxides (TCOs) like fluorine doped tin oxide (FTO) which is used in this work. The back contact does not need to be transparent. Hence, thin metal layers can be used.

The IV characteristics of a thin film solar cell are dominated by the contact properties between the different solar cell layers. Accordingly, the different contacts will be discussed briefly in the following and an equivalent circuit, used to describe the solar cells presented in this work, will be derived. This following section is based on the book Physics of Semiconductor Devices by S. M. Sze and Kwok K. Ng [47].

3.2.1 The p/n-contact

The p/n-contact is important for the minority charge carrier separation in a solar cell. A p/n-contact can be formed between the same semiconductor with different doping or different semiconductors. If the same semiconductor is used, the contact is called a homo junction, if different semiconductors are used, it is called a hetero junction. Since the homo junction is the simpler system, its IV characteristics will be discussed first and later developed to a hetero junction. The charge distribution, electric field, potential and band bending of a homo junction are presented in figure 3.4. Here, the case of an abrupt junction is used. In figure 3.4, ρ is the charge density, F the electric field and ψ the potential. N_A and N_D describe the donor and acceptor densities. W_{Dn} is the depletion region in the n-type semiconductor. All electrons from this region, induced by the n-doping, have recombined with the holes (induced by the p-doping) from the depletion region in the p-type semiconductor, W_{Dp} . Without electrons in the n-type and holes in the p-type semiconductor, only the ionized donor and acceptor atoms remain as charges in the depletion regions. The ionized donors are positively charged, the ionized acceptors negatively. Since only the space charges remain in the depletion regions, both regions together can be called the space charge region (SCR). The relation between charge, electric field and potential is given by the Poisson equation in (equation 3.2). To solve the Poisson equation, the following assumptions are made: (1) Both semiconductors are non-degenerate. (2) The depletion approximation is valid. All acceptors in the p-type semiconductor and all donors in the n-type semiconductor are ionized. (3) The semiconductor junction is in thermal equilibrium, no net current flows, the electric field outside the depletion region is zero and the positive and negative charges in the depletion region compensate each other. With those assumptions the Poisson equation can be solved resulting in the distributions shown in figure 3.4. Here, the electric field F describes the slope of the potential ψ and the charge density ρ the slope of the electric field. In addition, in equation 3.2, ϵ_s is the permittivity of the semiconductor. Accordingly, a constant charge distribution leads to a linear electric field and a quadratic potential distribution. From the potential distribution, the band energy diagram can be derived. Figure 3.4 shows that a depleted n-type semiconductor will show an upward band bending, while a depleted p-type semiconductor will show a downward band bending. The total band bending (the sum of the potentials in the n-type and p-type semiconductor) is called the built in potential ψ_{bi} .

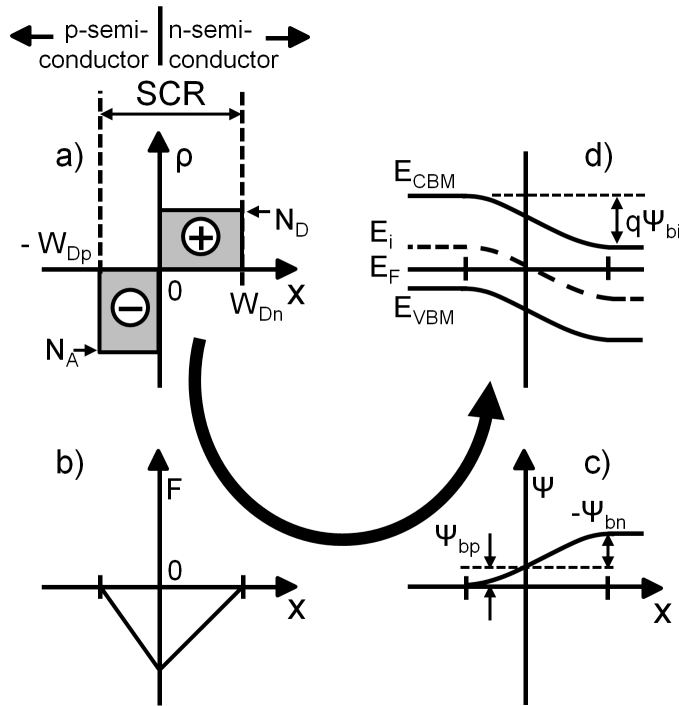


Figure 3.4.: Schematic depiction of the charge density (a), the electric field (b), the potential distribution (c) and the band energy diagram (d) of an abrupt p/n-homo junction. E_i denotes the intrinsic Fermi level of the semiconductor. [drawn after [47]]

$$-\frac{d^2\psi_{bi}}{dx^2} = \frac{dF}{dx} = \frac{\rho(x)}{\epsilon_s} \quad (3.2)$$

Across the p/n-junction, formally a diffusion current and a drift current flowing in opposite directions can be defined. Electrons will diffuse from the n-type to the p-type semiconductor. But, they will drift to the positive charged donor ions on the n-side. For the holes it is vice versa. Since an electric field is only present in the space charge region (see figure 3.4) the drift current is also confined to the space charge region. In addition, the drift current is limited by the amount of minority charge carriers in the space charge region. The diffusion current is driven by the concentration gradient of the charge carriers but is hindered by the potential barrier caused by the band bending. If no external potential is applied, both currents are equal and no net current exists (thermal equilibrium). If a potential is applied, it can reduce or enhance the potential barrier between the n-type and the p-type semiconductor and accordingly enhance or reduce the diffusion current through the space charge region. Accordingly, a diode can be operated in forward and reverse bias. In forward bias, the p side is on a positive potential compared to the n side, in reverse bias, the n side is on a positive potential compared to the p-side (see top row in figure 3.5).

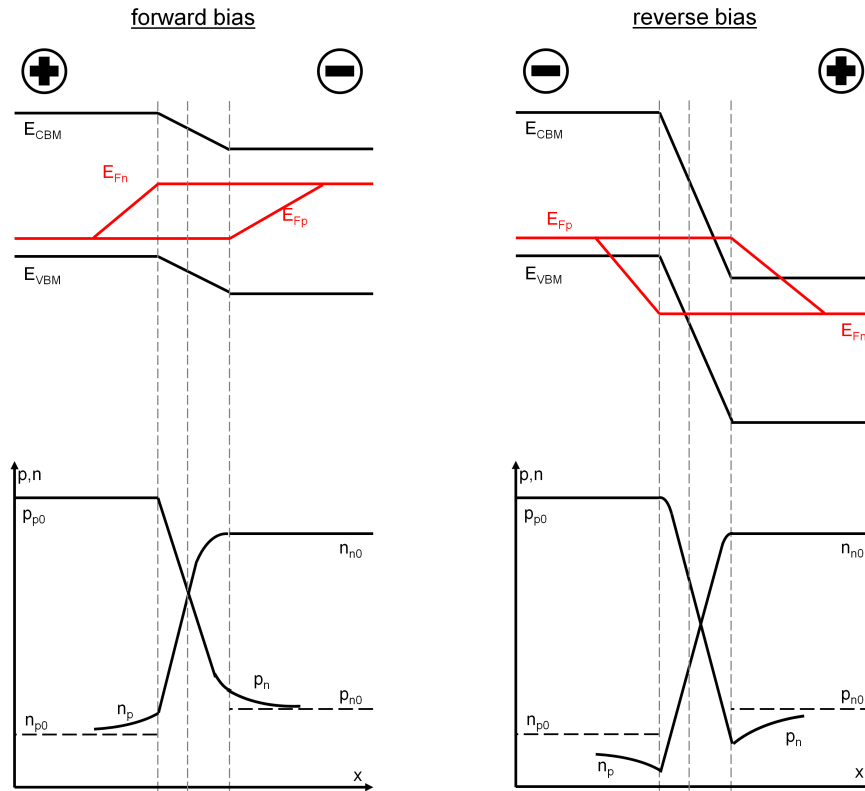


Figure 3.5.: Schematic depiction of the band energy diagram and the charge carrier densities for a p/n-homo junction under forward (left) and reverse bias (right). [drawn after [47]]

Under forward bias, the electron diffusion current in the space charge region from the n-side to the p-side and the hole diffusion current from the p-side to the n-side are enhanced. Since the generation of minority charge carriers in the space charge region is independent on the applied voltage, the drift current is, in a first approximation, unaffected by an applied voltage. This imbalance of the currents in the space charge region leads to minority charge carrier concentrations at the edges of the space charge region (p_n and n_p) which are higher than the equilibrium minority charge carrier concentrations p_{n0} and p_{n0} (middle row in figure 3.5). This increased minority charge carrier concentrations cause a minority charge carrier current away from the space charge region till the minority charge carriers have recombined with the majority charge carriers (or are extracted from the diode) and p_n and n_p equal p_{n0} and n_{p0} . In reverse bias, the diffusion currents are reduced and the space charge region (and the region close to its edges) is depleted of minority charge carriers. Under both bias conditions the minority charge carrier concentrations differ from their equilibrium values and can not be described with one Fermi level anymore. The use of quasi Fermi levels for the description of the disequilibrium concentrations of holes and electrons E_{Fp} and E_{Fn} solves the problem. The overall current through the diode is the sum of the electron current and the hole current. The electron current however is dominated by the electron current in the p-type semiconductor, the hole current by the hole current in the n-type semiconductor (bottom

row in figure 3.5). Accordingly, the total current through a p/n-junction is dominated by the minority charge carrier currents. The total current density is given by the Schockley equation in equation 3.3.

$$J = J_p + J_n = J_0 \left[e^{\frac{qV}{k_B T}} - 1 \right] \quad (3.3)$$

In equation 3.3, J_0 is the saturation current density, q the charge, k_B is Boltzmann's constant and V the applied voltage. The Schockley equation describes an ideal p/n-diode. The respective IV curves can be seen in figure 3.6 in linear and semilogarithmic scale.

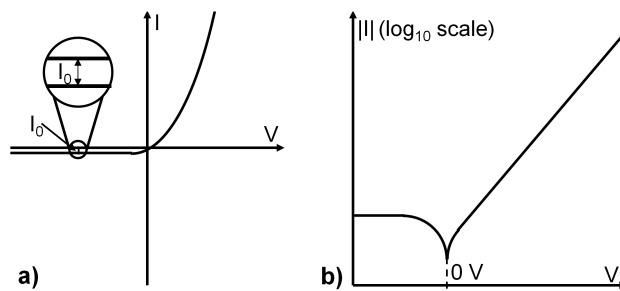


Figure 3.6.: Schematic IV characteristic of an ideal p/n-diode in linear (a) and semilogarithmic scale (b)

In a real diode, several effects can alter the shape of the IV curves as indicated in figure 3.7. Effects that can alter the shape of the IV curve are for example generation and recombination of charge carriers in the space charge region, pronounced charge carrier injection and the influence of series resistances. In addition, if a sufficiently high reverse bias is applied, the diode will break down [47]. For the reverse bias, two effects are shown in figure 3.7, the influence of finite parallel resistance R_p and the diode break down. The finite R_p describes a leakage current through the diode, which superimposes the diode current with its ohmic IV characteristics visible as a steady current increase with increasing reverse bias. The diode break down, however, can be caused for example by thermal instability of the diode, tunneling or avalanche multiplication [47]. As described above, the current of the ideal p/n-diode is the diffusion current. Hence, the diffusion regime in figure 3.7 could also be named the ideal regime. At small positive voltages, the diffusion current is superimposed by a recombination current of holes and electrons in the space charge region. This recombination current in the space charge region is a competing current to the diffusion current outside of the space charge region. Since it is also dependent on the minority charge carrier concentrations in the space charge region, it also shows an IV behavior of the type of equation 3.7, but with an additional factor of $1/2$ in the exponential exponent. This factor $1/2$ can be seen in the reduced steepness of the forward curve in figure 3.7 in the recombination region. If a resistance is in series with the diode, the current through the resistance and the current through the diode have

to be equal. Thus, for high positive voltages, the current through the resistance will limit the total current and flatten the IV characteristics in figure 3.7. The last effect shown in figure 3.7 is the high injection of minority charge carriers in such a way, that the minority charge carrier density is comparable to the majority charge carrier density. In this case, not only the diffusion current, but also the drift current have to be considered [47].

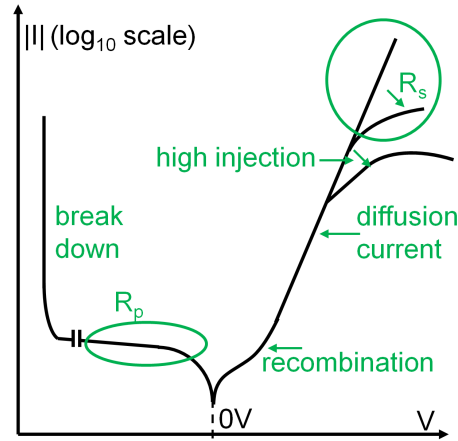


Figure 3.7.: Schematic IV characteristic of a real p/n-diode in semilogarithmic scale. Effects taken into account are a leakage current due to finite R_p and the diode break down for the reverse scan. For the forward scan, recombination of electrons and holes in the space charge region, the pronounced injection of minority charge carriers and the influence of a resistance in series to the diode are considered. The picture is drawn after [47].

In silicon solar cells, the photogenerated charges are separated over a p/n-homo junction. But for the thin film solar cells examined in this work, both semiconductor/semiconductor contacts (TiO_2/MAPI and $\text{MAPI}/\text{Spiro-MeOTAD}$) are hetero junctions. Thereby, the hetero junctions are separated into two groups, isotype junctions and anisotype junctions. Isotype junctions describe a hetero junction between two n- or two p-type semiconductors. Anisotype hetero junctions describe the contact between a p-type and an n-type semiconductor. Accordingly, the TiO_2/MAPI interface is an isotype hetero junction, as will be shown later experimentally, while the $\text{MAPI}/\text{Spiro-MeOTAD}$ interface is an anisotype hetero junction [49]. A schematic anisotype hetero junction between an n-type semiconductor with a smaller band gap and a p-type semiconductor with a wider band gap (for example the $\text{MAPI}/\text{doped Spiro-MeOTAD}$) is shown in figure 3.8. In figure 3.8, E_{vac} denotes the vacuum level, χ the electron affinity, ϕ the work function and I_p the ionization potential of the semiconductors. E_{VBM} is the valence band maximum, E_{CBM} the conduction band minimum, E_g the band gap and E_F the Fermi level. The conduction band offset ΔE_{CBM} is the difference of the electron affinities and the valence band offset ΔE_{VBM} the differences of the ionization potentials. ΔE_{CBM} and ΔE_{VBM} are independent on the doping as long as E_g and χ are independent on the doping. The band bendings ψ_b however are caused by the alignment of the Fermi levels and hence are dependent on the doping levels of the semiconductors. More specifically: the fraction of the band bending in a

semiconductor from the complete band bending at the junction ($\phi_2 - \phi_1$) and the width of the depletion region in the semiconductor are reversely proportional to the doping concentration in the semiconductor. The current density over the contact can be described by equation 3.4.

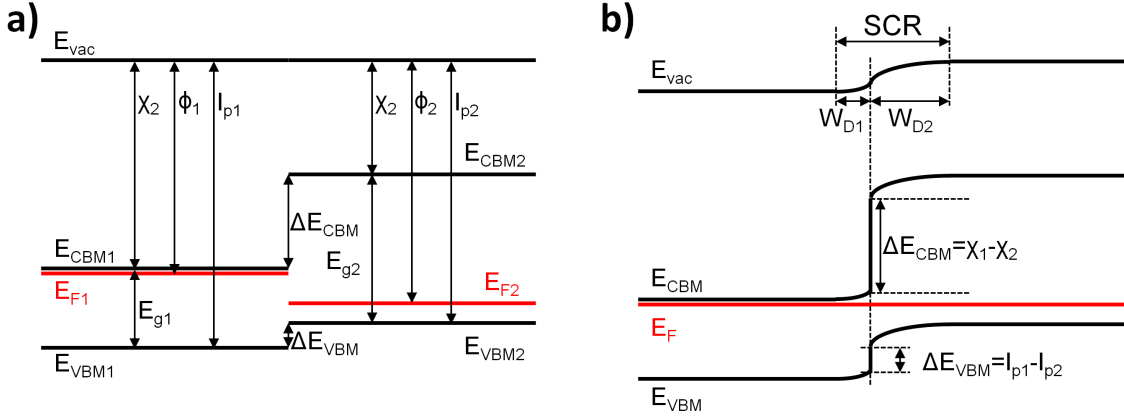


Figure 3.8.: Schematic drawing of an anisotype p/n-junction before (a) and after (b) the thermal equilibrium is established. [drawn after [47]]

$$J = J_n + J_p = \left(\frac{qD_{n2}n_{i2}^2}{L_{n2}N_{A2}} + \frac{qD_{p1}n_{i1}^2}{L_{p1}N_{D1}} \right) \cdot \left[e^{\frac{qV}{kT}} - 1 \right] \quad (3.4)$$

In equation 3.4, q is the charge, D is the diffusion coefficient, n_i is the equilibrium charge carrier concentration, L is the diffusion length, N_A is the acceptor concentration in the p-type semiconductor and N_D is the donor concentration in the n-type semiconductor. The subscript 1 denotes the n-type semiconductor, 2 the p-type semiconductor. The subscripts n and p denote values for electrons and holes, respectively. Since J_n and J_p in equation 3.4 are dominated by the minority charge carrier diffusion, equation 3.4 has the same form as equation 3.3. Only the J_0 is different, taking into account the different semiconductors. If the same semiconductor was used on both sides of the diode, equation 3.4 would reduce to equation 3.3.

In contrast to the MAPI/Spiro-MeOTAD anisotype junction, the TiO_2 /MAPI junction is an isotype junction. A schematic band energy diagram for the isotype junction is shown in figure 3.9. The current over the contact can again be described in the form of equation 3.3. But, the J_0 differs significantly from the J_0 of the p/n-junction. This is because the current through the junction is dominated by the thermionic emission of majority charge carriers and not by the diffusion of minority charge carriers.

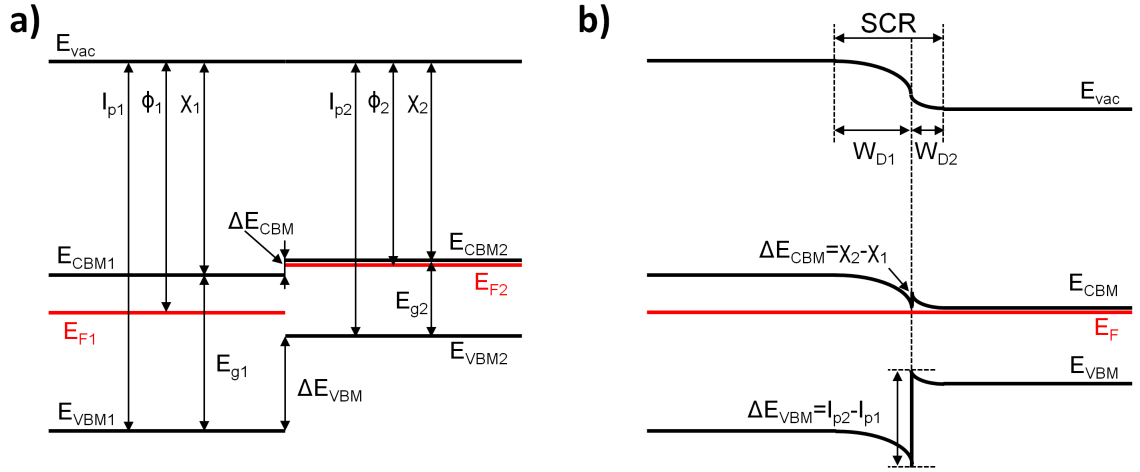


Figure 3.9.: Schematic drawing of an isotype n/n-junction before (a) and after (b) the thermal equilibrium is established. [drawn after [47]]

3.2.2 The Schottky contact

In addition to the semiconductor junctions, each solar cell contains metal/semiconductor junctions, so called Schottky junctions. In the solar cell layer stack used for this work, the FTO/TiO₂ junction is a junction between a degenerate semiconductor to be approximated by metal and an n-type semiconductor, the Spiro-MeOTAD/Au junction is a junction between a p-type semiconductor and a metal. If a potential is applied on a Schottky contact, the barrier height for the current from the metal to the semiconductor will not be altered. Only the barrier height and hence the current over the barrier from the semiconductor to the metal will be reduced in forward bias and enlarged in reverse bias, leading to a net current from the semiconductor to the metal under forward bias and from the metal to the semiconductor under reverse bias. The current through the Schottky junction is, in contrast to the p/n-junction, a majority charge carrier current and can often be described by the thermionic emission after Bethe. The respective dependence of the current density on the voltage for a contact between a metal and an n-type semiconductor is given in equation 3.5.

$$J_n = \left[A^* T^2 e^{-\frac{q\Phi_{Bn}}{kT}} \right] \left[e^{\frac{qV}{kT}} - 1 \right] \quad (3.5)$$

In equation 3.5, A^* is the effective Richardson constant and Φ_{Bn} the equilibrium barrier height for electrons. The positive current direction goes from the semiconductor to the metal. Among other boundary conditions for the description with the thermionic emission, an important one is that the charge carrier supply to the barrier in the semiconductor is sufficient to make the thermionic emission over the barrier the limiting process for the charge transport. This condition is given either by high charge carrier mobilities in the semiconductor or by sufficiently thin semiconducting layers. The hole mobility in Spiro-

MeOTAD is, even if doped, in the range of $\approx 2 \cdot 10^{-3} \text{cm}^2 \text{V}^{-1} \text{s}^{-1}$ [50]. With this value, the current voltage characteristics of the Spiro-MeOTAD/Au contact can probably not be described with the thermionic emission model alone. The charge carrier supply through the depletion region can be taken into account by the diffusion theory by Schottky [47]. The thermionic emission diffusion theory by Crowell and Sze combines the thermionic emission theory and the diffusion theory and results in equation 3.6.

$$J = A^{**} T^2 e^{-\frac{q\Phi_{Bn}}{kT}} \left[e^{\frac{qV}{kT}} - 1 \right] \quad (3.6)$$

In equation 3.6, Φ_{Bn} is the equilibrium barrier height for electrons. The reduced effective Richardson constant A^{**} contains the information whether the emission over the barrier is limited by the thermionic emission or by the diffusion processes. But, since no material properties are derived from the saturation currents of the Schottky diodes in this work, they are described by the generalized expression shown in equation 3.7.

$$J = J_0 \left[e^{\frac{qV}{kT}} - 1 \right] \quad (3.7)$$

In several semiconducting devices like solar cells, contacts between a metal and a semiconductor are unavoidable but their diode IV characteristics are not desired. The contacts are desired to be ohmic. To reach this, two ways are possible. The first one is to keep the barrier height is small as possible to ease thermionic emission over the barrier. The second approach is to keep the barrier width as small as possible, for example due to higher doping in the semiconductor or the implementation of highly doped interlayers, to allow tunneling through the barrier or thermionic emission activated tunneling through the barrier.

3.2.3 The equivalent circuit in the dark

With the IV characteristics of the three different types of diodes present in the examined solar cells, an equivalent circuit for the solar cell can be derived. This is done in figure 3.10.

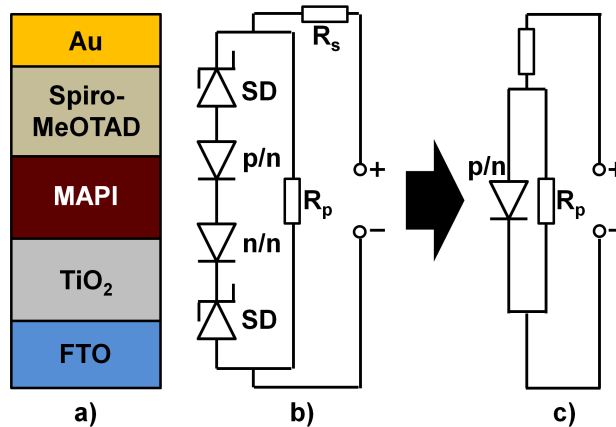


Figure 3.10.: Schematic layer stack of the solar solar cells used in this work (a) and equivalent circuits for a solar cell in the dark (b) and (c). In (c) the simplified equivalent circuit is shown, possessing only a substitutional p/n-diode. SD denotes a Schottky diode.

Since the influences of the different diodes can not be separated for the IV measurements performed in this work and all present diode types can be described by an equation in the form of equation 3.3, a reduced equivalent circuit, with only one substitutional p/n-diode will be used (figure 3.10 c). However, the presence of the other three junctions will contribute to J_0 and should always be kept in mind when evaluating the IV characteristics of a solar cell. The series resistance R_s includes every resistance in series with the solar cell, for example the resistance of the complete IV measurement setup and the resistances of the gold, Spiro-MeOTAD, TiO₂ and FTO layers. Due to imperfections of the layers, e.g. pin holes or strong variations of the layer thickness, a fraction of the current running through the solar cell will bypass the diode. This current is described by R_p . In addition, R_p accounts for the loss of charge carriers due to certain recombination processes. In total, for a good solar cell performance, a large R_p and a small R_s are desirable.

3.2.4 IV characteristics under light

For all of the descriptions above, the solar cell was in the dark. In the following section, the effect of illumination on the solar cell will be described and the dark equivalent circuit developed in figure 3.10 will be extended to the dark/light equivalent circuit in figure 3.11. Please note that for the description of the equivalent circuits not the current density but the absolute current is used, for convenience.

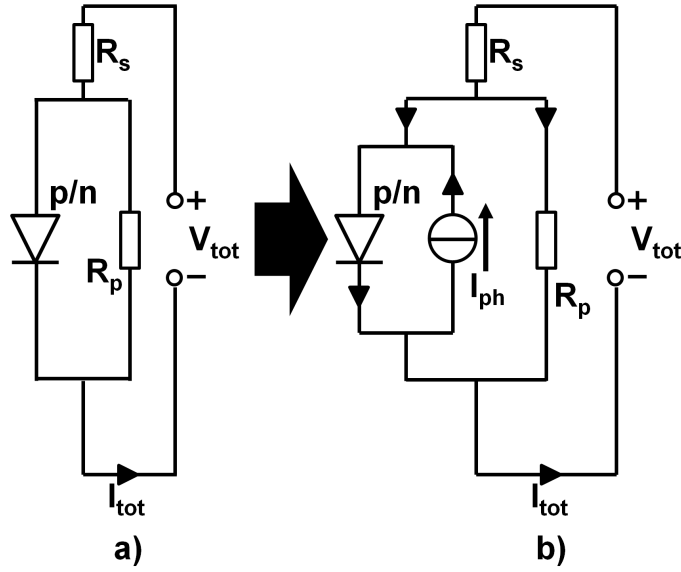


Figure 3.11.: Equivalent circuits for a solar cell in the dark (a) and operated under illumination (b). The photogenerated current is described by an ideal current source.

Figure 3.11 a shows the equivalent circuit in the dark, figure 3.11 b under illumination. The difference between both circuits is the photocurrent, symbolized by an ideal current source in figure 3.11 b. The direction of the photocurrent is opposite to the forward current of the diode. Hence, the photogenerated electrons will move towards the n-type semiconductor side and the photogenerated holes towards the p-type semiconductor side. The IV characteristics of the illuminated solar cell are shown in equation 3.8.

$$I_{\text{tot}} = I_s = I_{\text{cell}} = \frac{V_s}{R_s} = \frac{V_p}{R_p} + I_{p/n} - I_{ph} \quad (3.8)$$

In equation 3.8, I_s is the current through the series resistance and I_{cell} the current through the solar cell. Both currents have to be equal due to the serial arrangement. Hence, the smaller current will dominate the IV characteristics of the total current I_{tot} . The other measures in equation 3.8 are the series resistance R_s , the voltage dropping over R_s , V_s the resistance parallel to the solar cell R_p , the voltage dropping over R_p , V_p , the current through the substitutional p/n-diode $I_{p/n}$ and the photogenerated current I_{ph} . Under the condition that the series resistance R_s is sufficiently small to make I_s sufficiently large, I_{tot} will be dominated by I_{cell} and can be written as equation 3.9.

$$I_{\text{tot}} = I_0 \left[e^{\frac{q}{kT} \cdot (V_{\text{tot}} - R_s \cdot I_{\text{tot}})} - 1 \right] - I_{ph} + \frac{V_{\text{tot}} - R_s \cdot I_{\text{tot}}}{R_p} \quad (3.9)$$

Due to the parallel arrangement V_p has to be equal to V_{sc} and due to the serial arrangement of R_s it can be derived that $V_{sc} = V_p = V_{tot} - R_s \cdot I_{tot}$. In the IV characteristics of a solar cell, two points are special, the open circuit voltage, where $I_{tot}=0A$ and the short circuit current where $V_{tot}=0V$. Figure 3.12 shows the equivalent circuit of a solar cell in open circuit and short circuit conditions.

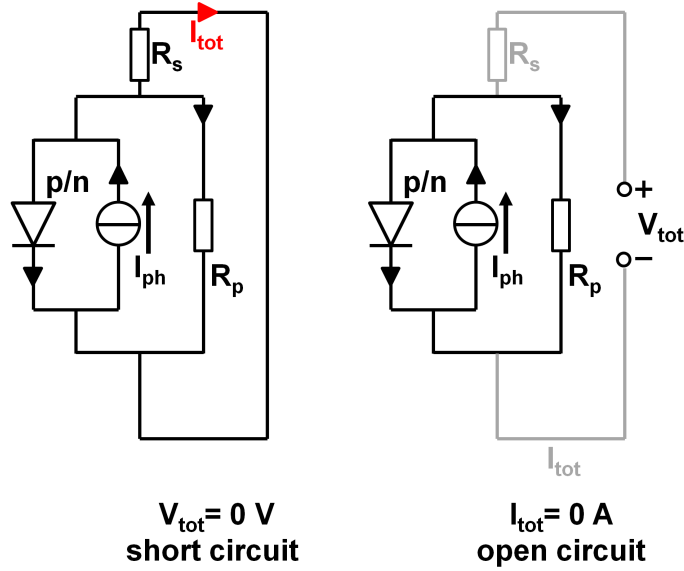


Figure 3.12.: Equivalent circuits for a solar cell operated under short circuit (left) and open circuit (right) conditions. Those elements of the equivalent circuit which are excluded by the respective condition are drawn in gray. Note that the total current will change direction in short circuit conditions, due to the dominance of the photocurrent.

Under open circuit conditions, no total current flows through the circuit. Hence the term $R_s \cdot I_{tot}$ vanishes and equation 3.9 can be simplified to equation 3.10. Equation 3.10 shows that, under open circuit conditions, the IV characteristics are not directly dependent on R_s . Under open circuit conditions, V_{tot} is called open circuit voltage (V_{oc}). The V_{oc} develops due to the accumulation of photogenerated charges at the contacts of a solar cell and can be considered as the energetically splitting of the quasi Fermi levels, as a first approximation.

$$0 = I_0 \left[e^{\frac{q}{kT} \cdot V_{tot}} - 1 \right] - I_{ph} + \frac{V_{tot}}{R_p} \quad (3.10)$$

In case that the solar cell is operated under short circuit conditions, $V_{tot}=0V$, equation 3.9 can be simplified to equation 3.11.

$$I_{tot} = -I_{ph} + I_0 \left[e^{\frac{q}{kT} \cdot (-R_s \cdot I_{tot})} - 1 \right] - \left(\frac{R_s}{R_p} \cdot I_{tot} \right) \quad (3.11)$$

Similar to the open circuit voltage, the total current under short circuit conditions is called the short circuit current I_{sc} . For an ideal case, the short circuit current would be $-I_{ph}$. The current contributions from the diode and the parallel resistance describe the deviations of a real solar cell from an ideal solar cell. Figure 3.13 shows the schematic IV characteristics of a solar cell in the dark and under illumination. The comparison of equation 3.9 with equation 3.3 shows that the IV characteristics of a solar cell in the dark correspond with the ones of a p/n-diode. Hence all effects described in figure 3.7 are also valid for a solar cell.

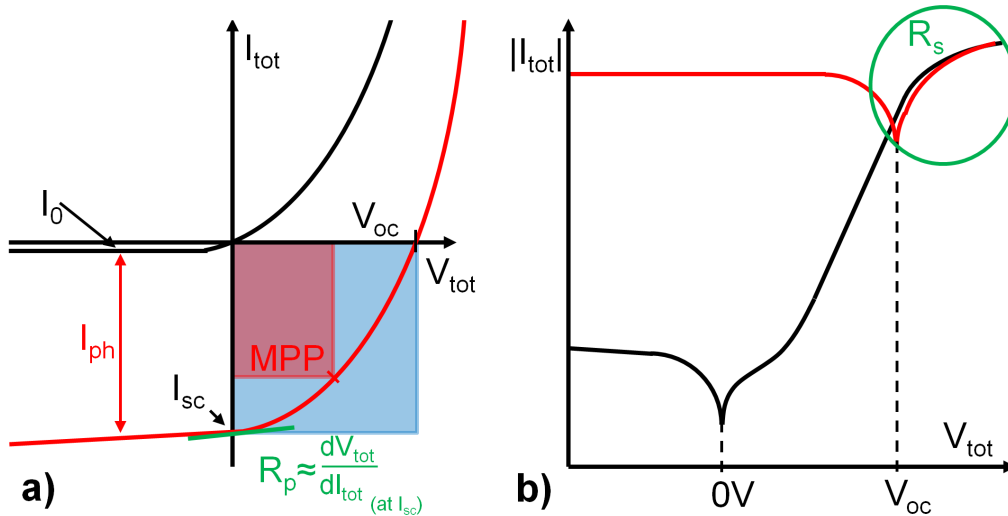


Figure 3.13.: Schematic IV curve of a solar cell in linear (a) and semilogarithmic (b) scale. The IV curves measured in the dark are denoted in black, the ones measured under illumination are denoted in red. The $|I_{tot}|$ axis in b is given in \log_{10} scale. R_p is determined on the IV characteristics of the solar cell under illumination to include the recombination of photogenerated charge carriers.

The IV curve of the illuminated solar cell however is less influenced by the effects described in figure 3.7. The main deviation of the illuminated IV curve from an ideal diode characteristic is the current limitation by the series resistance, as can be seen in figure 3.13 b. In addition to the solar cell parameters which are already discussed, figure 3.13 shows an additional one, the maximum power point MPP. This point describes the voltage at which the solar cell produces the largest possible electrical power output. The fill factor describes the ratio between the actual maximum of the electrical power output (MPP) and the product of V_{oc} and I_{sc} . Graphically, the fill factor is the ratio of the blue to the red square in figure 3.13 (see also equation 3.12).

$$FF = \frac{V_{MPP} \cdot I_{MPP}}{V_{oc} \cdot I_{sc}} \quad (3.12)$$

The efficiency η of a solar cell is defined as the ratio of the maximum of the electrical power output P_{el} and the radiation power input P_{rad} and can be calculated with equation 3.13. Since P_{rad} is usually given in Wm^{-2} , the active area of the solar cell A_{cell} is included in equation 3.13.

$$\eta = \frac{P_{el}}{P_{rad}} = \frac{V_{MPP} \cdot I_{MPP}}{P_{rad} \cdot A_{cell}} = \frac{V_{oc} \cdot I_{sc} \cdot FF}{P_{rad} \cdot A_{cell}} \quad (3.13)$$

3.2.5 Solar spectrum and Shockley-Queisser limit

The radiation spectrum emitted from the sun reaches from the infra red to the UV regime and can be approximated with the radiation spectrum of a black body at 5800 K [51]. The spectrum can be plotted as power density per photon wavelength and is shown in figure 3.14. The integral over all photon energies yields a power density of $1353 W/m^2$. This power density is achieved outside of the earth's atmosphere and is relevant for solar cells in space applications (e.g. satellites). For planetary solar panels, the radiation absorption in the atmosphere has to be considered. This is done by weighting the solar spectrum with the air-mass coefficient d_{ath} which can be calculated with equation 3.14 [51].

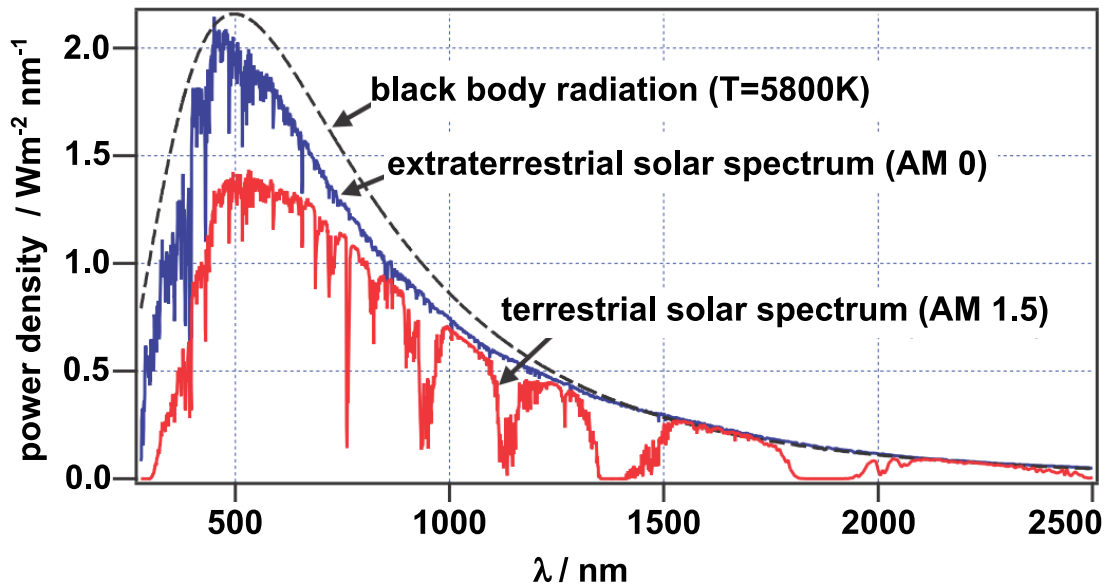


Figure 3.14.: Solar spectrum just outside the earth's atmosphere (AM0) and at the surface for an angle of incidence around 48° (AM1.5). The spectrum of a black body at 5800 K without atmospheric absorption is given for comparison. [Image taken from [52] and modified, original image drawn according to [53].]

$$d_{ath} = \frac{d_{ath0}}{\cos(\gamma)} \quad (3.14)$$

In equation 3.14, $d_{\text{ath}0}$ is the thickness of the atmosphere normal to the earth surface and γ the angle of incidence with respect to the surface normal. The weighting with the air-mass coefficient is denoted as AMx spectrum with $x=0$ for the spectrum just outside the earth's atmosphere and $x=1$ for direct incidence. For moderate climate regions (e.g. northern Europe) the angle of incidence is around 48° which corresponds to an AM1.5 spectrum. This spectrum is used as the standard spectrum for solar cell efficiency determination and corresponds to an integrated power density of 1000 W/m^2 [51].

A theoretical efficiency maximum of a single junction solar cell in dependence on the band gap of the absorber material was published by Shockley and Queisser in 1961 [48] and is schematically shown in figure 3.15. For a band gap around 1.6 eV, the detailed balance maximum (theoretical efficiency maximum) is close to 30%, under the assumption that the solar cell is irradiated from a complete hemisphere. To estimate the efficiency maximum, Shockley and Queisser introduced a voltage factor, describing that the open circuit voltage is smaller than the band gap of the absorber at temperatures above 0K. They also introduced an impedance matching factor which is referred to as fill factor in the equations above. This fill factor takes into account, that I_{MPP} and V_{MPP} are always smaller than I_{sc} and V_{oc} [48].

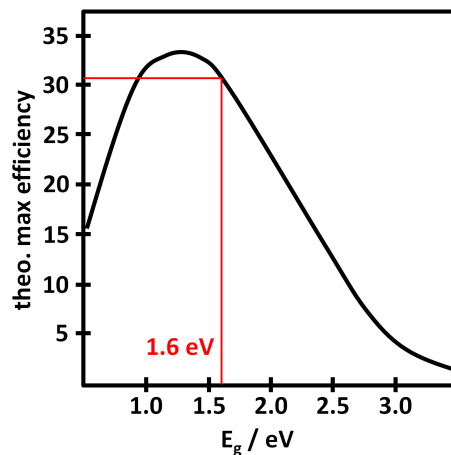


Figure 3.15.: Theoretical maximum efficiency of a single junction solar cell in dependence on the absorber band gap according to the Shockley-Queisser limit under AM1.5G illumination. [drawn after [54]]

3.3 Thin film deposition under high vacuum conditions

Thin film deposition by sublimation of precursors in powder form is the main fabrication method used for this work. Hence, in the following, a short overview of the basic mechanisms involved in thin film fabrication from the gas phase will be presented.

3.3.1 Adsorption on solid surfaces and layer growth

The first step of a thin film deposition is the adsorption of layer atoms or molecules from the gas phase onto a solid (substrate) surface. Hence, general terminology describing adsorption and film growth will be presented in the following. This section is based on the books “Solid Surfaces, Interfaces and Thin Films” by H. Lüth and “Physikalische Chemie” by P. W. Atkins and J. de Paula, which are recommended for further reading [55, 56].

Adsorption can be separated into two processes, physisorption and chemisorption. Physisorption describes the adhesion of an atom or a molecule onto a surface by Van der Waals interactions. Those are long range interactions, but weak in strength. The physisorption is schematically shown in figure 3.16 a. It is characterized by a shallow potential well and a large equilibrium distance z_0 between the potential well minimum and the sample's surface. In contrast to physisorption, chemisorption describes the adhesion of atoms or molecules to a surface by chemical bonds, covalent or ionic. The chemical bonds have a shorter range than the Van der Waals forces but the interactions are stronger (figure 3.16 b). A special case of the chemisorption is the dissociative chemisorption shown in figure 3.16 c. Here, a molecule is physisorbed at first non-dissociative. But, the potential well minimum of the physisorption is only a local minimum. The global minimum of the potential energy is reached in the potential well minimum of the chemisorption, which can be reached by the dissociation of the physisorbed molecule. To reach the potential well of the chemisorption, the activation energy E_{act} has to be overcome.

After the description of the different adsorption mechanisms, the adsorptions kinetics will be discussed below. The coverage of a solid surface by adsorbate molecules or atoms is determined by the adsorption and the desorption of the adsorbate species. Neglecting desorption for a moment, the evolution of the surface coverage can be described by the number of adsorbate molecules which hit the surface (condense on the surface) per unit area and time (dN_{cond}/dt) and the probability that those molecules will stick to the surface (equation 3.15). This probability is described by the sticking coefficient S .

$$\Theta(t) = \frac{1}{\Theta_0} \cdot \int S \frac{dN_{cond}}{dt} dt = \frac{1}{\Theta_0} \cdot \int S \frac{P}{\sqrt{2\pi M k_B T}} dt \quad (3.15)$$

In equation 3.15, $\Theta(t)$ is the relative coverage (occupied adsorption sites divided by available adsorption sites), Θ_0 is the number of available adsorption sites, p is the pressure, M the molecular weight of the adsorbing species, k_B is Boltzmann's constant and T is the temperature.

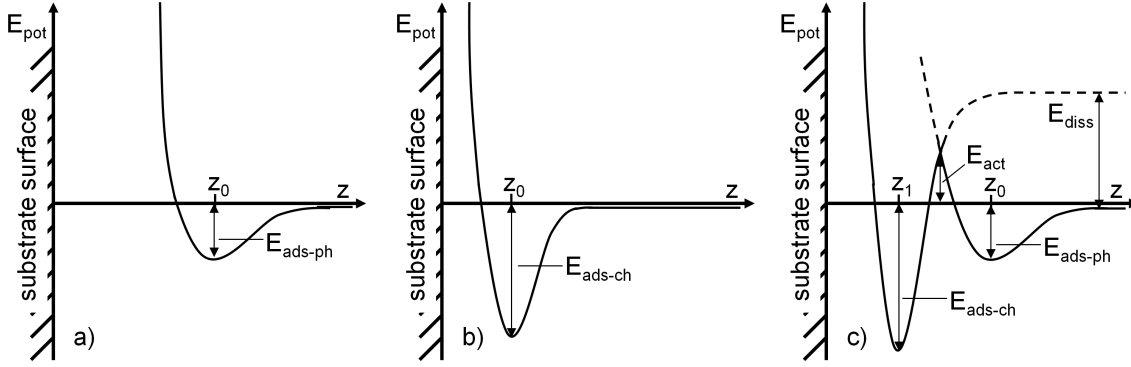


Figure 3.16.: Schematic illustration of the potential energy E_{pot} in dependence on the distance z from the samples surface for physisorption a), non-dissociative chemisorption b) and dissociative chemisorption c). The adhesion between the adsorbed species and the surface is denoted with E_{abs-ph} for physisorption and E_{abs-ch} for chemisorption. E_{diss} is the dissociation energy of the molecule during the dissociative chemisorption and E_{act} the activation energy for the dissociation. z_0 and z_1 are the equilibrium distances of the adsorbed species from the surface.

3.3.2 Temperature dependence of the sublimation pressure

The closed space sublimation possesses some specific attributes compared to an open sublimation. Due to the closed crucible, the reaction volume is less influenced by the vacuum pumps, allowing a higher pressure in the crucible compared to the surrounding chamber. Since the crucible pressure can be higher than the chamber pressure, higher partial pressures of the sublimed material can be achieved inside the CSS crucible compared to an open sublimation. In addition, the distance between the precursor material and the substrate is shorter compared to an open sublimation. Furthermore, since the crucible and the substrate are both heated, the complete reaction volume is heated. Last but not least, the cross section of the source equals approximately the size of the substrate with the vector of the deposition parallel to the substrate's normal, reducing directional effects of the deposition and facilitating a homogeneous deposition.

The sublimation pressure, the pressure at which the gaseous and the solid phase of a substance are in equilibrium for a given temperature, can be described with the Clausius-Clapeyron equation (equation 3.16) [56].

$$\frac{d \ln(p_s)}{dT} = \frac{\Delta_S H}{RT^2} \quad (3.16)$$

In equation 3.16, p_s is the sublimation pressure, T the temperature, R the ideal gas constant and $\Delta_s H$ the sublimation enthalpy. Under the condition, that $\Delta_s H$ is independent on the temperature, equation 3.16 can be integrated to equation 3.17 [56].

$$p_s = p_s^* \cdot e^{-\zeta} \text{ with } \zeta = \frac{\Delta_s H}{R} \cdot \left(\frac{1}{T} - \frac{1}{T^*} \right) \quad (3.17)$$

In equation 3.17, p^* is the (known) sublimation pressure at the temperature T^* . To account for the escape of sublimed molecules from the CSS crucible into the vacuum chamber, equation 3.17 is extended by the temperature dependent constant $p_{\text{loss}}(T)$, resulting in equation 3.18.

$$p_s = p_s^* \cdot e^{-\frac{\Delta_s H}{R} \cdot \left(\frac{1}{T} - \frac{1}{T^*} \right)} - p_{\text{loss}}(T) \quad (3.18)$$

The sublimation pressure is an upper limit of the actual partial pressure in the crucible. In addition, the time needed to establish an equilibrium pressure might be temperature dependent and needs to be considered in a quantitative description of the pressure evolution. Nevertheless, equation 3.18 can serve for a qualitative approximation of the temperature dependence of the pressure inside the crucible during a CSS process. With this, equation 3.15 can be rewritten to equation 3.19 which approximately describes the surface coverage during a CSS process in dependence on the transformation time t_t ¹, the crucible temperature T_c and the substrate temperature T_s .

$$\Theta(t_t) = \frac{1}{\Theta_0} \cdot \int S \cdot \frac{p_s^* \cdot e^{-\frac{\Delta_s H}{R} \cdot \left(\frac{1}{T_c} - \frac{1}{T^*} \right)} - p_{\text{loss}}(T_c)}{\sqrt{2\pi M k_B T_s}} dt_t \quad (3.19)$$

3.3.3 Transformation - inward diffusion and reaction

The first step of the CSS process is the sublimation of MAI. Thereby, MAI is reported to sublime dissociatively [42, 57]. While Juarez-Perez report the dissociation of MAI during the sublimation mainly into CH_3I and NH_3 , Bækbo et al. found CH_3NH_2 and HI as dominant decomposition products for the sublimation of MAI under UHV conditions, in the temperature regime up to 130°C [42, 57]. However, for temperatures above 160°C Bækbo et al. also observe the presence of NH_3 and CH_3I which they relate to the further decomposition of HI and CH_3NH_2 at elevated temperatures [42].

¹ At this point, the transformation time t_t is actually a deposition time. However, in order to comply with the nomenclature used in the experimental and the results chapters with respect to the CSS process step, it is introduced here already as transformation time.

The actual transformation of a lead salt layer to perovskite can be determined by three processes, the adsorption of the MAI dissociation products on the layer, their inward diffusion and the transformation of lead salt layer to MAPI. The adsorption process step is already described above, the transformation step will be discussed in detail in the results chapter. The inward diffusion of a diffusing species into a layer can be described by solving Fick's second law under consideration of certain boundary conditions. Fick's second law is shown in equation 3.20 for a case in which the diffusion is limited to one direction. The assumption of an one-directional diffusion is considered reasonable for this work since the inward diffusion of the gaseous species into the lead salts during the CSS process step will be directed from the layer surface towards the substrate. The following description is based on the book "Materials Science and Engineering" by Callister et al. [58].

$$\frac{\partial c(x, t)}{\partial t} = D \cdot \frac{\partial^2 c(x, t)}{\partial x^2} \quad (3.20)$$

In equation 3.20, $c(x, t)$ is the time dependent concentration at the position x , t the time and D the diffusion coefficient. As boundary condition for the solution of Fick's second law it is assumed that the diffusing species have a constant concentration at the position $x=0$ and serve as a stationary constant source (non-steady-state diffusion). In addition, it is assumed that the concentration of the diffusing species is 0 at $t=0$ in the whole layer. The diffusion coefficient D is assumed to be independent on the concentration. Considering this boundary conditions, the solution of Fick's second law can be described with the error function in equation 3.21.

$$c(x, t) = c_0 - c_0 \cdot \operatorname{erf}\left(\frac{x}{2\sqrt{Dt}}\right) \quad (3.21)$$

In equation 3.21, c_0 is the constant concentration directly at the layer surface. The solution of Fick's second law is taken from ref. [58]. Here, the additional boundary condition of a semi-infinite solid $0 \leq x \leq \infty$ is formulated. However, even if the x coordinate is limited to $0 \leq x \leq d$, with d the layer thickness, equation 3.21 is assumed to be suited to qualitatively describe the inward diffusion of a diffusing species into a layer in this work. The diffusion coefficient D is dependent on the temperature T . This dependence can be described with equation 3.22.

$$D(T) = D_0 \cdot e^{-\frac{E_{\text{act}}}{k_{\text{B}}T}} \quad (3.22)$$

In equation 3.22, $D(T)$ is the diffusion coefficient at the temperature T , D_0 a prefactor, E_{act} is the activation energy of the diffusion process and k_B is Boltzmann's constant. As soon as CH_3I and NH_3 start to diffuse into the lead salt layers, the chemical reactions have to be considered. The velocity of the transformation can be diffusion controlled, in case the reaction velocity is faster than the diffusion velocity, or reaction controlled, in case the diffusion velocity is faster than the reaction velocity. The ratio of the reaction and the diffusion velocity can be described by the Péclet number.

Equations 3.21 and 3.22 describe a rather simple case for the inward diffusion of an adsorbed species and neglect the influence of different bulk diffusion mechanisms on one hand and of grain boundary and pinhole diffusion on the other hand. Besides, the inward diffusion of adsorbed species into the lead salt layer will be dependent on their properties, for example their size. In addition, even if NH_3 and CH_3I or HI and CH_3NH_2 , respectively, are the main products of the dissociative sublimation of MAI, the mass spectrometry measurements of Juarez-Perez et al. and Bækbo et al. indicate the presence of numerous other dissociation products in the gas phase [42, 57]. Furthermore, during the adsorption on the layer surface, the adsorbed species might dissociate into their components. Hence, the adsorption and desorption kinetics, the diffusion mechanisms and kinetics, and the different sublimation pressures of a broad range of chemical species as well as the different possible chemical reactions of the adsorbed molecules with the lead salt base layer need to be considered to quantitatively describe the transformation of a lead salt to MAPI in the CSS process, making such a description quite challenging.

3.4 Analysis techniques

In this section, the working principle of the analysis techniques used in this work will be summarized.

3.4.1 Photoelectron Spectroscopy

This summary is based on the chapter about photoelectron spectroscopy in the PhD Thesis of Dr. Mirko Weidner which gives an in depth overview over the topic and is recommended for further reading [59], technical details are taken from the manual of the ESCALAB 250XL PE spectrometer by Thermo Fisher Scientific [60].

During a photoelectron spectroscopy (PES) experiment, a sample is irradiated with electromagnetic radiation. Usually X-rays (XPS) or radiation with wavelengths in the UV regime (UPS) are used. In the sample, the energy of the incident photons is transferred to electrons of the sample atoms. If the energy of the incident photons is sufficiently high to excite a photoelectron out of the sample, the kinetic energy of the photoelectron can be measured and provides information about the atom and the orbital it originates from. The photoemission process is often described with the three step model by Berglund and Spicer. The first step is the photoionization of a sample atom. Here, an electron is excited from an atomic orbital, leaving behind a hole and the atom in an excited state. Accordingly, PES does not measure the energy of the atom in its ground state (initial state) but the energetic difference between the atom in its ground and in its excited state (final state). All effects taking place simultaneously to the photoionization process are called intrinsic effects. After the photoexcitation, the electron needs to travel to the sample surface (step 2) and escape from the sample (step 3). Effects influencing the photoelectron (for example altering its kinetic energy) during step two and three are referred to as extrinsic effects.

A schematic depiction of an ESCALAB 250XL PE spectrometer is shown in figure 3.17. The whole system is pumped down to ultra high vacuum in order to avoid inelastic scattering of the photoelectrons with atmospheric atoms or molecules. The sample is placed on a sample stage, which is usually grounded during XPS measurements and put on a defined potential during UPS measurements. In this work, the sample was either irradiated by a monochromatized X-ray source ($\text{AlK}\alpha$ with 1486.6 eV) or a non-monochromatized UV lamp (HeI with 21.22 eV). In addition to the photoelectron excitation sources, the sample can be irradiated with a white light lamp, with electron and ion sources for charge compensation and the sample surface can be treated with an argon sputter gun. The photoelectrons are collected and focused by a magnetic collection lens and further focused by two electrostatic lenses on the entrance slit of the hemispherical analyzer. At the entrance slit, the photoelectrons are retarded by the retardation voltage V_R to the pass energy E_{pass} . The pass energy is defined by the potential of the analyzer hemispheres. Only electrons with a kinetic energy inside the range $E_{\text{pass}} \pm \Delta E$ (which is not the ΔE used for

the calibration of the spectrometer) can pass through the analyzer and reach the channeltrons. With decreasing E_{pass} , ΔE also becomes smaller leading to improved resolution on the cost of decreasing intensity. All measurements in this work were performed with the spectrometer in constant analyzer energy mode, meaning that E_{pass} is independent on the kinetic energy of the photoelectrons. The value defining which binding energy is probed is the retardation voltage V_R . In figure 3.17, it can be seen that the photoelectrons enter the analyzer not parallel to the lens column but at an angle. Accordingly, their path is not only defined by their kinetic energy but also by their entrance angle. Thereby, every channeltron is reached by electrons with the energy $E_{\text{pass}} \pm \Delta E$. The arrangement of the channeltrons accounts for the entrance angle of the photoelectrons and does not reassemble the uncertainty of the pass energy ΔE . Further information about the technical realization of the PES measurements using the ESCALAB 250XL spectrometer can be found in the ESCALAB 250XL manual [60].

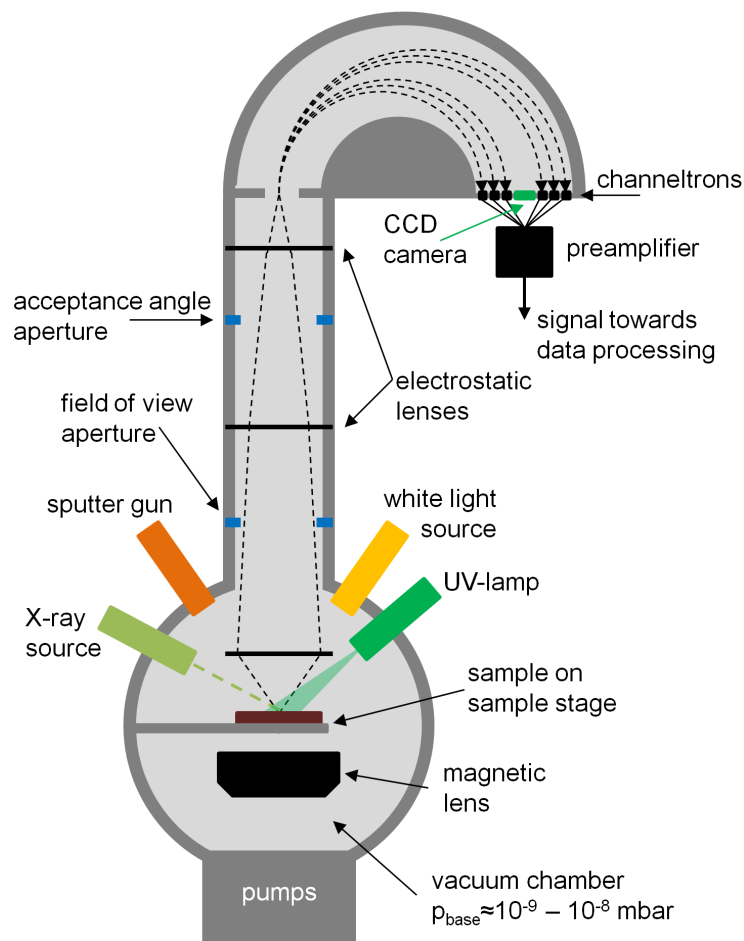


Figure 3.17.: Schematic arrangement of a PES measurement setup. The dashed lines denote the outer boundaries of the path of the photoelectrons when the magnetic collection lens is used. The dashed lines inside the hemispherical analyzer correspond to the paths of those electrons which have exactly the energy E_{pass} .

During a PES measurement, the kinetic energy of the photoelectrons is measured. But, the binding energy of the electrons is plotted. The binding energy is defined as the energy an electron needs to reach the Fermi level of a sample. Calibration measurements are used to shift the PE spectra in a way that the Fermi level is at 0 eV. Those calibration measurements are performed on clean metal samples and will be described in more detail in the experimental section (section 4.3.1).

PE spectra consist of a background, caused by inelastically scattered electrons, the characteristic emission lines and satellites of the emission lines. The emission lines have the shape of a convolution of a Lorentzian and a Gaussian function. The Lorentzian contribution originates from life time uncertainty of the photohole. The Gaussian contribution results from the finite line width of the X-ray beam and the energy resolution of the spectrometer. The binding energy associated with a certain orbital of a certain element, and hence a certain emission line, may be different in different samples. The reason for this is the dependence of the binding energy on the electrostatic surrounding of the probed atom. Prominent conditions are for example the oxidation state and the chemical environment of the probed atom. Binding energy shifts caused by the oxidation state and the chemical environment are referred to as chemical shifts.

Several effects can lead to a broadening of the characteristic emission lines or to satellite lines. Two of the most important effects are the spin-orbit coupling and the shake up effect. The spin-orbit coupling is caused by the effect that when an electron is excited from a fully occupied orbital (core orbital) it leaves a photohole with a spin of either $+1/2$ or $-1/2$ behind. If the angular momentum l of the orbital is $\neq 0$ (all but s orbitals) the spin momentum will couple with the angular momentum leading to a total angular momentum of $j = l \pm 1/2$. Since those two possible states will alter the energetic state of the photoexcited atom (final state), two core emission lines corresponding to the two states will occur in PE spectra with an intensity ratio according to the degeneracy of the states ($2j + 1$). If the binding energy difference between the two states is large enough, two distinct emission lines will be observable, if the binding energy difference is small, the two emissions will overlap. The shake up effect can be described as an energy transfer from a photoelectron to an other electron which is excited into a continuum (e.g. an unoccupied band in solids). Thereby, the amount of transferred energy is small compared to the kinetic energy of the photoelectron. For metallic samples, such kinetic energy losses lead to an asymmetry of the core emission lines towards the higher binding energy side. In case of a semiconducting (or insulating) sample, if the transferred energy is sufficient to excite an electron over the band gap, an additional shake up line will occur with the energetic difference of the band gap from the main emission line. The band gap energy constitutes a minimum of the shake up energy for a semiconducting sample. Since unoccupied bands above the conduction band minimum also form a continuum of energy levels, the shake up satellite will show an asymmetric shape on the high binding energy side, similar to the one described for metallic samples, while the main emission line will be symmetric.

The background in PE spectra results mostly from inelastically scattered photoelectrons and electrons which are excited due to inelastic scattering events of the primary photoelectrons. Those electrons are referred to as secondary electrons. For the description of the background of PE spectra, two procedures are widely used, the one proposed by Shirley et al. and the one proposed by Tougaard et al. [61]. Shirley assumed that the number of electrons which are scattered inelastically and add to the background signal is proportional to the total number of excited photoelectrons [61–63]. Tougaard took into consideration that the amount of photoelectrons which are scattered inelastically is dependent on their kinetic energy [61, 62]. The background electrons do not contain information over the specific elements present in a sample. However, from the distribution of electrons with low kinetic energy, the secondary electrons, inside the sample, only those with a kinetic energy high enough to overcome the work function of the sample will be detected during a PES experiment. Accordingly, PE spectra show a rather sharp edge at the high binding energy side, the secondary electron edge (SEE), which can be used to determine the work function of the sample according to equation 3.23.

$$\phi = h\nu - E_{SEE} \quad (3.23)$$

An important feature of PES measurements is the information depth which is rather low (in the order of magnitude of 10 nm). This is due to the requirement that only photoelectrons which did not experience inelastic scattering events (primary photoelectrons) can be used for analysis. This surface sensitivity is a two sided medal. On one hand, it allows a precise examination of the sample surface, on the other hand the bulk properties of a sample can not be probed with PES. However, in case of a homogenous sample some information about the bulk properties can be derived from the surface properties. The information depth is dependent on the mean free path of the photoelectrons λ_p , the distance they can travel in the sample without inelastic scattering. The mean free path however is dependent on the kinetic energy of the photoelectrons. A rule of thumb is that 95 % of the detected electrons originate from a depth of three times their mean free path. As mentioned above the binding energy of a photoelectron is characteristic for a certain orbital belonging to an element with a certain atomic number Z. Accordingly, a quantitative analysis of the element ratios at the sample surface is possible. Thereby, the number of electrons emitted from a certain orbital is assumed to be proportional to the number of those orbitals, and hence atoms, present in the sample. To obtain an elemental surface composition from PES measurements, certain conditions, like the ionization cross sections, the information depth and specific instrumental conditions have to be considered. The ionization cross sections describe the probability that an electron from a certain orbital (of a certain element) is photoexcited. Atomic sensitivity factors (ASFs) summarize many of the conditions important for a quantitative composition analysis and can be used as weighting factors for the integrated intensities for samples which are thicker than

$3\lambda_{p\text{-max}}$ (see equation 3.24). Here, $\lambda_{p\text{-max}}$ is the maximum mean free path of the different probed core electrons. In equation 3.24, n_x is the density of atoms and I_x is the emission intensity (integral of the emission line).

$$\frac{n_a}{n_b} = \frac{I_a \cdot ASF_b}{I_b \cdot ASF_a} \quad (3.24)$$

Common ASFs are those presented by Wagner et al. and common ionization cross sections are the ones presented by Scofield et al. [64,65]. Wagner provides a set of empirical ASFs, based on the results obtained from 135 compounds based on 62 elements [64]. However, under certain conditions, the use of the plain ionization cross sections can be more appropriate. Scofield et al. calculated atomic photoionization cross sections based on the Hartree-Slater atomic model and normalized them to the C1s emission line [65]. The element ratios calculated from PES results need to be taken with care. Surface effects like segregations, or inhomogeneous element distributions might lead to over- or underestimations of certain elements. In addition, the uncertainty of the determination of the absolute composition can be around 10 % [62]. The relative surface composition provides a better reproducibility [62]. Elements which are only present in low atomic concentrations might not even be detected during PES measurements. A way to estimate the detection threshold of homogeneously distributed elements is presented by Shard et al. [66] and will be discussed in the experimental chapter.

3.4.2 X-ray diffraction

This whole section is based on the book “Moderne Röntgenbeugung” by Spieß et. al. [67], which provides an in depth description of the information summarized in this chapter. For a detailed discussion of crystal structures and crystal symmetry, the book “Kristallographie” by Borchardt-Ott and Sowa is recommended [68].

X-ray diffraction and Bragg-Brentano geometry

In this work, X-ray diffraction in Bragg-Brentano geometry is used and will be discussed below. When a crystalline sample is irradiated with X-rays, the X-rays are diffracted on the electron clouds of the lattice atoms. The diffraction of X-rays on a crystal lattice can be described by Bragg’s law (equation 3.25).

$$n \cdot \lambda = 2d_{hkl} \cdot \sin(\theta) \quad (3.25)$$

In equation 3.25, d_{hkl} is the spacing between the lattice planes in the crystallographic direction hkl, λ is the wavelength of the X-rays, θ the incidence angle of the X-rays and n an integer number. To achieve constructive interference, the optical path difference (Gangunterschied) of parallel incident X-rays which are diffracted on parallel lattice planes has to be an integer multiple (n) of the wavelength of the incident X-rays. The graphical representation of equation 3.25 is depicted in figure 3.18.

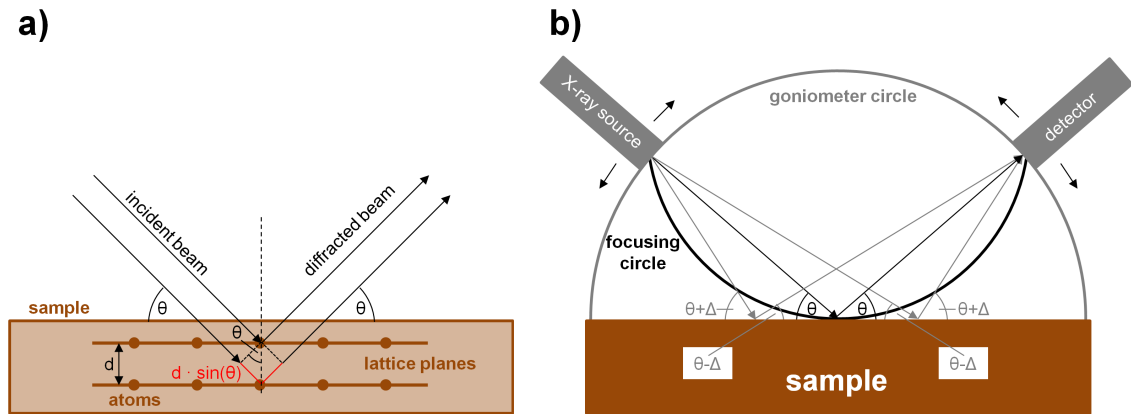


Figure 3.18.: (a) Schematic representation of the X-ray diffraction on parallel lattice planes according to Bragg's law. The path difference is shown in red. (b) Schematic representation of a Bragg-Brentano setup.

Besides the graphical description of Bragg's law, figure 3.18 also shows a schematic description of a XRD measurement in Bragg-Brentano geometry. Here the sample is irradiated under the angle θ with respect to its surface. The geometry is defined by two circles, the goniometer circle and the focusing circle. The goniometer circle has a fixed radius. The X-ray source and the detector move on this circle. The focusing circle is defined by the sample, the X-ray source and the detector. To be in focus, the sample surface has to be exactly tangential to the focusing circle. With the X-ray source and the detector moving, the radius of the focusing circle becomes smaller for higher θ . A special condition of the measurements in Bragg-Brentano geometry is that only the X-rays diffracted on lattice planes parallel to the sample surface are detected. Hence, to get a good statistic over the crystal structure of the sample, many small crystallites are needed. Another measurement characteristic which has to be taken into account is the divergence of the X-ray beam. The divergence of the X-ray beam leads to an angle dependent area of the sample which is irradiated. Under the condition that the X-ray source and the detector have an equal divergence, the angles of the incident and the reflected X-rays add up to 2θ also at the edges of the incident beam. Hence, the whole irradiated sample area contributes to the intensity measured for an angle 2θ (see figure 3.18). Since the divergence of the incident beam decreases with increasing θ , the probed sample area also decreases with θ . The angle dependence of the probed area superimposes the intensity patterns of the sample with an overestimation of reflections at small angles compared to those at high angles. Besides the divergence of the X-rays, other effects have to be considered when evaluating

measurements in the Bragg-Brentano geometry. Those are for example the angle dependent penetration depth of the X-rays or that the sample surface might not be completely tangential to the focusing circle in the whole illuminated area (for example, due to sample roughness, or sample adjustment). In general, the systematic measurement errors are less severe at higher angles 2θ . Therefore, the reflections at high angles, are best suited for the evaluation of XRD measurements, for example for the determination of the space group of an examined material.

Rietveld refinement

The Rietveld refinement is based on the approach to match the intensities measured at all measuring points n during a diffraction experiment (I_{nm}) with intensities which are calculated based on known crystallographic parameters (I_{nc}). When a sufficient match between the measured and the calculated intensities can be achieved, the crystallographic parameters used for the calculated intensities are assumed to belong to the sample. Some parameters which can be used for a refinement are shown in equation 3.26.

$$I_{nc} = s \sum_K |F_K|^2 \cdot L_K \cdot H_K \cdot P_K \cdot A_X \cdot S_r \cdot E_X \cdot \Phi(2\theta_n - 2\theta_K) + I_{nb} \quad (3.26)$$

In equation 3.26, s is a scaling factor, A_X accounts for the absorption and E_X for the extinction of the X-rays in the sample, S_r describes the influence of the surface roughness of the sample and I_{nb} is the background intensity at the measurement point n . The subscript “K” denotes the hkl of a reflection. The structure factor F_K is the Fourier transform of the electron density in a solid and depends on the atomic number of the atoms present in the solid and their position inside the unit cell. The reflection profile function $\Phi(2\theta_n - 2\theta_K)$ describes the shape of a reflection with respect to its calculated reflection position $2\theta_K$. The multiplicity of a reflection H_K describes the number of different lattice planes contributing to the intensity of the reflection. The polarization factor P_K describes the angle and polarization dependent attenuation of the intensity of the diffracted X-rays. The Lorentz factor L_K takes into account that in reality Bragg’s law is not only fulfilled by a sharp angle θ but by a (geometry and θ dependent) regime $\Delta\theta$ around that angle. All parameters shown in equation 3.26 are refined simultaneously, for example under usage of the least squares method. The background is fitted either with a phenomenological or a physical function (for example polynomials of higher order) which itself can provide information over the sample, for example over amorphous phase contributions. If more phases are present in one sample, the parameters shown in equation 3.26 are simultaneously refined for each phase. Besides the phase specific refinement parameters, shown in equation 3.26, global, experiment specific parameters have to be considered in a Rietveld refinement. Those are for example: the instrument characteristics, the wavelength of the used X-rays and

sample adjustment. With sufficient information about every crystalline phase present in the sample (e.g. space group, texture, chemical composition, atomic positions in the unit cell), the Rietveld refinement can be used for a quantitative phase analysis. If amorphous phases are present in the sample, they have to be considered explicitly during the phase analysis.

3.4.3 Scanning electron spectroscopy

This section is based on the book “Solid Surfaces, Interfaces and Thin Films” by H. Lüth [55]. In scanning electron microscopy (SEM), a sample is scanned with an electron beam and the excited species are detected in dependence on the position of the electron beam. The primary electrons are generated for example by a field emission gun (FEG) and focused into the first crossover point (see figure 3.19). The energy of the primary electrons is in the range of 10 keV. Magnetic lenses reduce the lateral extension of the spot in a way, that the spot size on the sample is significantly smaller compared to the spot size at the first crossover point, down to 1-10 nm. The position of the spot on the sample can be varied by two deflection coils between the magnetic lenses. During a SEM measurement, usually four species are probed, back scattered electrons, secondary electrons, Auger electrons and X-rays (see figure 3.19 b). Back scattered electrons are primary electrons which are scattered elastically on the sample atoms. The amount of primary electrons which are scattered elastically increases with the atomic number of the elements present in the sample. Hence, the detection of the BSE electrons gives an elemental contrast of the sample. In addition, characteristic inelastic scattering events cause an energy loss of the primary electrons, for example due to plasmon excitations, which yields further information about the sample. Care needs to be taken when examining rough samples for which the topology can superimpose the elemental contrast. Secondary electrons are electrons which have undergone several inelastic scattering events on their way to the sample surface. After they have overcome the work function of the sample (left the sample) they usually have an energy in the range between 0-50 eV. Due to various inelastic scattering events on their way through the sample, they provide only very limited information on the elements present in the sample but are sensitive to the topology of the sample surface. Auger electrons and characteristic X-rays are both element specific but show significantly different information depths and lateral resolutions. Auger electrons originate from a depth of 0.5-2 nm and allow a spacial resolution in the range of the spot size of the incident electrons. X-rays however originate from a depth of 0.1-10 μm and show, due to the pear shape of the excited volume, reduced lateral resolution compared to the Auger electrons. Figure 3.19 gives a schematic overview over a SEM measurement setup ².

² Information depths for SE, BSE and characteristic X-rays in (b) according to the slides of the lecture “Principles and Methods of Scanning Electron Microscopy” by Dr. P. Komissinsky, attended during winter term 2017.

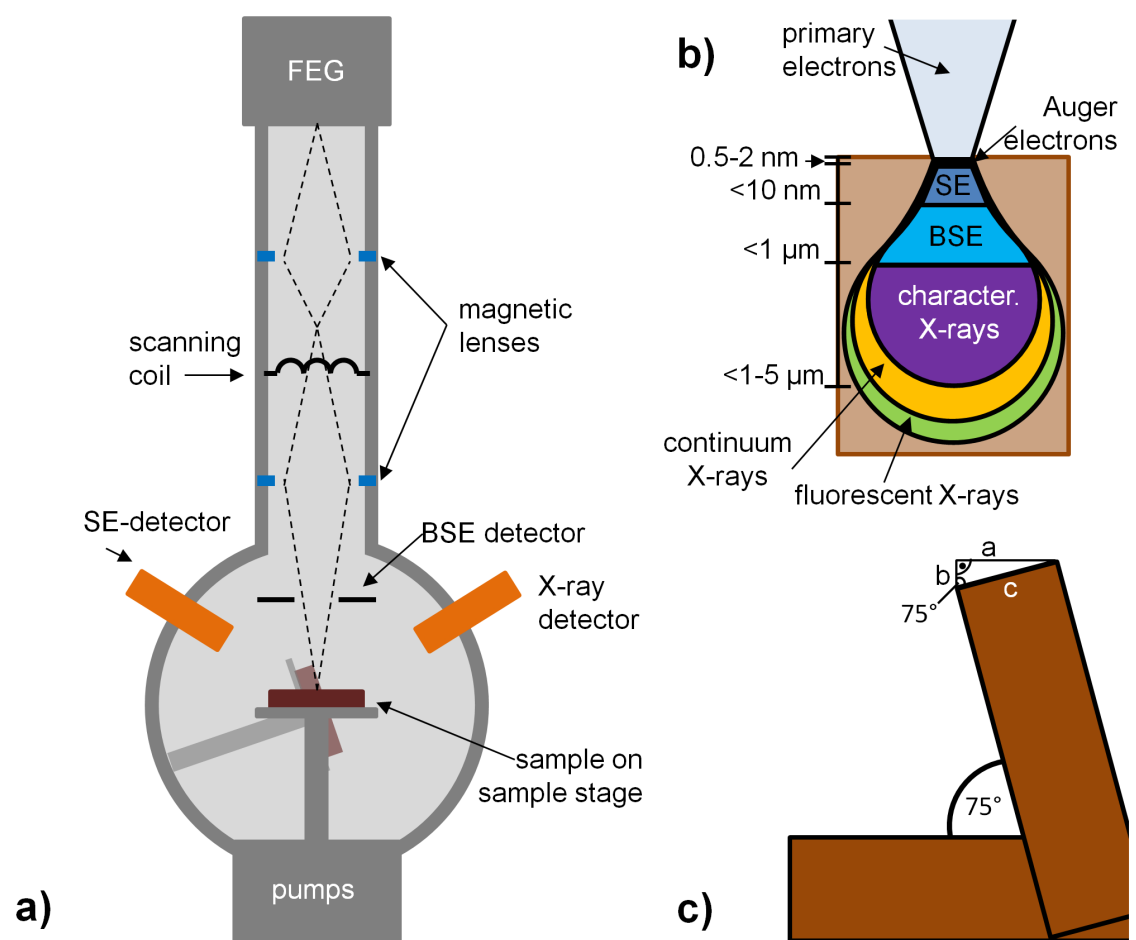


Figure 3.19.: Schematic depiction of a scanning electron microscope (a), the excitation volumina of the different excited species (b) and a magnified depiction of the tilted sample position used for the cross section experiments (c).

Figure 3.19 c shows the sample tilted by 75°. This position can be used to examine the cross section of the sample. But, when quantitative measures are derived from the cross section measurements, the angle between the sample cross section (c in figure 3.19 c) and the horizontal measurement plane (a in figure 3.19) has to be considered. This can be done with equation 3.27.

$$c = \frac{a}{\sin(75^\circ)} \tag{3.27}$$

3.4.4 UV/VIS absorption spectroscopy

UV/VIS spectroscopy is based on the absorption of radiation with wavelengths in the visible and UV regime. The absorption of radiation in dependence on the penetration depth d_{pen} can be described by the Lambert-Beer law in equation 3.28 [56].

$$I_b(E_{ph}, d_{pen}) = I_{b0}(E_{ph}) \cdot e^{-\alpha_{h\nu} \cdot d_{pen}} \quad (3.28)$$

In equation 3.28, $I_b(E_{ph}, d_{pen})$ is the photon energy dependent intensity of the incident beam after penetrating a medium at the thickness d_{pen} , $\alpha_{h\nu}$ is the photon energy dependent absorption coefficient and $I_{b0}(E_{ph})$ the photon energy dependent intensity of the incident beam. In this work, not the absorption but the transmission and the directed reflection are measured in a measurement setup which is shown schematically in figure 3.20.

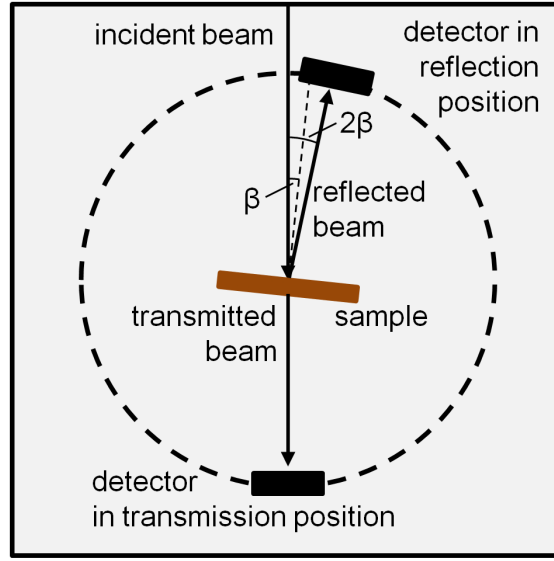


Figure 3.20.: Schematic depiction of the setup used for the UV/VIS measurements in this work. The angle β is the angle between the sample normal and the incident beam.

The wavelength of the incident beam in figure 3.20 is defined by Bragg's law, using two crystal monochromators. The sample normal has to be slightly rotated with respect to the incoming beam (angle β) to be able to measure the directed reflection under the angle 2β . The transmission is measured directly opposite to the entrance window of the incident beam. In this setup, only directed reflection and transmission of the incident beam are measured, diffuse (scattered) reflection is not accounted for. To be able to compare the UV/VIS spectra of different samples, the photon energy dependent absorption coefficient $\alpha_{h\nu}$, which is normalized to the layer thickness, is used in this work and can be calculated from the transmission $T_{h\nu}$ (in %), the directed reflection $R_{h\nu}$ (in %) and the effective layer thickness d_{eff} with equation 3.29.

$$\alpha_{h\nu} = -\ln\left(\frac{T_{h\nu}}{100 - R_{h\nu}}\right) \cdot \frac{1}{d_{eff}} \quad (3.29)$$

Equation 3.29 is derived from the Lambert-Beer law in equation 3.28 and is appropriate for a thin film of strong absorbing material [69, 70]. Due to the rotated sample, an effective layer thickness has to be taken into account, when measuring the transmission. The effective layer thickness can be calculated by equation 3.30.

$$d_{\text{eff}} = \frac{d}{\cos(\beta)} \quad (3.30)$$

3.4.5 Photoluminescence spectroscopy

Photoluminescence spectroscopy can be used to probe the optical activity of a material and to determine the energy of the photons emitted during the radiative recombination processes. In photoluminescence spectroscopy experiments, the sample is irradiated with monochromatized light with an energy well above the band gap energy of the sample material. Thereby, electrons are excited to energy levels above the conduction band minimum and consecutively recombine with their holes. If the recombination process is radiative, radiation of defined wavelengths will be emitted, which can be detected. Besides radiative recombination, Shockley-Hall-Read and Auger recombination are important but non-radiative recombination mechanisms. Thereby, Shockley-Hall-Read recombination describes the recombination of an electron hole pair via an impurity or trap state with an energetic level close to the middle of the band gap. In Auger recombination, an electron hole pair recombines from band to band. But instead of emitting a photon, the energy is transferred to a third charge carrier. More detailed information on recombination mechanisms and PL measurements can be found in the book “Semiconductor material and device characterization” by D. K. Schroder [70]. A schematic depiction of a PL setup is shown in figure 3.21. When the incident beam emitted by the monochromatized light source in figure 3.21 reaches the sample, the photoexcitation and radiative recombination leads to an undirected emission. The emitted radiation passes through the emission filter into the analyzer and finally reaches the detector. In this work, emission filters made from colored glass have been used which have a sharp transmission onset and cut out all wavelengths below a certain (filter specific) limit. The filter is used to protect the detector from the directed reflection of the incident beam. However, integer multiples of the wavelength of the incident beam (which also fulfill Bragg’s law and pass the excitation monochromator) can pass through the emission filter. Superpositions of those integer multiples of the wavelength of the incident beam with the PL emission can be reduced by rotating the sample in a way that the directed reflection of the incident beam does not reach the detector. The width of the incident beam and the accepted angular range of the emitted radiation can be defined by the width of the excitation and the emission slit, respectively. Thereby, a smaller slit causes a better resolution but on the cost of lower intensity. During a PL measurement, only radiative recombination can be probed. Hence, it is possible

to determine whether radiative or non-radiative recombination is dominant in a sample. Furthermore, for every radiative recombination process, a PL emission, corresponding to the energy of the photons emitted during the process can be detected. In an ideal case, only one PL emission corresponding to the optical band gap will appear. If more emissions occur, they might be related to trap states inside the band gap. Accordingly, the trap density and energetic position in the band gap can be estimated. Advanced PL setups are even able to measure time-resolved photoluminescence, which allows to determine, for example, the lifetime of photo generated charge carriers.

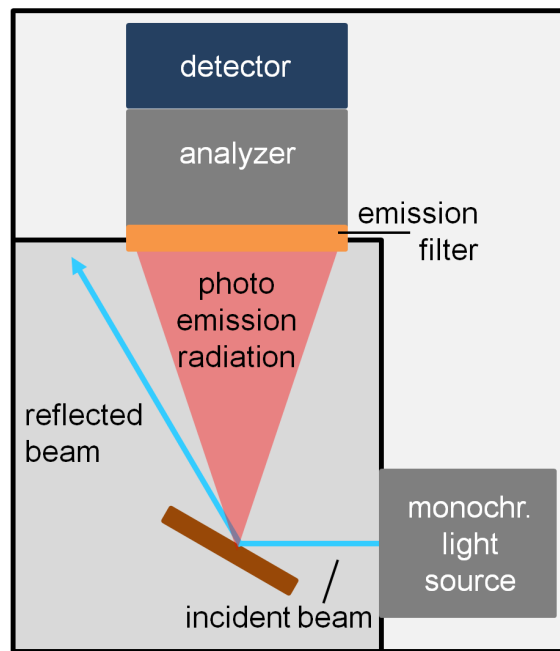


Figure 3.21.: Schematic depiction of the setup used for the PL measurements in this work. The measuring chamber is denoted in dark gray.



4 Experimental

In the experimental chapter, the synthesis and the characterization of the samples used in this work are described. Figure 4.1 gives a first, quick overview over the experimental procedure. After the substrate preparation in air, the samples are introduced into the vacuum system and the perovskite is deposited. After the perovskite deposition, the samples are either directly examined with PES, XRD, PL spectroscopy, UV/VIS spectroscopy or SEM or are processed further in the glove box for solar cell fabrication with consecutive IV measurements. The detailed experimental procedure is described below. Some parts of this chapter are taken from our publication [1].

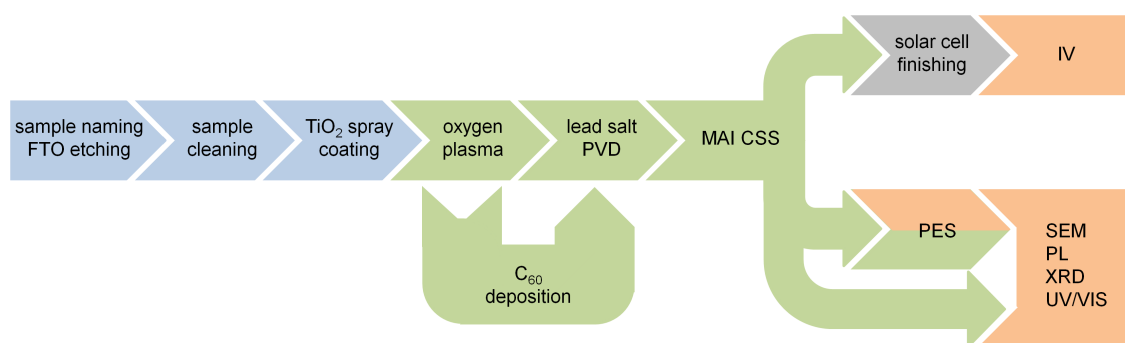


Figure 4.1.: Flowchart of the sample preparation and characterization in this work. Blue denotes fabrication steps in air, green fabrication steps in high vacuum and gray fabrication steps in the glove box. The sample characterization steps are denoted in orange. The PES measurements are carried out without breaking the vacuum conditions and are therefore denoted in green and orange.

4.1 Materials

Materials

PbI₂ (99.9985 % purity) was purchased from Alfa Aesar. CH₃NH₃I (MAI) was purchased from Greatcell Solar (and Dyesol). Titanium diisopropoxide bis(acetylacetonate) (TIAA), Fullerene-C₆₀, 4-tert-Butylpyridine, Bis(trifluoromethane) sulfonimide lithium salt and PbCl₂ (99.999 % purity) were purchased from Sigma Aldrich and Spiro-MeOTAD (99.8 % purity) from Borun New Material Technology. All materials were used without further purification.

4.2 Synthesis

4.2.1 Substrate preparation

Sample naming and FTO etching

Glass substrates covered with fluorine doped tin oxide (FTO) (Pilkington Tec15) were used for all samples presented in this work. The substrates were labeled with a diamond pen according to the scheme ABCD. Here, A is the day of fabrication, B the month, C are the initials of the person who prepared the substrates (e.g. RD for Ralph Dachauer) and D is a serial number (roman digits) to identify the substrates within one batch. After the labeling, the FTO substrates were cleaned of glass dust with pressurized nitrogen. The FTO layer was structured in order to prevent a short circuit of the FTO front contact and the Spiro-MeOTAD back contact, in case the probing pins should penetrate through the Au/Spiro-MeOTAD back contact during the IV measurements. To do so, the FTO front electrode was covered with tape, leaving a 3 mm broad stripe of the FTO uncovered. This uncovered FTO was removed by etching with zinc powder and 6M HCl. After the FTO etching a compact TiO_2 layer was deposited onto the substrates. The different substrate fabrication steps are schematically shown in figure 4.2.

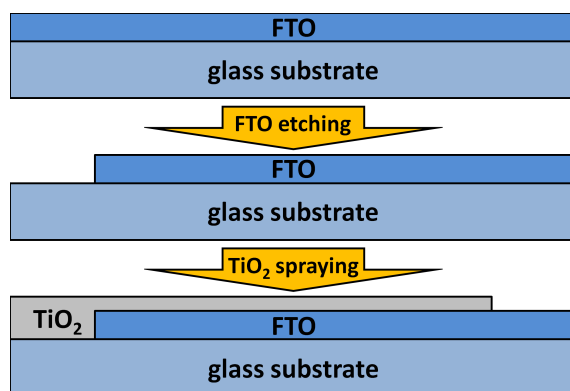


Figure 4.2.: Schematic depiction of the used substrates: as purchased, after the FTO etching and after the TiO_2 spray pyrolysis.

Titanium dioxide spray coating

After the FTO etching, an about 30-50 nm thick compact TiO_2 film was deposited onto the substrates by spray pyrolysis. Before the spray pyrolysis, the substrates were mechanically cleaned. To do so, the substrates were rinsed with isopropanol and VE water and cleaned with detergent. In a last step, the substrates were rinsed with tap water and VE water and dried with pressurized nitrogen. The substrates were packed in closed aluminum

boxes to protect them from dust. For the spray pyrolysis, a solution of 500 μL Titanium diisopropoxide bis(acetylacetonate)(TiAA) diluted in isopropanol and 18 mL ethanol was prepared in an argon filled glove box. As final preparation step, the substrates were cleaned with an oxygen plasma for 5 min to remove surface contaminations prior to the spray pyrolysis. A plasma generator type “zepto” from Diener electronic was used. For the oxygen plasma a gas flow of 1 normal liter per hour (20 °C, 1013mbar) and a main power of the plasma generator of 0.5 W (at 40kHz) were used as parameters. Before the spray pyrolysis started, the spraying gun was rinsed with isopropanol, to remove possible contaminations. After the cleaning, the TiAA solution was filled in the pressure container (see figure 4.3 a) and the substrates were placed under the gun according to figure 4.3 b. During the spray pyrolysis process, the FTO area for the front contact was covered by a mask to prevent the TiO_2 film from being deposited there (see figure 4.2 and 4.3 b).

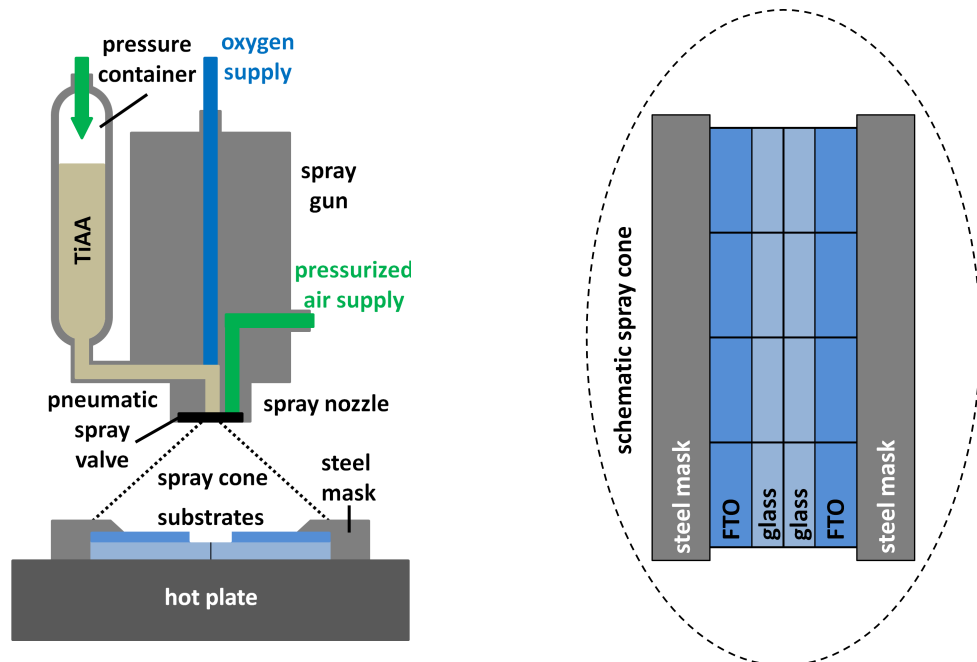


Figure 4.3.: Schematic depiction of the spray pyrolysis setup used for the deposition of the compact TiO_2 layers in this work (left). The oxygen supply is denoted in blue, the pressurized air supply for the pressure container and the pneumatic spray valve in green. Layout of the substrate arrangement during the spray pyrolysis (right).

During the spray coating program, the substrates were preheated to 450-500 °C during 25 min in order to establish a homogenous substrate temperature, needed for the pyrolysis of the precursor solution. Afterward, the solution was sprayed onto the substrates with one 10 s long spray. The spray duration was defined by a pneumatic valve (operated with pressurized air). Oxygen was used as spray gas. Finally, the TiO_2 layers were sintered at 450-500 °C for 30 min and cooled down to a temperature close to room temperature. A more detailed description of the spray pyrolysis setup and the development of the used parameter set can be found in the Advanced Research Lab report of M.Sc. Tim Hellmann [71]. After the cooling period, the conductivity of the FTO front electrodes of

the substrates planned for solar cells was measured with a multimeter to control that no TiO_2 was deposited there. The samples were stored in air in separate plastic boxes till they were used for perovskite deposition.

The fabrication scheme for the glass/FTO/ TiO_2 substrates presented above is valid for all samples presented in sections 5.2 to 5.4 instead of some samples used in the PES experiments. For those samples, the preparation of the TiO_2 layers show some minor deviations. The reason for this is the optimization of the deposition techniques and parameters for the spray coated TiO_2 layers in our group, taking place at the same time as the experiments on the MAPI absorber, presented in this work. Nevertheless, all FTO substrates are prepared in the same manner and all TiO_2 layers are spray coated from a solution of TiAA in isopropanol and ethanol.

4.2.2 Vacuum deposition

All vacuum depositions were carried out at the Darmstadt Integrated System for Solar Cell research (DAISY-SOL). A schematic depiction of the DAISY-SOL can be found in figure 4.4. The integrated system combines several thin film deposition techniques with the possibility to examine the fabricated layers with PES, without breaking the vacuum conditions. For the PES measurements an ESCALAB 250XL photoelectron spectrometer from Thermo Fisher Scientific is used. The vacuum in the deposition chambers is in the range on 10^{-9} mbar to 10^{-6} mbar, in the dispenser, the transfer and the PES analysis chamber in the range of 10^{-9} mbar.

Substrate mounting and preparation

Before the substrates were introduced into the vacuum system, they were mounted into sample holders to allow the transfer from chamber to chamber in the vacuum system (see figure 4.5). Thereby, a mask was used to prevent the perovskite from depositing on the FTO front contact. The substrates were introduced into the vacuum system by an entry lock (see figure 4.4). In the vacuum system, the substrates were treated with an oxygen plasma in order to remove surface contaminations. The plasma treatment was carried out in the sputter chamber for 10 min with 50 mA main power, an extraction voltage of -1 kV and an ion energy of 0.5 kV. The oxygen flow was adjusted to yield a chamber pressure of $1 \cdot 10^{-4}$ mbar. A Gen II plasma source and respective power and voltage supplies by tectra were used. The treatment time was defined by a shutter.

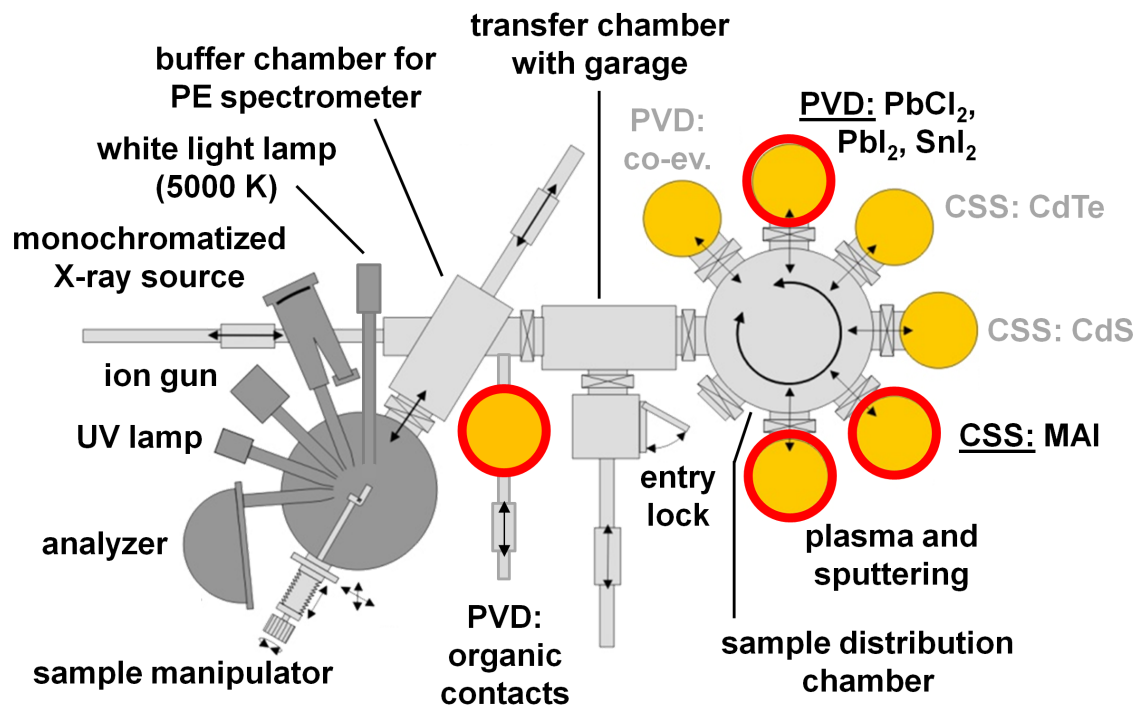


Figure 4.4.: Schematic sketch of the DAISY-SOL. Parts of the system used for this work are labeled in black, the fabrication chambers encircled in red. The labels of the PVD chamber and the CSS chamber used for all vacuum deposited MAPI layers in this work, are underlined.

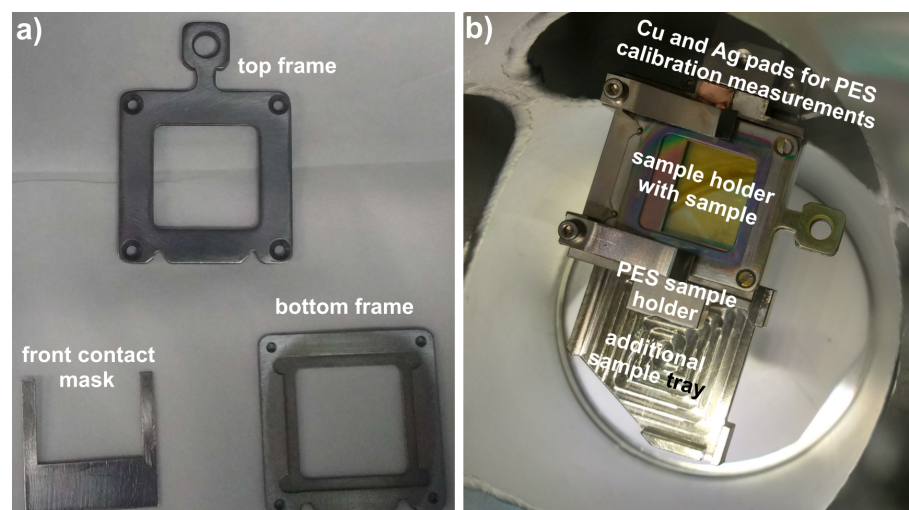


Figure 4.5.: Photograph of the different parts of a sample holder used for the vacuum deposition steps in the DAISY-SOL (a). A substrate is placed on the bottom frame with the FTO/TiO₂ pointing upwards. The front contact mask and the top frame are placed on the substrate and the top and bottom frame are connected with screws. A mounted sample holder with a sample is shown in (b). In (b) the sample holder is placed on the PES sample holder, the Cu and the Ag pad used for XPS calibration measurements are visible above the sample holder. In front of the sample holder, an additional sample tray can be seen which can be used to temporarily store a sample.

Deposition of lead iodide and lead chloride layers by PVD

After the plasma treatment, the lead salts were deposited in a PVD process, using SFC-40-10-385-WK-SHE effusion cells from CREATEC, EA-PS 3032-10 B power supplies from EA Elektro-Automatik and a mini8 multiple loop process controller from Eurotherm, with the respective iTools software. The schematic setup of the deposition chamber can be found in figure 4.6. The abbreviation PVD is used for physical vapor deposition. In this work, PVD describes the vapor deposition of the lead salt layers which are sublimed into the vacuum chamber (see figure 4.6). Thus, the lead salt layer deposition is referred to as an open sublimation, in contrast to the closed space sublimation. The base pressure and the pressure during the lead salt deposition in the PVD chamber were in the range of $1 - 6 \cdot 10^{-8}$ mbar. The distance d_{PVD} between the sample and the evaporation sources was about 15-20 cm.

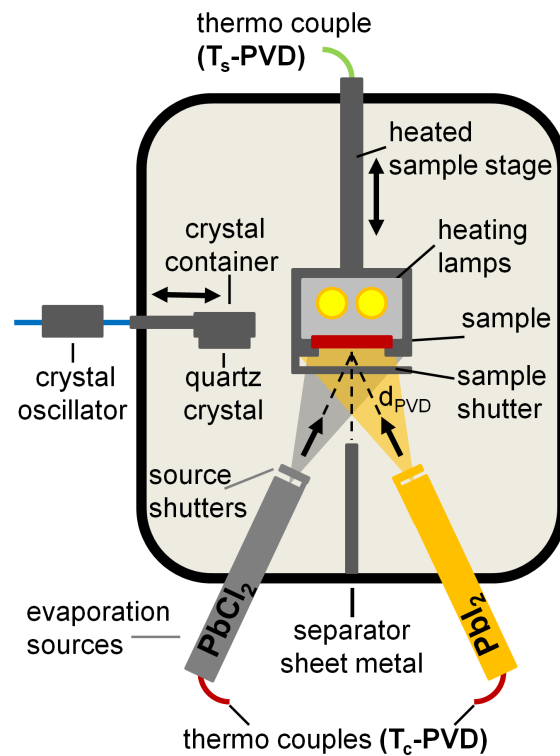


Figure 4.6.: Schematic depiction of the PVD chamber used to deposit PbI_2 and PbCl_2 layers. Double arrows indicate relevant moving directions.

In the effusion cell, the crucibles were heated resistively by a current flowing through tantalum wires, the substrates were heated with two halogen lamps (direct current). The deposition rates of the lead salts were controlled with a gold coated quartz crystal (6MHz), an INFICON 782-900-010 oscillator and an INFICON SQM-160 rate/thickness controller. To measure the deposition rates, the sample stage was wind up to the top of the deposition chamber and the quartz crystal was placed at the position of the substrate during the deposition (see figure 4.6). The lead salt layers presented in the following chapters

were always prepared in a similar manner: The crucibles were heated with 10 K/min to a temperature 10 °C below the desired source temperature and with 1 K/min to the desired source temperature. Afterward, the lead salt layers were deposited, followed by a cool down phase of the sample and the sources. The deposition time was defined by automatic source and sample shutters, controlled by the iTools software. If not denoted otherwise, all PbI₂ and PbCl₂ layers presented in the following chapters are deposited at a substrate temperature of about 50 °C. The PbI₂ layers were deposited with a nominal deposition rate of 0.5 Å/s (T_c around 242 °C), the PbCl₂ layers were deposited with a nominal deposition rate of 2 Å/s (T_c around 328 °C). The deposition rates were measured before and/or after the depositions when applicable. The actual deposition rates may differ from the nominal deposition rates. Those deviations are monitored by the quartz crystal measurements and taken into account when evaluating the results. To match the deposition rates, which are calculated from the quartz crystal oscillation modulation and displayed by the SQM-160 controller, with the actual deposition rates, the material density, the z-factor (empirical measure for the aging of the crystal) and the tooling factor have to be adjusted. A z-factor of 1 is used for PbCl₂ and PbI₂. A density of 5.85 g/cm³ was used for PbCl₂ and of 6.16g/cm³ for PbI₂. The tooling factor was obtained with equation 4.1 by the comparison of desired layer thicknesses and the actual layer thicknesses taken from SEM cross section measurements.

$$\text{tooling}_{\text{new}} = \text{tooling}_{\text{old}} \cdot \frac{d_{\text{act}}}{d_{\text{nom}}} \quad (4.1)$$

In equation 4.1, $\text{tooling}_{\text{new}}$ is the corrected tooling factor, $\text{tooling}_{\text{old}}$ is the previous tooling factor (1 for the first tooling) and d_{act} is the actual layer thickness. The nominal layer thickness d_{nom} is calculated from the deposition rate, displayed by the SQM-160 controller and the deposition time. The tooling factor takes several characteristics of the deposition (e.g. positions of the quartz crystal and the sample or different adsorption kinetics on the quartz and the sample) into account. In the PVD chamber, two tooling factors for each material were used. The overall tooling was performed for the deposition of a PbCl₂ layer and takes into account the geometric aspects. Secondly a material specific tooling factor was determined. The crucible temperatures were measured with type C thermocouples inside the effusion cells. The substrate temperature was not measured directly on the substrate but on the substrate holder plate. A calibration curve, connecting the measured substrate holder plate temperature with the substrate surface temperature was recorded and is shown in figure A.1 in the appendix. To prevent the effusion cells and the substrate heating from overshooting the temperatures desired for the deposition, the PID parameters (Proportional-Integral-Derivative parameters) for the Eurotherm controller were calibrated using the autotune function of the Itools software.

Both lead salts, PbI_2 and PbCl_2 were used till the crucibles were empty. When the crucibles needed to be refilled they were removed from the deposition chamber and transported to the glove box. There, left over material was removed from the crucible and fresh lead salts loaded into the crucibles. The crucibles were reinstalled in the deposition chamber and the chamber was pumped. Before the first deposition the crucibles were carefully heated to a common deposition temperature with plateaus around 60°C and 120°C . This was done in order to remove water and other volatile contaminations prior to the first deposition. Each crucible was exclusively used for one material.

Transformation of the lead salts to MAPI by closed space sublimation of MAI

After the lead salt deposition, the substrates were transferred into the CSS chamber without breaking the vacuum conditions. The base pressure in the CSS chamber was in the range of $1 - 5 \cdot 10^{-7}$ mbar. In the CSS chamber, the substrates were placed directly on the crucible, the lead salt layer facing downward. Figure 4.7 a shows the CSS setup schematically.

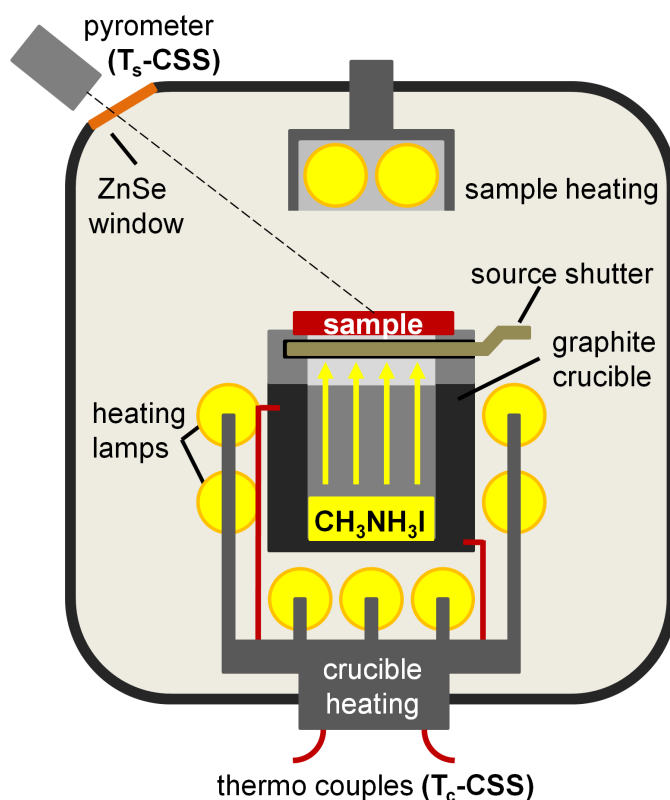


Figure 4.7.: Schematic illustration of the CSS chamber used for the transformation of PbCl_2 or PbI_2 to MAPI by exposure to MAI vapor.

To transform the lead salt layers to MAPI, a temperature program similar to the one used for the PVD deposition was applied. In a typical deposition, the crucibles and the substrate were heated to a temperature 10 °C below the desired temperature in 10 min and to the desired crucible and substrate temperatures in additional 10 min. The deposition time was controlled using a manual shutter. After the deposition, the substrates were left on the crucible to cool down. Some early samples were prepared without the shutter but with a molybdenum sample stage. They were exposed to the MAI vapor during the heating period additional to the transformation time period. After the transformation time those samples were flipped around, the MAPI layer facing towards the chamber and not the crucible anymore. In this work, only the sample used to obtain the PES results for MAPI derived from PbCl_2 with $T_s = 130^\circ\text{C}$ was flipped. Some early samples presented in section 5.1 are fabricated without shutter or flipping. Those samples will be specially mentioned.

In the CSS chamber, the crucible and the sample were heated with halogen lamps operated with alternating current. The substrate temperature was controlled by a pyrometer, looking on the sample through a ZnSe window. The crucible temperature was controlled using two type K thermocouples placed in the wall and the bottom of the graphite crucible. The power supply of the lamps was controlled by Eurotherm controllers with the respective Itools software. The calibration of the pyrometer was carried out by the comparison of the substrate temperatures of a calibration sample measured with the pyrometer to the temperatures measured with a thermocouple. The calibration curves can be found in figure A.2 in the appendix. It has to be mentioned that both, the pyrometer and the thermocouple, read the temperature on the back side of the substrate. The temperature at the front side may differ from those temperatures but is not accessible for measurement due to the closed CSS crucible.

The MAI powder in the crucible was used for several depositions. When the crucible was refilled, the whole crucible heating unit was removed from the chamber and transferred into a fume hood. The crucible was removed from the heating unit, the residual MAI was removed from the crucible and the crucible was cleaned. The shutter was disassembled and also cleaned. Afterward, the crucible was filled, reinstalled into the heating unit and the position of all insulating ceramics checked before the reinstallation of the heating unit into the chamber. The fresh MAI powder was stored in the glove box and only exposed to air directly before the filling of the crucible. The function of the heating lamps was checked with a multimeter before the chamber was pumped again. Thereby, one lamp (including cables, etc.) has a resistance of about 20 Ω . Accordingly, the two side lamp arrays should show a resistance of about 10 Ω (2 lamps parallel), the bottom array should show about 7 Ω (3 lamps parallel). When the chamber was pumped down, the crucible was carefully heated to a temperature above 100 °C to remove any water or volatile contaminations.

Deposition of C₆₀

In this work only few C₆₀ layers were used, exclusively for solar cell fabrication. In those cases, a 5-10 nm thick C₆₀ layer was deposited by sublimation under vacuum conditions and provided for further processing by Dr. C. Das. The C₆₀ deposition was carried out between the oxygen plasma and the lead salt deposition.

4.2.3 Solar cell finishing

If solar cells were fabricated from the vacuum deposited MAPI layers, the layout shown in figure 4.8 was used. The HTL was always Spiro-MeOTAD which was deposited by spin coating onto the MAPI layers in a LABstar glove box from MBRAUN after a heat treatment in a tube furnace in air. Gold was sputtered onto the Spiro-MeOTAD as back contact. The transfers between the vacuum system, the tube furnace and the glove box were all carried out in air.

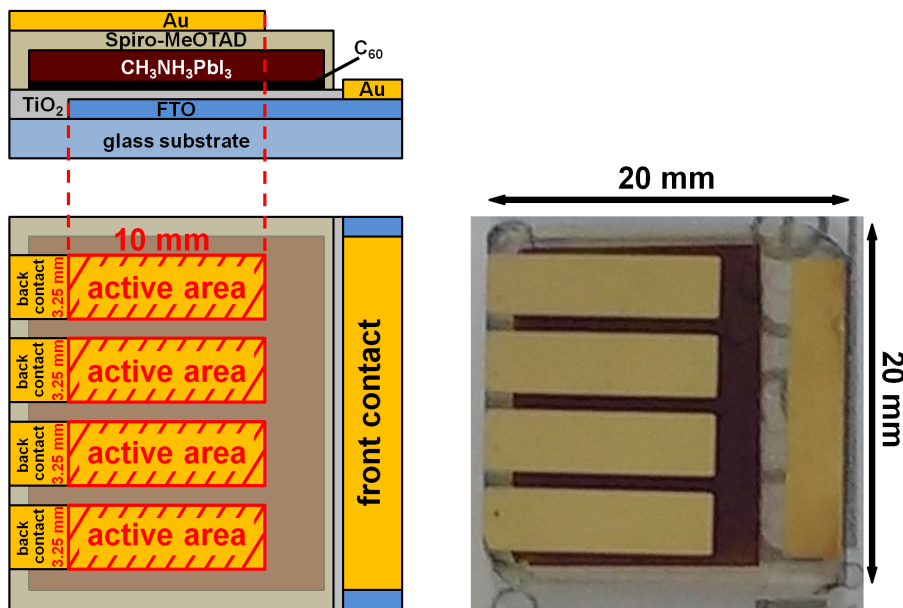


Figure 4.8.: Schematic cut (left top), top view (left bottom) and a typical photograph (right) of the used solar cell structure.

Figure 4.8 shows that on each substrate four solar cells were fabricated. The active area of each cell is defined by the gold back and the FTO front contact to a size of 3.25x10 mm. The solar cell production steps are described in detail below.

Heat treatment in the tube furnace

Between the vacuum deposition of the perovskite and the back contact deposition in the glove box, the MAPI layers intended to be implemented into solar cells were heat treated in air in a tube furnace. To do so, the tube furnace was preheated to 100 °C. After the preheating phase the substrates were introduced into the tube furnace and heat treated for 30 min. After a short cooling period, the substrates were introduced into the glove box for the deposition of the Spiro-MeOTAD HTL.

Spin coating of Spiro-MeOTAD

As a first step for the back contact deposition, the Spiro-MeOTAD solution was prepared. To do so, 40 mg Spiro-MeOTAD powder were dissolved in 500 μ L chlorobenzene in a glass vial. In addition, 14.26 μ L of 4-tert-Butylpyridine and 8.76 μ L of Bis(trifluoromethane) sulfonimide lithium salt (LiTFSI) solution in acetonitril (71.75 mg in 0.5 mL acetonitril) were added as dopands for the Spiro-MeOTAD. The glass vial was carefully shaken till all powders were dissolved. To apply the Spiro-MeOTAD solution onto the MAPI layers, each substrate was placed on a spin coater and 200 μ L of the solution were pipetted onto the substrate. After a delay of 20 s, the substrates were spun for 30 s at 23 rps. After the spin coating, the substrates were moved from the glove box to a fume hood and the Spiro-MeOTAD layer was removed from the FTO front contact using isopropanol and cotton buds. As a last step, 60-100 nm of gold were deposited by sputter coating onto the substrates to form the back contact electrodes and the FTO contact pad.

Removal of excess MAI

In addition to the conventional route for solar cell fabrication, described above, different methods for the removal of excess MAI from the fabricated MAPI layers prior to the Spiro-MeOTAD deposition have been tested. PES experiments on CSS fabricated MAPI layers directly after the fabrication, after a heat treatment in the tube furnace and after a heat treatment and a consecutive cleaning of the MAPI layers with isopropanol in the glove box were carried out during the bachelor thesis of Christian Ondobo. The results of those experiments indicate that a heat treatment in the tube furnace does not remove excess MAI from the MAPI layers. However, the results also indicate that excess MAI on top of the MAPI layers can be washed off with water free isopropanol in the glove box prior to the Spiro-MeOTAD spin coating step. In addition, the in vacuo annealing steps, used for the high temperature CSS parameter sets in this work, also reduce the amount of MAI on top of the MAPI layers. Yet, the reduction of the amount of MAI by in vacuo annealing appears to be a slow process even at high temperatures and possesses the risk of a degradation of the MAPI layers. Furthermore, it remains unclear whether excess MAI

re-sublimes from the MAPI layer surface or diffuses into the MAPI layers to complete the transformation reaction. The removal of excess MAI by washing with isopropanol and by a vacuum annealing treatment were tested for the solar cell production but did not yield a significant increase of the solar cell performance and were therefore not applied to the MAPI layers used for the solar cells presented in this work.

4.3 Analysis

In the following sections, the experimental procedure of the characterization of the samples used in this work is described, starting with photoemission spectroscopy.

4.3.1 Photoemission spectroscopy (PES)

The XPS and UPS measurements were carried out with an ESCALAB 250XL photoelectron spectrometer from Thermo Fisher Scientific. During all measurements, the chamber illumination (KL 1500 LCD Halogen lamp from Schott) was switched on, as will be discussed later. The XPS measurements were carried out with monochromatized AlK α radiation with a wavelength of 1486.6 eV, the UPS measurements with non-monochromatized HeI radiation with a wavelength of 21.22 eV. For the UPS measurements a bias of -4V was applied. The measured XP spectra were calibrated in binding energy and intensity scale using one of two calibration data sets: The first set of calibration data was the Fermi edge of silver together with the Ag3d^{5/2} and Cu2p^{3/2} core line emission. Both metals were cleaned with an argon plasma in the measurement chamber, prior to the calibration measurements. Alternatively, the data were calibrated using the Fermi edge of a freshly prepared gold layer together with the Au4f^{7/2}, Au4d^{5/2} and Au4p^{3/2} core line emissions. The UPS spectra were referenced to the Fermi edge of Ag or Au. In general, the complete calibration measurement set was carried out one time per measurement day with control measurements of the Ag3d (Au4f) emission, between two samples and after the last measurement. The complete calibration was repeated if those control measurements showed deviations from the original calibration measurement. The evaluation of the measured data was performed using IGOR Pro 6 software. The background in the XPS detail spectra was corrected using a Shirley background function (line background for C1s during the transformation of PbI₂ to MAPI in figure A.7 in the appendix) as can be seen in figure 4.9.

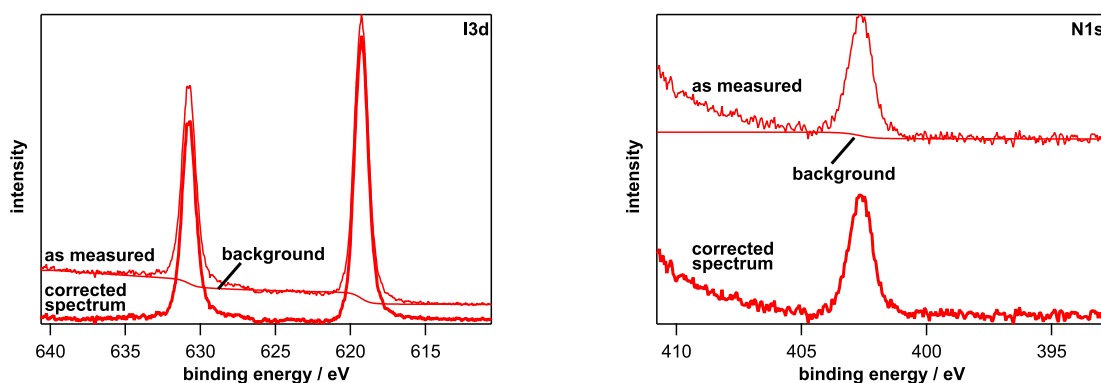


Figure 4.9.: Exemplarily depiction of the background correction according to a Shirley function used in this work.

The core line binding energy positions were obtained by determining the maximum position of an emission line by fitting the line with a convolution of a Gaussian and a Lorentzian function. The Fermi levels, the valence band maximum energy positions and the secondary electron edges were determined graphically, according to the scheme shown in figure 4.10.

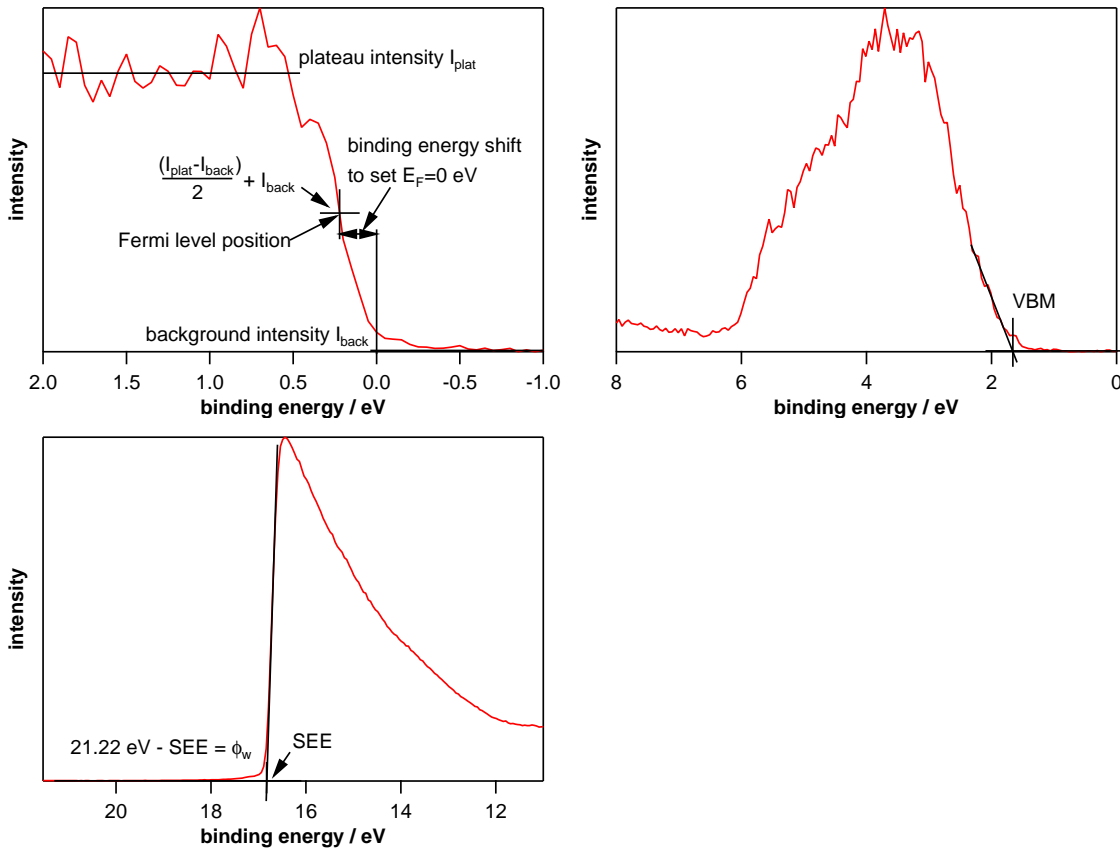


Figure 4.10.: Graphical determination of the Fermi level, the valence band maximum energy position and the work function.

As can be seen in figure 4.10, the Fermi level position was determined by approximating the intensity of the background (I_{back}) and of the emission plateau (I_{plat}) with horizontal lines. From those approximations, the mean intensity was determined according to the equation presented in figure 4.10 and the binding energy position corresponding to that mean intensity was used as Fermi energy and set to 0 eV. To determine the valence band maximum binding energy position, the intersection of a linear fit of the background with a linear fit of the valence band edge was used. The secondary electron edge was determined similarly. The work functions were calculated by subtracting the position of the the secondary electron edge, after Fermi energy calibration, from the energy of the incident photons (21.22 eV for HeI measurements). The surface stoichiometry was obtained by weighting the areas under the core emission lines after the background correction with Scofield ionization cross sections [65].

Measurement uncertainties

In photoemission experiments, the width of a core emission line is in the range of several hundred meV. However, since the emission lines are fitted to obtain their maximum positions, considerably smaller binding energy shifts can be determined. The measurement uncertainty for the core line positions obtained with XPS measurements is estimated to be 50 meV.

The calibration of the measured spectra in intensity scale was carried out using either the Ag3d^{5/2} emission or the Au4f^{7/2} emission after Shirley background corrections. The change of the reference metals was caused by instrumental necessities. Accordingly, two sets of XP spectra are used in this work which are self-consistent, those with a calibration in intensity scale using Ag and those using Au. To connect both sets, the intensity of the I3d^{5/2} and the Pb4f^{7/2} emission of stoichiometric MAPI samples fabricated at substrate temperatures of 90 °C (intensity calibration with Au) and 130 °C (intensity calibration with Ag) are assumed as equal after a Shirley background correction. The calibration of the XP spectra in intensity scale is only relevant for the graphical presentation of the XP spectra in this work. The calibration of the binding energy scale and the determination of the relative surface stoichiometries are completely independent on this procedure. To minimize the effect of measurement uncertainties on the determination of the surface stoichiometry of the samples examined with XPS, relative compositions (for example I/Pb) will be used in this work for the comparison of the stoichiometries of different samples. However, an uncertainty in the range of 5-10 % for the relative compositions remains. Of special interest is the detection limit of specific elements in a certain matrix, for example of chlorine in a CH₃NH₃PbI₃ matrix. A possibility to estimate such a detection limit with equation 4.2 is presented by Shard et al. for binary compounds [66]. In equation 4.2, X_x is the minimal detectable concentration of an element in a certain matrix, measured with a certain spectrometer. X_{ref} is the minimal detectable concentration of the element in the respective matrix presented by Shard et al.. The term at the end of the equation is spectrometer related. It allows to modify the detection limits presented by Shard et al. when the intensity (area) of the Ag3d^{5/2} emission line I_x and the spacing of the data points of the measured spectrum ϵ_x are known for the used spectrometer. For the XPS measurements presented in this work, $\epsilon_x=0.05$ eV and $I_x \approx 5.5 \cdot 10^4$ cps for the Ag3d^{5/2} emission are used. For the case of chlorine in a CH₃NH₃PbI₃ matrix, $X_{ref} \approx 1$ is used, since $X_{ref} \approx 1$ is presented by Shard et al. for Cl in an iodine matrix and Cl in a lead matrix. With those values, the minimal detectable concentration of chlorine in a CH₃NH₃PbI₃ matrix, X_x , is estimated to be around 1 atomic percent.

$$X_x \approx X_{ref} \cdot \left(\epsilon_x \cdot \frac{10^6}{I_x} \right)^{0.5} \quad (4.2)$$

Approximation of the valence band spectra

In chapter 5.3, section 5.3.3, the valence band spectra of a freshly prepared PbCl_2 layer and the spectra measured after consecutive transformation steps of the PbCl_2 layer to MAPI are presented. Those valence band spectra are approximated by the superposition of reference spectra for PbCl_2 , PbI_2 , MAPI and MAI. The approximation was carried out in IGOR Pro 6 according to the following procedure. Firstly, all spectra, were cut off at a binding energy position as close as possible to 9 eV. Afterward, the starting point of all spectra was set to 9 eV. Thereby the difference between the original and the new starting position was 0.01 or 0.02 eV. Since that difference is below the measurement uncertainty of the XPS measurements, it will be ignored for the evaluation of the fits. Finally, the valence band waves were either cut off or extended with zeros to a total length of 215 entries. This complete procedure was necessary to enable the superposition of the reference valence band spectra and the valence band spectra measured during the transformation experiment. Finally, the approximations of the valence band spectra, measured during the stepwise transformation of PbCl_2 to MAPI were done according to equation 4.3. In equation 4.3, Υ is the superposition of the reference spectra, Ψ_A is the reference spectra of phase A, a the scaling factor used for the reference spectra Ψ_A , Ψ_B the reference spectra of phase B and b the scaling factor for the reference spectra Ψ_B and so on.

$$\Upsilon = \Psi_A \cdot a + \Psi_B \cdot b + \dots \quad (4.3)$$

4.3.2 X-ray diffraction (XRD)

The XRD measurements and Rietveld refinements were conducted by the “Material Design by Synthesis” group of Prof. Dr. O. Clemens. Thereby, a Bruker ASX D8 diffractometer in Bragg-Brentano geometry with $\text{CuK}\alpha_{1,2}$ radiation was used. The samples were mounted into sealed, air tight holders under argon atmosphere to prevent oxidation and degradation during the measurements. As measurement parameters a step size of 0.007° , a fixed divergence slit and an integration time of either 0.4 s (glass/FTO/ TiO_2 substrate, MAPI derived from PbCl_2 at $T_s = 75^\circ\text{C}$), 1.1 s (MAI) or 4.4 s (PbI_2 , PbCl_2 and MAPI) per step were used for the XRD experiments presented in sections 5.2 and 5.3. The counting time was increased to 16 s per step for the high angle regime in order to obtain a highly resolved pattern, which could indicate the symmetry of the formed perovskite phase. Background subtraction on the shown diffraction patterns was carried out using EVA software by Bruker. The Rietveld refinements were carried out with TOPAS V5 software from Bruker [72]. Graphical depictions of the crystal structures were created using Diamond 4 software from Crystal Impact.

4.3.3 Scanning electron spectroscopy (SEM)

SEM samples were prepared by attaching a fabricated sample to an aluminum sample holder with a carbon pad and contacting it with silver conducting paint. If cross section images were intended, in order to have a freshly prepared edge, the sample was broken into two parts before one of the parts was attached to the aluminum sample holder. The samples were stored in the glove box till the measurements were conducted. The SEM measurements were carried out by K. Lakus-Wollny, using a XL30FEG Philips SEM in secondary electron mode. The cross sections were measured under an angle of 75° with respect to the horizontal plane (see figure 3.19). This angle was taken into account when calculating the layer thicknesses. Layer thicknesses were determined graphically on the cross section images. To do so, the layer thickness was measured at several positions, distributed over the whole cross section. The mean value of those lengths was determined and converted to the layer thickness in nm using the μ -bar of the images. The grain sizes presented in this work are a semi quantitative measure. Grains considered to show typical grain sizes were chosen by eye and approximated with geometrical forms of known area. The area of those geometrical approximations was then considered as a measure of the actual grain sizes and transformed to grain sizes in μm^2 by usage of the μ -bar. The uncertainty of the optical determination is estimated to be $\leq 5\%$ for the mean layer thickness and for the grain size using an error propagation approach. However, the mean layer thicknesses are dependent on the position and the amount of measurement spots. This dependence may cause an additional error for the mean layer thicknesses.

4.3.4 UV/VIS absorption spectroscopy

For the UV/VIS measurements a Cary 7000 Spectrometer by Agilent Technologies was used. The samples were measured at room temperature in air. The sample normal was rotated 6° (angle β in figure 3.20) with respect to the incoming beam. Directed reflection and transmission spectra were measured with the detector at 12° and 180° with respect to the incoming beam. Both measurements were carried out with 90° P polarization and a fixed spectral band width of the incident beam of 4 nm. From the reflection and transmission measurements and the layer thickness determined with SEM, the absorption coefficients α_{h} , were calculated according to equation 3.29 [69, 70].

4.3.5 Photoluminescence spectroscopy

Photoluminescence spectroscopy was carried out at room temperature in air using a Cary Eclipse spectrometer from Varian. All measurements presented in this work were carried out either with an emission and excitation slit width of 20 nm. To excite charge carriers in the sample, radiation of either 450 nm (bare glass/FTO/TiO₂ substrate and substrate with PbI₂, PbCl₂, MAI and MAPI derived from PbCl₂ at $T_s = 75^\circ\text{C}$ during the CSS process) or 480 nm (all other MAPI samples) was used. Corresponding to the excitation wavelength, an emission filter (from SCHOTT AG) cutting out radiation with a wavelength below 475 nm and 530 nm, respectively, was used.

4.3.6 IV measurements on solar cells

The IV measurements were carried out in air under simulated AM1.5G illumination using an Oriel Corporation 81150 solar simulator together with an Oriel 68811 arc lamp power supply and a Keithley 2400 SourceMeter. The light intensity was calibrated using a bolometer and an E_c -meter 202 controller from PRC Krochmann. The solar cells were measured from -0.2 V to 1.2 V and back to -0.1 V with steps of 0.1 V and a holding time of 1 s at each step. Before each measurement, one voltage sweep from -1 V to 1.5 V without illumination was applied to fill deep trap states and reduce hysteresis. To measure the dark curves, all lights in the lab were switched off and the curtains closed (for measurements at night). If dark measurements were carried out during day time, the measured samples were covered, to protect them from illumination. The J_{sc} , V_{oc} and maximum power point (MPP) were determined iteratively over a time range of 30 s for the J_{sc} and V_{oc} and 180 s for the MPP. Thereby, to determine J_{sc} , the sample was kept at 0 V and the current was measured. To determine V_{oc} , a measured net current of 0 A was used as criteria. To determine the MPP, a starting voltage of 0.6 V was used. During the determination of the MPP, a ΔV is added to and subtracted from this voltage, the corresponding currents are measured (delay time at each voltage = 10 s) and the output powers P_{el} calculated. The maximization of the output power is used as criteria for the adjustment of the voltage steps. With increasing measurement time, ΔV decreases from 0.1 V to 0.001 V, till V_{MPP} and the corresponding J_{MPP} are finally determined. From J_{sc} , V_{oc} and the MPP the fill factor is calculated. Current densities are calculated for a cell area of 3.25x10 mm, efficiencies for an radiation power P_{rad} of 1000 Wm⁻².

5 Results and discussion

5.1 Prerequisites

Before the results of this work are presented and discussed in detail, some terms need to be specified and some measurement conditions to be defined. Furthermore, in this first section of the results and discussion chapter, general aspects, basic to the following sections, will be described. Some parts of this section are taken from our publication [1].

5.1.1 The glass/FTO/titanium dioxide substrate

As described in the experimental section, the samples used during this work were fabricated on glass/FTO substrates with a spray coated 30-50 nm thick TiO₂ hole blocking layer. Hence, it is reasonable to discuss the morphology and the PES properties of those substrates. The XRD, UV/VIS and PL properties will be presented when needed in the following sections.

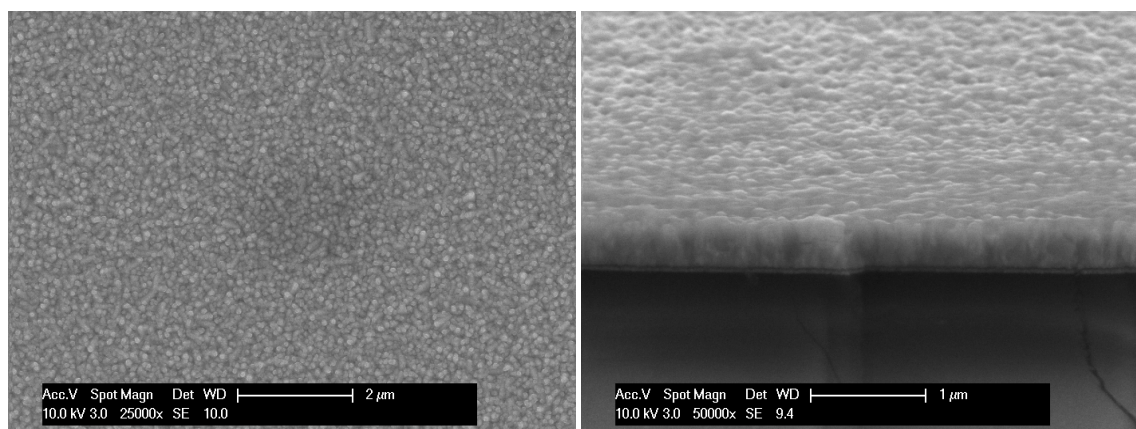


Figure 5.1.: SEM images in SE contrast of a glass/FTO/TiO₂ substrate in top view (left) and tilted 75° with respect to the horizontal (right).

The top view SEM in figure 5.1 shows a fine grained morphology and homogenous grain size distribution. No pinholes or other macroscopic defects are observable. The cross section image in figure 5.1 shows a columnar grain growth of the FTO grains. The 30-50 nm thin TiO₂ layer is too thin to be seen in the SEM images. The XP survey spectra of glass/FTO/TiO₂ substrates are presented in figure 5.2. The high binding energy regime of the survey spectra shows that minimal contaminations of Zn and Cu might be present

in the samples. The Zn could be a residue from the FTO etching process, possible origins of the copper are unclear. Since there is no indication of tin in the survey spectra, it can be confirmed that the compact TiO₂ layers are dense and at least about 10 nm thick. From the comparison of the “as is” and the plasma treated sample, the use of the oxygen plasma to remove carbon contaminations from the substrate becomes apparent. The plasma treated sample shows a little contamination of iodine (I3d lines visible at 624 eV and 636 eV), which is, due to its high volatility, present everywhere in the integrated system. For the fabrication of the MAPI layers, plasma treated glass/FTO/TiO₂ substrates were used and are marked with a thick line in the following PE spectra in this section.

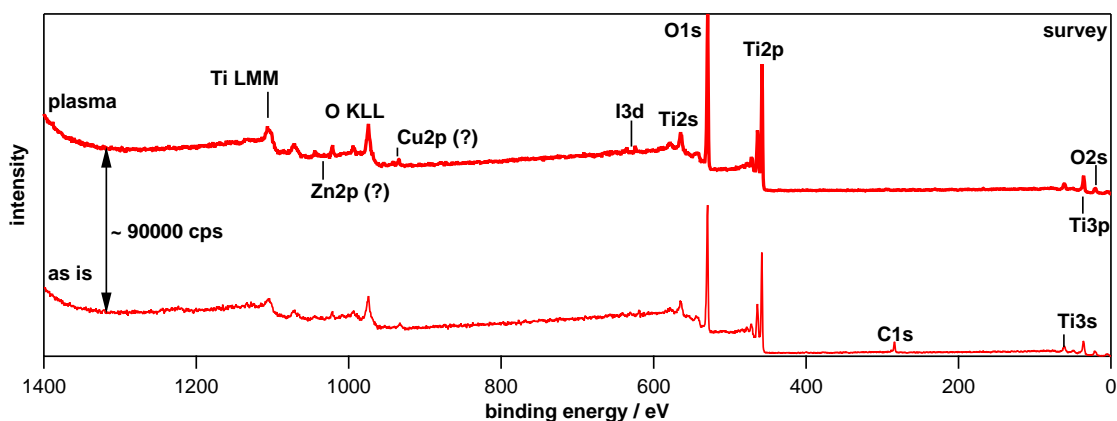


Figure 5.2.: Survey XPS spectra of 30-50 nm TiO₂ on a glass/FTO substrate measured with XPS, “as is” (bottom) and after an oxygen plasma treatment (top). The plasma treated condition, used as substrate for the MAPI layer fabrication, is marked with a thick line.

To get more detailed information about the influence of the plasma treatment on the PES properties of the glass/FTO/TiO₂ substrates, core emission and valence band spectra were measured and are presented in figures 5.3 and 5.4 and table 5.1. The Ti2p lines in figure 5.3 have a symmetric shape, without pronounced shoulders, which is a good indication, that all the titanium in the layers has the oxidation state Ti⁴⁺ [73, 74]. An incomplete reaction would lead to the presence of a Ti³⁺ emission, originating from the presence of Ti₂O₃ or defect states, which would become visible as lower binding energy shoulder on the Ti2p emissions. [73, 74]. The O1s lines show a shoulder at higher binding energies. Since there is no low BE shoulder on the Ti2p lines, the O1s shoulder is probably not related to the presence of Ti₂O₃. The presence of the high binding energy shoulder on the O1s line is also reported in literature for TiO₂ and numerous other transition metal oxides [75–77]. Yet, its origin is not completely understood. Possible explanations range from final state effects to surface contaminations, including stoichiometric effects and the presence of peroxides [75–78]. For the “as is” sample, surface contaminations are surely contributing to the shoulder. But, since the shoulder does not disappear along with the carbon line during the plasma treatment, surface contaminations can not be its only cause.

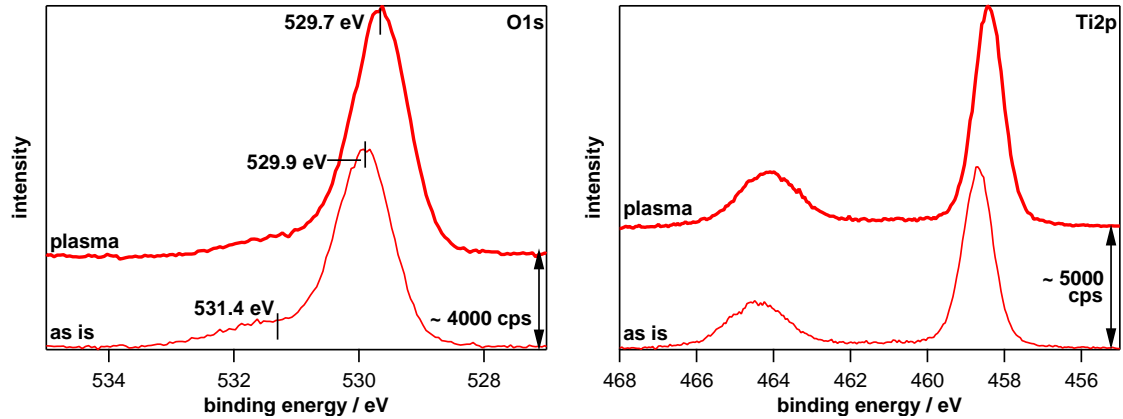


Figure 5.3.: O1s and Ti2p core line XP spectra of 30-50 nm TiO₂ on a glass/FTO substrate measured with XPS, “as is” (bottom) and after an oxygen plasma treatment (top). The plasma treated condition, used as substrate for the MAPI layer fabrication, is marked with a thick line.

The core line spectra in figure 5.3 indicate that the plasma treatment shifts both, the O1s and the Ti2p lines to lower binding energies. To get a more general impression on the effect of the plasma treatment, the core line and valence band maximum positions of several glass/FTO/TiO₂ substrates in different conditions are presented in table 5.1. The sample used in figures 5.2, 5.3 and 5.4 is 108RDV. Only samples with sufficiently low surface contaminations after the plasma treatment are considered in table 5.1.

Table 5.1.: Core line and valence band maximum positions, work functions ϕ and electron affinities χ of several glass/FTO/TiO₂ substrates measured “as is” and after an oxygen plasma treatment. All binding energies are given in eV. The electron affinities are calculated from the work functions and the XPS valence band maximum positions. A band gap of 3.25 eV was used and taken from literature [76].

condition	sample	O1s	Ti2p ^{3/2}	VBM (XPS)	VBM (UPS)	ϕ	χ
as is	108RDV	529.92	458.69	2.29	2.85	4.46	3.50
	19RDII	530.13	458.88	2.56	x	x	x
O ₂ plasma	108RDV	529.66	458.42	2.29	2.24	5.47	4.51
	108RDIV	529.75	458.47	2.39	x	x	x
	<i>1711RDI</i>	<i>530.13</i>	<i>458.89</i>	<i>3.04</i>	x	x	x

The core line positions for a certain condition are quite consistent. Only, the plasma treated sample 1711RDI shows shifted line positions compared to the other samples. The reason for this might be that, compared to the other TiO₂ layers, 1711RDI contains a larger amount of the anatase TiO₂ modification, as will be discussed below. The values for 1711RDI are written italic in tables 5.1 and 5.2 and are not included into the following mean values. The mean values of the O1s binding energies in table 5.1 of the “as is” samples are 530.03 eV (458.79 eV for Ti2p^{3/2}) and 529.71 eV (458.45 eV) for the plasma treated samples. The comparison of those values with literature data for rutile of 530.0 eV

for O1s and 458.7 eV for Ti2p^{3/2} shows a good agreement for the “as is” samples [75]. The shift of the core emission lines of about 0.3 eV to lower binding energies is in accordance with a change from a reduced TiO₂ surface to a stoichiometric or an oxidized TiO₂ surface during the oxygen plasma treatment and indicates a corresponding band bending at the TiO₂ layer surface [78]. The analysis of the XP valence band spectra in figure 5.4 a and of the UP spectra in figure 5.4 b yields further information on the effect of the oxygen plasma on the TiO₂ layer surface.

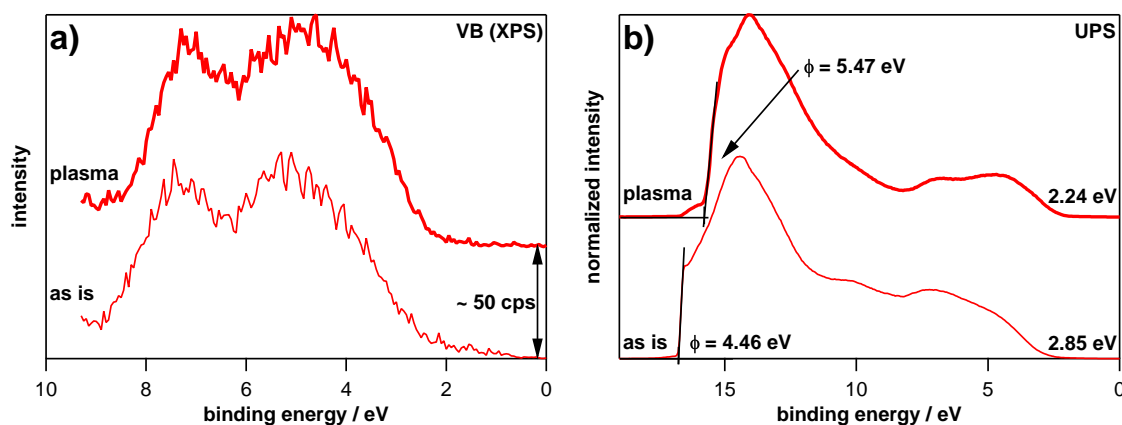


Figure 5.4.: Valence band spectra measured with XPS (a) and UP spectra (b) of 30-50 nm TiO₂ on a glass/FTO substrate, “as is” (bottom) and after an oxygen plasma treatment (top). The UP spectra are normalized in intensity scale. The plasma treated condition, used as substrate for the MAPI layer fabrication, is marked with a thick line.

A reasonable explanation for the observed band bending would be the replacement of OH⁻ adsorbates by O₂⁻ adsorbates during the plasma treatment of the TiO₂ layer [79–83]. The OH⁻ adsorbates can be formed by the dissociative adsorption of water [79, 82, 84–86]. Since the TiO₂ layers used in this work were fabricated and stored in air and hence experience ambient humidity, the adsorption of water, molecular and dissociative, can well be assumed. The presence of OH⁻ adsorbates is further indicated by the high binding energy shoulder of the O1s line of the “as is” sample in figure 5.3 a [87]. The OH⁻ groups are reported to adsorb, however not exclusively, at oxygen vacancies [79, 82, 83]. Reckers proved the existence of oxygen vacancies even on in situ cleaved anatase crystals [79]. However, in XPS experiments on those cleaved crystals no Ti³⁺ line was determinable [79]. Hence, the absence of the Ti³⁺ line is no sufficient indication for the absence of oxygen vacancies and oxygen vacancies are likely to be present also in the spray coated TiO₂ layers examined in this work although no Ti³⁺ line could be determined in Ti2p spectra in figure 5.3 b [78]. However, the use of oxygen as carrier gas during the spray pyrolysis might reduce their density. The adsorbed OH⁻ molecules are reported to transfer an electron to the TiO₂, causing an accumulation layer and a respective downward band bending, or a reduction of the TiO₂ work function, respectively [79, 81–83]. Accordingly, such a downward band bending is also assumed for the TiO₂ layers presented in this work for the “as is” condition. Additionally, to the downward band bending, the formation of a surface dipole due to the adsorption of molecular water

on TiO₂ is reported in the work of Reckers for the exposure of in situ cleaved anatase surfaces to air [79, 82]. Such a dipole, more specifically the removal of such a dipole during the plasma treatment, is also indicated for the TiO₂ layers used in this work by the work function change during the plasma treatment (see figure 5.4 b for comparison). In figure 5.4 a, both effects, the downward band bending and the surface dipole are implemented into the band energy diagram of the TiO₂ layer in the “as is” condition. During the oxygen plasma, it is likely that the OH⁻ adsorbates on the TiO₂ layer are replaced by O₂⁻ adsorbates [79, 80, 88]. The presence of those O₂⁻ adsorbates will cause an accumulation of holes at the TiO₂ surface and hence an upward band bending [79, 80, 83]. The removal of the downward band bending (removal of OH⁻ adsorbates) and the development of the upward band bending (O₂⁻ adsorption) during the plasma treatment can not be separated. Only the total band bending is assessable. Hence, to be able to draw the schematic band energy diagrams in figure 5.5, the total band bending was separated in a band bending attributed to the presence of OH⁻ adsorbates in the “as is” condition, Ψ_{b-ai} , and into a band bending attributed to the presence of O₂⁻ adsorbates after the plasma treatment, $\Psi_{b-pl} = 0.27 \text{ eV} - \Psi_{b-ai}$. Thereby, considering a reduced oxygen vacancy density on the “as is” sample due to the use of oxygen during the spray pyrolysis, the larger part, 0.17 eV, is attributed to the O₂⁻ adsorbates. The energy levels for the flat band condition of the TiO₂ layer in figure 5.5 are obtained by correcting the energy levels measured after the plasma treatment with the assumed O₂⁻ related band bending of 0.17 eV. This procedure yields assumed bulk values of 2.46 eV for the VBM and of 5.30 eV for the work function. The remaining band bending of 0.1 eV is attributed to the OH⁻ adsorbates. The distribution of the band bendings to OH⁻ and O₂⁻ adsorbates is in accordance with the band bendings presented by Reckers, for the exposure of an in situ cleaved anatase crystal exposed to air and a mild oxygen plasma, respectively [79]. The interface dipole layer in the “as is” sample is likely sufficiently thin to be tunneled by electrons and is neglected in the following discussion. Considering only the conduction band offset between the TiO₂ in the “as is” condition and MAPI, the electron transfer from MAPI into TiO₂ is likely to be unhindered. However, for the n/n-isotype hetero junction, the band banding and hence the difference for the work functions might become relevant, as will be discussed in section 5.2.3 in chapter 5.2 by means of the role of PbI₂ in a perovskite solar cell. Nevertheless, since similar processed TiO₂ layers yielded efficiencies above 10 % for solar cells with the MAPI absorber fabricated by co-deposition of MAI and PbI₂ by M.Sc. Maximilian Stöhr¹ [89], also the TiO₂ layers fabricated in this work can be assumed to be suited for the fabrication of solar cells. The plasma treatment removes the OH⁻ adsorbates but leads to O₂⁻ adsorbates on the TiO₂ surface, causing an upward band bending at the surface of the plasma treated TiO₂ layer. This upward band bending alone will probably not significantly influence the electron transfer between MAPI and TiO₂. However, the O₂⁻ adsorbates might react with any layer deposited onto the TiO₂, forming an interface phase which can well be detrimental for the electron transport.

¹ With a C₆₀ buffer layer

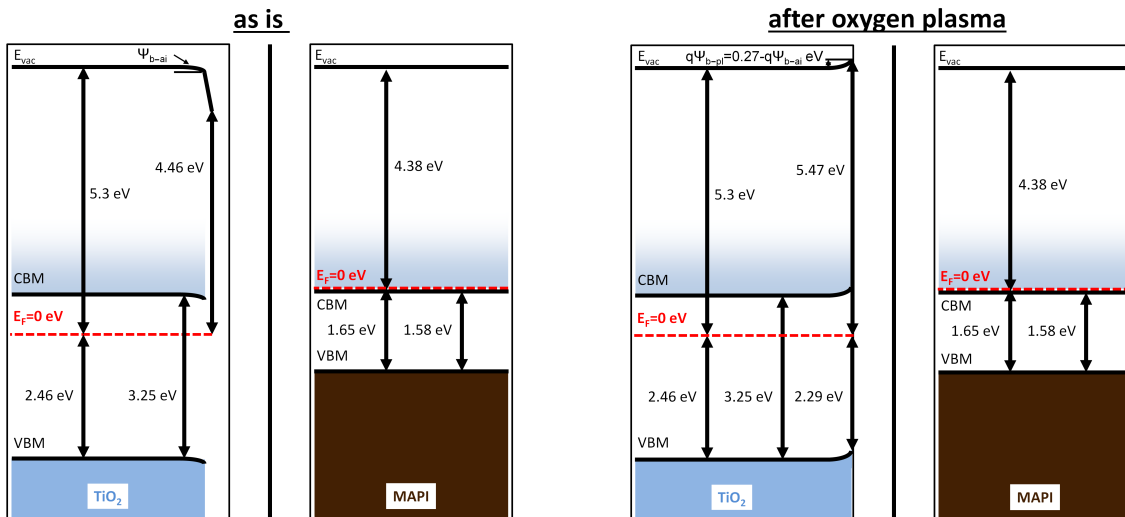


Figure 5.5.: Anderson alignment of MAPI and TiO₂ “as is” (a) and after an oxygen plasma treatment (b). The VBM positions were derived from XPS experiments. For TiO₂, a band gap of 3.25 eV was used and taken from literature [76].

Accordingly, for the use in a solar cell, measures have to be taken to remove or passivate the O₂⁻ adsorbates on the TiO₂ layers. For both conditions, “as is” and plasma treated, Reckers reports a pronounced influence of UV radiation and X-rays [79]. In the “as is” condition both illuminations enhance the downward band bending, but the influence of the UV light is more pronounced than the one of the X-rays [79]. This effect is well in accordance with the observation that the VBM position determined from UPS spectra, which were measured after the XP spectra, indicates a more pronounced downward band bending than the VBM position derived from the XP spectra. For oxygen plasma treated TiO₂ layers, Reckers reports an annihilation of the upward band bending within 10 min of X-ray illumination and the development of a downward band bending during 60 min of illumination with UV light [79]. However, Reckers used a mild oxygen plasma. The TiO₂ layers used in this work were treated with a strong oxygen plasma. Hence, the illumination with UV light during the UPS measurements is assumed to be too short to remove the O₂⁻ adsorbates (same VBM position for XPS and UPS experiments) and it can well be assumed that O₂⁻ adsorbates persist after the PES measurements, but their amount might be reduced. The effect of the X-ray and UV radiation is apparently weaker for the plasma treated condition as for the “as is” condition, is also the reason, why the measurements on the plasma treated sample were used to estimate the TiO₂ bulk positions of the energy levels in figure 5.5. Furthermore, since the XPS measurements were carried out before the UPS measurements and the influence of X-rays on the band bending is weaker than the one of UV radiation, the VBM positions derived from the XP spectra were used in figure 5.5. Considering that the number of the O₂⁻ adsorbates might be decreased during the PES measurements, their influence on interface effects between the TiO₂ and any deposited layer on top of the TiO₂ will be even more pronounced without the measurement, supporting the assumed need, to remove

or passivate the O_2^- adsorbates before the deposition of the solar cell absorber layer onto the glass/FTO/TiO₂ substrate. Besides the differences in the PE spectra of samples in the “as is” and the plasma treated condition, similar processed samples from different batches also show some deviations, as figure 5.6 indicates for two plasma treated samples.

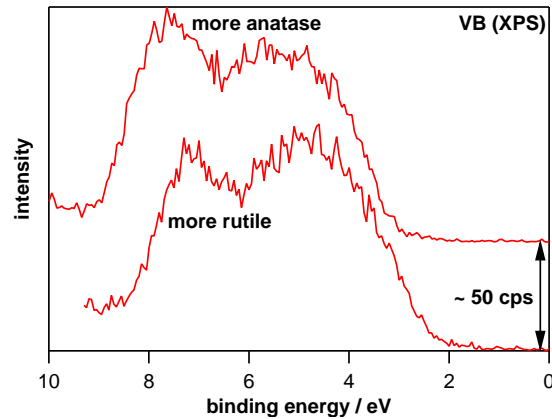


Figure 5.6.: Comparison of the valence band spectra of the plasma treated sample from figure 5.4 (bottom) and a similar fabricated plasma treated sample (top). The core line positions of the upper sample can be found in table 5.1 as 1711RDI.

The comparison of the valence band spectra of the two plasma treated samples in figure 5.6 indicates that the spray coated TiO₂ layers appear to be neither pure rutile nor pure anatase. Apparently, even the fractions of rutile and anatase can vary, leading to different valence band structures and a different valence band onset (for example from 2.29 eV compared to 3.04 eV for the samples presented in figure 5.6). Which crystal structure appears to be dominant can be derived by the relative intensities of the feature around 5 eV to the one around 7 eV [73, 90]. Here the sample with the lower valence band maximum position is more rutile dominated, while the sample with the higher valence band maximum position is more anatase dominated. Valence band spectra of pure anatase and pure rutile can be found in references [73] and [90]. In literature, measured valence band maximum positions for TiO₂ in different modifications and fabrication techniques range from 2.21 eV to 3.28 eV [76, 77]. Hence, considering the probable upward band bending due to the oxygen plasma treatment, the valence band maximum positions of 3.04 eV for the anatase dominated sample and of 2.3 - 2.5 eV for the rutile dominated samples fit well to literature values. The varying crystallographic character of the layers is also indicated by the binding energy differences between the Ti2p^{3/2} line, the O1s line and the valence band maximum. The binding energy difference is about 0.3-0.5 eV larger for rutile than for anatase [73, 90]. All plasma treated samples but 1711RDI presented in tables 5.1 and 5.2 show a binding energy difference of about 456.1 eV for Ti2p^{3/2} to the VBM and about 527.4 eV for the O1s line to the VBM. Those binding energy differences are close to the ones for polycrystalline rutile films reported by Pfeifer et al. (about 456.1-456.2 eV and about 527.45-527.55 eV). On the other hand, with about 455.8 eV and 527.1 eV, the core

line positions of 1711RDI are closer to the ones presented for polycrystalline anatase films (about 455.85-456.05 eV and about 527.05-527.30 eV) [73, 90]. Hence, the comparison of the binding energy differences in figure 5.6 and table 5.2 gives a further indication that the phase contributions of rutile and anatase may vary for similar processed TiO₂ layers, originating from different batches.

Table 5.2.: Distances in eV between the core lines and the valence band maximum (all measured with XPS) of several glass/FTO/TiO₂ substrates measured "as is" and after an oxygen plasma treatment.

condition	sample	O1s - VBM (XPS)	Ti2p ^{3/2} - VBM (XPS)	O1s - Ti2p ^{3/2}
as is	108RDV	456.40	527.63	71.23
	19RDII	456.32	527.57	71.25
O ₂ plasma	108RDV	456.13	527.37	71.24
	108RDIV	456.08	527.36	71.28
	1711RDI	455.85	527.09	71.24

5.1.2 MAPI layer fabrication protocols

Close versus closed space sublimation

The terms close and closed space sublimation are often used in an equivalent meaning. In this work close space sublimation means the use of a spacer between the CSS crucible and the substrate which opens a slit of about 22 mm x 1 mm. The closed space sublimation uses no spacer. The use of a spacer could be advantageous for the transformation of PbCl_2 to MAPI in a CSS process, because it would allow gaseous reaction products like MgCl to leave the CSS crucible. But, it also lets a fraction of the sublimed MAI, or some of its decomposition products, escape from the CSS crucible leading to a reduced MAI partial pressure inside the CSS crucible. The effect of the reduced pressure on the transformation process of PbCl_2 layers to MAPI is shown in figure 5.7². The comparison of the main reflections for PbI_2 and MAPI in figure 5.7 shows that for a certain substrate temperature the PbI_2 phase fraction is larger for the close space sublimation compared with the closed space sublimation. Thereby, a large PbI_2 content indicates an incomplete transformation of the PbCl_2 layer to the perovskite, as will be discussed in section 5.3.3. Accordingly, for a certain crucible temperature, the closed space sublimation yields a complete or mostly complete transformation of PbCl_2 to MAPI at higher substrate temperatures compared to the close space sublimation. Since one goal of this work was to increase the substrate temperature in the Pb-salt/MAPI transformation process, in the following, only samples fabricated with the closed space sublimation will be discussed. Accordingly, the abbreviation CSS will be used for closed space sublimation.

Optimization of CSS parameters

First optimizations

Figure 5.7 already indicates that there is a minimum temperature difference between T_c and T_s for the closed space sublimation, needed to ensure a good transformation of the lead salt to MAPI. To define that temperature difference, further experiments were performed resulting in the observation that a crucible temperature roughly 30 °C higher than the substrate temperature leads to a good transformation of Pb-salts to MAPI.

Fine tuning of the parameters

To determine the temperature window of the two step process presented in this work, four defined substrate temperatures, 75 °C, 90 °C, 130 °C and 150 °C, will be used. The crucible temperatures and the transformation times were fine tuned for those substrate

² The XRD measurements shown in figure 5.7 are pre-experiments. For those measurements the parameter sets for the XRD measurements are different from those described in section 4.3.2 but are consistent for the measurement set.

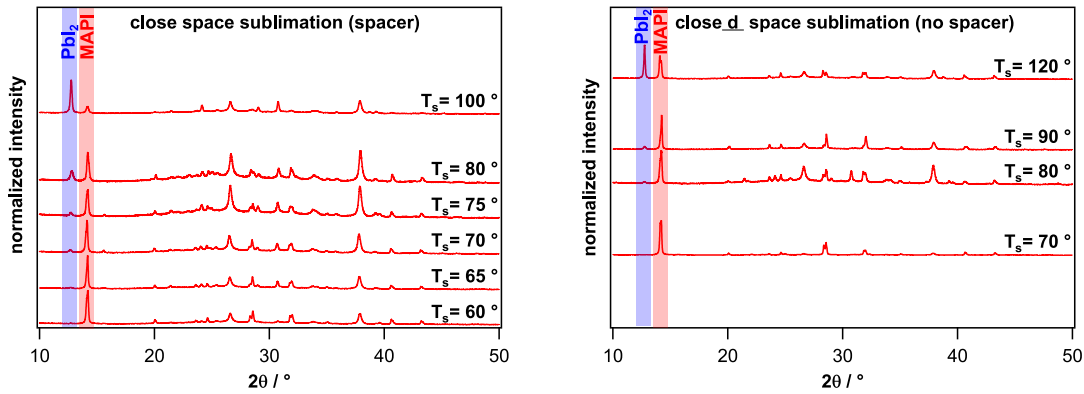


Figure 5.7.: XRD patterns of MAPI fabricated from PbCl_2 layers on glass/FTO/ TiO_2 substrates at $T_c = 120^\circ\text{C}$ during the CSS process, with (left) and without (right) a slit between the CSS crucible and the sample. This corresponds to close (left) and closed (right) space sublimation. All samples were fabricated without shutter or flipping during the CSS process step. The transparent bars mark the main reflections of PbI_2 (dark blue) and MAPI (red) and are guides to the eye. The ratios between the PbI_2 and the MAPI main reflections serve as a measure to assess how far the transformation of PbCl_2 to MAPI is advanced. No background correction was performed for all samples. The diffraction patterns are normalized in intensity scale.

temperatures to achieve a good transformation. The criterion chosen here to define the best $T_c/T_s/t_t$ sets is a complete transformation of the lead salt layers to the $\text{CH}_3\text{NH}_3\text{PbI}_3$ perovskite without lead salt residuals below or surplus $\text{CH}_3\text{NH}_3\text{I}$ on top of the MAPI layer. To determine the phase fractions of the lead salts in the MAPI layers, XRD was used. As mentioned above, PbI_2 constitutes an intermediate phase between PbCl_2 and MAPI, as will be discussed in detail in section 5.3.3. Furthermore, the intensity of the PbCl_2 reflections is rather low compared to the ones of the PbI_2 and MAPI main reflections (see figure 5.44 for comparison). Hence, since the PbCl_2 reflections are not observable also for incomplete transformations of PbCl_2 to MAPI, the main reflection of PbI_2 is used to assess the transformation of PbI_2 and PbCl_2 to MAPI. The crucible temperature is treated as the coarse parameter for the optimization of the CSS transformation³ and was adjusted in a first step (see figure 5.8). The transformation time t_t is, as a first approximation, dependent on the inward diffusion of the MAI dissociation products. It is the fine tuning parameter for the transformation and was optimized in a second step (see figure 5.9). A theoretic description of the physical processes contributing to the transformation of the lead salts to MAPI is given in section 3.3. The PbI_2 content in the layers shown in figures 5.8 and 5.9 is even less than suggested by comparison of relative intensities of the PbI_2 reflection and the MAPI reflection, due to a pronounced texture of the PbI_2 , as will be discussed in chapter 5.2.

³ Reference experiments, carried out with the CSS chamber, indicate an exponential increase of the crucible pressure with increasing crucible temperature.

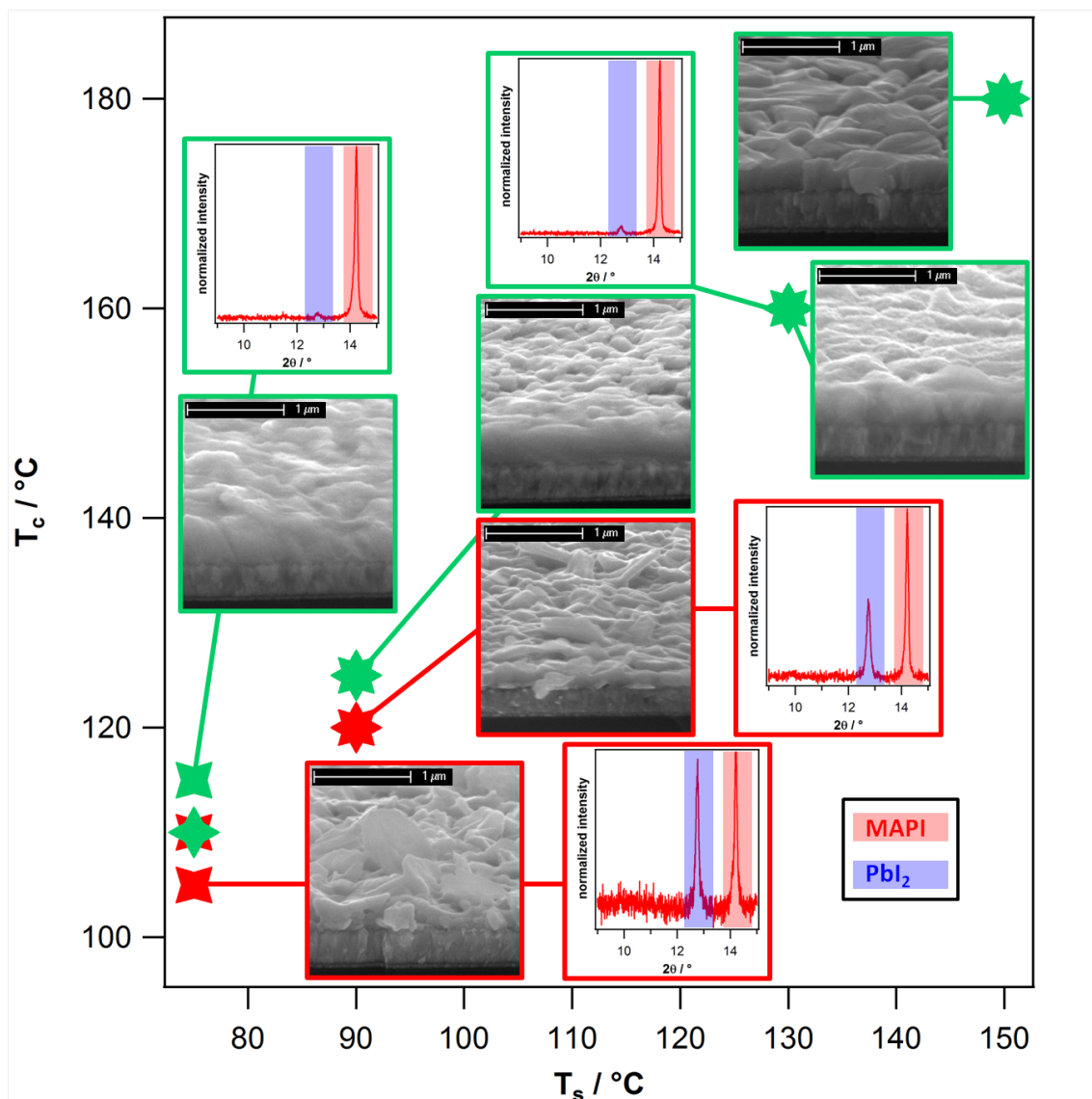


Figure 5.8.: Crucible temperature T_c versus substrate temperature T_s during the CSS step of the fabrication of MAPI layers from PbI_2 and PbCl_2 . The best T_c/T_s sets are marked green, insufficient T_c/T_s sets are marked red. A complete transformation without residual PbI_2 or PbCl_2 and no surplus MAPI is applied as criterion to determine the best T_c/T_s pairs. Parameter sets used for the transformation of PbI_2 to MAPI are denoted with a tilted star (X), parameter sets used for the transformation of PbCl_2 to MAPI are denoted with a vertical star (+). The SEM and XRD results are shown exemplarily and are all taken from MAPI samples fabricated from PbI_2 . The signal to noise ratio varies due to different integration times during the XRD measurements. The transformation times were optimized in a second step. The optimization of the transformation times is shown in figure 5.9 on the next page.

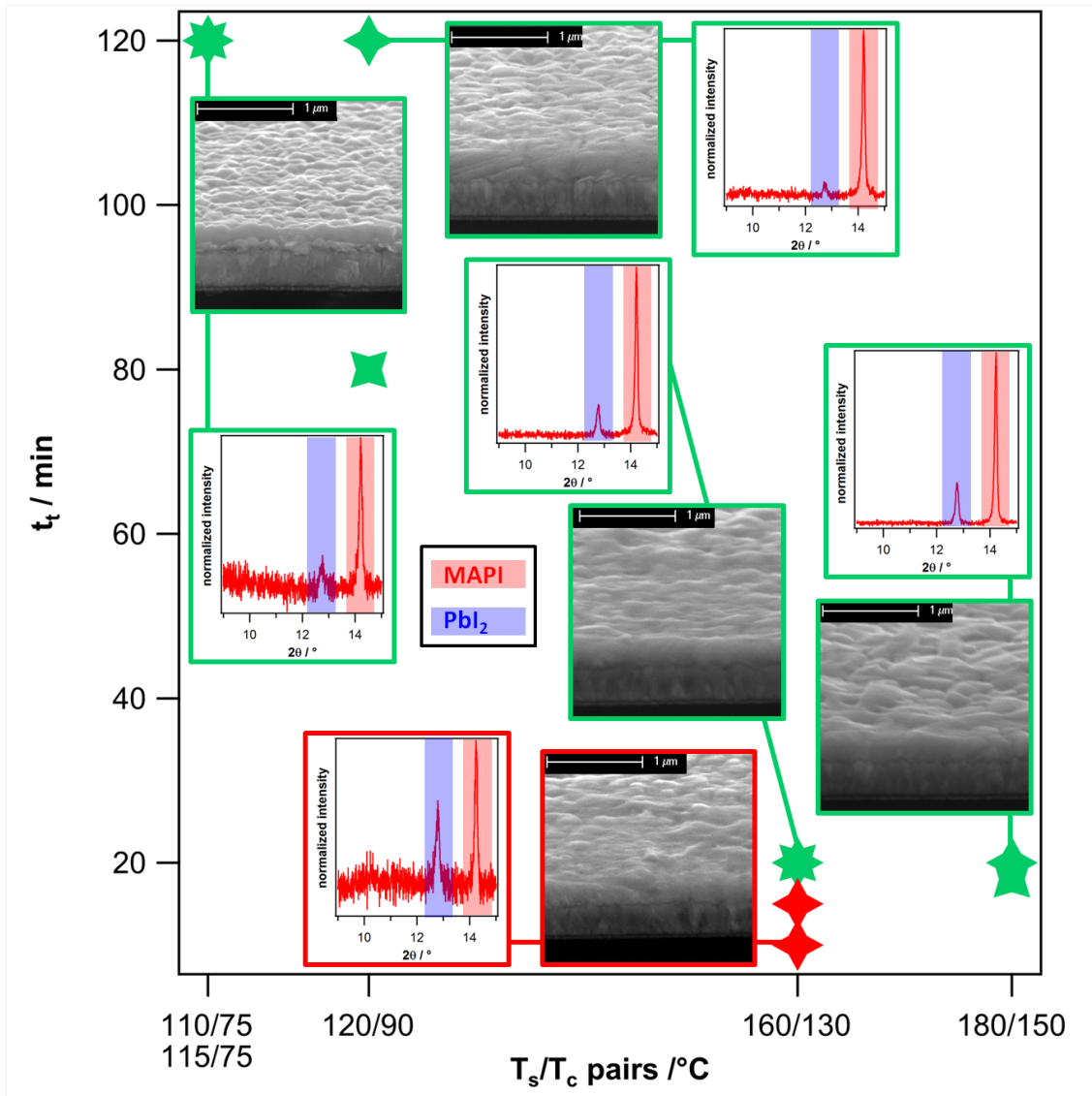


Figure 5.9.: Transformation times for the best T_c/T_s pairs found in figure 5.8 (same samples in both graphs). The criterion for the best parameter sets and all meanings of symbols match the ones in figure 5.8. Only, the SEM and XRD results shown in the graph are from the MAPI samples fabricated from $PbCl_2$ instead of PbI_2 . The signal to noise ratio varies due to different integration times during the XRD measurements.

The tendency of the earlier experiments, that a difference of roughly 30 °C between T_c and T_s results in a good transformation of the lead salts to MAPI can be validated for the transformation of $PbCl_2$ as well as of PbI_2 layers with the experiments shown in figure 5.8. Figure 5.9 shows that with increasing substrate and crucible temperatures, the transformation times decreased drastically from 120 min for the $T_s=75$ °C samples to 20 min, with additional 10 min annealing time, for the $T_s=130$ °C samples. The parameter sets used for the optimization experiments are summarized in table 5.3.

Table 5.3.: Transformation parameters and Pb-salt layer thicknesses (calculated from the deposition rates) for all samples used in the optimization experiments presented in figures 5.8 and 5.9.

lead salt	success	$T_c / ^\circ\text{C}$	$T_s / ^\circ\text{C}$	t_t / min	t_a / min	$d_{\text{pb-salt}} / \text{nm}$
PbI ₂	good	115	75	120	0	202
		125	90	80	0	180
		160	130	20	10	180
		180	150	18	12	180
	insufficient	105	75	120	0	238
		110	75	120	0	202
		120	90	120	0	150
PbCl ₂	good	110	75	120	0	136
		125	90	120	0	104
		160	130	20	10	107
		180	150	20	10	107
	insufficient	120	90	95	0	150
		160	130	10	0	104
		160	130	15	15	104

Table 5.3 shows that the PbCl₂ layers are generally thinner than PbI₂ layers. This difference is intentional. The reason for this is the different theoretical volume increase during the transformation of PbI₂ and PbCl₂ to MAPI, combined with the aim to get MAPI layers from PbI₂ and PbCl₂ with roughly the same thickness. For an intended MAPI layer thickness of 300 nm, this results in a nominal layer thickness of 150 nm for PbI₂ and 100 nm for PbCl₂. The layer thickness of 300 nm was intended for the MAPI layers to ensure that life time and mean free path of the photoexcited charge carriers are sufficient to reach the charge transport layers. Due to fluctuations in the rate monitoring during the Pb-salt deposition, the actual film thicknesses are assumed to be 180-200 nm for PbI₂ and about 110 nm for PbCl₂. Only for the $T_s=75^\circ$ samples thicker lead salt layers were chosen to apply transformation parameters found in earlier experiments.

In summary, during the optimization of the CSS parameters, for both lead salts and for all four substrate temperatures, $T_c/T_s/t_t$ transformation parameter sets could be found which were suited to achieve MAPI layers with a high (crystalline) phase purity.

5.1.3 Relevant measurement effects

When working with MAPI layers, some specific measurement effects have to be taken into account. The two most relevant for this work will be presented in the following.

Beam damage to MAPI layers during SEM measurements

In SEM measurements, the MAPI layers examined in this work appear to form cracks along their grain boundaries. Those cracks are also reported in literature [91]. If the cracks were a feature of the MAPI layers, they would be detrimental to the electrical performance of solar cells fabricated from those layers. The reason is that the cracks lead to short circuits between the front and back contact of a solar cell. Figure 5.10 shows SEM measurements of a MAPI layer fabricated from PbCl_2 . A spot on the layer without defects is chosen (figure 5.10 a). Then, the beam is zoomed in on the spot, increasing the areal electron beam intensity by focusing on a smaller area (figure 5.10 b) and zoomed out again (figure 5.10 c). Only after increased electron beam stress, the cracks in the MAPI layer are observed. The most probable reason for the crack formation is heating of the sample due to the energy input of the electron beam combined with insufficient heat dissipation in the MAPI layer. Materials containing heavy elements like iodine or lead are susceptible to degradation under electron beam radiation due to the large energy input [92]. The thermal conductivity of MAPI at room temperature is reported to be $0.5 \text{ W}/(\text{K} \cdot \text{m})$ for single crystals and $0.3 \text{ W}/(\text{K} \cdot \text{m})$ for polycrystals by Pisoni et al. and about $1 \text{ W}/(\text{K} \cdot \text{m})$ by Kovalsky et al. and hence very low [93, 94]. This heating can lead to several effects like thermal expansion of the grains, sublimation of a low sublimation point phase at the grain boundaries or release of stresses in the layers induced by the limited possibility of the lead salt grains to expand during the transformation of the Pb-salts to MAPI. All these effects could lead to the observed crack formation during the SEM measurements. The sensibility of MAPI towards heating by the electron beam is also reported in literature [95].

Influence of ambient illumination on PE spectra of MAPI layers

Since MAPI is a solar cell absorber, the effect of ambient illumination during photoemission measurements has to be taken into account, when evaluating the PE spectra. For MAPI layers on PEDOT:PSS and MAPI single crystals, significant line shifting due to a photovoltage is reported in literature [96]. Hence, the influence of illumination on the PES features of the MAPI layers on the glass/FTO/ TiO_2 substrates used in this work needs to be examined. To do so, a wet chemical prepared (by M.Sc. Claudiu Mortan) MAPI layer on a glass/FTO/c- TiO_2 /m- TiO_2 ⁴ substrate was mounted to a special sample holder in a

⁴ m- TiO_2 corresponds to mesoporous TiO_2

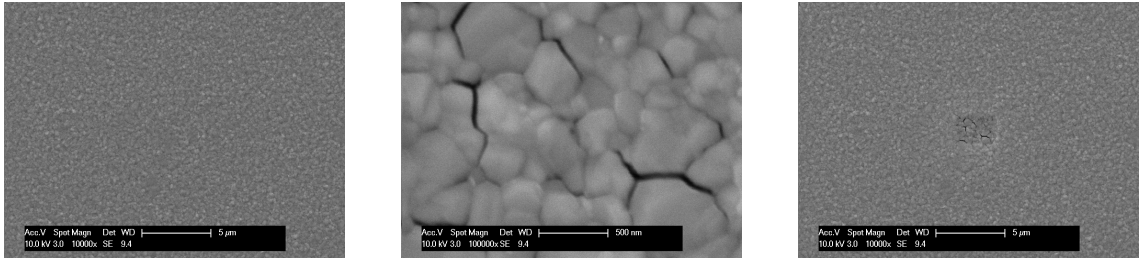


Figure 5.10.: Degradation of a MAPI layer due electron beam irradiation (before zooming (a), zoomed image (b) and after the zooming (c)). The SEM images are in SE contrast. The MAPI sample is made from PbCl_2 . The sample was fabricated without shutter or flipping during the CSS process step and was heat treated in air for 30 min at 120°C between the CSS and the SEM measurement.

way, that the FTO electrode was grounded⁵. The MAPI layer was not contacted, meaning the junction was used in open circuit conditions (see figure 5.11). If a photovoltage occurs, it should be maximized by this setup. The sample was measured in the dark and ambient light. In addition a Solar Raptor high intensity discharge lamp (color temperature 5000 K) was used to enlarge possible photoeffects. The corresponding core level and valence band spectra are shown in figure 5.12. The wet chemical prepared sample was used to ensure to have a photoactive MAPI layer. Figure 5.12 shows no significant effect of the illumination on the half cell. The core line positions of iodine show a minimum value 619.48 eV (amb + 100 % lamp) and a maximum value of 619.56 eV (ch.ill). The core line positions of lead showed a minimum of 138.49 eV and a maximum of 138.57 eV (at similar conditions as iodine). If a photovoltage would develop in the MAPI layer it should cause a shift of the line positions with increasing light intensity. But, also considering the measurement inaccuracy of 0.05 eV, no such systematic shift can be determined. Furthermore, for this measurement the MAPI layer was kept under open circuit conditions, to enhance the effect of a possible photovoltage. In standard measurements, the MAPI layers are grounded by the metal frame of the sample holder (see figure 4.5). Making the development of a photovoltage even less likely. Hence, any illumination effects can be neglected in the following.

The finding that illumination during the measurements does not influence the PES features of the MAPI layers on glass/FTO/ TiO_2 substrates appears to be in contrast to the results presented by Zu et al. for MAPI on PEDOT:PSS [96] but are in fact well in accordance. The reason are the different substrates and cell configurations. PEDOT:PSS is a hole conducting electrode while FTO/ TiO_2 is an electron conducting electrode. Accordingly, if charge carriers are generated in the half cell, with PEDOT:PSS as substrate, the electrons will move to the MAPI surface while with FTO/ TiO_2 as a substrate the holes will move to the surface. Since Zu et al. explain the observed influence of white light illumination during the measurement with the filling of surface trap states with electrons, it is consistent that no such effect is observable when only holes reach the surface.

⁵ Experiments conducted together with M.Sc. Michael Wußler.

Furthermore, the core line and valence band maximum positions presented in figure 5.12 are in accordance with the positions presented by Zu et al. for PES measurements in the dark [96]. In addition, recent experiments in our group, by Wußler et al., show that the presence of a hole conducting (in this case Spiro-MeOTAD) layer is crucial for the development of a photovoltage in perovskite solar cells⁶. Since, no such layer is present during the PES experiments presented in this work, the absence of a photovoltage is well in accordance with those results.

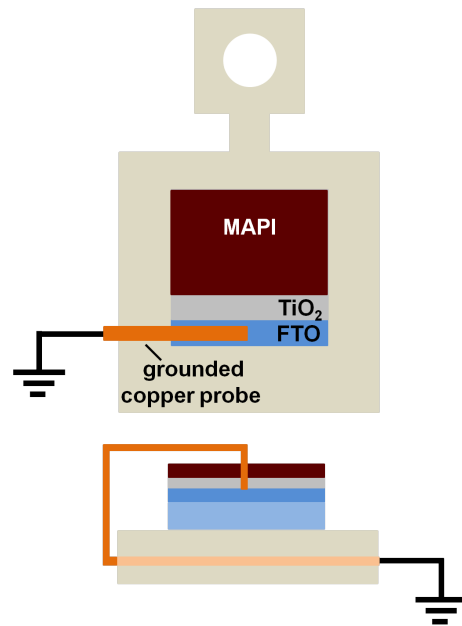


Figure 5.11.: Sample holder used to evaluate the influence of light on the PES experiments of a MAPI layer on a glass/FTO/c-TiO₂/m-TiO₂ substrate. The insulating holder is made from PTFE. Only the FTO front contact is grounded by a copper probe which is connected to the PE spectrometer sample stage.

⁶ unpublished work

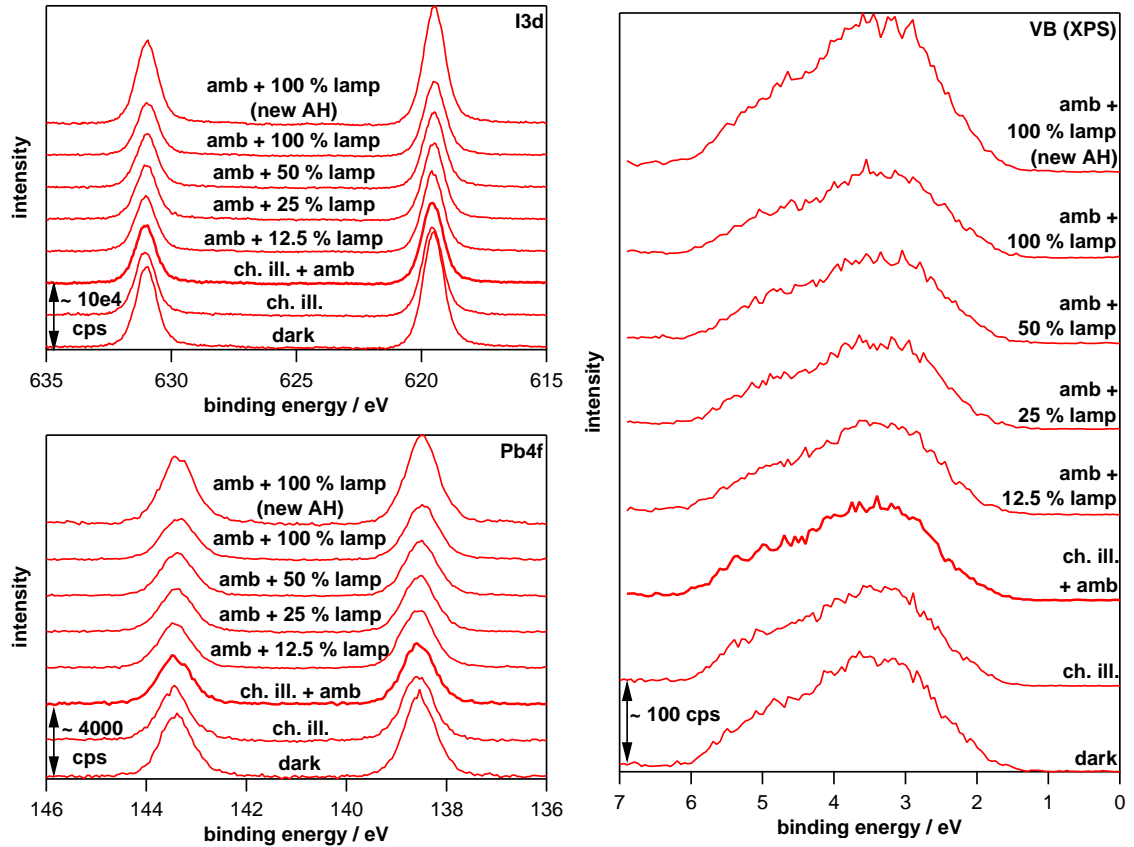


Figure 5.12.: XP spectra of a wet chemically prepared MAPI layer on a glass/FTO/*c*-TiO₂/*m*-TiO₂ substrate under different illumination intensities. For the dark measurement, all lamps inside the measurement chamber were switched off and the windows covered with aluminum foil. The chamber illumination measurement (ch. ill.) was carried out with the windows still covered but the chamber illumination, a KL 1500 LCD Halogen lamp from Schott, switched on. Ambient means that the measurement chamber windows were uncovered. Hence, ch. ill.+ amb means that the chamber lamp was on and the windows uncovered. In addition, experiments were carried out with the chamber lamp off, the windows uncovered and a Solar Raptor high intensity discharge lamp (color temperature 5000 K) used for additional light intensity. The intensity of the additional lamp was regulated by the use of gray filters to 12.5%, 25%, 50% and 100% of its irradiation power. The results of the amb + 100% lamp measurement were confirmed with a new sample height adjustment (new AH). The measurement condition used in the following sections (ch. ill. + amb.) is denoted by a thick line.

5.1.4 Most important facts

- For the experiments presented in the following, closed space sublimation (CSS) was used since it allows higher substrate temperatures compared to close space sublimation.
- For the CSS process, four substrate temperatures (75 °C, 90 °C, 130 °C, 150 °C) were chosen in order to extend the fabrication temperature window beyond that of an open sublimation process under high vacuum conditions. The crucible temperature and transformation time were adjusted to obtain most complete transformations.
- During SEM measurements, the MAPI layers crack along their grain boundaries, most likely due to the heat input of the electron beam.
- PES measurements under white light with different intensities show that PES results are independent on illumination for the junction FTO/TiO₂/MAPI.
- For the ex situ prepared TiO₂ layers used in this work, after the oxygen plasma treatment a shift of the O1s and Ti2p core emission lines to lower binding energies is observed. This shift is likely related to a change from OH⁻ to O₂⁻ surface adsorbates during the plasma treatment, removing a surface dipole and changing the band bending from downward in the “as is” condition to upward after the plasma treatment.
- Due to a varying ratio between the rutile and the anatase modification in the spray coated TiO₂ layers, the line shape in the valence band region and the valence band maximum position can vary between different batches of TiO₂ layers even though the same fabrication parameters were used for the batches.

After the general terminology and measurement boundary conditions are now defined, the aim of the next sections will be to present the MAPI fabricated with the two step CSS, its properties and the mechanisms behind its formation. Therefore, the next sections will start with the most intuitive process, the fabrication of MAPI from PbI_2 by exposure to MAI vapor. This will be followed by the fabrication of MAPI from PbCl_2 and the comparing discussion of the photoactivity of the obtained absorber materials. Some parts of this section are taken from our publication [1].

5.2 MAPI fabricated from lead iodide

From all characteristics of the examined MAPI layers, the layer morphology showed the most pronounced substrate temperature dependence and will be addressed first.

5.2.1 Morphology

When discussing the morphology of the MAPI layers, it is reasonable to start with the morphology of the PbI_2 layers to be able to determine its influence on the morphology of the derived MAPI layers. Accordingly, the top view and the cross section SEM images of a PVD fabricated PbI_2 layer are shown in figure 5.13.

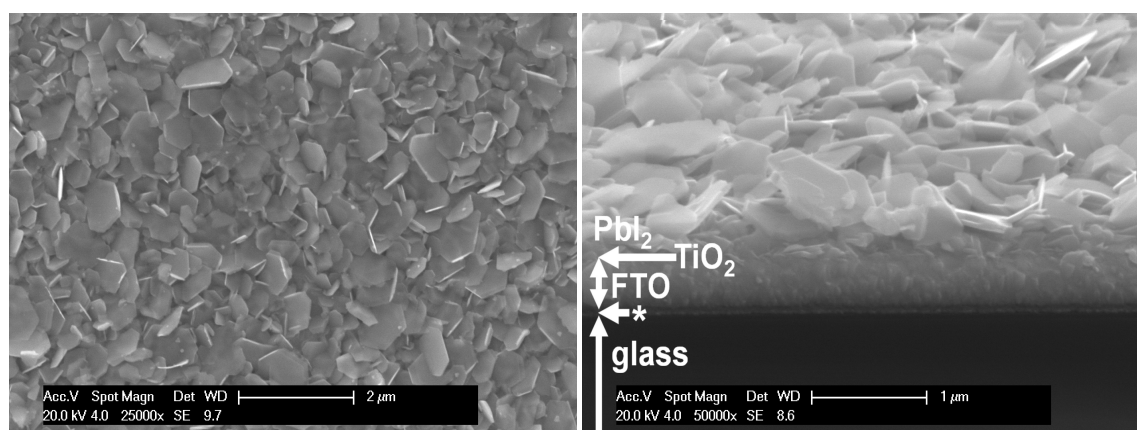


Figure 5.13.: SEM images in SE contrast of a PbI_2 layer deposited by PVD on a glass/FTO/ TiO_2 substrate in top view (left) and tilted 75° with respect to the horizontal (right).

The PbI_2 layer in figure 5.13 shows a rough surface, with randomly oriented flake like grains of varying size. The grains show the distinct shape of a distorted hexagon. The flake like morphology of the vapor deposited PbI_2 layer is consistent with the morphologies reported for vacuum deposited PbI_2 layers [97]. The rough, flake like morphology of the PVD deposited PbI_2 layers leads to the need of a recrystallization during the CSS

transformation process to MAPI in order to obtain the smooth, pinhole free absorber layers, required for solar cell applications. The comparison of the PbI_2 morphology presented in figure 5.13 with the MAPI layers in figure 5.14 suggests that the transformation of PbI_2 to MAPI is dominated by three processes, which take place at the same time. The first one is the transformation of PbI_2 to MAPI by incorporation of MAI into the PbI_2 layer. The transformation leads to a volume increase of the flake like grains visible in figure 5.14 for substrate temperatures of 75 °C and 90 °C. Beneath the flake like grains in figure 5.14 a recrystallized dense and small grained MAPI layer is visible already at $T_s=75$ °C and 90 °C. Hence, the recrystallization of the MAPI layer from a flake like morphology to a globular and dense morphology is identified as second process. It seems that during this process the non-recrystallized flakes originate from large, freestanding former PbI_2 flakes. Those flakes would be the last to recrystallize, stick out and hence appear to be on top of the recrystallized layer. It is interesting to mention that the top views of the $T_s=75$ °C and 90 °C samples clearly show the flake like grains while the cross sections appear to be smoother. A possible explanation is that the angle between the flakes and the sample surface is small, leading to the impression that the flakes are smooth grains. But, a close inspection reveals that the flakes also exist in the cross sections. With increasing substrate temperature, the recrystallization of the MAPI layers becomes more pronounced reducing the fraction of the flake like morphology successively until it is nearly vanishing at $T_s=130$ °C, forming a dense and smooth MAPI layer. The size of the recrystallized grains increases with increasing substrate temperature. While for $T_s=75$ °C a typical size of a recrystallized grain is around $0.1 \mu\text{m}^2$, at a substrate temperature of 90 °C it is about $0.2 \mu\text{m}^2$. For $T_s=130$ °C the grain growth continues to a typical grain size around $0.3 \mu\text{m}^2$ and to around $1.5 \mu\text{m}^2$ for $T_s=150$ °C. Therefore an Ostwald ripening like grain growth is identified as the third process determining the morphology of the MAPI layers. The MAPI layer fabricated at $T_s=150$ °C shows the largest grains but appears to be rougher than the layer fabricated at $T_s=130$ °C. Considering this increased layer roughness at $T_s=150$ °C, a substrate temperature of 130 °C was chosen as the best compromise between grain size and layer roughness. At this substrate temperature, smooth, dense and homogenous MAPI layers with reasonably large grains can be fabricated, making them promising for solar cell applications. The typical grain sizes were estimated from medium sized recrystallized grains (not for the flakes) for every T_s and are a guide to access the grain growth. There are smaller and bigger grains in every layer. The layer thicknesses were determined to be ≈ 400 nm for $T_s=75$ °C, ≈ 430 nm for $T_s=90$ °C, ≈ 320 nm for $T_s=130$ °C and ≈ 330 nm for $T_s=150$ °C.

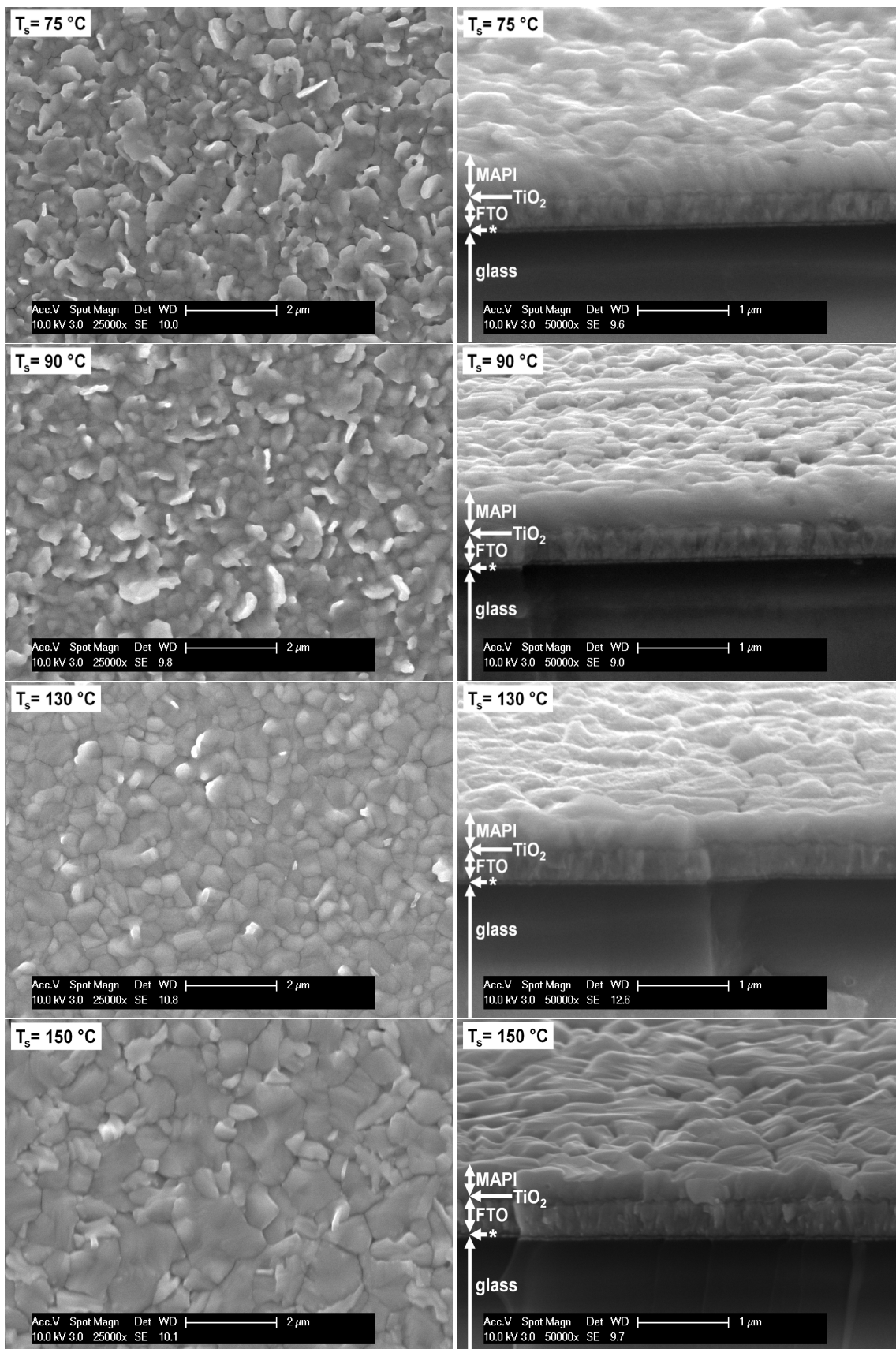


Figure 5.14.: SEM images in SE contrast of MAPI layers fabricated at a T_s of 75 °C ($t_t = 120$ min), 90 °C ($t_t = 80$ min), 130 °C ($t_t = 20$ min, $t_a = 20$ min) and 150 °C ($t_t = 18$ min, $t_a = 12$ min) during the CSS process from PVD deposited PbI₂ layers on glass/FTO/TiO₂ substrates in top view (left) and cross section (tilted 75°) (right). (© 2019 WILEY-VCH Verlag GmbH & Co. KGaA, Weinheim, used with permission)

5.2.2 Crystal structure

With increasing substrate temperature, the morphology of the MAPI layers changes significantly. Whether the composition or crystal structure of the formed layers is also dependent on the substrate temperature during the transformation process was investigated with X-ray diffraction (XRD). Figure 5.15 shows the survey diffraction patterns of MAPI samples fabricated from PbI_2 on glass/FTO/ TiO_2 substrates at substrate temperatures of 75 °C, 90 °C, 130 °C and 150 °C. For comparison XRD patterns of the bare glass/FTO/ TiO_2 substrate and PbI_2 and MAI layers on glass/FTO/ TiO_2 substrates are given. The phase compositions are determined using Rietveld refinements. According to the Rietveld refinements, MAPI perovskite, mainly in its orthorhombic modification, is the dominant crystallographic phase in the diffraction patterns for all substrate temperatures in figure 5.15. In addition, small amounts of residual PbI_2 and FTO can be identified. The TiO_2 layer between the FTO and the perovskite is too thin to be detected in XRD.

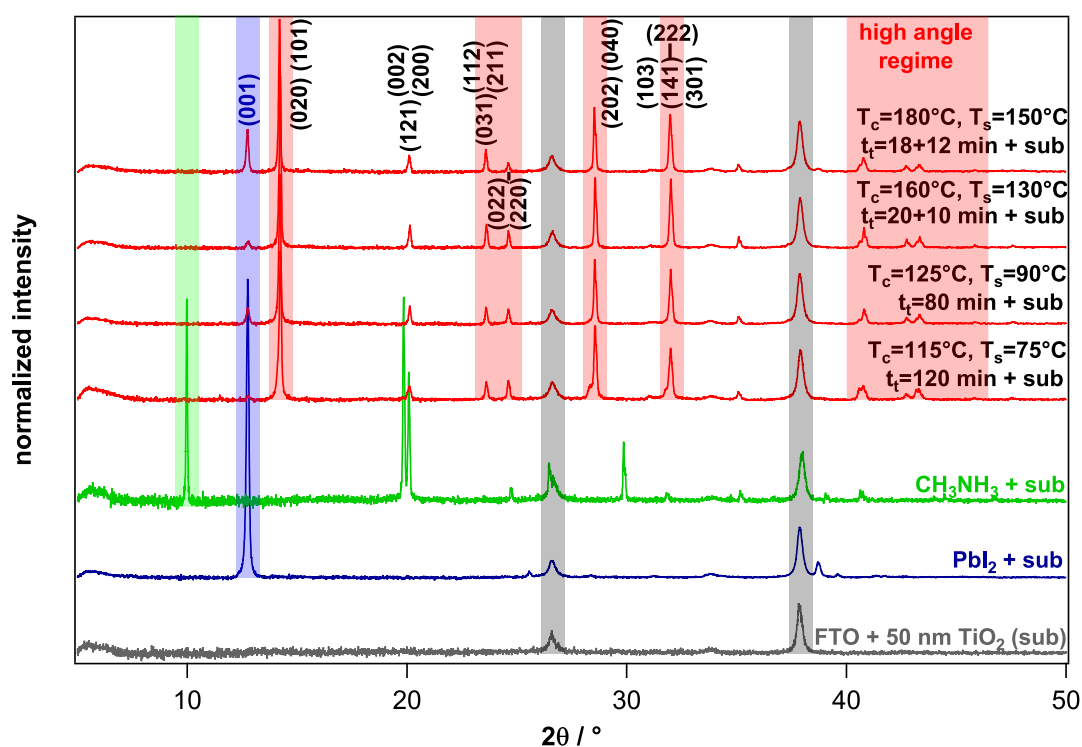


Figure 5.15.: XRD patterns of MAPI layers fabricated from PbI_2 on glass/FTO/ TiO_2 substrates at substrate temperatures of 75 °C, 90 °C, 130 °C and 150 °C during the CSS process. The transparent bars are guides to the eye. For comparison, XRD patterns of the glass/FTO/ TiO_2 substrate and the substrate with PbI_2 and MAI are given. The annotation “+ sub” denotes that reflections of the FTO/ TiO_2 electrode are visible in every XRD pattern in addition to the reflections of the respective layer. For all samples a background correction was performed. The hump at 5° is an artifact of that correction but does not overlap with relevant features of the XRD pattern. The XRD patterns are normalized to the substrate reflection at 37.9°.

There is no indication for a thick MAI capping layer. However, a thin MAI layer would not be detectable in the XRD pattern. If PbI_2 can be observed in the XRD patterns, a rough quantification shows that the PbI_2 content of all samples is below 1 %.

In addition to the composition of the crystallographic phases, the crystal structure and the lattice constants of the examined PbI_2 and MAPI were derived from the Rietveld refinements and will be discussed in the following. Figure 5.16 exemplarily shows the fits obtained by Rietveld refinement for a PbI_2 sample.

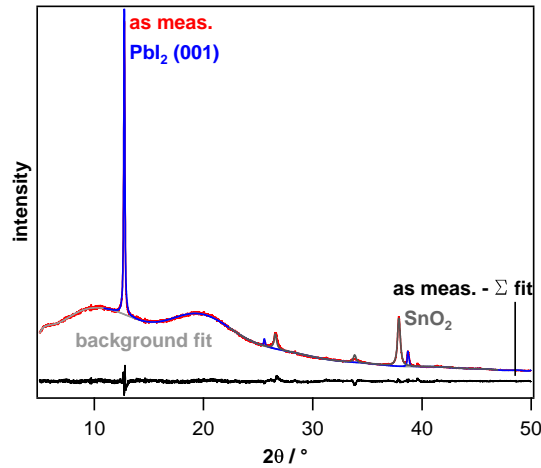


Figure 5.16.: XRD pattern of a PbI_2 layer deposited by PVD on a glass/FTO/ TiO_2 substrate. The measured curve is denoted in red, the background in light gray, the Rietveld refinement of the FTO/ TiO_2 electrode in dark gray and the Rietveld refinement of the PbI_2 layer in dark blue. The difference between the measured curve and the superposition of the PbI_2 , the background and the FTO/ TiO_2 fits is denoted in black with “as meas. - Σ fit”.

For the Rietveld refinement in figure 5.16, the FTO/ TiO_2 electrode can sufficiently be fitted with a refinement for SnO_2 . After the background correction, the PbI_2 layer can be identified to be polycrystalline with a trigonal crystal structure (space group $P\bar{3}m1$) and single crystalline texture (only $00l$ reflections are observable). The pronounced texture of the PbI_2 is in accordance with literature [97–100] and explains the impression that the intensity of the PbI_2 reflections in the MAPI samples in figure 5.15 and 5.18 at 12.65° appears to be too high for a phase content below 1 %. The trigonal crystal structure can be described in the hexagonal crystal system. Both crystal structures can be described by the lattice vectors $a=b \neq c$ and $\alpha = 120^\circ$, $\beta = 90^\circ$ [68]. The only difference is that the base area of the trigonal crystal structure is only a third of the base plane of the hexagonal crystal structure [68]. Hence, the hexagonal flake like habitus of the PbI_2 grains found in the SEM pictures in figure 5.13 fits well to the trigonal crystal structure. The crystallographic data obtained for PbI_2 by the Rietveld refinement were used to create the depiction of the PbI_2 crystal structure in figure 5.17. The illustrations in figure 5.17 are intended as a guide to visually access the general aspects of the crystal structure of PbI_2 and might differ from the real material when it comes to a detailed description.

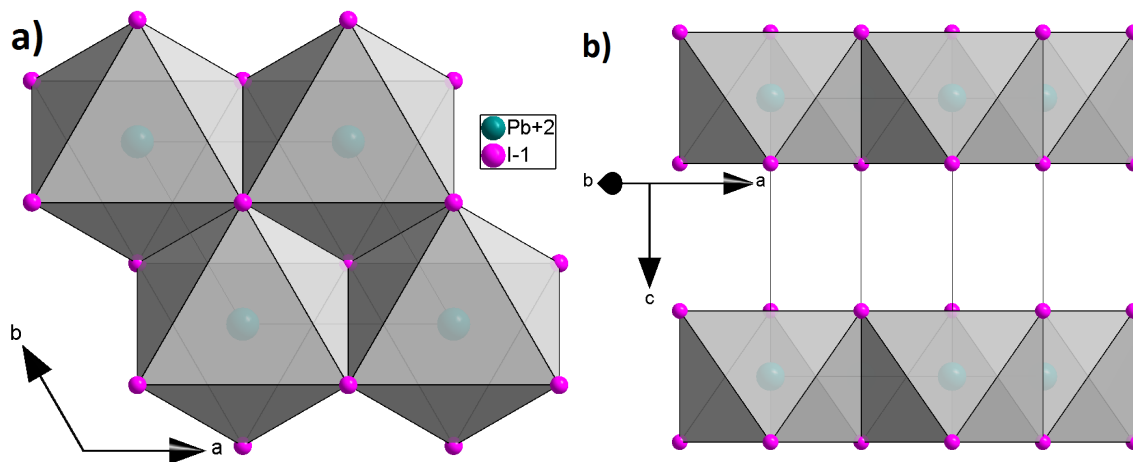


Figure 5.17.: Illustration of the crystal structure of PVD fabricated PbI_2 . The viewing directions are a) along the $[001]$ and b) along the $[010]$ axis.

The unit cell of the PVD fabricated PbI_2 in figure 5.17 shows that PbI_2 already possesses the lead iodine octahedra, which will form the inorganic lattice of MAPI. But in contrast to the corner sharing PbI_3 octahedra of MAPI, the PbI_2 octahedra of PbI_2 are edge sharing. In addition, the PbI_2 octahedra form a layered structure, well in accordance with the flake like hexagonal PbI_2 crystals observed in the SEM images in figure 5.13. Now, the volume increase due to the incorporation of MAI, mentioned above as process one, can be readily explained by the reordering of the octahedra from flat, edge sharing layers to the corner sharing inorganic perovskite network with embedded MA^+ cations.

The Rietveld refinements for MAPI fabricated at a substrate temperature of 75°C and 130°C are shown in figure 5.18. To fit the PbI_2 phase, the refinement for the PbI_2 sample shown in figure 5.16 was used as starting point. The comparison of the Rietveld refinements for MAPI in figure 5.18 leads to an interesting observation. For both substrate temperatures, 75°C and 130°C , the orthorhombic modification is dominant, but especially for the $T_s=75^\circ\text{C}$ sample, also a contribution of the cubic perovskite modification can be observed as additional reflections, overlapping with the orthorhombic reflections around 28.6 and 32.0° (encircled reflections in figure 5.18). The cubic contribution is small for $T_s=75^\circ\text{C}$ sample and appears to decrease further with increasing substrate temperature, till it nearly vanishes at $T_s=130^\circ\text{C}$. The orthorhombic crystal structure with the space group $Pnma$ is derived from the reflection splitting, especially at high 2θ angles. Figure 5.19 shows the corresponding XRD patterns of the high 2θ regime which were measured with an enlarged integration time of 16 s. In figure 5.19, only the Rietveld analysis for MAPI fabricated from PbI_2 at a substrate temperature of 130°C is shown. The plots of $T_s=90^\circ\text{C}$, 130°C and 150°C are given in the appendix. The comparison of the detailed XRD patterns in figure 5.19 b shows that the orthorhombic crystal structure is found for all four substrate temperatures. Besides the orthorhombic crystal structure and the space group, a small degree of texture of the orthorhombic perovskite phase was further indicated by the reflection splitting.

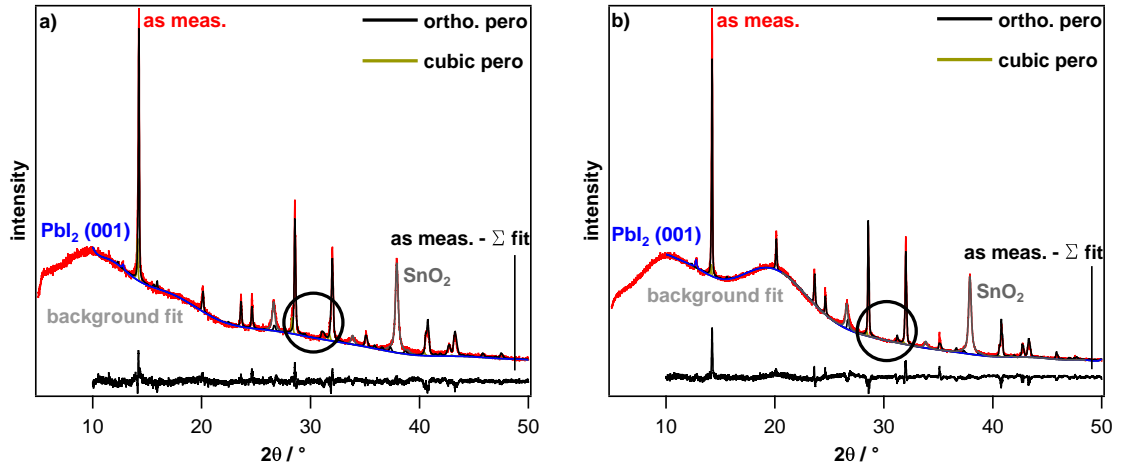


Figure 5.18.: XRD patterns of MAPI layers fabricated from PVD deposited PbI_2 on glass/FTO/ TiO_2 substrates at substrate temperatures of 75 °C (a) and 130 °C (b) during the CSS process. The measured curves are red, the background is light gray, the Rietveld refinement of the FTO/ TiO_2 electrode is dark gray and the one of PbI_2 is dark blue. The Rietveld refinements of the perovskite phases are black for the orthorhombic and green for the cubic phase. The difference between the measured curve and the superposition of the perovskite, the PbI_2 , the background and the FTO/ TiO_2 electrode fits is denoted in black with “as meas. - Σ fit”. The reflections at 28.6° and 32.0°, showing the cubic phase in the most clear manner, are encircled.

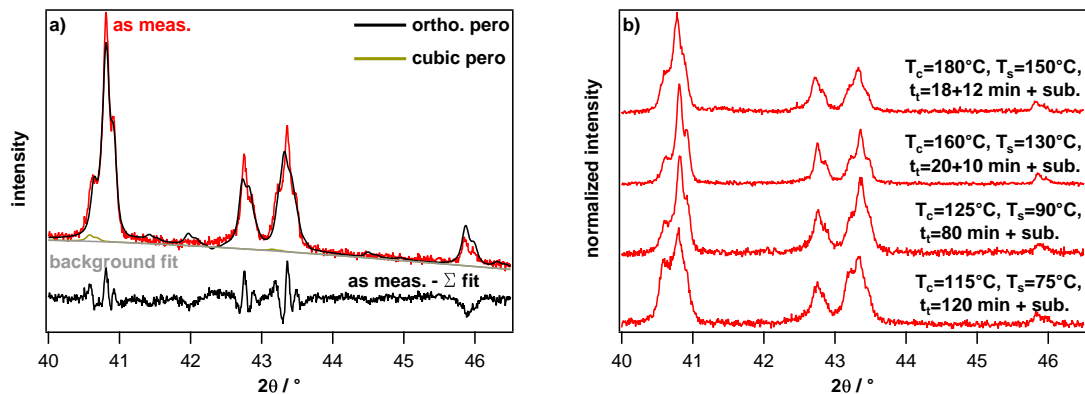


Figure 5.19.: Detailed XRD pattern of a MAPI layer fabricated from PbI_2 on a glass/FTO/ TiO_2 substrate at $T_s=130$ °C during the CSS process with Rietveld refinements for cubic and orthorhombic perovskite crystal structures (a). The measured curve is red and the background is light gray. The Rietveld refinements of the perovskite phases are black for the orthorhombic and green for the cubic phase. The difference between the measured curve and the superposition of the perovskite refinements and the background is denoted in black with “as meas. - Σ fit”. Detailed XRD patterns of MAPI layers fabricated at substrate temperatures of 75 °C, 90 °C, 130 °C and 150 °C during the CSS process (b). The diffraction patterns in (b) are normalized in intensity scale.

The found $Pnma$ crystal structure is unusual for MAPI at room temperature but reported as the low temperature phase of MAPI (phase transition reported around -112 °C) [92, 101–105]. The most reported room temperature modification of MAPI is tetragonal $I4/mcm$ [92, 101, 104]. However, the orthorhombic $Pnma$ phase is consistent with the

hierarchical development of the lower symmetry perovskite crystal structures from the archetype perovskite phase, cubic $Pm\bar{3}m$ [92, 106]. The deviations from the archetype, resulting in the tetragonal and orthorhombic crystal structures, are discussed to be related to the tilting/rotation of the PbI_6 octahedra, which reduce the symmetry of the crystal lattice [92, 104–107]. Thus, the phase transitions from cubic to orthorhombic have the character of an order-disorder transition, consistent with an entropy change associated with the phase transitions [92, 101, 104, 105, 107, 108]. While Kawamura et al. identify the rotation of the PbI_6 octahedra itself as ordering parameter, Deretzis et al. and Baikie et al. name the ordering of the MA^+ ion as the cause of the ordering phase transitions. The positive charge of the MA^+ ion is located at the NH_3^+ part. This charge forms ionic bondings with 3 iodine ions, to restore the iodine coordination of 3 which is the most favorable for iodine and is lost during the flipping of the PbI_6 octahedron during the PbI_2 to MAPI transformation [104, 107]. Accordingly, the iodine atoms leave their ideal positions to come closer to the positive charge causing the tilting of the octahedra [107]. In the most symmetrical cubic phase, the MA^+ ions are oriented randomly, canceling out the lattice distortions macroscopically [101, 104, 107, 108]. Compared to the cubic phase, the degrees of freedom for MA^+ orientation are reduced in the tetragonal phase and even more in the orthorhombic phase [92, 101, 104, 105, 108]. Baikie et al. even report the MA^+ ion to be completely ordered in the orthorhombic phase [92]. Hence, the phase transition from cubic to tetragonal to orthorhombic coincide with an ordering of the MA^+ ion. An illustration of the unit cell of 2step CSS MAPI fabricated at $T_s=90^\circ\text{C}$ from PbI_2 using the atomic positions, space group and unit cell dimensions obtained from the Rietveld refinement is shown in figure 5.20. It has to be pointed out that the illustration is intended as an aid to visualize the crystal structure of MAPI. The orientation of the MA^+ cation is chosen randomly during the refinement and does not contain any information about the MA^+ orientation in the real perovskite. Furthermore, the actual tilting, the rotation and the distortion of the PbI_3 octahedra in the real perovskite may be different to the one shown in figure 5.20. However, figure 5.20 corresponds to the general structure of the unit cell of the fabricated MAPI layers and is in agreement with illustrations of orthogonal MAPI presented in literature [92].

With the Rietveld refinements, the dimensions of the unit cells of the PbI_2 sample and the MAPI samples fabricated at different substrate temperatures can be determined and are presented in table 5.4. The comparison with literature shows that the lengths of the a axis of the PVD fabricated PbI_2 are well in accordance with literature (4.558(3) Å calculated versus 4.59 Å from literature) [98]. However, the c axis of the PVD fabricated layer appears to be longer then reported in literature (6.989(3) Å calculated versus 6.78 Å from literature), leading to a larger unit cell volume of the PVD fabricated PbI_2 (145.212 Å³) compared to literature values (123.7 Å³) [98, 109].

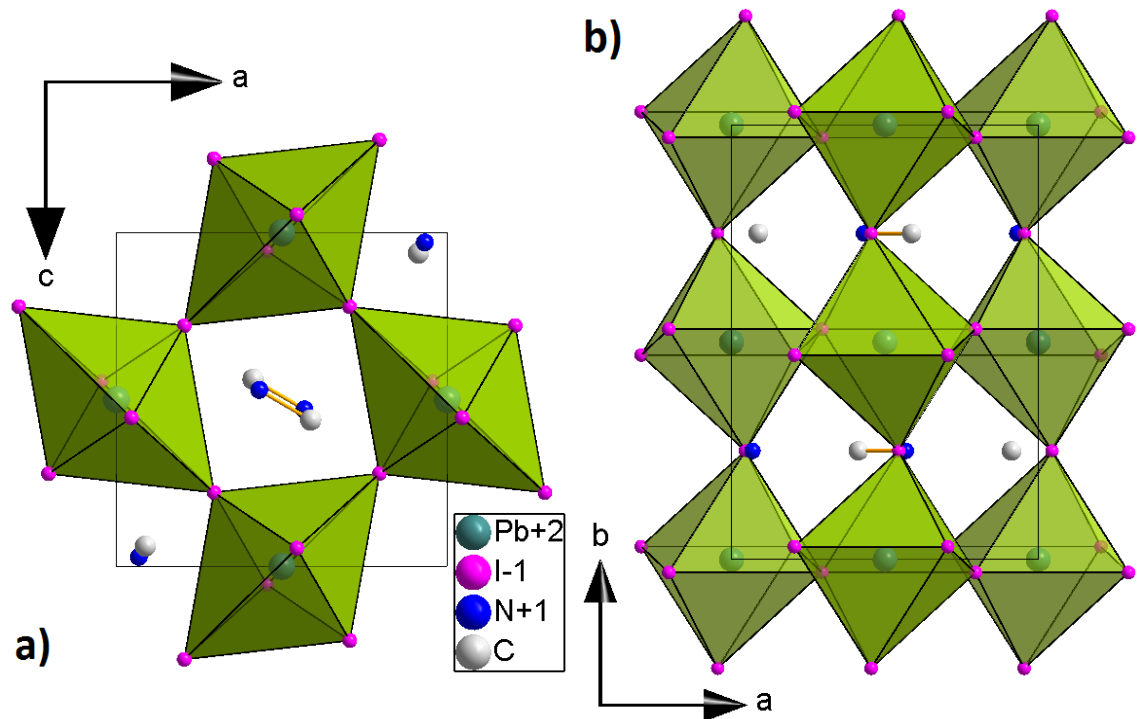


Figure 5.20.: Illustration of crystal structure of MAPI. The viewing directions are along a) [010], b) [001]. This illustration is an aid to visualize the crystal structure of MAPI. The orientation of the MA⁺ cation is not representative for the orientation in the real perovskite.

For MAPI in its tetragonal room temperature phase the following lattice constants can be found: Deretzis et al. found $a=b=8.86$ Å and $c=12.67$ Å (RT (assumed); layer) [107]; Kawamura et al. found $a=b=8.80$ Å and $c=12.69$ Å (220 K; single crystal) [104] and Baikie et al. found $a=b=8.85$ Å and $c=12.44$ Å (25 °C; powder diffraction experiments) [92]. The comparison of the unit cell parameters of the MAPI samples with these literature values shows that two axis fit well into the length regime presented in literature. Only one axis of the basal plane appears to be slightly elongated, separating the orthorhombic from the tetragonal crystal structure.

Table 5.4.: Unit cell dimensions in the directions a, b and c (see figures 5.17 and 5.20 for comparison) of MAPI samples fabricated from PbI₂ on glass/FTO/TiO₂ substrates at substrate temperatures during the CSS process of 75 °C, 90 °C, 130 °C and 150 °C. The unit cell dimensions of a PVD fabricated PbI₂ layer on a glass/FTO/TiO₂ substrate is given for comparison. The volumes are calculated with $a \cdot b \cdot c$.

$T_s / ^\circ\text{C}$	$a / \text{Å}$	$b / \text{Å}$	$c / \text{Å}$	$V / \text{Å}^3$
75	8.836(3)	12.546(3)	8.915(3)	988.482
90	8.827(3)	12.532(3)	8.902(3)	984.896
130	8.826(3)	12.542(3)	8.902(3)	985.590
150	8.825(3)	12.544(3)	8.901(3)	985.536
PbI ₂	4.558(3)	4.558(3)	6.989(3)	145.212

5.2.3 Optoelectronic structure

Besides the morphology and the crystal structure, their optical and electronic properties are key requirements for solar cell absorbers. To probe those properties UV/VIS and PE spectroscopy were performed for MAPI, PbI_2 and MAI samples. All examined layers were prepared under vacuum conditions and the PES was performed without breaking the vacuum conditions. The obtained results will be presented and discussed in the following, starting with the absorption coefficients. In figure 5.21, the absorption coefficients $\alpha_{h\nu}$ of four MAPI samples and a PbI_2 reference sample (all on glass/FTO/ TiO_2 substrates) are plotted against the photon energy E_{ph} . The unit of the absorption coefficient is $1/\text{cm}$ which corresponds to $1/(\text{cm layer thickness})$ for this work. The general shape of the $\alpha_{h\nu}$ over E_{ph} curves and the absorption edge are in good agreement with what has been reported in literature for $\text{CH}_3\text{NH}_3\text{PbI}_3$ prepared with different wet chemical and vapor phase methods [33, 40, 43, 110–112]. The marked positions are obtained by the intersection of the absorption edge with the regime where no excitation over the band gap occurs. This position is assumed to be the onset of the fundamental absorption and accordingly serves as a measure of the optical band gap.

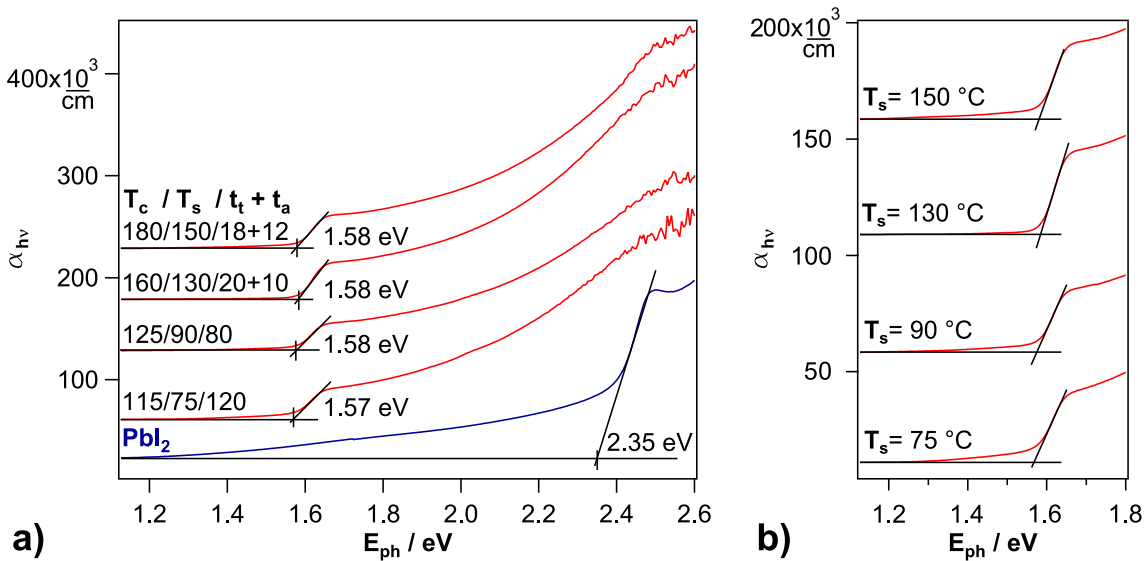


Figure 5.21.: (a) Absorption coefficient $\alpha_{h\nu}$ of PbI_2 and MAPI on glass/FTO/ TiO_2 substrates plotted against the photon energy E_{ph} . An offset of 50000 $1/\text{cm}$ is used for each MAPI spectra. Only between 75°C and 90°C substrate temperature an offset of 70000 $1/\text{cm}$ is used. The fabrication parameters of the MAPI layers are given in the way: crucible temperature / substrate temperature / transformation time + annealing time. In (b) the photon energy regime around the fundamental absorption edge of MAPI is enlarged. The absorption coefficient of PbI_2 is not shown. Again, an offset of 50000 $1/\text{cm}$ is used between the spectra. The spectra are labeled with the substrate temperature during the CSS process step.

With 1.57 - 1.58 eV for MAPI and 2.35 eV for PbI_2 the determined optical band gaps fit well to literature values [109,113–115]. Furthermore, the optical band gaps derived from the spectra in figure 5.21 fit to the band gaps around 1.7 eV measured with a combination of photoemission spectroscopy and inverse photoemission spectroscopy, presented in literature [116–118]. All of the spectra in figure 5.21 have two characteristics in common. The first one is that the adsorption coefficient does not drop to zero for photon energies below the onset of the fundamental absorption but shows a plateau of approximately constant values. The second characteristic is that the onset of the fundamental absorption is not perfectly sharp. In fact, the comparison with the SEM images in figure 5.14 indicates that the onset of the fundamental absorption of the MAPI layers in figure 5.21 becomes more diffuse with increasing surface roughness. UV/VIS measurements on the the bare glass/FTO/ TiO_2 substrate (not shown) identify the absorption in the substrate as cause of the plateau of the absorption coefficients at photon energies below the fundamental absorption. In addition, results by Shirayama et al. indicate that effect of surface roughness on the optical spectra might also contribute to the observation of the plateau of the absorption coefficients at photon energies below the fundamental absorption [119]. The reason for this is surface light scattering, which is not detected during the reflection and transmission measurements, is mistaken for absorption [119]. To obtain their results, Shirayama et al. prepared ultrasmooth MAPI layers by laser evaporation and used spectroscopic ellipsometry to determine the optical constants of MAPI [119]. Based on these constants, they calculated the influence of layer roughness on the course of the absorption coefficient over the photon energy [119]. Concerning the second common characteristic of the $\alpha_{h\nu}$ spectra in figure 5.21, the dependence of the sharpness of the onset of the fundamental absorption on the surface roughness, a diffuse onset of the fundamental absorption of MAPI is in agreement with the results of Shirayama et al. for rough MAPI layers [119]. However, in their calculations, the sharpness of the onset appears not to vary with varying surface roughness [119]. Still, since the calculations by Shirayama et al. indicate that the diffuse onset of the fundamental absorption is generally related to the surface roughness, its scaling with varying surface roughness is plausible. Besides the surface roughness, an additional effect needs some consideration. MAPI is reported to form shallow defect states either close to the VBM or close to the CBM [120–122]. Such defect states might well contribute to the diffuse onset of the absorption edge.

In conclusion, the plateau of the absorption coefficients in figure 5.21 at photon energies below the onset of the fundamental absorption is mainly caused by the absorption in the glass/FTO/ TiO_2 substrate, possibly enhanced by the effect of surface light scattering due to surface roughness. The effect of a varying surface roughness might also explain the varying sharpness of the onset of the fundamental absorption of the $\alpha_{h\nu}$ over E_{ph} curves in figure 5.21 [119]. However, the spectra in figure 5.21 show a dependence of the sharpness of the onset of the fundamental absorption on the roughness. In contrast, no such dependence can be determined in the work of Shirayama et al. [119]. Considering this discrepancy, the influence of other effects, especially the presence of defects needs to be

considered. The results obtained from the UV/VIS absorption data will be compared with the results from the PL spectroscopy experiments in section 5.4. There, the presence and influence of defects will be discussed in further detail.

The electronic properties of the MAPI layer surface were probed with PES. Since the core level positions and elemental surface compositions do not vary significantly for different substrate temperatures, only the MAPI spectra for $T_s=90^\circ\text{C}$ are shown in the following. The PES spectra for the other substrate temperatures can be found in the appendix. Figure 5.22 shows representative survey spectra for MAPI, MAI and PbI_2 .

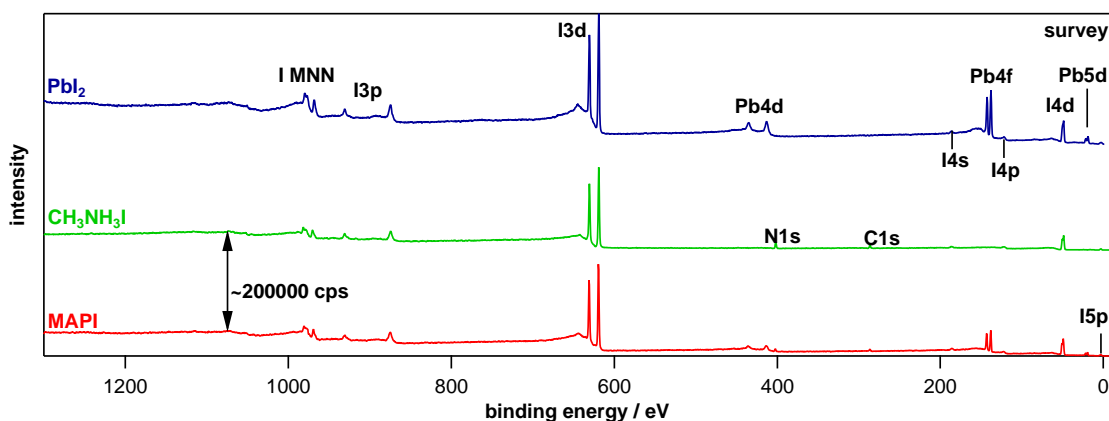


Figure 5.22.: Survey spectra of MAPI (red), PbI_2 (dark blue) and MAI (green) measured with XPS directly after the layer fabrication, without breaking the vacuum conditions. The offset between the MAPI and MAI is given as a guide to the eye for the intensity. Only the most prominent lines are labeled.

The survey spectra in figure 5.22 show no lead in MAI and no organic contaminations in PbI_2 . Furthermore, no other contaminations can be determined for the samples shown in figure 5.22. Only, the $T_s=150^\circ\text{C}$ sample shown in the appendix shows a tin contamination, which can be associated with the presence of MASI [123]. The cause of the tin contamination is most likely the parallel work on MAPI and MASI in the CSS chamber of our lab. Since the TiO_2 layers have been proven to be dense in section 5.1, it can be excluded that the Sn contaminations originate from the FTO substrate. Another interesting observation is that the survey spectra in figure 5.22 already show that the intensity of the Pb emissions decreases with respect to the intensities of the iodine emissions of MAPI compared to PbI_2 , well in accordance with the element ratios presented in table 5.6. The core line positions, valence band maximum positions and work functions of MAPI, fabricated at substrate temperatures of 75°C , 90°C , 130°C and 150°C during the CSS process step, as well as for PbI_2 and MAI are shown in table 5.5. Due to the contaminations, only the core level positions, but no valence band maximum positions are presented in table 5.5 for the $T_s=150^\circ\text{C}$ MAPI sample. The measured core level and valence band maximum positions and work functions are in accordance with literature values for MAPI prepared with wet chemical methods and by evaporation under vacuum conditions [96, 113, 116, 124–130]. The surface ratios for the MAPI samples in table 5.6 are sufficiently close to stoichiometric

ratios (I/N/Pb = 3/1/1) to assume a clean MAPI surface. This indicates that no surplus MAI is on top of the MAPI layers and that unreacted PbI₂, which is indicated by the XRD patterns in figure 5.15, is most likely located deep inside the bulk material not influencing the PES results of the MAPI layers [126]. The element ratios at the surface of the T_s=150 °C sample get significantly closer to stoichiometric ones when considering Sn and Pb together (I/(Pb+Sn)=3.0 and N/(Pb+Sn)=0.9).

Table 5.5.: Core level positions, valence band maximum positions and work functions for PbI₂, MAI and MAPI fabricated from PbI₂ at T_s of 75 °C, 90 °C, 130 °C and 150 °C during the CSS process. T_s is given in °C and all binding energies are given in eV.

T _s	I3d ^{5/2}	N1s	C1s	Pb4f ^{7/2}	VBM (XPS)	VBM (UPS)	φ
75	619.50	402.59	286.55	138.54	1.65	x	x
90	619.47	402.62	286.58	138.57	1.65	1.61	4.38
130	619.50	402.60	286.40	138.57	1.65	x	x
150	619.51	402.56	286.54	138.52	x	x	x
PbI ₂	619.60	x	x	138.67	1.76	1.86	5.08
MAI	619.11	402.05	286.52	x	2.14	2.22	4.21

Table 5.6.: Element ratios at the sample surface of MAPI derived from PbI₂, of PbI₂ and of MAI samples obtained from XPS measurements with Scofield ionization cross sections.

T _s / °C	I/Pb	N/Pb	I/N
75	3.1	0.9	3.4
90	3.1	1.0	3.1
130	3.0	0.9	3.5
150	3.7	1.1	3.4
including Sn	3.0	0.9	3.4
ideal MAPI	3	1	3
PbI ₂	2.0	x	x
MAI	x	x	1.1

The valence band spectra measured with XPS and UPS as well as the SEE measured with UPS are presented in figure 5.23. The valence band maximum positions of CH₃NH₃PbI₃ and CH₃NH₃PbI_{3-x}Cl_x perovskites are reported to vary between a slight (nearly intrinsic) and a pronounced (E_F pinned to the conduction band) n-type character. Also for the work functions a broad range from 3.85 eV to 4.95 eV for wet chemical prepared MAPI layers and from 4.19 eV to 4.86 eV for MAPI layers fabricated by evaporation under vacuum conditions is reported [113,116,124–128]. Evidently, the work function and the valence band maximum position are dependent on several factors, for example, the substrate material, the fabrication technique used for the MAPI layers, and illumination conditions during the measurement [96, 113, 116, 124–129, 131]. However, stoichiometric samples fabricated with the most common fabrication methods as examined with photoemission spectroscopy in literature show (at least slight) n-type behavior [113,116,124–128]. A p-type character

is reported for MAPI single crystals or requires intentional modifications of the fabrication process of the MAPI layers, for example by modifying the stoichiometry or controlling the kind and the density of defects in the MAPI layers [121, 132–135]. Accordingly, the n-type behavior of the MAPI layers examined in this work is well in accordance with stoichiometric MAPI, and not a specific feature of the 2step CSS. Furthermore, the valence band maximum positions of MAPI layers fabricated from PbI_2 show no or only small variations, even if the processing temperatures are varied (see table 5.5). This indicates that even the high temperature sets of $160^\circ\text{C}/130^\circ\text{C}$ and $180^\circ\text{C}/150^\circ\text{C}$ do not alter the doping density of the MAPI layers significantly. For solar cells fabricated on an n-type substrate a strong n-type characteristic of the MAPI yields several advantages for the electron selective contact (here to the FTO/ TiO_2 electrode), constituting good electron transfer from MAPI to the ETL and only small losses for the V_{oc} in a solar cell [113, 129]. Only interface effects might hinder the electron extraction [113, 129]. Since the n-type character of the MAPI will be fully developed after the deposition of the n-type substrate, the HTL needs to be selected appropriate to minimize the extraction barrier for holes, to keep the V_{oc} loss as small as possible and provide sufficient charge carrier separation at the same time.

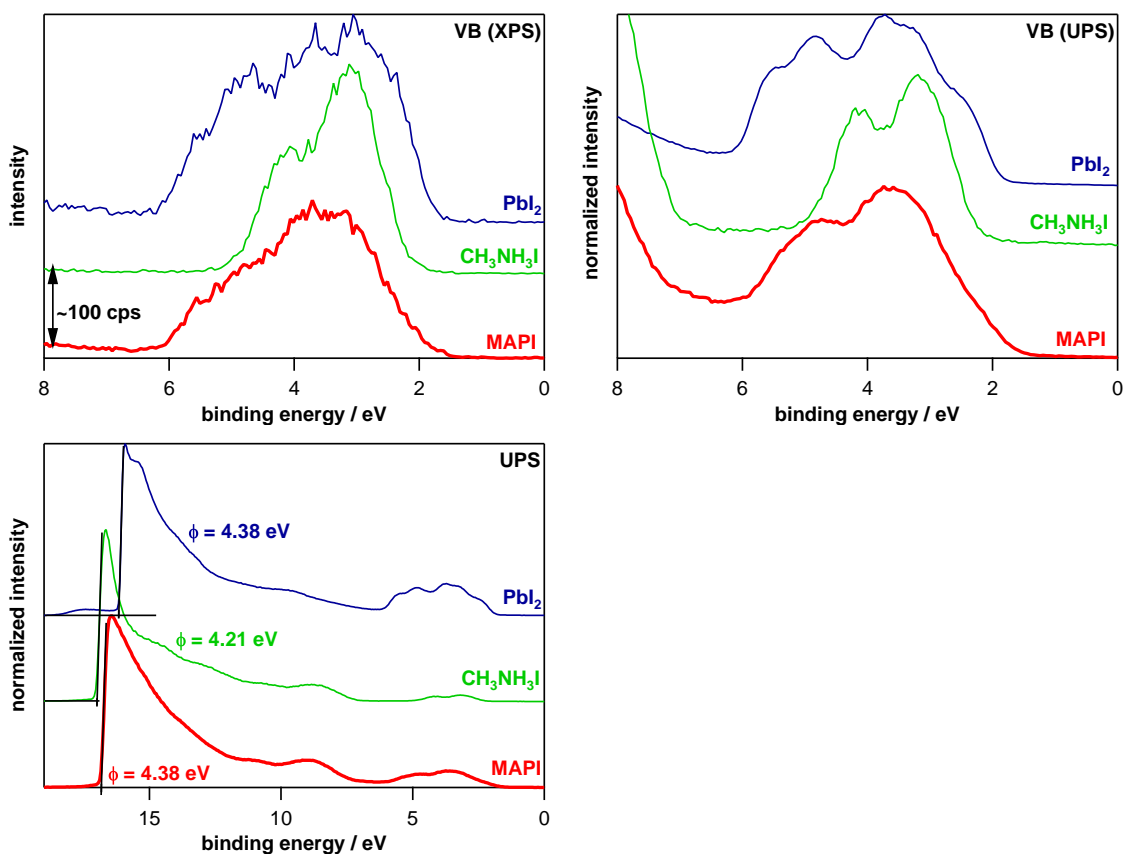


Figure 5.23.: Valence band (XPS and UPS) and survey UP spectra of MAPI (red), PbI_2 (dark blue) and MAI (green) measured directly after the layer fabrication, without breaking the vacuum conditions. The offset between MAPI and MAI in the XPS spectra is given as a guide to the eye for the intensity. The UP spectra are normalized in intensity scale.

The band gap measured with UV/VIS is smaller than the energetic difference between the valence band and the Fermi level measured with PES. This would mean that MAPI is degenerately n-type and should behave more like a metal than like a semiconductor. But, this is not the case. In IV measurements, MAPI layers behave like semiconductors. For this observation, different explanations are conceivable. For example, the formation of excitons in addition to free charge carriers during the UV/VIS experiments could explain that the band gap appears to be smaller than the energetic difference between E_F and the VBM. Concerning the excitation of excitons compared to the excitation of free charge carriers, different opinions can be found in literature [102, 136–139]. Shi et al. propose the excitation of two types of excitons at room temperature, in addition to the band-band excitation. The first exciton type has a binding energy of 17 meV and is accordingly dissociated at room temperature [136]. In addition to that first exciton, Shi et al. propose a bound exciton with a binding energy of 67 meV [136]. They report that the presence of both excitons shifts the onset of the absorption edge from 1.645 eV to about 1.53 eV [136]. Thereby, the excitation of the dissociated exciton species leads to a shift of the optical gap to approximately 1.56 eV and the excitation of the non-dissociated exciton species to a further shift to approximately 1.53 eV [136]. The presence of an exciton species with a binding energy in the range of $k_B T$ at room temperature is in agreement with other literature sources [102, 138, 140]. Nevertheless, even when the excitation of excitons is considered, MAPI is reported to be dominated by a non-excitonic behavior in several literature sources [102, 137–139]. For the MAPI samples presented in this work, no evidence for the bound excitons reported by Shi et al. can be found. Furthermore, the observed onset of the absorption over the energy gap is at higher photon energies (1.57-1.58 eV) compared to the onset which would be expected in case of a significant contribution of the excitation of the low binding energy excitons and is in accordance with optical band gaps reported in literature [109, 113–115]. However, since the observed absorption edge is close to the one which would be expected in case of the excitation of the dissociated excitons reported by Shi et al., the excitation of those excitons still appears to be possible. Hence, a certain influence of the formation of excitons on the optical absorption properties of the perovskites, for example on the onset of the absorption edge might be present. Another influence which can cause an underestimation of the optical band gap derived from optical spectra is the surface roughness of the MAPI layers [119]. Furthermore, since the presence of defects can additionally influence the onset of the fundamental absorption, they may also affect the determination of the optical band gap. Hence, besides the possible influence of excitons, the underestimation of the optical gap due to surface roughness and the influence of defects may add to the impression that the optical gap is smaller than the energetic distance between E_F and the VBM. However, as mentioned above, the band gaps determined from the optical spectra in figure 5.21 fit well to literature values [109, 113–115]. In addition, the energetic difference between the VBM and the band gap is in the range of the measurement errors for the determination of those values. Hence, it is not possible to unambiguously determine the exact energetic differ-

ence and to decide on its actual origin. The results for the band gap, the valence band maximum position and the work function of PbI_2 , MAPI and MAI are summarized in the band energy diagrams in figure 5.24.

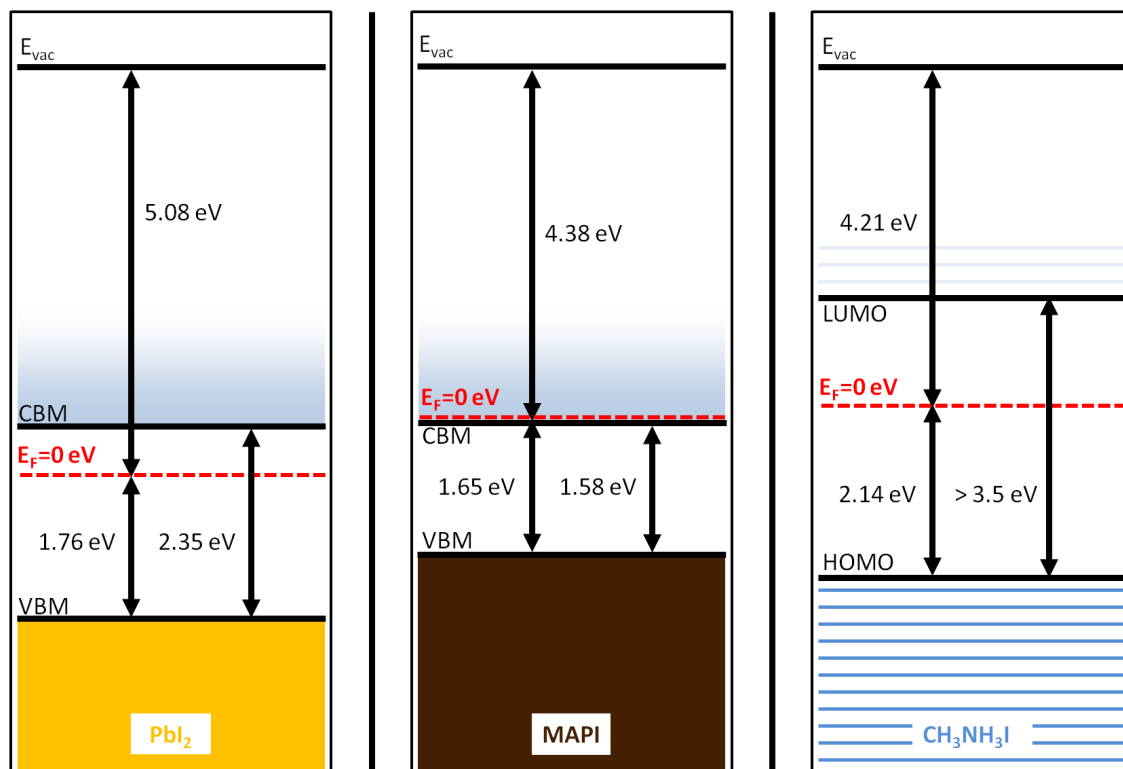


Figure 5.24.: Band energy diagrams of PbI_2 , MAPI and MAI derived from the PES data presented in table 5.5 and UV/VIS data from figure 5.21. The vacuum levels are aligned. The LUMO of MAI is drawn at 3.5 eV above the HOMO. This was done because the used glass/FTO/ TiO_2 substrates show an absorption edge between 3.5 eV and 4 eV. Since no absorption edge for MAI could be determined up to these photon energies, the band gap of MAI is assumed to be larger than 3.5 eV.

Even though the phase contents derived from XRD and the surface stoichiometries derived from XPS, indicate no MAI on top of the examined MAPI layers and a low PbI_2 content in the examined MAPI layers, it is reasonable to assume that those phases may occur within the absorber layers for some depositions. Hence, the possible energetic alignment of MAPI, $\text{CH}_3\text{NH}_3\text{I}$ and PbI_2 should be discussed next. The Anderson alignment in figure 5.24 shows that the valence band offset between MAPI and PbI_2 is $\Delta E_{\text{VBM}} = 0.81$ eV and the conduction band offset is $\Delta E_{\text{CBM}} = 0.04$ eV. Since an offset of 0.04 eV is below the PES measurement uncertainty, the conduction band offset of PbI_2 and MAPI is treated as zero. The Anderson alignment of MAPI and MAI shows a ΔE_{VBM} of 0.32 eV. Following the Anderson rule and treating ΔE_{VBM} and ΔE_{CBM} as the barrier heights, the MAPI/MAI contact would hinder the hole extraction from MAPI into Spiro-MeOTAD. The PbI_2 /MAPI contact would be hole blocking but not electron blocking. However, the PbI_2 /MAPI contact is a semiconductor isotype hetero junction. In that case, the charge transport over the barrier

can be described in terms of thermionic emission of majority charge carriers, similar to a Schottky contact [47]. With that, not only the conduction band offset will influence the electron extraction from MAPI into PbI_2 , but also the band bending, which constitutes a potential barrier for the charge transport through the PbI_2 /MAPI interface [47]. A graphic depiction of a possible contact between PbI_2 and MAPI, considering the band bending, is shown in figure 5.25. A first approximation of the distribution of the total band bending between PbI_2 and MAPI could be derived from the charge distribution in the space charge regions under application of the Poisson equation (equation 3.4). However, since the PbI_2 /MAPI contact is an isotype hetero junction, the combination of the knowledge about the doping concentrations in PbI_2 and MAPI (assessable by the distance between Fermi level and CBM) and the depletion approximation is not sufficient to approximate the charge distribution, as is would be for a p/n-junction. The knowledge of the width of the space charge regions in PbI_2 and MAPI is crucial in order to estimate whether the main part of the band bending takes place in MAPI or in PbI_2 . Unfortunately, only an interface experiment between MAPI and PbI_2 would yield the needed information about the widths of the space charge regions. Hence, the band bending distribution in figure 5.25 is hypothetical, assuming a wider space charge region in PbI_2 compared to MAPI and accordingly the larger part of the band bending in PbI_2 .

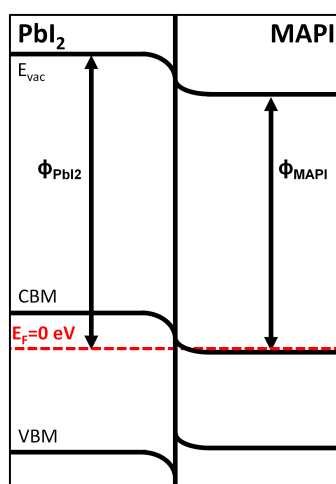


Figure 5.25.: Schematic depiction of the band bending at PbI_2 /MAPI junction in the dark.

The considerations on the PbI_2 /MAPI contact described till now treat the contact in the dark. Illumination further complicates the case. Here, the band bending of MAPI will be superimposed by the electrical field caused by photoexcited charge carriers. Under open circuit conditions, the photoexcited holes will accumulate in the Spiro-MeOTAD/gold electrode and the photoexcited electrons in the FTO/ TiO_2 electrode. The resulting electric field will reduce the influence of the band bending on the electron extraction. However, since the MAPI/ PbI_2 contact is probably not the photoactive contact of the solar cell, the potential barrier caused by the band bending will not be fully annihilated also under illumination and the electron transfer from MAPI into the FTO/ TiO_2 electrode will

remain to be hindered by the PbI_2/MAPI contact. Furthermore, with a DC conductivity of $5 - 10 \cdot 10^{-9} \text{ S/m}$ [141] (compared to an electrical conductivity around 500 S/m for MAPI [115]), PbI_2 is quite insulating. Thus, in conclusion, thin, dense layers of PbI_2 will increase the serial resistance of a solar cell and need to be avoided, on one hand because of the contact between PbI_2 and MAPI and on the other hand because of the insulating properties of PbI_2 . A more dedicated discussion on the incorporating the 2step CSS fabricated MAPI layers in planar solar cells will be given in section 5.4.2.

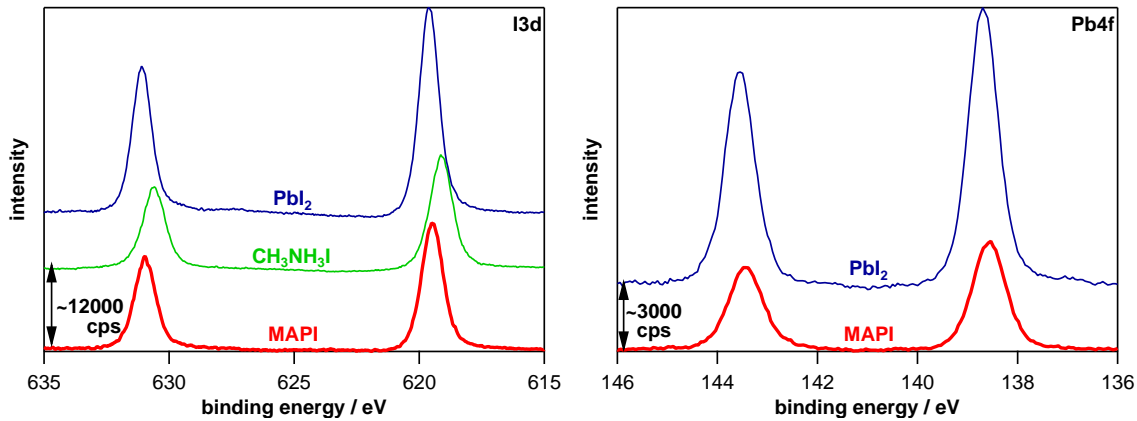


Figure 5.26.: I3d and Pb4f detail spectra of MAPI (red), PbI_2 (dark blue) and MAI (green) measured with XPS directly after the layer fabrication, without breaking the vacuum conditions. The offset between MAPI and MAI is given as a guide to the eye for the intensity.

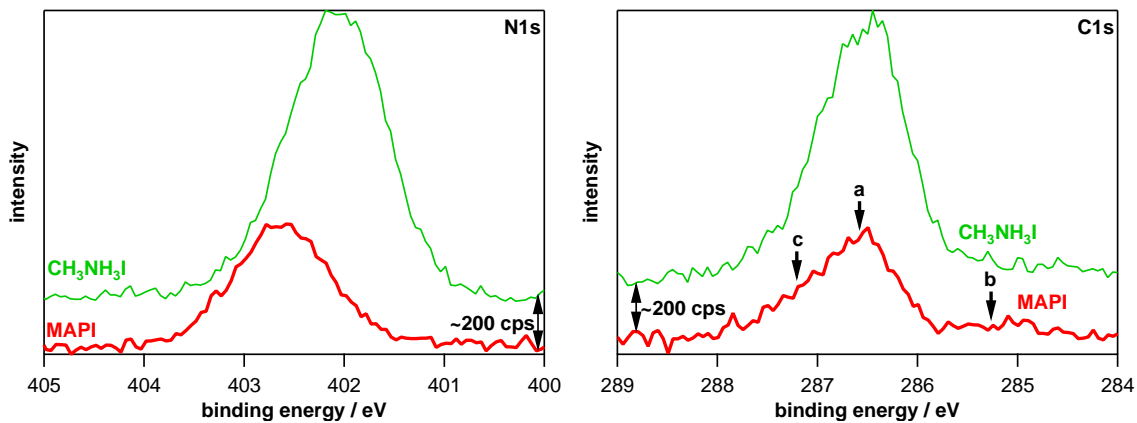
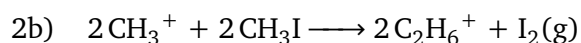
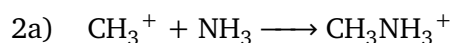
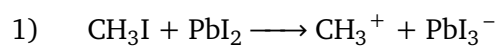
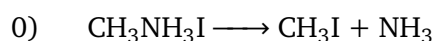


Figure 5.27.: N1s and C1s detail spectra of MAPI (red) and MAI (green) measured with XPS directly after the layer fabrication, without breaking the vacuum conditions. The offset between MAPI and MAI is given as a guide to the eye for the intensity. There is no PbI_2 curve since PbI_2 does not contain any nitrogen or carbon. In the C1s spectrum, the main emission, belonging to MAPI is denoted with "a", the low binding energy emission with "b" and the high binding energy shoulder of the MAPI emission with "c".

The shapes of the I3d, Pb4f and N1s emissions in figures 5.26 and 5.27 indicate that only one species of iodine, lead and nitrogen is present in the MAPI samples. In contrast, the C1s emission of MAPI shows a second emission on the lower binding energy side (b) and possibly also a third one on the higher binding energy side (c) of the C1s central emission (a) in figure 5.27. However, due to the low signal to noise ratio, the presence of the shoulder on the higher binding energy side can not be determined unambiguously. The comparison with literature identifies the central C1s line as the one belonging to the CH_3NH_3^+ cation of MAPI [126]. The lower binding energy shoulder is associated with CH_3I , CH_3NH_2 or carbon contaminations [125, 126, 129]. Due to the in vacuo nature of our experiments, we rule out carbon contaminations in such significant concentration. This leaves the other possibilities to be discussed. The most probable explanation appears to be a CH_3I excess in the layers [126]. Stepwise transformation experiments from PbI_2 to MAPI, performed by Liu et al. show that the lower binding energy component appears prior the main MAPI component [126]. This observations could not be repeated in our lab, where the C1s main component of MAPI appeared directly during the stepwise transformation of PbI_2 to MAPI (see figure A.7 in the appendix). However, it still appears plausible that the low BE component is related to CH_3I . Juarez-Perez et al. [57] have shown, that MAI will most likely not sublime as MAI but as CH_3I and NH_3 . The comparison of the vapor pressures of CH_3I and NH_3 shows that it is likely that CH_3I will adsorb onto the substrate while the NH_3 stays in the gas phase [142]. Accordingly, it appears plausible that CH_3I is incorporated into the MAPI layers prior to NH_3 and that more CH_3I than NH_3 is incorporated into the MAPI layer. However, since the I3d emissions in figure 5.26 do not show any shoulder line, the identification of CH_3I as origin of the C1s low BE shoulder is not completely unambiguous. Furthermore, if the shoulder would belong to a nitrogen containing compound like CH_3NH_2 , there should be a shoulder in the N1s spectra as well. In addition, CH_3 or CH_3^+ are assumed to be too reactive to stay in significant amounts in the MAPI layer. Another explanation for the C1s low BE shoulder could be the replacement of a fraction of the MA^+ cations by C_2H_6^+ . A possible reaction for the formation of the C_2H_6^+ cation is proposed below.



Reaction 0 describes the dissociation of MAI which takes place already during the sublimation of MAI [57]. Reaction 1 describes, the reordering of the octahedra from edge sharing to corner sharing (see also section 5.2.2). During the reorientation, an additional I is implemented into the inorganic lattice, leaving a CH_3^+ ion. This ion will react. Two possibilities are shown in reaction 2a and 2b. Reaction 2a yields the standard organic cation of MAPI. Reaction 2b describes the reaction of a CH_3^+ ion with surplus CH_3I to C_2H_6^+ under the emission of I_2 gas. Since the ethan ion would only contain carbon and hydrogen atoms, its presence would be in agreement with the observation, that only the C1s emission did show shoulder lines in the PES experiments. Yet, this explanation remains mostly speculative. An alternative dissociation of MAI during the sublimation process, the dissociation into HI and CH_3NH_2 was indicated by results of Nenon et al. in 2016 [143]. Recently, Bækbo et al. published results that indicate a combination of the two dissociation mechanisms [42]. They observe that MAI evaporated mainly as HI and CH_3NH_2 in the temperature regime up to 130°C under ultra high vacuum conditions [42]. For temperatures above 160°C they observe the presence of NH_3 and CH_3I and suggest those molecules as products of further dissociation of HI and CH_3NH_2 [42]. However, Juarez-Perez et al. do not observe the presence of HI and CH_3NH_2 [42, 57]. Thus, in conclusion, the reaction mechanism proposed above is valid at least for the two high temperature parameter sets ($130^\circ\text{C}/160^\circ\text{C}$ and $150^\circ\text{C}/180^\circ\text{C}$). For the lower temperature sets, the presence of HI and CH_3NH_2 in the gas phase in addition to NH_3 and CH_3I needs to be kept in mind. However, since the low BE emission of the C1s emission appears to be independent on the process temperature regime and can hardly be explained based on the presence of HI and CH_3NH_2 , the dissociation of MAI into NH_3 and CH_3I is considered as dominant dissociation path of MAI for the examined CSS process. With respect to the adsorption mechanisms described in section 3.3, the adsorption of CH_3I appears to be a dissociative chemisorption while the adsorption of NH_3 is expected to be a non-dissociative chemisorption. The high BE shoulder of the C1s emission is difficult to identify. Since the core lines of the other elements do not show any shoulder, the C1s high BE shoulder probably does not belong to any compound of carbon with iodine, nitrogen or lead.

The comparison of the MAPI spectra with the PbI_2 spectra in figure 5.26 shows that it is difficult to distinguish the materials by the positions of their I3d or Pb4f emissions or by their binding energy differences (see table 5.5). However, the measured PbI_2 and MAPI spectra show a different line shape in the valence band region, which may be used to differentiate between PbI_2 and MAPI. In addition, the surface stoichiometry and the occurrence of C and N can be used to differentiate between PbI_2 and MAPI in PES experiments. The determination of the absolute core line positions of iodine, nitrogen and carbon in MAI is not trivial. MAI is an insulating organic material. Hence, for thick layers, charging can be expected during XPS measurements. On the other hand, for very thin films (thickness below 20 nm) charging is unlikely, but the core line positions might be affected by the substrate or the interface to the substrate. To solve the problem a MAI layer

was deposited onto a glass/FTO/TiO₂ substrate and a layer thickness was chosen that no substrate signal (Sn, Ti or O) was detected anymore. On the other hand, the layer was sufficiently thin that no distinct XRD signal of the MAI layer was observable (diffraction pattern not shown). The line positions and element ratios for this sample are shown in figures 5.23 to 5.27 and tables 5.5 and 5.6. Thereby, the comparison of MAI and MAPI shows that both materials can be readily distinguished not only by the layer stoichiometry but also by the binding energy positions of I3d, N1s, C1s and the valence band maximum position.

5.2.4 The titanium dioxide/lead iodide interface

When the preparation of a perovskite absorber layer with a two step process is discussed, it is important to start with the PbI_2 deposition step. In contrast to the co-evaporation processes, the PbI_2 deposition step will define the interface between the glass/FTO/ TiO_2 substrate and the absorber layer. Possible chemical reactions, dipole formations and other interface effects will happen during this first step and strongly influence the interface characteristics also after the conversion of the PbI_2 to MAPI in the CSS. Furthermore, since no organic molecules are involved in the interface formation during the lead salt deposition of a two step process, the observed effects might be different between a co-evaporation and a sequential deposition process of MAPI. Accordingly, the $\text{TiO}_2/\text{PbI}_2$ interface will be discussed in the following, starting with the survey XP spectra in figure 5.28. The spectra shown in figure 5.28 are measured on the oxygen plasma treated glass/FTO/ TiO_2 substrate (0 s) and between consecutive PbI_2 deposition steps. The deposition times are given cumulative, e.g. 5 s = 1 s + 4 s.

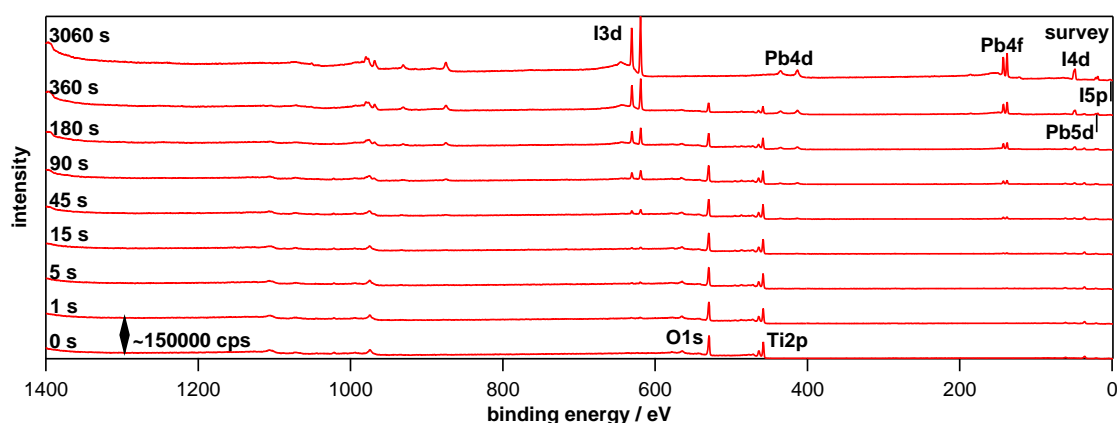


Figure 5.28.: XP survey spectra measured on the bare glass/FTO/ TiO_2 substrate and between consecutive PbI_2 depositions without breaking the vacuum conditions. The shown deposition times are cumulative deposition times. The offset between the 0 s and 1 s measurements is given as a guide to the eye for the intensity. Only the most prominent lines are labeled.

The survey spectra of the glass/FTO/ TiO_2 substrate in figure 5.28 shows no significant contaminations. Only a minor amount of zinc might be present in the spectra of the bare glass/FTO/ TiO_2 substrate. The deposition of the PbI_2 layer can be seen in the decreasing intensity of the O1s and the Ti2p lines while the intensity of the I3d and Pb4f lines increases constantly till no indication of the substrate remains after 3060 s of PbI_2 deposition. It has to be mentioned that the PbI_2 source apparently was contaminated with tin visible from the Sn3d emissions in figure 5.29 (for comparison see also figure A.5 and A.6 in the appendix). The comparison of the tin content with the lead content in the PbI_2 layer shows that tin is more than a contamination for the first 4 deposition steps. From the fifth deposition step onward the ratio of Sn to Pb is sufficiently low to treat Sn as

contamination till no Sn emission is observed anymore after 3060 s of PbI_2 deposition. In addition, in accordance with a reasonable stoichiometric I/Pb ratio of 1.9, the PbI_2 valence band maximum position obtained after 3060 s is not compromised by Sn5s states, which would lead to a significant lower valence band onset [144]. Since neither the pristine substrate nor the thick PbI_2 layer show any indications of tin, both flat band valence band maximum positions are assumed to be independent on the tin contamination and are in agreement with previous results (see figure 5.29 and 5.4 and tables 5.5 and 5.1). In addition, lead will most likely not react with tin, and is used to follow the energy level shift of the PbI_2 layer.

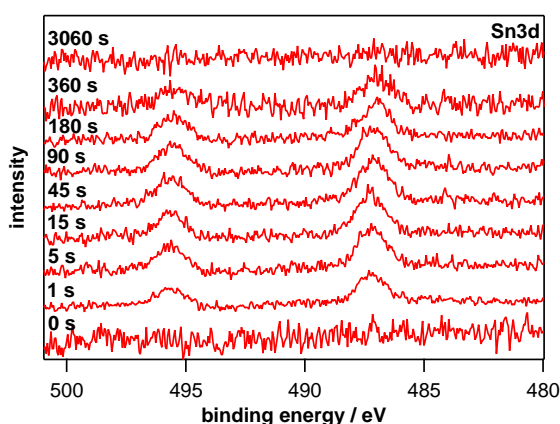


Figure 5.29.: Sn3d XP detail spectra measured on the bare glass/FTO/ TiO_2 substrate and between consecutive PbI_2 depositions without breaking the vacuum conditions. The shown deposition times are cumulative deposition times. No background correction was performed for the spectra in this figure.

An interesting observation is the evolution of the I3d line in figure 5.30. Even on the pristine substrate, a minor $\text{I3d}^{5/2}$ emission around 624.2 eV (marked with an arrow in figure 5.30) can be observed. This emission is clearly distinguishable from the PbI_2 $\text{I3d}^{5/2}$ emission at 619.4 eV and vanishes after 45 s of PbI_2 deposition. The binding energy position of the I3d emissions directly rules out, that it belongs to PbI_2 or SnI_2 where it would be in its I^- state [87]. Also the presence of iodine in I_2 does not fit to the binding energy [87]. A chemical reaction between the substrate and the iodine appears to be a good explanation for the second iodine line. Olthof et al. describe the catalytic activity of metal oxides during the co-deposition of MAPI [129]. They describe the formation of an about 3 nm thick interface layer containing mostly C, N and I species on ITO and MoO_3 . Only after this interface layer is completed, the formation of the MAPI layer begins. The presence of organic buffer layers avoids the formation of the interface layer [129]. But, since neither N nor C are available for the formation of the interface layer during the lead salt deposition of a two step process, the formation of an inorganic interface layer appears plausible. A possible reaction would be the one of iodine with O_2^- adsorbates on the TiO_2 after the plasma treatment (see section 5.1.1). This reaction can form a number of compounds like iodates and periodates [87, 142]. Thereby, the binding energies of

623 eV to 624 eV, reported for periodates and similar compounds with iodine in its I^{5+} or I^{7+} state, correspond to the binding energies observed in figure 5.30 [87, 145]. The formation of lead(II) iodate ($Pb(IO_3)_2$), which is a salt stable at room temperature [146], appears to be a plausible reaction. Since $Pb(IO_3)_2$ includes not only iodine but also lead and oxygen the PE spectra of those elements might also give some indication for the presence of $Pb(IO_3)_2$. However, the intensity of the I3d emissions belonging to $Pb(IO_3)_2$ is low. Accordingly, also the O1s and Pb4f emissions related to $Pb(IO_3)_2$ will be weak in intensity. In addition, in $Pb(IO_3)_2$ oxygen is in its O^{2-} state. Hence, the O1s emission of $Pb(IO_3)_2$ is likely superimposed by the O1s emission originating from the O^{2-} in TiO_2 and no O1s emission originating from the presence of $Pb(IO_3)_2$ can be determined in the O1s detail spectra. The O1s detail spectra are shown in figure A.8 in the appendix. The Pb4f detail spectra measured on the bare substrate and after 1 s, 5 s and 15 s of PbI_2 deposition are shown in figure 5.30 b. In figure 5.30 b, only the Pb emission associated with PbI_2 can be determined. However, the lead in $Pb(IO_3)_2$ is in the same oxidation state as in PbI_2 (Pb^{2+}) and the Pb4f emissions of the $Pb(IO_3)_2$ phase are probably superimposed by the Pb4f emissions of PbI_2 . Only the I3d emissions of $Pb(IO_3)_2$ are clearly distinguishable from the ones of PbI_2 since iodine is in its I^{5+} state in $Pb(IO_3)_2$ compared to the I^{-1} state in PbI_2 . In addition, the deposition of an iodate or a periodate would explain the binding energy position of the minor iodine emission on the pristine substrate which is at too high binding energies for I_2 contaminations [87]. The formation of $Pb(IO_3)_2$ is the most plausible assumption based on the analysis of the XP spectra. However, we cannot exclude numerous other compounds containing iodine, oxygen and lead which could form parallel to or instead of $Pb(IO_3)_2$ and explain the iodine emission around 624.2 eV. A deposition of iodine prior to the deposition of lead with a possible intercalation of iodine into the TiO_2 can be ruled out since the I3d emissions as well as the Pb4f emissions can both be determined already after 1 s of PbI_2 deposition.

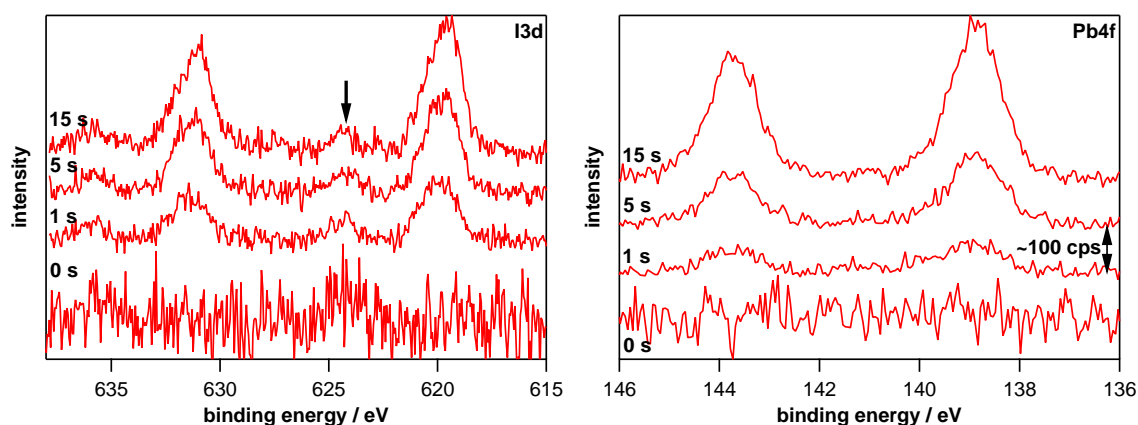


Figure 5.30.: I3d and Pb4f XP detail spectra for the bare glass/FTO/ TiO_2 substrate and after cumulative PbI_2 deposition times of 1 s, 5 s and 15 s. No background correction was performed for the spectra in this figure. The I3d emission around 624.2 eV is marked with an arrow.

In order to illustrate the energy level shifting associated with the formation of the PbI_2 layer, the core line spectra of $\text{Ti}2p$ and $\text{Pb}4f$ are shown in figure 5.31, exemplarily for the glass/FTO/ TiO_2 substrate and the PbI_2 layer. The detail spectra of $\text{I}3d$ and $\text{O}1s$ for all deposition steps can be found in figure A.8 in the appendix.

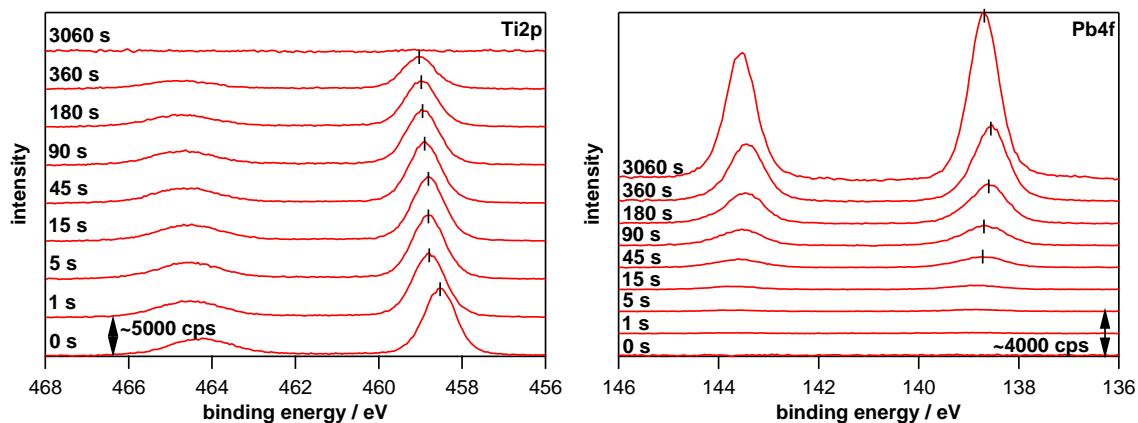


Figure 5.31.: $\text{Ti}2p$ and $\text{Pb}4f$ XP detail spectra measured on the bare glass/FTO/ TiO_2 substrate and between consecutive PbI_2 depositions without breaking the vacuum conditions. The shown deposition times are the cumulative deposition times. The offsets are given as a guide to the eye for the intensity.

The $\text{Ti}2p^{3/2}$ line in figure 5.31 shows a steady shift towards higher binding energies which is most pronounced between the bare substrate and the first PbI_2 deposition. The $\text{Pb}4f^{7/2}$ line, however, steadily shifts to lower binding energies up to 360 s, recovers partly during the last deposition step towards higher binding energies but does not reach its initial position again. To illustrate the energy level shift more clearly, the assumed shift of the valence bands for substrate and layer are shown in figure 5.32. Since the valence band spectra of the substrate and the layer superimpose each other for all deposition steps but 0 s and 3060 s, the valence band maximum positions can not be determined directly from the measured spectra. But following the assumption that the energetic difference between the valence band and the core lines is fixed, the intermediate valence band maximum positions can be obtained by using the positions of the pristine substrate and the thick PbI_2 layer and applying the shifts of the core lines, as done in figure 5.32 a.

The VBM shifts derived from Ti and O are quite parallel. Hence, the band bending of the substrate is well defined and corresponds to the one seen in the $\text{Ti}2p$ detail spectra. For the layer however, there is a discrepancy between the I and the Pb shift for deposition times from 15 s to 180 s. Probable reasons for the discrepancy between the iodide and the lead shift in figure 5.32 a are related to the interface reaction described above. Since lead is assumed to be less influenced by those effects, its shift is used to describe the layer band bending. During an interface experiment the layer shift is superimposed by the substrate shift and needs to be corrected. This correction is shown in figure 5.32 b as black curve. For the PbI_2 layer the valence band maximum position directly at the interface (which would correspond to a 0 s position) is assumed to be similar to the one

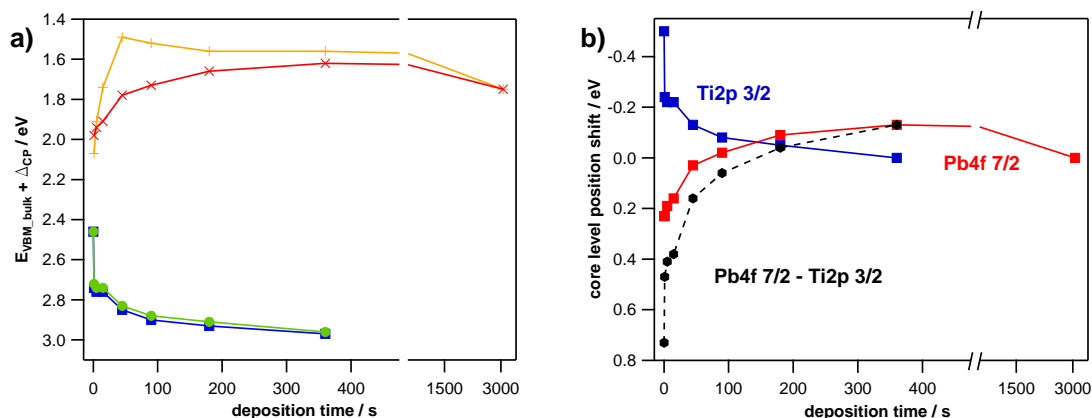


Figure 5.32.: (a) Shift of the valence band maximum positions of Ti, O, I and Pb with cumulative PbI_2 deposition time. The bulk valence band maximum positions (0 s for Ti and O and 3060 s for I and Pb) are used as references. The binding energy shift is then assumed to be the one of $\text{O}1s$, $\text{Ti}2p^{3/2}$, $\text{I}3d^{5/2}$ and $\text{Pb}4f^{7/2}$. (b) Shift of the $\text{Pb}4f^{7/2}$ (red) and $\text{Ti}2p^{3/2}$ (blue) core lines with respect to their position after a PbI_2 deposition time of 3060 s for $\text{Pb}4f^{7/2}$ and 360 s for $\text{Ti}2p^{3/2}$. From this plot, the band bending of the glass/ FTO/TiO_2 substrate and the PbI_2 layer can be derived. For the band bending of the substrate, the shift of the $\text{Ti}2p^{3/2}$ line can be used directly. To obtain the band bending of the PbI_2 layer, the substrate energy level shift is subtracted from the layer shift, resulting in the black curve which shows the PbI_2 layer band bending. Shifts towards higher binding energies are positive, shifts towards lower binding energies negative in both graphs.

measured after the first deposition step but has to be corrected for the substrate shift between 0s and 1s deposition time which is 0.26 eV. This procedure results in a total band bending for the PbI_2 layer of 0.73 eV. Figure 5.32 b shows that the band bendings of the TiO_2 layer of the substrate and the PbI_2 layer point downward. Since band bendings are caused by a charge transfer, it is unusual that substrate and layer show a band bending in the same direction. Considering the observed formation of the $\text{Pb}(\text{IO}_3)_2$ phase during the first deposition steps, a significant part of the downward band bending of the TiO_2 is probably caused by this reaction of lead and iodine with the O_2^- adsorbates on the TiO_2 . In this context, the formation of $\text{Pb}(\text{IO}_3)_2$ would remove the O_2^- adsorbates and therefore the corresponding upward band bending, described in section 5.1.1. Accordingly, a pronounced contribution of the downward band bending observed in this interface experiment would not be an actual downward band bending but the removal of an upward band bending. An observation which requires a comment is the VBM position of the TiO_2 layer examined in this experiment. In section 5.1.1, in figure 5.5, a VBM position of 2.46 eV was proposed as flat band position for TiO_2 . In contrast, in the discussion above, a VBM position of 2.46 eV was attributed to an upward band bending which is removed during the PbI_2 deposition. The solution for this apparent contradiction are the line shapes of the valence band regions of the TiO_2 layer examined in this section and the TiO_2 layer used to draw the band energy diagram in section 5.1.1. While the TiO_2 layer in section 5.1.1 was more rutile dominated, the TiO_2 layer used for the interface experiment appears to be more anatase dominated and accordingly shows a generally larger energetic distance

between the VBM and the Fermi level (see also section 5.1.1 for comparison). Hence, a VBM of 2.46 eV for the plasma treated TiO₂ layer used in this experiment with consecutive downward band bending due to the removal of O₂⁻ adsorbates during the PbI₂ deposition is in accordance with the results presented in section 5.1.1, especially considering that the TiO₂ band bending might not be completely caused by the removal of the O₂⁻ adsorbates but partly also by an actual charge transfer during the interface formation ($\phi_{\text{PbI}_2} < \phi_{\text{TiO}_2}$). The valence band spectra of the bare glass/FTO/TiO₂ substrate and the finished PbI₂ layer can be found in the appendix in figure A.8.

Due to the observed formation of the Pb(IO₃)₂ interface layer the electronic shift of the Pb and I core levels might be superimposed by a chemical shift. Hence, the assumption that the energetic difference between the valence band maximum and the core level positions is constant might not be valid. The examination of the work functions, measured after every deposition step, would allow to track the surface potential during the experiment and to check whether the electronic shift of the Pb and I core levels is superimposed by a chemical shift or not. Unfortunately, the work functions were only measured for the clean glass/FTO/TiO₂ substrate and the thick PbI₂ layer. Accordingly, the work functions are only drawn for the pristine substrate and thick layer in the schematic band energy diagram of the TiO₂/PbI₂ interface in figure 5.33. In addition, since it was not possible to differentiate between chemical and electronic core line shifts, the band bending of the PbI₂ layer is not drawn.

In conclusion, the presented results indicate that chemical reactions are involved in the formation of the interface between TiO₂ and PbI₂. The corresponding interface layers might persist even after the transformation of PbI₂ to MAPI and influence the charge extraction from the MAPI absorber to the FTO/TiO₂ ETL. The interface layers might even cause increased hysteresis due to voltage driven migration of ions and should be kept in mind for the discussion of the IV characteristics of MAPI solar cells [129].

5.2.5 Most important facts

- SEM images show that MAPI layers have to be recrystallized during the transformation of PbI₂ to MAPI in order to achieve a morphology suitable for solar cells. The transformation of PbI₂ to MAPI happens in three steps: Transformation of PbI₂ to MAPI, recrystallization and grain growth. The best morphology is achieved at $T_s = 130^\circ\text{C}$.
- The CSS transformation yields MAPI with high perovskite phase purity for $T_s = 75^\circ\text{C}$, 90°C , 130°C and 150°C . The perovskite crystal structure is dominated by the orthorhombic modification, indicating a high degree of order of the MA⁺ cations. For MAPI, the orthorhombic modification is uncommon at room temperature but is reported as low temperature modification (below -112°C).

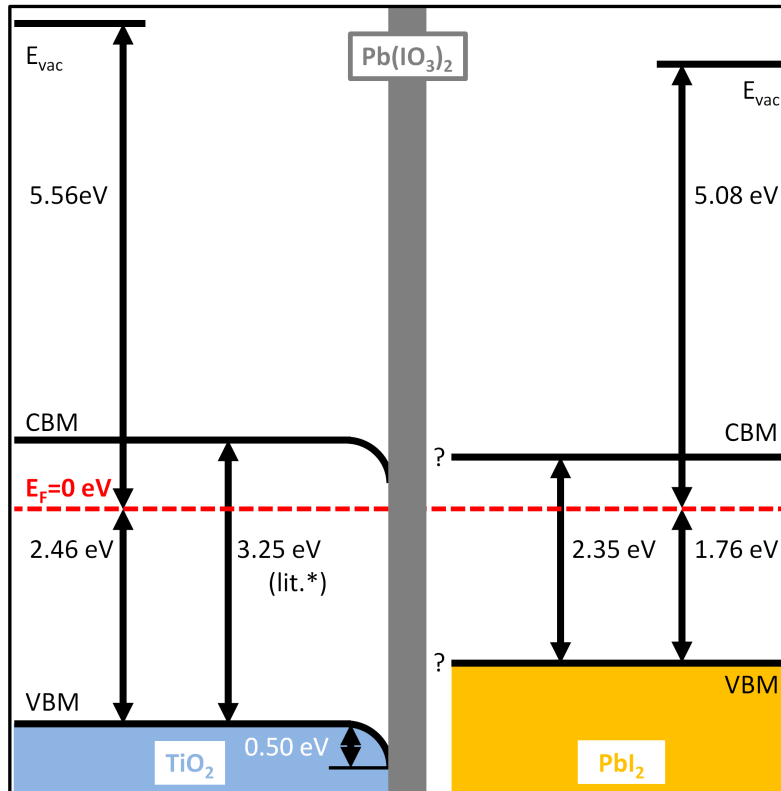


Figure 5.33.: Schematic band energy diagram of the $\text{TiO}_2/\text{PbI}_2$ interface. The band gap for TiO_2 was taken from [76].

- An optical absorption edge onset at about 1.58 eV could be determined with UV/VIS spectroscopy, well in accordance with band gaps reported in literature.
- The XPS and UPS results of the 2step CSS MAPI are well in accordance with literature values for stoichiometric MAPI. The MAPI Fermi level is pinned to the conduction band. MAPI and MAI can be differentiated by their core line positions. MAPI and PbI_2 cannot be differentiated by the binding energy positions of their core emission lines.
- For a two step process, the $\text{TiO}_2/\text{PbI}_2$ interface is important because it strongly determines the TiO_2/MAPI interface after the transformation. During an interface experiment, a pronounced shift of the $\text{Ti}2p$ and $\text{O}1s$ emissions during the first transformation steps is observed. This shift indicates, in combination with the occurrence of an additional $\text{I}3d^{5/2}$ emission around 624.2 eV, that a $\text{Pb}(\text{IO}_3)_2$ interface layer is likely to form between TiO_2 and PbI_2 .

5.3 MAPI synthesized from lead chloride

The use of lead chloride instead of lead iodide, with its different crystal structure, a different thin film morphology and different electronic properties, may alter and possibly improve the characteristics of the resulting perovskite. In addition, compared to the pure iodine $\text{CH}_3\text{NH}_3\text{PbI}_3$ perovskite, the presence of chlorine in a mixed halide perovskite is reported to be advantageous for the solar cell performance, the light absorption of the absorber material, the charge carrier life time, mobility and diffusion length in the perovskite [43, 147, 148]. Accordingly, in addition to PbI_2 , PbCl_2 was used as a base layer for the perovskite fabrication. The perovskites derived from PbI_2 and from PbCl_2 are compared in the following, starting with their electronic properties and followed by their morphology and crystal structure. Finally, the evolution of MAPI from a PbCl_2 layer will be discussed in detail. To differentiate between MAPI derived from PbI_2 and MAPI derived from PbCl_2 in the following, the former will be referred to as $\text{MAPI}_{\text{PbI}_2}$ and the latter as $\text{MAPI}_{\text{PbCl}_2}$.

5.3.1 Optoelectronic structure

Since most of the advantages associated with the presence of chlorine in MAPI concern the electronic properties of the MAPI layers, the characterization of these properties will be presented first, starting with PES and UV/VIS spectroscopy. Similar to the PE spectra of MAPI derived from PbI_2 , the detail spectra of MAPI fabricated from PbCl_2 show no systematic dependence on the substrate temperatures. Hence, only spectra for MAPI, fabricated from PbCl_2 at a substrate temperature of 130°C during the CSS process, are shown in the following and are compared to PVD fabricated PbCl_2 and MAPI fabricated from PbI_2 at $T_s=90^\circ\text{C}$. These samples are considered to be representative for PbCl_2 and MAPI fabricated from PbCl_2 and PbI_2 , respectively. The spectra for MAPI fabricated at substrate temperatures of 90°C and 150°C are shown in figures A.9 and A.10 the appendix. For $T_s=75^\circ\text{C}$, no spectra could be measured due to problems with the PE spectrometer. All samples were freshly prepared by PVD (PbCl_2) or sequential CSS (MAPI) and are measured directly after the fabrication without breaking the vacuum conditions. The survey spectra of the representative samples are shown in figure 5.34 and show no contaminations. However, it should be mentioned, that due to the work on MAPI and MASI within different projects executed at the time in the vacuum chambers of our lab, the $T_s=150^\circ\text{C}$ sample was found to contain some Sn. This contamination appears not to affect the core level positions of I, N, C and Pb, but alters the VBM position. The iodine and lead features of the $T_s=90^\circ\text{C}$ sample, shown in the appendix are slightly shifted towards lower binding energies compared to the other samples. As this shift was observed for this sample only, it is not considered as systematic effect. The evaluation of the PbCl_2 survey spectrum shows that the presence of chlorine can be determined by the $\text{Cl}2p$ lines. Interestingly, those

lines can not be found neither in the survey spectra of the $\text{MAPI}_{\text{PbCl}_2}$ sample in figure 5.34 nor in the $\text{Cl}2\text{p}$ detail spectra of the $\text{MAPI}_{\text{PbCl}_2}$ sample in figure 5.35. The core line positions, valence band maximum positions and work functions of the examined $\text{MAPI}_{\text{PbCl}_2}$ samples and of a PbCl_2 reference sample are shown in table 5.7 and the element ratios at the sample surfaces in table 5.8.

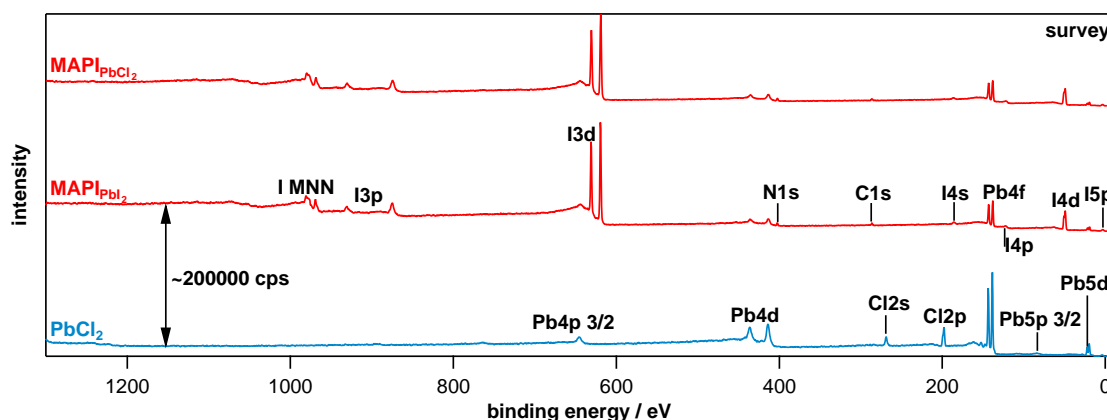


Figure 5.34.: Survey spectra of MAPI fabricated from PbCl_2 (red), MAPI fabricated from PbI_2 (red) and PbCl_2 (turquoise) measured with XPS directly after the layer fabrication, without breaking the vacuum conditions. The offset between PbCl_2 and $\text{MAPI}_{\text{PbI}_2}$ is given as a guide to the eye for the intensity. Only the most prominent lines are labeled.

Table 5.7.: Core emission line binding energy positions, valence band maximum positions and work functions of MAPI fabricated from PbCl_2 , MAPI fabricated from PbI_2 ($T_s=90^\circ\text{C}$) and of PbCl_2 . All energy values are given in eV.

sample	I3d ^{5/2}	N1s	C1s	Pb4f ^{7/2}	VBM (XPS)	VBM (UPS)	ϕ
$T_s=90^\circ\text{C}$	619.26	402.62	286.60	138.42	1.61	1.37	4.46
$T_s=130^\circ\text{C}$	619.55	402.64	286.61	138.65	1.71	1.62	4.27
$T_s=150^\circ\text{C}$	619.53	402.64	286.55	138.62	x	x	x
$\text{MAPI}_{\text{PbI}_2}$	619.47	402.62	286.58	138.57	1.65	1.61	4.38
PbCl_2	Cl2p ^{3/2} at 198.18			138.93	2.43	2.28	4.92

Table 5.8.: Element ratios at the sample surface of MAPI derived from PbCl_2 , of MAPI derived from PbI_2 ($T_s=90^\circ\text{C}$) and of PbCl_2 samples obtained from XPS measurements with Scofield ionization cross sections.

sample	I/Pb	Cl/Pb	N/Pb	I/N
$T_s=90^\circ\text{C}$	3.1	x	1.1	2.9
$T_s=130^\circ\text{C}$	3.0	x	0.8	3.6
$T_s=150^\circ\text{C}$	3.1	x	0.9	3.3
$\text{MAPI}_{\text{PbI}_2}$	3.1	x	1.0	3.1
PbCl_2	x	1.9	x	x

As for $\text{MAPI}_{\text{PbI}_2}$, the element ratios for $\text{MAPI}_{\text{PbCl}_2}$, obtained by the areas under the core emission lines with Scofield ionization cross sections, are close enough to ideal ones to assume a stoichiometric surface composition. Considering the estimated detection threshold of chlorine in MAPI, the Cl content is assumed to be below 1 atomic percent (detailed estimation of the detection threshold of Cl can be found in the experimental section) [66]. Accordingly, it appears not to be adequate to consider a mixed halide perovskite in case of the CSS MAPI from PbCl_2 . It is more appropriate to relate it to a PbCl_2 derived $\text{CH}_3\text{NH}_3\text{PbI}_3$. The detail spectra of iodine, chlorine and lead are shown in figures 5.35 and 5.36.

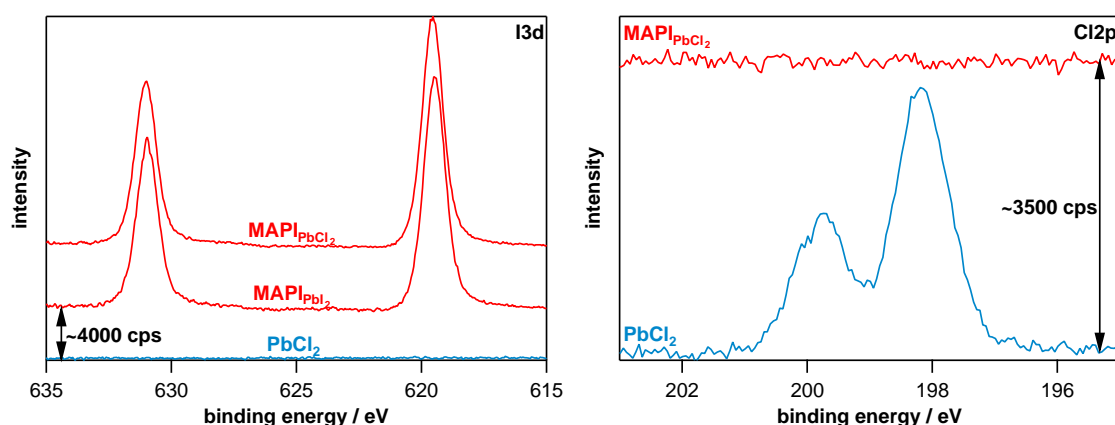


Figure 5.35.: XP detail spectra of the I3d and Cl2p emissions of MAPI fabricated from PbCl_2 (red), MAPI fabricated from PbI_2 (red) and of PbCl_2 (turquoise). The spectra were measured directly after the layer fabrication, without breaking the vacuum conditions. The offset between PbCl_2 and $\text{MAPI}_{\text{PbI}_2}$ is given as a guide to the eye for the intensity.

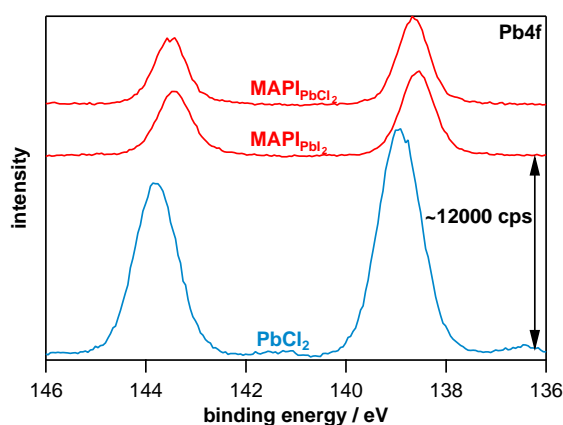


Figure 5.36.: XP detail spectra of the Pb4f emissions of MAPI fabricated from PbCl_2 (red), MAPI fabricated from PbI_2 (red) and of PbCl_2 (turquoise). The spectra were measured directly after the layer fabrication, without breaking the vacuum conditions. The offset between PbCl_2 and $\text{MAPI}_{\text{PbI}_2}$ is given as a guide to the eye for the intensity.

Figures 5.35 and 5.36 and table 5.7 show that PbCl_2 and MAPI can readily be distinguished not only by the presence of iodine or chlorine but also by the binding energy position of the $\text{Pb}4f$ lines. On the other hand it is impossible to distinguish between MAPI fabricated from PbI_2 and from PbCl_2 by means of core emission line positions, binding energy differences or elemental composition (see figures 5.35, 5.36, 5.37 and tables 5.7 and 5.8). Accordingly, also a modified doping by chlorine is unlikely, since it should manifest not only in a shift of the valence band maximum but also in a shift of the core lines.

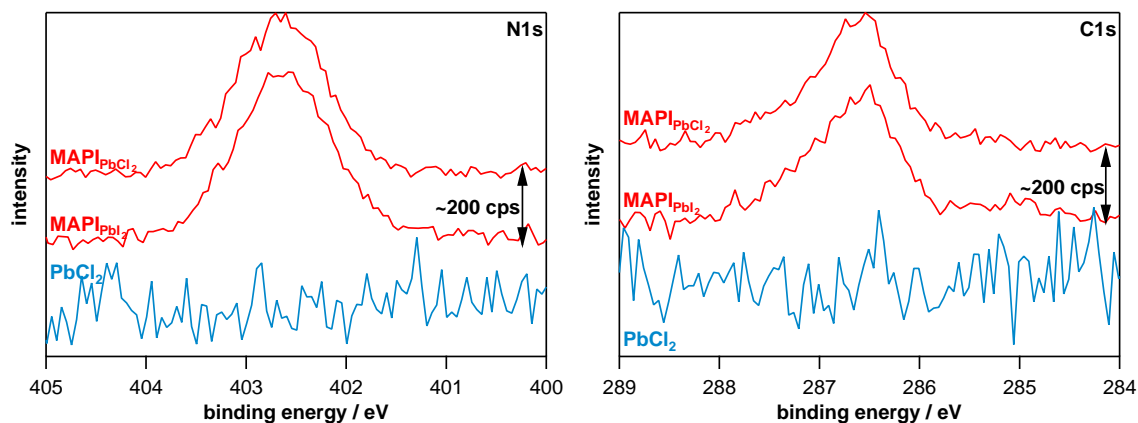


Figure 5.37.: XP detail spectra of the N1s and C1s emissions of MAPI fabricated from PbCl_2 (red), MAPI fabricated from PbI_2 (red) and of PbCl_2 (turquoise). The spectra were measured directly after the layer fabrication, without breaking the vacuum conditions. The offset between PbCl_2 and $\text{MAPI}_{\text{PbI}_2}$ is given as a guide to the eye for the intensity.

The N1s and C1s emissions in figure 5.37 show the same shapes for MAPI from PbCl_2 as for MAPI from PbI_2 . Accordingly, the lower binding energy emission as well as the high binding energy shoulder appear to be independent on the base layer lead salt. This finding is in accordance with the explanation given in section 5.2 for the evolution of the C1s emission at lower binding energies. There, the low BE emission is explained by the formation of C_2H_6^+ due to a surplus of CH_3^+ and CH_3I in the layer which is also plausible in $\text{MAPI}_{\text{PbCl}_2}$. The valence band maximum positions and the work functions of samples considered as representative for MAPI fabricated from PbCl_2 and PbI_2 show no significant difference (see figure 5.38 and figure A.11 in the appendix). The work function is in both cases around 4.3-4.4 eV and the valence band around 1.7 eV for XPS and at 1.6 eV for UPS measurements.

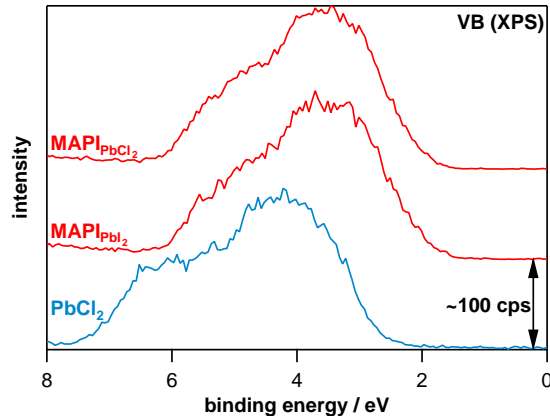


Figure 5.38.: Valence band spectra measured with XPS of MAPI fabricated from PbCl_2 (red), MAPI fabricated from PbI_2 (red) and of PbCl_2 (turquoise). The spectra were measured directly after the layer fabrication, without breaking the vacuum conditions. The offset between PbCl_2 and $\text{MAPI}_{\text{PbI}_2}$ is given as a guide to the eye for the intensity.

The assumption that the 2step CSS MAPI derived from PbCl_2 is $\text{CH}_3\text{NH}_3\text{PbI}_3$ and not a mixed halide perovskite is further supported by the UV/VIS experiments in figure 5.39. The band gap, as a material property, is independent on the use of PbI_2 or PbCl_2 as lead salt layer. Furthermore, as for $\text{MAPI}_{\text{PbI}_2}$, the optical absorption edge onset of $\text{MAPI}_{\text{PbCl}_2}$ does not change with increasing substrate temperature and is with 1.59 eV well in accordance with literature values for the band gap of MAPI (see figure 5.40) [109, 113–116, 149]. However, figure 5.39 b shows some differences in the optical spectra of $\text{MAPI}_{\text{PbI}_2}$ and $\text{MAPI}_{\text{PbCl}_2}$. The directed reflection of the $\text{MAPI}_{\text{PbCl}_2}$ layer is two times as high as the one of the $\text{MAPI}_{\text{PbI}_2}$ layer, indicating that the $\text{MAPI}_{\text{PbCl}_2}$ layers are less rough compared to the $\text{MAPI}_{\text{PbI}_2}$ layers. This observation is supported by the comparison of the curves of the absorption coefficients over the photon energy in figure 5.39 a [119].

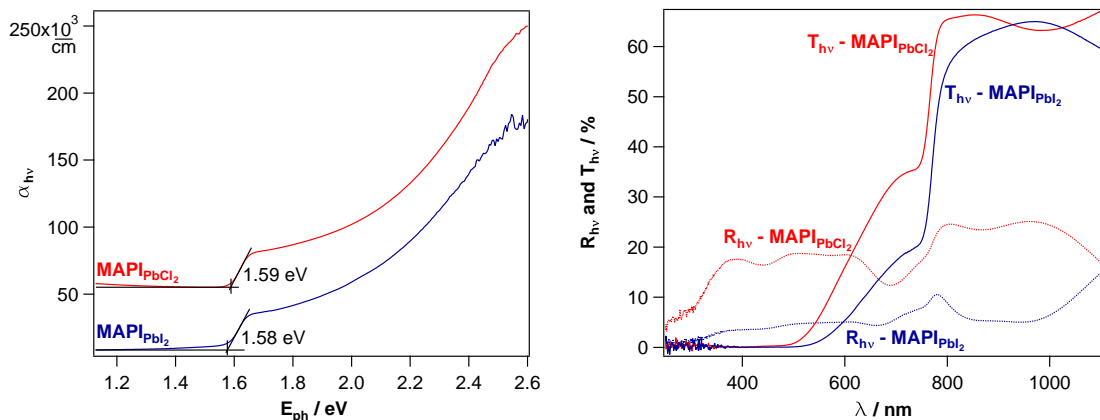


Figure 5.39.: Comparison of the absorption coefficients $\alpha_{h\nu}$ (offset 50000 cm^{-1}) (left) and the directed reflection $R_{h\nu}$ and the transmission $T_{h\nu}$ (right) of MAPI fabricated from PbCl_2 (red) and from PbI_2 (dark blue) at a T_s of 90°C during the CSS process step on glass/FTO/ TiO_2 substrates.

In contrast to $\text{MAPI}_{\text{pbI}_2}$, in figure 5.40 not only the energetic position but also the sharpness of the onset of the fundamental absorption of $\text{MAPI}_{\text{pbCl}_2}$ appears to be similar for all examined substrate temperatures. This observation indicates that the $\text{MAPI}_{\text{pbCl}_2}$ layers are not just smoother than the $\text{MAPI}_{\text{pbI}_2}$ layers but that their layer roughness is also less dependent on the substrate temperature, in accordance with SEM images of $\text{MAPI}_{\text{pbCl}_2}$, as will be discussed below. As for $\text{MAPI}_{\text{pbI}_2}$, the results obtained from the UV/VIS absorption data will be compared with the results from the photoluminescence spectroscopy experiments in section 5.4.

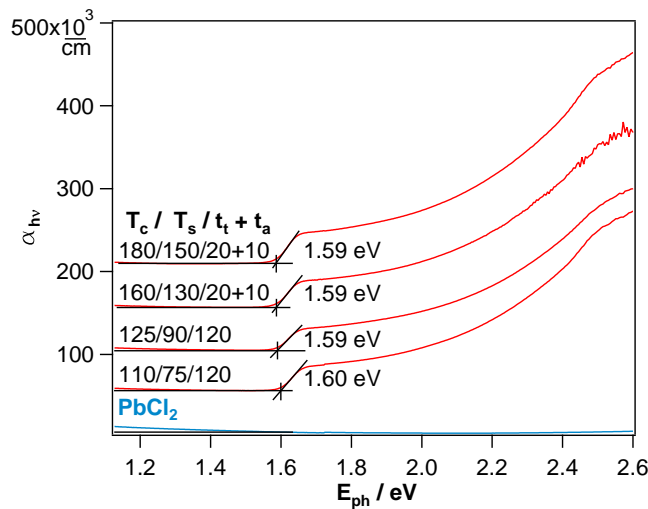


Figure 5.40.: Absorption coefficient $\alpha_{h\nu}$, plotted against the photon energy for PbCl_2 and MAPI fabricated from PbCl_2 at CSS substrate temperatures of 75 °C, 90 °C, 130 °C and 150 °C on glass/FTO/ TiO_2 substrates. An offset of 50000 1/cm is used for each MAPI spectra.

With the PES results, summarized in table 5.7 and the band gaps presented in figure 5.40 band energy diagrams for PbCl_2 and $\text{MAPI}_{\text{PbCl}_2}$ can be drawn and are shown in figure 5.41. It was not possible to determine a significant difference between the absorption spectra of the bare glass/FTO/ TiO_2 substrate and the substrate with a PbCl_2 layer till the transmission of the substrate drops near zero in the energy range between 3.5 eV and 4 eV. Hence, the band gap of PbCl_2 is assumed to be larger than 4 eV in accordance with literature [150]. The Anderson alignment in figure 5.41 shows that the conduction band offset between PbCl_2 and MAPI is 2.2 eV (assuming a band gap of 5 eV [150]) and the valence band offset 1.2 eV. The PbCl_2 /MAPI contact will therefore be electron and hole blocking. Thus, besides a PbI_2 layer, also a thin, dense PbCl_2 layer has to be avoided in a solar cell.

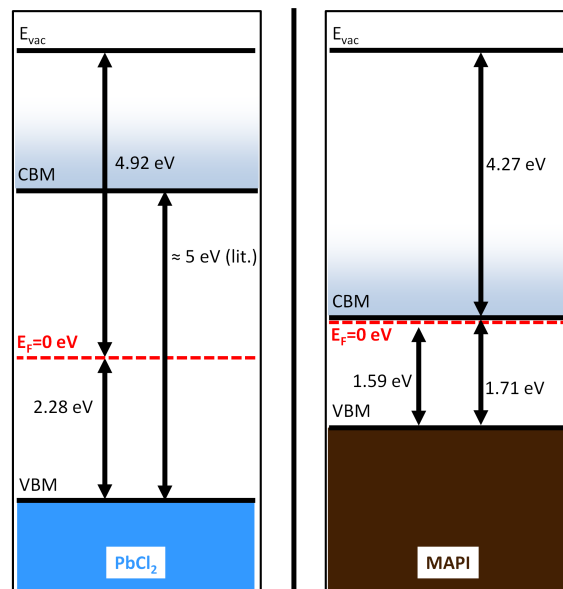


Figure 5.41.: Band energy diagrams of PbCl_2 and $\text{MAPI}_{\text{PbCl}_2}$ derived from the PES data presented in figure 5.38 and table 5.7 and the UV/VIS data presented in figure 5.40. The band gap around 5 eV for PbCl_2 is taken from literature [150].

5.3.2 Morphology and crystal structure

The UV/VIS measurements in figure 5.39 already indicated that the $\text{MAPI}_{\text{PbCl}_2}$ layers are smoother than the $\text{MAPI}_{\text{PbI}_2}$ layers. To confirm this indication, $\text{MAPI}_{\text{PbCl}_2}$ layers fabricated at substrate temperatures of 75 °C, 90 °C, 130 °C and 150 °C were examined with SEM. The results will be presented in the following and will be compared to the results obtained for $\text{MAPI}_{\text{PbI}_2}$. As for $\text{MAPI}_{\text{PbI}_2}$ it is reasonable to assume that the $\text{MAPI}_{\text{PbCl}_2}$ layer morphology will to some extent be dependent on the PbCl_2 layer morphology. Therefore, the SEM images of an about 110 nm thick PbCl_2 layer deposited by PVD onto a glass/FTO/ TiO_2 substrate at a substrate temperature of 50 °C are shown in figure 5.42.

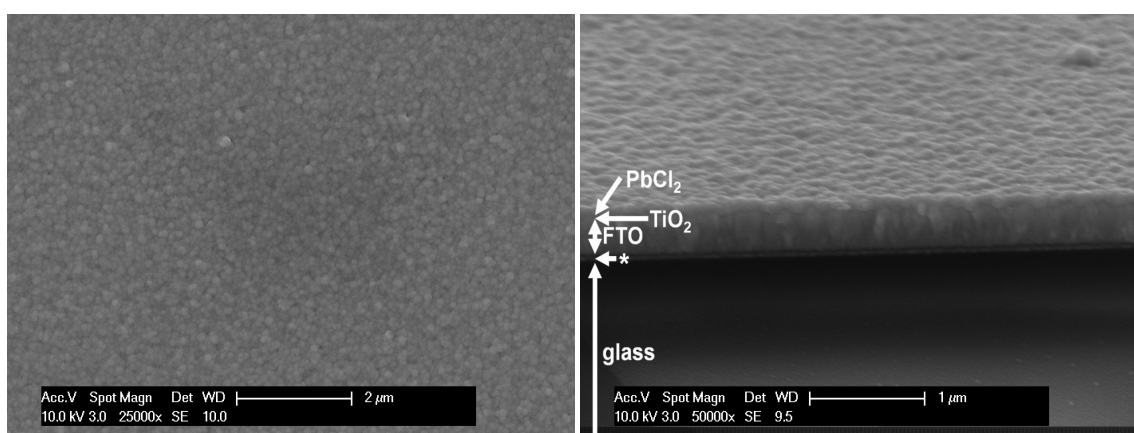


Figure 5.42.: SEM images in SE contrast of an about 110 nm thick PbCl_2 layer deposited by PVD onto a glass/FTO/ TiO_2 substrate. Top view (left) and cross section (tilted 75°) (right).

Figure 5.42 shows that PbCl_2 forms compact rather smooth layers with small, globular grains and only few defects (dark spots in the top view image in figure 5.42). The smooth, globular appearance of the PbCl_2 layer in the top view SEM images is in accordance with literature [109] and differs significantly from the flake like PbI_2 morphology. The SEM images for MAPI layers fabricated from PbCl_2 at substrate temperatures of 75 °C, 90 °C, 130 °C and 150 °C during the CSS process are shown in figure 5.43.

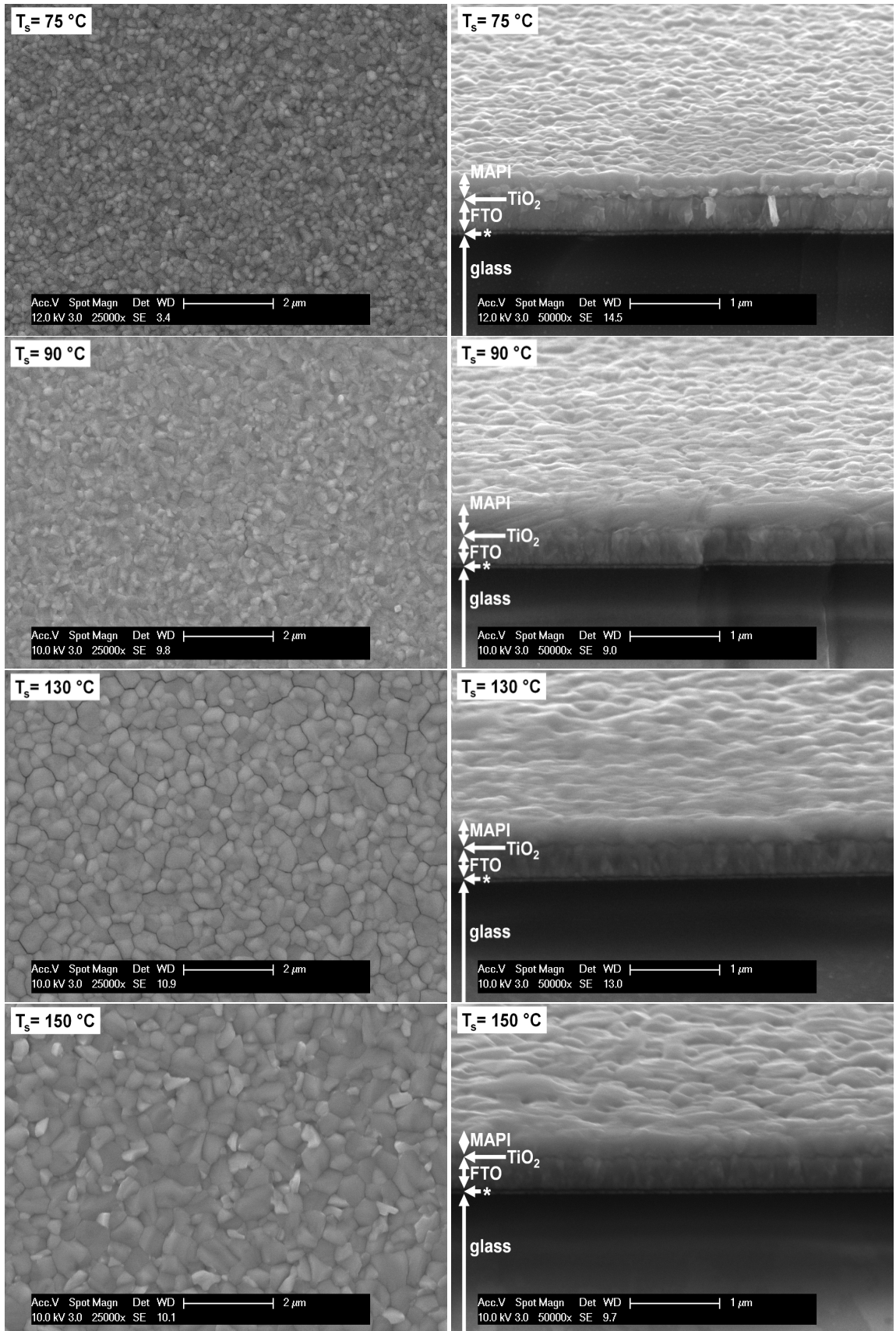


Figure 5.43.: SEM images in SE contrast of MAPI layers fabricated from PbCl_2 on glass/FTO/TiO₂ substrates at substrate temperatures of 75 °C, 90 °C, 130 °C and 150 °C during the CSS process. Top view (left) and cross section (tilted 75°) (right).

Figure 5.43 shows that a less pronounced recrystallization occurs during the transformation of PbCl_2 to MAPI compared to the transformation of PbI_2 to MAPI. The main difference between the morphologies of the MAPI layer fabricated at $T_s=75^\circ\text{C}$ and a PbCl_2 layer is the grain size, accompanied by a recrystallization from a globular to an edgy grain shape. The transformation from PbCl_2 to MAPI on one hand and the recrystallization and the grain growth on the other hand appear to be separate processes, taking place simultaneously, similar to the findings for $\text{MAPI}_{\text{PbI}_2}$. The cross section image of the $T_s=75^\circ\text{C}$ sample in figure 5.43 shows that beneath the large grains, there is a layer of smaller grains. On the first impression, these grains could be assumed to be either PbCl_2 or PbI_2 . But, the XRD patterns in figure 5.44 show no PbCl_2 and a PbI_2 content which is too small to explain the small grained layer. Hence, the most probable explanation is that the layer is small grained MAPI beneath recrystallized large grained MAPI. Accordingly, the recrystallization front appears to move from the layer surface to the substrate. With increasing substrate temperature, from $T_s=75^\circ\text{C}$ to $T_s=90^\circ\text{C}$, the small grained phase disappears, the edgy habitus of the grains becomes more pronounced and the size of the edgy grains increases. At $T_s=130^\circ\text{C}$ and $T_s=150^\circ\text{C}$ a further increase of the grain size is observed and the shape of the grains becomes more round again. This observations are in agreement with the Ostwald ripening like grain growth process also described for the PbI_2 to MAPI transformation. Accordingly, even if their appearance is different, the same three processes, transformation, recrystallization and grain growth, can be determined for the evolution of the morphology with increasing substrate temperature for MAPI derived from PbI_2 and for MAPI derived from PbCl_2 . The comparison of the SEM images in figures 5.14 and 5.43 shows that at all substrate temperatures the MAPI layers fabricated from PbCl_2 show smaller grains than the ones from PbI_2 . On the other hand, the MAPI from PbCl_2 is smoother than MAPI from PbI_2 at substrate temperatures of 75°C and 90°C . At $T_s=130^\circ\text{C}$ the roughness of $\text{MAPI}_{\text{PbCl}_2}$ and $\text{MAPI}_{\text{PbI}_2}$ appears to be similar and at 150°C the MAPI layers from both lead salts become rougher again. But, while the $T_s=150^\circ\text{C}$ MAPI layers from PbI_2 show pinholes at the grain boundaries, the roughening is less pronounced for MAPI from PbCl_2 in a way that it can still be considered for the production of solar cells. In conclusion, from a morphological point of view, MAPI from PbCl_2 appears to be better suited for solar cell fabrication than MAPI from PbI_2 for low substrate temperatures of 75°C and 90°C because of the smoother surface with less pinholes and for $T_s=150^\circ\text{C}$ because the grains boundaries will less likely form weak diodes. At 130°C however, MAPI from PbI_2 is more promising for solar cell applications due to its larger grains. The layer thicknesses for the $\text{MAPI}_{\text{PbCl}_2}$ layers in figure 5.43 were determined to be about 240 nm for $T_s=75^\circ\text{C}$, 270 nm for $T_s=90^\circ\text{C}$, 260 nm for $T_s=130^\circ\text{C}$ and 220 nm for $T_s=150^\circ\text{C}$. The different crystal structures of PbI_2 and PbCl_2 might influence the crystal structure of the derived MAPI layers. To examine this influence, XRD experiments were carried out on the $\text{MAPI}_{\text{PbCl}_2}$ layers and will be discussed and compared to the $\text{MAPI}_{\text{PbI}_2}$ XRD results in the following, starting with the survey XRD patterns in figure 5.44.

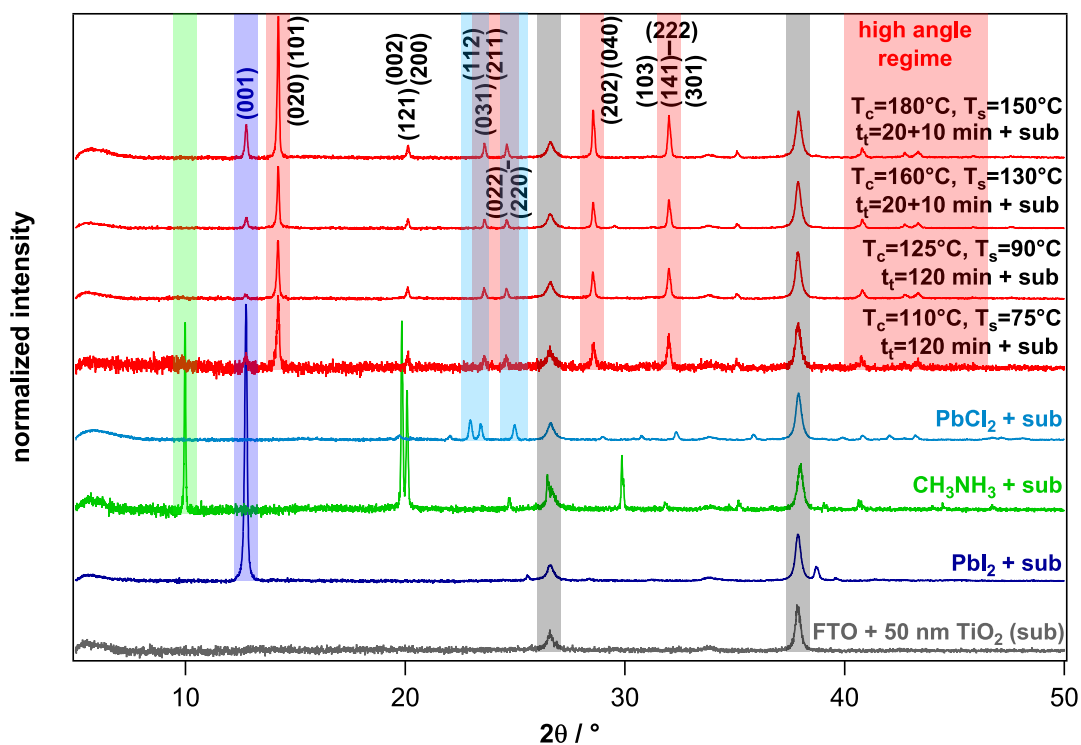


Figure 5.44.: XRD patterns of MAPI layers fabricated from PbCl_2 on glass/FTO/ TiO_2 substrates at substrate temperatures of 75 °C, 90 °C, 130 °C and 150 °C during the CSS process. For comparison XRD patterns of the glass/FTO/ TiO_2 substrate and the glass/FTO/ TiO_2 substrate with PbI_2 , MAI and PbCl_2 are given. The annotation “+ sub” denotes that reflections of the FTO/ TiO_2 electrode are visible in every XRD pattern in addition to the reflections of the respective layer. For all samples a background correction was performed. The hump at 5° is an artifact of that correction but does not overlap with relevant features of the XRD pattern. The XRD patterns are normalized to the substrate reflection at 37.9°.

Similar to $\text{MAPI}_{\text{PbI}_2}$, figure 5.44 shows that it is possible to fabricate MAPI layers from PbCl_2 up to substrate temperatures of 150 °C with the orthorhombic MAPI modification identified in section 5.2 as dominating phase. Additionally, reflections originating from PbI_2 and the FTO/ TiO_2 electrode are observable. No indication for the presences of MAI or PbCl_2 can be found in the MAPI diffraction patterns. The sample fabricated at a substrate temperature of 75 °C appears to show a contribution of MAPI in the cubic modification, also determined for the low T_s samples of $\text{MAPI}_{\text{PbI}_2}$. But, due to the low signal to noise ratio of the sample, this phase contribution can not be determined unambiguously. Based on the observation that no PbI_2 reflections other than the (001) reflection can be determined for the MAPI samples in figure 5.44, the PbI_2 in $\text{MAPI}_{\text{PbCl}_2}$ probably possesses the same single crystalline texture as found in the $\text{MAPI}_{\text{PbI}_2}$ layers. Hence, the PbI_2 contents can once again be assumed to be below 1%. The $\text{MAPI}_{\text{PbCl}_2}$ layers show the presence of PbI_2 but not of PbCl_2 . This observation is probably due to the formation of PbI_2 as an intermediate phase during the transformation of PbCl_2 to MAPI and will be discussed in detail below [148].

The detailed XRD patterns for MAPI layers fabricated from PbCl_2 at $T_s = 90^\circ\text{C}$ and $T_s = 150^\circ\text{C}$ are shown in figure 5.45 a. The verification of the orthorhombic $Pnma$ crystal structure for $\text{MAPI}_{\text{PbCl}_2}$ by means of Rietveld refinement is shown in figure 5.45 b.

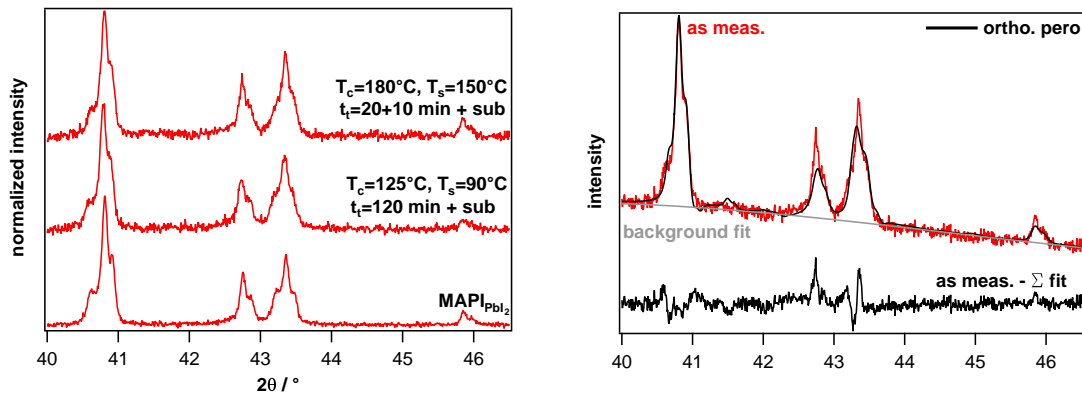


Figure 5.45.: a) Detailed XRD patterns of MAPI layers fabricated from PbCl_2 on glass/FTO/ TiO_2 substrates at substrate temperatures of 90°C and 150°C during the CSS process. The diffraction pattern of a MAPI layer fabricated from PbI_2 at a substrate temperature of 130°C during the CSS process is given for comparison. The diffraction patterns are normalized in intensity scale. b) Detailed XRD pattern of a MAPI layer fabricated from PbCl_2 at a substrate temperature of 150°C during the CSS process (red). A Rietveld refinement assuming an orthorhombic crystal structure of the MAPI is denoted in black. The difference between the measured curve and the superposition of the background and the Rietveld refinement is denoted in black with “as meas. - Σ fit”.

The comparison of the detailed XRD patterns of MAPI from PbI_2 and from PbCl_2 in figure 5.45 a shows that the orthorhombic $Pnma$ crystal structure, which is possibly slightly textured, is consistent for the 2step CSS MAPI, independent on the substrate temperature or the used lead salt. The lead salts themselves however show some differences concerning their crystal structures, as the visualization of the crystal structures of PbI_2 and PbCl_2 in figure 5.46 illustrates.

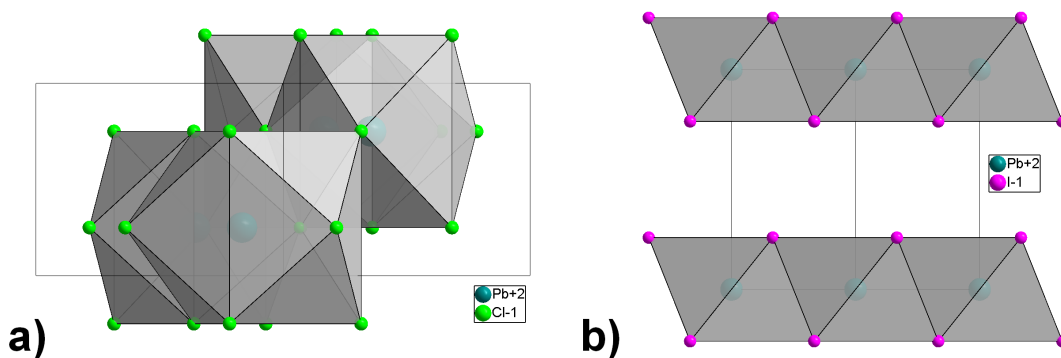


Figure 5.46.: Visualization of the crystal structures of PVD fabricated PbCl_2 (a) PbI_2 (b).

The unit cell dimensions, space groups and atomic positions used for the illustrations in figure 5.46 are taken from Rietveld refinements of PVD fabricated layers on glass/FTO/TiO₂ substrates for both materials. The trigonal PbI₂ already possesses the PbI₆ octahedra, forming the inorganic lattice of MAPI. In contrast, the examined PbCl₂ is found to have an orthorhombic crystal structure of the the space group *Pnam* where the lead atoms are coordinated with nine chlorine atoms. This crystal structure is in accordance with literature [151, 152]. Hence, in PbCl₂ a more pronounced atomic reorganization is needed to form MAPI compared to the reorientation of the PbI₆ octahedra in PbI₂. In addition, figure 5.46 shows that while PbI₂ forms a layered structure, PbCl₂ does not. This observation is reflected in the SEM images in figures 5.13 and 5.42 where PbI₂ forms a flake like and PbCl₂ a globular morphology. Again, as in the previous section, figure 5.46 is intended as a guide to visually access the general aspects of the crystal structures of PbI₂ and PbCl₂ and might differ from the real materials when it comes to a detailed description.

The unit cell dimensions for PVD deposited PbCl₂ and MAPI fabricated at substrate temperatures during the CSS process of 90 °C and 150 °C are given in table 5.9. There is no significant change in the lattice parameters of MAPI with changing substrate temperatures and lead salts.

Table 5.9.: Unit cell dimensions of MAPI samples fabricated from PbCl₂ on glass/FTO/TiO₂ substrates at substrate temperatures during the CSS process of 75 °C, 90 °C, 130 °C and 150 °C. The unit cell dimensions of a PVD fabricated PbCl₂ layer on a glass/FTO/TiO₂ substrate is given for comparison. The volumes are calculated with $a \cdot b \cdot c$.

T_s	$a / \text{Å}$	$b / \text{Å}$	$c / \text{Å}$	$V / \text{Å}^3$
90	8.821(3)	12.546(3)	8.896(3)	984.504
150	8.825(3)	12.546(3)	8.895(3)	984.841
PbCl ₂	7.628(3)	9.051(3)	4.537(3)	313.239

5.3.3 Evolution of MAPI from lead chloride

Both lead salts, PbI_2 and PbCl_2 yield MAPI with the same crystal structure and optoelectronic properties yet with different layer morphologies. In addition, the XRD patterns in figure 5.44 show PbI_2 but no PbCl_2 , suggesting that PbI_2 might be an intermediate phase during the transformation of PbCl_2 to MAPI, which would be in agreement with literature [148]. To verify this hypothesis for the examined 2step CSS process and to clarify the mechanism of the transformation of PbCl_2 to MAPI, the evolution of $\text{MAPI}_{\text{PbCl}_2}$ from PbCl_2 was examined with stepwise in vacuo PES experiments. The understanding of the formation of MAPI, the most simple organic-inorganic hybrid perovskite, will help to modify the fabrication techniques for more complicated perovskites in order to tune their properties, overcoming the limitations of the organic-inorganic hybrid perovskites but conserving their strengths. The experiment was carried out with $T_s = 90^\circ\text{C}$ and $T_c = 125^\circ\text{C}$, a standard CSS parameter set. The used CSS temperature profile is shown in figure 5.47.

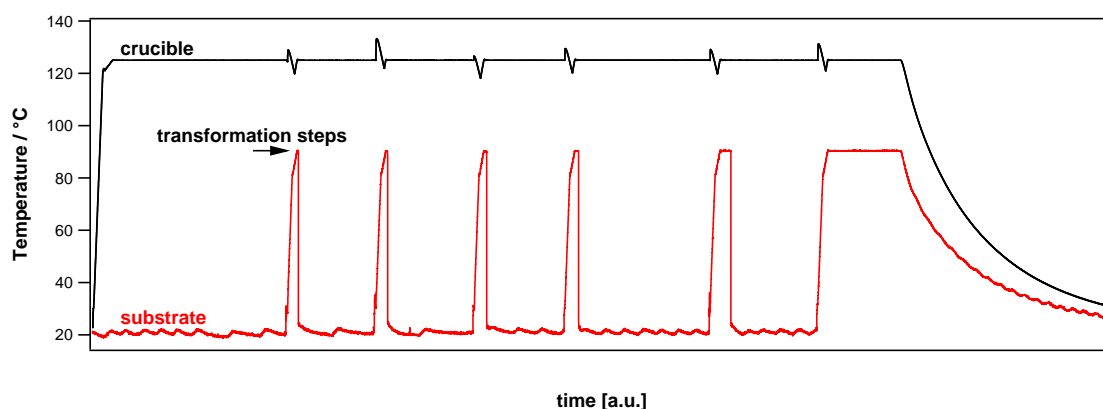


Figure 5.47.: Temperature profile of the stepwise transformation of PbCl_2 to MAPI using the CSS. During the PES measurements the crucible was kept at 125°C with the shutter closed, the substrate heating was turned off. Before each transformation step the substrate was heated to 90°C within 10 min and the shutter opened for a defined transformation time.

In figure 5.47, it can be seen that the crucible is preheated before the first transformation step and then kept at a temperature of 125°C . The substrate however has to be heated up for every deposition step. A fast heating step to a substrate temperature around 80°C was applied and a slow heating step to a substrate temperature of 90°C . After each heating step it was assured that the crucible temperature was 125°C and the substrate temperature 90°C . During the experiment, transformation steps of 10 s, 50 s, 70 s, 170 s, 600 s and 4500 s were applied, leading to the cumulative transformation times of (0 s = bare PbCl_2 layer), 10 s, 60 s, 130 s, 300 s, 900 s and 5400 s. After the last transformation step the source shutter was left open and the sample cooled down over night. The last PES measurements were then performed on the next morning. Every PES measurement was carried out at different positions on the sample to minimize the effect of beam damage.

However, some beam damage was observed on the sample after the last transformation step. Accordingly, for the last measurement (5400 s) a position without observable beam damage was chosen. For all other PES measurements, no beam damage was observed. After that last measurement, the sample was removed from the vacuum system and broken into two parts. One part was prepared for SEM, the other for XRD measurements. The results obtained during the experiment are shown in the following.

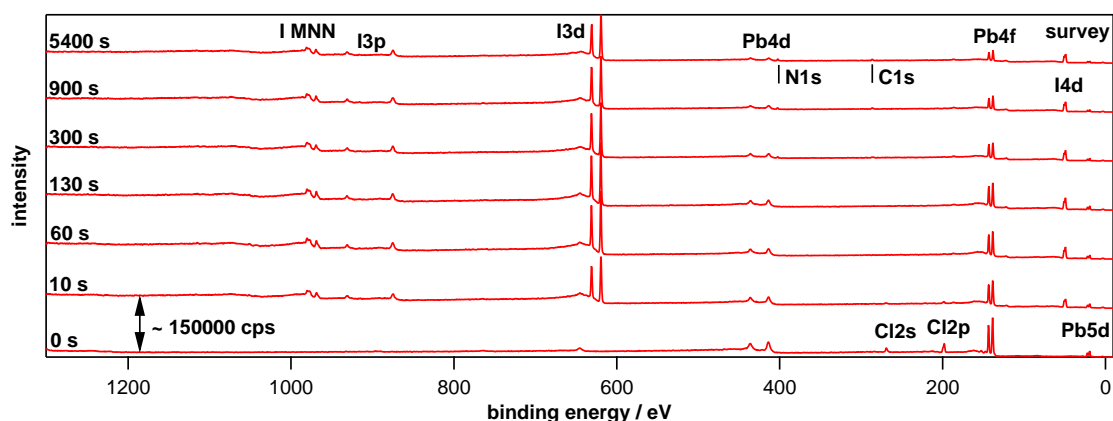


Figure 5.48.: XP survey spectra measured on a freshly prepared PbCl₂ layer and during the stepwise transformation of the PbCl₂ layer to MAPI, without breaking the vacuum conditions. The shown transformation times are cumulative transformation times. The offset between the spectra is given as a guide to the eye for the intensity. Only the most prominent lines are labeled.

In the survey spectrum of the pristine PbCl₂ layer (0 s in figure 5.48) no contaminations can be observed. After about 10 s of transformation, a significant amount of iodine is incorporated in the layer, accompanied by a pronounced reduction of the Cl_{2p} and Cl_{2s} emission line intensities and of the lead emission line intensities. However, the N_{1s} and C_{1s} emissions occur only after 300 s of transformation. To get further insight in the transformation mechanisms, the detail spectra for the I_{3d}, Cl_{2p}, Pb_{4f}, N_{1s} and C_{1s} emissions are shown in the figures 5.49 to 5.51.

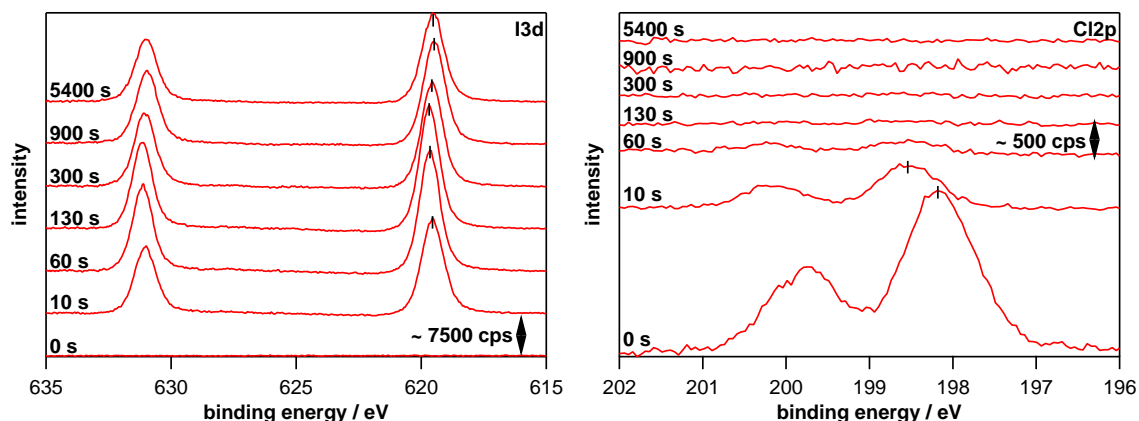


Figure 5.49.: XP detail spectra of the I3d and Cl2p emissions measured on a freshly prepared PbCl₂ layer and during the stepwise transformation of the PbCl₂ layer to MAPI, without breaking the vacuum conditions. The shown transformation times are cumulative transformation times. The offsets are given as a guide to the eye for the intensity.

The intensity of the Cl2p emission decreases steadily till it is not observable any more after 130 s of transformation. In addition, the intensity of the I3d emission increases till 130 s and decreases afterward. The simultaneity of the increasing I3d intensity with the decreasing Cl2p intensity indicates the replacement of Cl⁻ ions with I⁻ ions in PbX₂. The decreasing I3d intensity from 300 s till 5400 s however indicates the transformation of PbI₂ to MAPI (see figure 5.26 for comparison). The start of the transformation of the PbI₂ to MAPI around 300 s is in accordance with the evolution of the N1s and C1s emissions presented in figure 5.50.

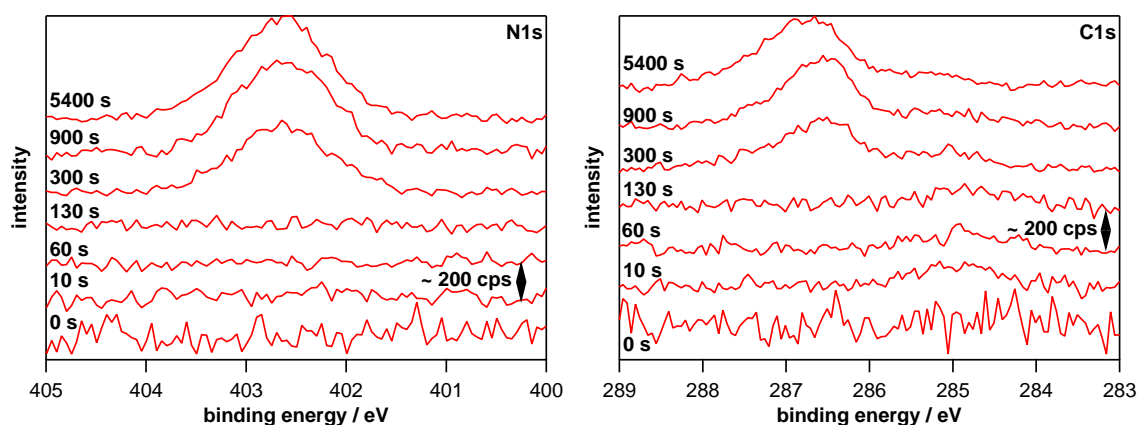
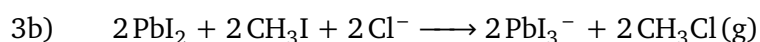
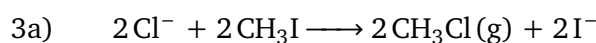
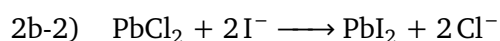
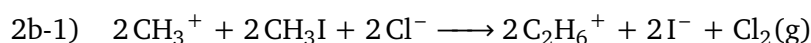
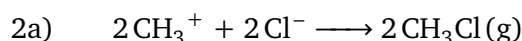
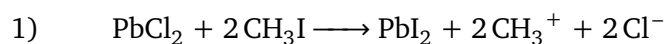


Figure 5.50.: XP detail spectra of the N1s and C1s emissions measured on a freshly prepared PbCl₂ layer and during the stepwise transformation of the PbCl₂ layer to MAPI, without breaking the vacuum conditions. The shown transformation times are cumulative transformation times. The offsets are given as a guide to the eye for the intensity.

In figure 5.50, the N1s and C1s features belonging to MAPI appear after 300 s of transformation. But, a low binding energy C1s emission is clearly observable in figure 5.50 already after 10 s of transformation. This is an indication for the inward diffusion of CH₃I prior to the inward diffusion of NH₃ [126, 148]. A reaction scheme for the transformation of PbCl₂ to MAPI is proposed below.



The only source of iodine available for the replacement of chlorine is CH₃I, diffusing into the layer and leaving CH₃⁺ ions after the replacement (reaction 1). The CH₃⁺ ions can react with the Cl⁻ ions and form CH₃Cl which diffuses to the sample surface and sublimates (reaction 2a). The combination of reaction 1 with reaction 2a would be the most intuitive way for the transformation of PbCl₂ to PbI₂. However, since the low binding energy component of the carbon 1s emission is clearly visible in figure 5.50 before the C1s MAPI emission occurs, the transformation of PbCl₂ to PbI₂ appears to include a carbon containing species which remains in the sample. Reactions 2b-1 to 3b show a corresponding reaction mechanism which could take place simultaneously to reaction 2a. In reaction 2b-1 the CH₃⁺ ion reacts with CH₃I forming C₂H₆⁺, which explains the observed low binding energy component of the C1s emission. The assumption of the formation of C₂H₆⁺ is further supported by the binding energy position of the low binding energy C1s emission, which is in the same range as the C1s emission associated with the presence of C₂H₆⁺ as described in section 5.2.3. In the reaction 2b-2 the I⁻ ions formed in reaction 2b-1 are used for the transformation of PbCl₂ to PbI₂ leaving two Cl⁻ ions on the product side. Possible reactions for those chlorine ions are proposed in reactions 3a and 3b. In reaction 3a, the chlorine ions react with CH₃I resulting in CH₃Cl, which is removed from the sample, and two I⁻ ions which can be reused in a new reaction 2b-2. On the other hand, the C₂H₆⁺ cation, formed in reaction 2b-1 needs to be charge compensated. Reaction 3b shows the consumption of the Cl⁻ ions from reaction 2b-2 during the formation of PbI₃⁻, which charge compensates the C₂H₆⁺ cation and possibly locally starts to form the inorganic lattice of the later perovskite. Accordingly, the reaction of PbCl₂ with CH₃I appears to include three reaction sets, possibly taking place at the same time. The first one is the combination of reaction 1 and reaction 2a. The second one is the combination

of reaction 2b-2 and reaction 3a, after reaction 2b-2 was initiated by reaction 2b-1. Last but not least, each time reaction 2b-1 takes place, due to the requirement of charge neutrality, reaction 3b has also to happen (via reaction 2b-2). Since reaction combinations one and two result in the formation of PbI_2 but reaction combination 3 in the formation of PbI_3^- , both product species will be present during the reaction of PbCl_2 with CH_3I . However, since PbI_2 is formed by two reaction combinations and PbI_3^- only by one, with increasing transformation time, PbI_2 will be more and more the dominant phase. In addition, since the intensity of the C1s low binding energy emission in figure 5.50 does not scale with the transformation time, it might well be, that reactions 2 and 3 take place only during the beginning of the transformation process and that the formation of PbI_2 via the combination of reaction 1 and 2a is the dominant process during the reaction of PbCl_2 and CH_3I . In that case, the assumption that PbI_2 is the dominant product of the reaction of PbCl_2 and CH_3I is supported further. When a sufficient amount of NH_3 is present in the layer, the formation of CH_3NH_3^+ cations and hence the evolution from PbI_2 to the MAPI perovskite, as described in section 5.2.3, occurs. Apparently this stage is reached after 300 s during this experiment. The shift of the Pb4f emission in figure 5.51 shows the complete transformation of PbCl_2 to MAPI in one picture.

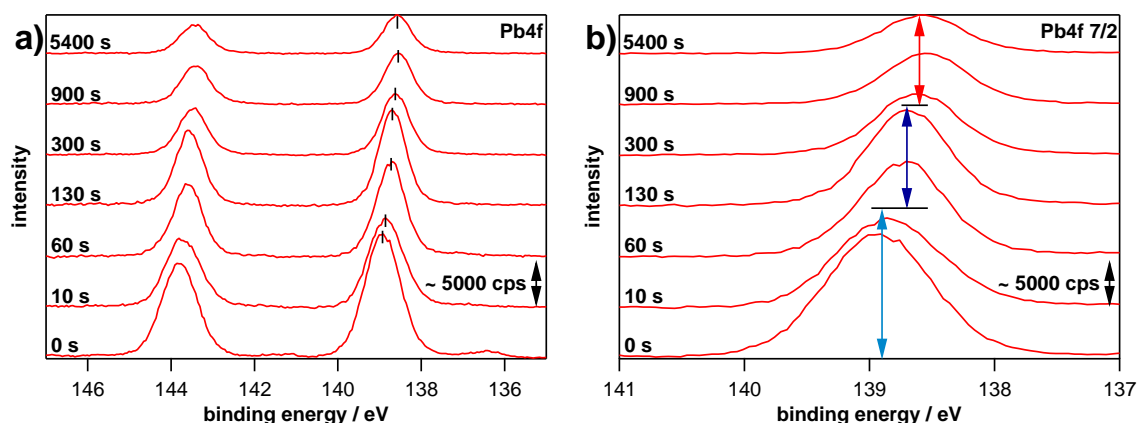


Figure 5.51.: XP detail spectra of the Pb4f emissions measured on a freshly prepared PbCl_2 layer and during the stepwise transformation of the PbCl_2 layer to MAPI, without breaking the vacuum conditions. Both Pb4f emissions (left) and higher magnification on $\text{Pb4f}^{7/2}$ emission (right). The turquoise arrow indicates a line position characteristic for PbCl_2 , the dark blue and red arrows indicate line positions characteristic for PbI_2 and MAPI, respectively. The shown transformation times are cumulative transformation times. The offsets are given as a guide to the eye for the intensity.

The arrows in figure 5.51 are drawn at 138.9 eV, 138.7 eV and 138.6 eV corresponding to the maximum of the $\text{Pb4f}^{7/2}$ emission in PbCl_2 , PbI_2 and MAPI (see also tables 5.5 and 5.7). The shift of the $\text{Pb4f}^{7/2}$ emission in figure 5.51 b corresponds well to the mechanism proposed above. For the pristine substrate, the binding energy position is dominated by PbCl_2 (turquoise arrow), during the following steps, the $\text{Pb4f}^{7/2}$ line shifts towards lower binding energies around 138.7 eV, associated with PbI_2 (dark blue arrow). Starting with

the measurement after 300 s of transformation, the Pb4f^{7/2} emission shifts to a position around 138.5-138.6 eV (red arrow), simultaneously with appearance of the N1s and C1s main emission, indicating the presence of MAPI. The binding energy positions of the core emission lines, the valence band maxima and the work functions measured during the experiment are summarized in table 5.10. The element ratios of I/Pb and N/Pb provide further information above the last deposition steps. After 900 s of transformation, the ratio of I/Pb is 3.1, the ratio of N/Pb 1.0. Those ratios indicate a complete transformation of PbCl₂ to stoichiometric MAPI, at least in the PES information depth. After 5400 s of transformation, the ratios change to 3.6 and 1.4 indicating a thin MAI capping layer (the lead emission is still visible) on top of the MAPI which is deposited probably during the cool down phase with open shutter.

Table 5.10.: Core emission line binding energy positions, valence band maximum positions and work functions measured on a freshly prepared PbCl₂ layer and during the stepwise transformation of the PbCl₂ layer to MAPI. All energy values are given in eV. The given transformation times *t* are cumulative transformation times.

<i>t</i> / s	I3d ^{5/2}	N1s	C1s	Cl2p ^{3/2}	Pb4f ^{7/2}	VBM (XPS)	VBM (UPS)	ϕ
0	x	x	x	198.18	138.93	2.43	2.28	4.92
10	619.55	x	x	198.54	138.86	1.81	1.87	4.77
60	619.65	x	x	x	138.72	1.67	1.90	4.86
130	619.68	x	x	x	138.69	1.62	1.88	4.73
300	619.57	402.64	286.48	x	138.62	1.55	1.64	4.47
900	619.48	402.62	286.51	x	138.55	1.58	1.58	4.43
5400	619.52	402.65	286.68	x	138.57	1.67	1.64	4.30

The valence band spectra in figure 5.52 support the transformation mechanisms of PbCl₂ to MAPI described above and provide further detail. For the freshly prepared PbCl₂ layer, the Cl3s and Cl3p features can be determined [87]. Already after 10 s of transformation, the Cl3s emission is not observable anymore and the valence band is dominated by I5p contributions [124]. However, at this stage, the Cl3p contribution at 6 eV is still clearly visible. For 60 s and 130 s the valence band spectra are dominated by PbI₂ (see also section 5.2.3 for comparison). The transformation of PbI₂ to MAPI includes the rearrangement of the PbI₆ octahedra from edge sharing to corner sharing. Furthermore, Lindblad et al. associate the I5p feature of the valence band with bonding I5p orbitals contributing to Pb-I-Pb bonds [124]. Considering this, the steadily decreasing intensity of the 5 eV feature with ongoing transformation is related to the reordering of the PbI₆ octahedra during the transformation of PbI₂ to MAPI.

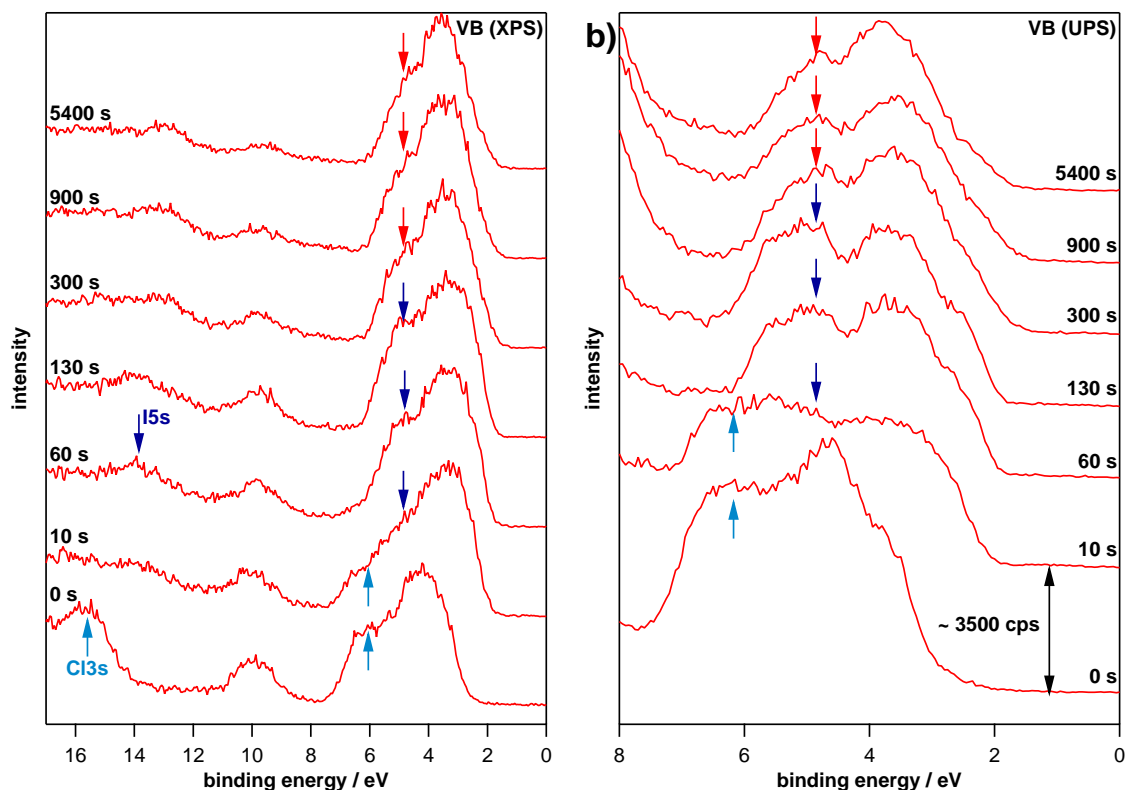


Figure 5.52.: Valence band spectra measured with XPS (a) and UPS (b) on a freshly prepared PbCl_2 layer and during the stepwise transformation of the PbCl_2 layer to MAPI, without breaking the vacuum conditions. The turquoise arrows indicate emissions characteristic for PbCl_2 , the dark blue and red arrows indicate features characteristic for PbI_2 and MAPI, respectively. The shown transformation times are cumulative transformation times. The offsets are given as a guide to the eye for the intensity.

The valence band spectra measured with XPS and presented in figure 5.52 allow an interesting procedure which may provide further detail on the transformation mechanism from PbCl_2 to MAPI, they can be approximated by a superposition of reference valence band spectra. This is done in figure 5.53. The valence band spectra of the freshly prepared PbCl_2 film is used as reference spectra for PbCl_2 . For MAPI, PbI_2 and MAI the valence band spectra presented in figure 5.23 a are used. For the approximation, the intensities of the reference spectra were scaled in a way that the total approximation yields the best optically match with the measured curves. For further detail see section 4.3.1 in the experimental chapter.

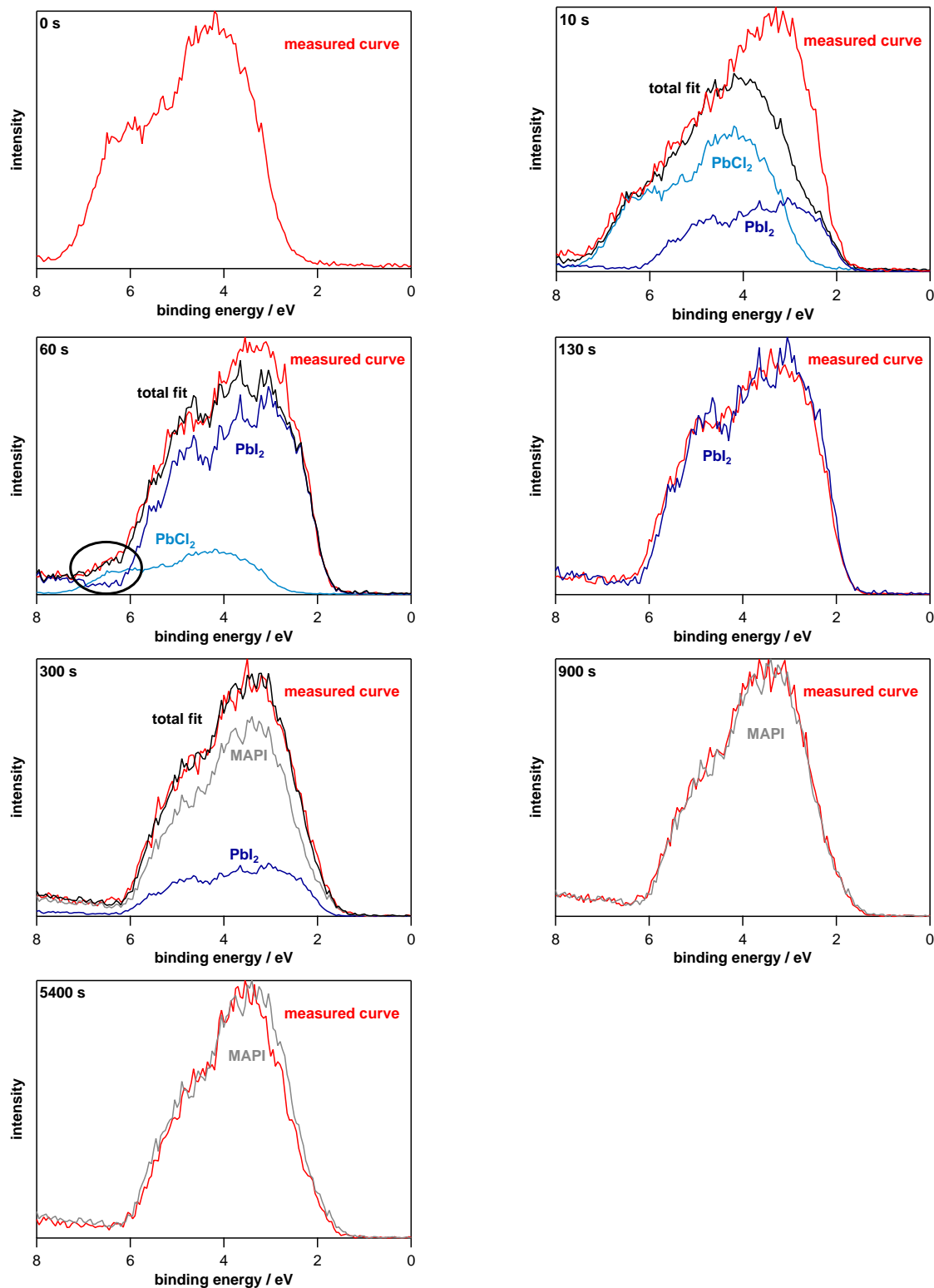


Figure 5.53.: Valence band spectra measured with XPS on a freshly prepared PbCl_2 layer and during the stepwise transformation of the PbCl_2 layer to MAPI, without breaking the vacuum conditions. The measured valence band spectra (red) are approximated by a superposition of reference spectra for PbCl_2 (turquoise), Pbl_2 (dark blue) and MAPI (gray). For further details on the approximation procedure see section 4.3.1 in the experimental chapter.

The approximations of the valence band spectra fit well to the evolution of the transformation of PbCl_2 to MAPI described above. The freshly prepared PbCl_2 layer and the spectra obtained after 10 s of transformation clearly show the presence of PbCl_2 . However, after 10 s a pronounced contribution of PbI_2 is visible. The spectra measured after 60 s and 130 s are dominated by PbI_2 . Nevertheless, a minor contribution of PbCl_2 can be determined in the 60 s spectra (encircled), which is difficult to identify in the spectra in figure 5.52. Hence, the transformation of PbCl_2 to PbI_2 in the XPS information depth is still incomplete after 60 s of transformation. However, after 130 s of transformation, the transformation of PbCl_2 to PbI_2 is complete and the valence band spectra corresponds well to the PbI_2 reference spectra. The fits of the valence band spectra measured after 10 s and 60 s of transformation yield an interesting observation, they can not be fitted with PbCl_2 and PbI_2 alone. An additional phase is present, which shows a strong contribution in the spectra measured after 10 s, a minor contribution in the spectra measured after 60 s and is not observable in the spectra measured after 130 s. Since the contribution of the additional phase appears to show high intensity at a binding energy position close to the one of the $\text{I}5\text{p}$, emission it could be speculated that it belongs to an iodine containing phase. First guesses would be MAI or MAPI. However, even when the reference spectra of those materials are used, the spectra measured after 10 s of transformation can not be approximated in a satisfying way. In addition, for MAPI and for MAI the presence of NH_3 in the layer would be necessary. Yet, the core level spectra shown above and the derived mechanism for the transformation of PbCl_2 to MAPI give no indication for the presence of NH_3 at this early stage of the transformation process. It rather appears that the additional phase might be an intermediate phase appearing during the transformation of PbCl_2 to PbI_2 .

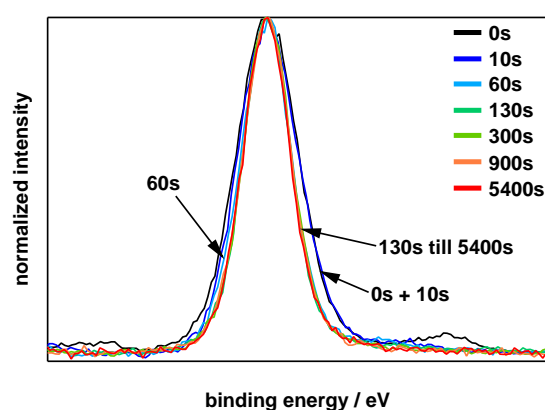


Figure 5.54.: Superposition of the $\text{Pb}4f^{7/2}$ emissions measured on a freshly prepared PbCl_2 layer and during the stepwise transformation of the PbCl_2 layer to MAPI, without breaking the vacuum conditions. The spectra are normalized in intensity scale and shifted in binding energy scale in a way, that their maxima are at the same binding energy position.

A further indication for the presence of an intermediate phase between PbCl_2 and PbI_2 might be the evaluation of the full width half maxima (FWHM) of the $\text{Pb}4f$ emissions in figure 5.54. Here, no broadening of the $\text{Pb}4f$ emissions between the 0 s and the 10 s spectra is observed. However, such a broadening would be expected in case the $\text{Pb}4f$ emission of PbCl_2 and PbI_2 , which show a binding energy difference in the range of 0.26 eV, would overlap. Hence, it could be speculated, that the $\text{Pb}4f$ emission of the 10 s spectra does not belong to an overlap of the $\text{Pb}4f$ emissions of PbCl_2 and PbI_2 but to the intermediate phase indicated by the valence band approximations in figure 5.53. Interestingly, the full width half maxima of the 0 s and 10 s spectra are quite similar. Those spectra are attributed to PbCl_2 (0 s) or are considered to be dominated by the postulated intermediate phase (10 s). On the other hand, the spectra from 130 s to 5400 s, which are considered as dominated by PbI_2 and MAPI, show a quite consistent FWHM as well. Only the $\text{Pb}4f$ emission in the spectrum recorded after 60 s of transformation shows a FWHM which is in between the one for PbCl_2 dominated spectra and the one for PbI_2 or MAPI dominated spectra. Here, a plausible explanation would be that the spectrum is already dominated by PbI_2 but with contributions of the intermediate phase or PbCl_2 . Such a phase composition would also be in accordance with the valence band fit in figure 5.53. Hence, two emissions with different binding energies would overlap, leading to a line broadening on the high binding energy side.

The valence band spectrum measured after 300 s of transformation is already dominated by MAPI and the spectrum obtained after 900 s corresponds well with pure MAPI. Even though the spectrum obtained after 5400 s appears to originate dominantly from MAPI, the fit is not as good as for the 900 s spectrum. This observation is probably due to the presence of the MAI capping layer, indicated by the surface stoichiometry. Considering that the MAI capping layer is likely quite thin (the $\text{Pb}4f$ emissions from MAPI are clearly visible), the evolution of a space charge region, caused by the contact between MAPI and MAI or other substrate effects might lead to a binding energy shift of the MAI capping layer observed in this experiment compared to the MAI reference spectra. Thus, even though the presence of MAI is the most probable explanation for the deviations of the valence band spectrum measured after 5400 s of transformation from the MAPI reference spectrum, the implementation of a MAI reference spectra did not yield a significant improvement of the fit and is not included in figure 5.53.

In conclusion, the PES data measured during the stepwise transformation of PbCl_2 to MAPI indicate a consistent transformation mechanism. In a first step PbCl_2 is transformed to PbI_2 by the reaction of CH_3I with PbCl_2 , possibly via an intermediate phase and accompanied by the formation of C_2H_6^+ and PbI_3^- . Thereby, the formation of C_2H_6^+ during the transformation of PbCl_2 to PbI_2 is a formation process of C_2H_6^+ in addition to the formation of C_2H_6^+ during the transformation of PbI_2 to MAPI described in section 5.2.3. Since no emission of chlorine could be determined after a transformation time of 130 s, the removal of the chlorine from the PbCl_2 by outward diffusion and sublimation

of CH_3Cl and Cl_2 is proposed. In a second step, the PbI_2 is transformed to MAPI by the incorporation of NH_3 into the layer. From equation 3.19 it can be derived that, under the condition of a constant crucible pressure, the surface coverage will be linearly dependent on t_t , in a first approximation. But, the evolution of the intensities of the I3d emissions in figure 5.49 and of the Pb4f emissions in figure 5.51 indicates that the dependence of the transformation process on t_t is not linear. The transformation of PbCl_2 (and probably also of PbI_2) to MAPI seems to be a diffusion controlled process, which might be described by equation 3.21 with the temperature dependence according to equation 3.22. However, since the temperature dependent adsorption, desorption, and diffusion behavior NH_3 is expected to be different from the other decomposition products of $\text{CH}_3\text{NH}_3\text{I}$, it must be considered in all details.

Stepwise transformation experiments of PbCl_2 to MAPI with an unheated substrate show the formation of undesired phases like MACl or CH_3Cl in the MAPI layer. This observation proves that a certain substrate temperature is needed to allow sufficient diffusion of the species involved in the transformation process and to ensure a good transformation of PbCl_2 to MAPI. However, to get a more detailed insight into the kinetics of the transformation of lead salts to MAPI, further experiments are needed.

As mentioned above, the MAPI layer was examined with XRD and SEM after the stepwise transformation was completed. The obtained X-ray diffraction pattern is shown in figure 5.55, the SEM images in figure A.13 in the appendix. The diffraction pattern shown in figure 5.55 was measured under Ar atmosphere but the sample was transported in air.

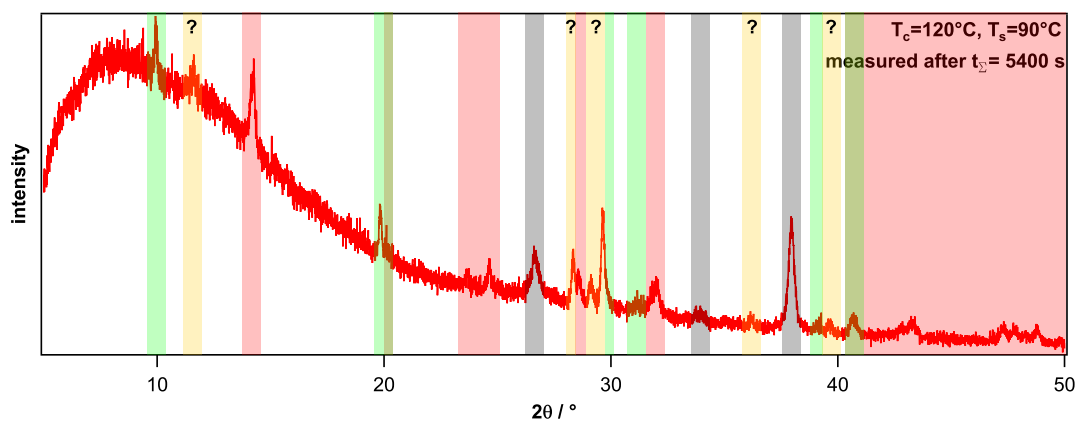


Figure 5.55.: X-ray diffraction pattern of the MAPI sample after the stepwise transformation (cumulative transformation time of 5400 s). The transparent bars are given to ease the identification of the crystalline phases present in the sample. Reflections belonging to MAPI are marked red, those belonging to MAI green and those belonging to the FTO/ TiO_2 electrode gray. In addition five unidentified reflections are marked yellow. The low signal to noise ratio is caused by the short integration time used for this measurement.

In the XRD pattern in figure 5.55, reflections associated with MAPI and MAI can be identified. No residual PbI_2 or PbCl_2 can be determined. Hence, it can be assumed, in accordance with the PES results, that the final step was chosen too long, leading to a MAI capping layer. Not all reflections associated with MAPI and MAI in figures 5.15 and 5.44, can also be determined in figure 5.55. The reason for that is probably the low signal to noise ratio in figure 5.55. In addition, it should be mentioned that while the PES results indicate only a thin MAI capping layer, the visibility of MAI in the XRD pattern in figure 5.55 can only be explained by a rather thick MAI capping layer. Those findings appear to contradict each other. However, the measurement point of the last PES measurements was not on the sample half used for the XRD measurement. Hence, an inhomogeneous thickness of the MAI capping layer can explain the observation that the MAI layer appears to be thicker in the XRD measurement as in the PES measurements. The combination of the surplus MAI with the transport in air might also explain the five unidentified reflections in figure 5.55 [153, 154]. At least the reflection around 11.6° is associated with the formation of lead halide complexes like $((\text{CH}_3\text{NH}_3)_4\text{PbI}_6 \cdot 2\text{H}_2\text{O})$ due to the presence of humidity and excess MAI [153, 154]. It appears plausible that also the other unidentified reflections could belong to such a complex phase. The involvement of water is an important feature. Since it is not present in significant amounts in the vacuum system, the complexes have most likely formed during the transport in air and do not influence the PES results. However, degradation of the sample due to the repeated heating and irradiation with X-rays as well as due to the extended exposure to the vacuum environment has to be considered as measurement uncertainty for this experiment.

5.3.4 Most important facts

- No Cl can be detected in PES measurements. Hence, the perovskite fabricated from PbCl_2 is considered rather a PbCl_2 derived MAPI than a mixed halide perovskite. Since the binding energy positions of the core lines are invariant towards the used lead salt, also a chlorine doping modification appears unlikely. Also, the band gap of $\text{MAPI}_{\text{PbCl}_2}$ corresponds to the one of $\text{MAPI}_{\text{PbI}_2}$.
- The layer morphology of PbCl_2 differs from the morphology of PbI_2 and the morphology of $\text{MAPI}_{\text{PbCl}_2}$ differs from the one of $\text{MAPI}_{\text{PbI}_2}$. However, similar to $\text{MAPI}_{\text{PbI}_2}$, the evolution of the layer morphology of $\text{MAPI}_{\text{PbCl}_2}$ is based on three mechanisms: transformation of the PbCl_2 to MAPI and the recrystallization and grain growth of the MAPI grains. Also, the qualitative dependence of these three processes on the substrate temperature appears to be similar for $\text{MAPI}_{\text{PbI}_2}$ and $\text{MAPI}_{\text{PbCl}_2}$.
- The stepwise transformation of PbCl_2 to MAPI was examined with PES. The results indicate that the transformation mechanism of PbCl_2 to MAPI includes the formation of PbI_2 and possibly an additional intermediate phase between PbCl_2 and PbI_2 . A reaction scheme for the transformation of PbCl_2 to MAPI is proposed.
- As for $\text{MAPI}_{\text{PbI}_2}$, an orthorhombic crystal structure of the space group *Pnma* was found to be the dominant modification also for $\text{MAPI}_{\text{PbCl}_2}$. Accordingly, the orthorhombic modification of MAPI, which is uncommon at room temperature, appears to be a feature of MAPI layers fabricated with the 2step CSS process, independent on whether PbI_2 or PbCl_2 is used as base layer.

5.4 Photoactivity

In the first sections of this results and discussion chapter, the characterization of the optoelectronic, crystallographic and morphological properties of MAPI, fabricated with the sequential CSS process were presented. In addition, the dependencies of those properties on the substrate temperature during the CSS process and the used lead salt were discussed. Furthermore, the evolution of the perovskite from PbI_2 and PbCl_2 was described. In this final results chapter, the photoactivity of the fabricated MAPI layers will be discussed by means of photoluminescence experiments and the implementation of the MAPI layers in planar solar cells. Some parts of this section are taken from our publication [1].

5.4.1 Photoluminescence

The photoluminescence (PL) measurements of MAPI layers fabricated from PbI_2 (a) and (c) as well as from PbCl_2 (b) and (d) at substrate temperatures of 75°C , 90°C , 130°C and 150°C on glass/FTO/ TiO_2 substrates are shown in figure 5.57. The main PL emission of the spectra at 1.61 - 1.62 eV is assigned to the optical band gap of MAPI. Figure 5.56 shows the comparison of the PL spectra of the MAPI layer fabricated from PbI_2 at a substrate temperature of 75°C during the CSS process, with a MAPI layer fabricated by co-evaporation of PbI_2 and MAI. The data for the co-evaporated sample were provided by M.Sc. Maximilian Stöhr.

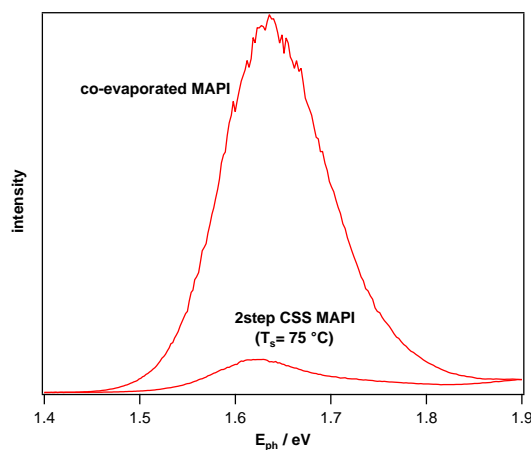


Figure 5.56.: PL spectra of two MAPI layers fabricated from PbI_2 on glass/FTO/ TiO_2 substrates by 2step CSS ($T_s=75^\circ\text{C}$, same measurement as in figure 5.57) and by co-evaporation of PbI_2 and MAI. The data for the co-evaporated sample were provided by M.Sc. Maximilian Stöhr.

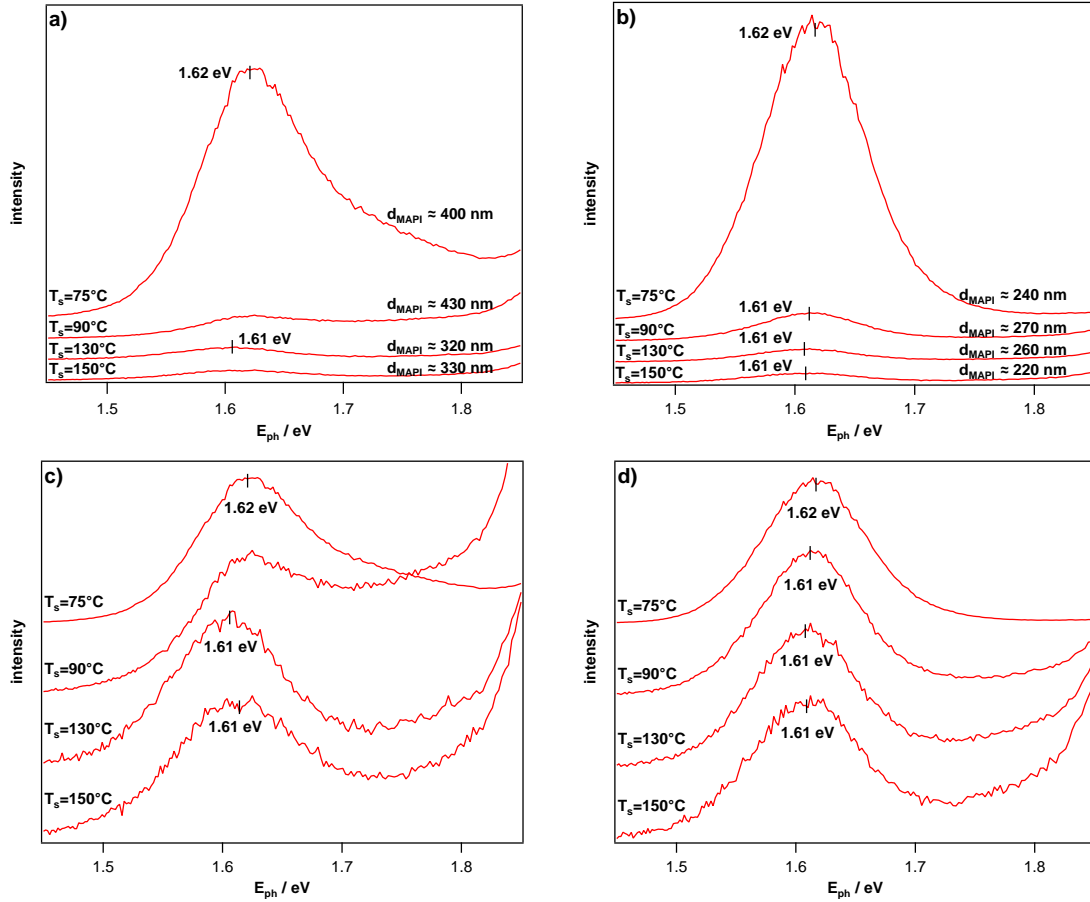


Figure 5.57.: Photoluminescence spectra of $\text{MAPI}_{\text{PbI}_2}$ samples, (a) and (c), and $\text{MAPI}_{\text{PbCl}_2}$ samples, (b) and (d), prepared on glass/FTO/ TiO_2 substrates at substrate temperatures of 75 °C, 90 °C, 130 °C and 150 °C during the CSS process. The spectra in (c) and (d) are normalized in intensity scale. The PL spectra of the bare glass/FTO/ TiO_2 substrate, PbCl_2 , PbI_2 and MAI show no emission in the presented photon energy range. All MAPI spectra but $\text{MAPI}_{\text{PbCl}_2}$ with $T_s=75^\circ\text{C}$ are measured with an incident beam wavelength of 480 nm, a 20 nm slit and an 530 nm emission filter. $\text{MAPI}_{\text{PbCl}_2}$ ($T_s=75^\circ\text{C}$) is measured with an incident beam wavelength of 450 nm and a 475 nm emission filter.

The spectra in figure 5.57 show that the 2step CSS MAPI layers fabricated at a substrate temperature of 75 °C have the highest PL intensities. The MAPI layers fabricated at the other substrate temperatures show intensities which are significantly lower than for the $T_s=75^\circ\text{C}$ sample⁷. Furthermore, figure 5.56 shows that the PL intensity of the $T_s=75^\circ\text{C}$ 2step CSS MAPI sample is considerably lower than the one of the co-evaporated sample. Taking into account, that the CSS MAPI spectrum used in figure 5.56 shows one of the highest intensities achieved with the 2step CSS MAPI layers, the overall PL intensity range of the 2step CSS MAPI layers appears to be low. The low PL intensities can be both, a promising or a problematic indication concerning the quality of the MAPI layers. On one hand, when discussing the PL intensity the conductive glass/FTO/ TiO_2 substrates have to be considered which can quench the PL intensity. Van Franeker et al. even use

⁷ A more detailed examination of the dependence of the PL intensity on T_s would not be reasonable since an unambiguous calibration of the spectra in intensity scale was not possible.

the quenching of the PL signal of a 390 nm thick MAPI layer as criteria to describe the charge transport properties and hence the quality of the MAPI layers and their suitability as solar cell absorbers [111]. On the other hand, non-radiative recombination mechanisms need to be considered. The dominant non-radiative recombination mechanisms are reported to be defects at grain boundaries or interfaces for perovskite solar cells with low efficiencies and Shockley-Hall-Read recombination via bulk defects for high efficiency solar cells [155]⁸. Concerning the grain boundaries, not the volume fraction of the grain boundaries appears to be most important but the type of grain boundaries and of the grain boundary defects [155, 156]. From the PL measurements, it is difficult to decide, whether the quenching of the intensity is caused by the extraction of photogenerated charges into the FTO/TiO₂ electrode or by non-radiative recombination. But, the comparison of the PL measurements with the IV measurements presented below will help to clarify the cause of the low PL intensity. Since all layers were fabricated on glass/FTO/TiO₂ substrates, a possible substrate effect should be canceled out when comparing the PL intensities. It is interesting that the PL intensities decrease with increasing substrate temperature for MAPI_{PbI₂} and for MAPI_{PbCl₂}. A possible explanation could be a temperature dependent defect density. However, since the valence band maximum positions appeared to be invariant towards the process temperatures, at least for the densities of charged defects, no pronounced substrate temperature dependence is expected. Interestingly, those samples which show the highest PL intensities are fabricated at the same substrate temperatures, 75 °C and 90 °C, for which the presence of the cubic MAPI modification was indicated by the XRD measurements, at least for MAPI derived from PbI₂. Hence, a certain correlation between the presence of MAPI in its cubic modification and the PL intensity could be assumed. For the MAPI layers derived from PbCl₂ this correlation is less well developed, since all MAPI layers with $T_s \geq 90^\circ\text{C}$ do not show the cubic phase modification. Still, for the $T_s = 75^\circ\text{C}$ layer, which shows the highest PL intensity, the indication for the presence of the cubic phase modification is given. Although, the assumption of a correlation between the PL intensity and the cubic MAPI modification is speculative, it can be readily explained. Recently, reports of a substantial contribution of the reorientation of the MA⁺ cations to the dielectric constant of MAPI and therefore to the screening of charged species in MAPI can be found [101, 102]. In the cubic modification, the MA⁺ cations can rotate freely while in the orthorhombic modification, the degree of orientational freedom of the MA⁺ cations is limited [92, 101, 104, 105, 108]. This limited ability for reorientation leads to a reduced dielectric constant and a reduced charge screening, resulting in reduced life times and mean free paths of photoexcited charge carriers [101, 102]. Considering those effects, the influence of the non-radiative recombination mechanisms will be more pronounced in the orthorhombic compared to the cubic MAPI modification. Hence, it is plausible that the PL intensities are generally higher for the cubic perovskite modification than for the orthorhombic modification and that the overall PL intensity for the 2step CSS MAPI layers scales to some extent with the cubic phase fraction.

⁸ for mixed perovskite containing Cs, MA, FA, Pb, I and Br

The slight variation between the band gaps determined with UV/VIS spectroscopy (1.58 - 1.60 eV) and PL spectroscopy (1.61 - 1.62 eV) is related to the determination procedures used during the evaluation of the UV/VIS and PL spectra. In the PL measurements no background subtraction was performed and in the UV/VIS experiments the onset of the absorption over the band gap was considered as optical band gap. Hence, the possible influences of defect states and surface roughness on the onset of the fundamental absorption, as discussed in section 5.2.3, might lead to an underestimation of the optical band gap determined from the UV/VIS measurements and explain the discrepancy between the optical band gaps derived from UV/VIS and from PL spectroscopy measurements. Furthermore, the comparison of the PL and UV/VIS results identifies the surface roughness as main cause of the varying sharpness of the onset of the fundamental absorption in the UV/VIS experiments in figures 5.21 and 5.40. If defects were the dominating influence for the sharpness of the fundamental absorption, there should be some correlation between the intensity of the PL emission and the sharpness of the fundamental UV/VIS absorption onset. But, no such correlation can be determined by the comparison of the UV/VIS spectra in figures 5.21 and 5.40 and the PL spectra in figure 5.57. Nevertheless, even though defects do not appear to determine the sharpness of the onset of the fundamental absorption in UV/VIS measurements, the low PL intensities still constitute an indication for the general presence of defects in the MAPI layers. The assumption that the influence of defects on the UV/VIS spectra is probably superimposed by the influence of the surface roughness of the MAPI layers and the absorption of the glass/FTO/TiO₂ substrate, even though defects are present in the fabricated MAPI layers, is further supported by the comparison of the UV/VIS data measured during this work with spectra found in literature. This comparison shows that the course of the absorption coefficient over the photon energy is well in accordance with literature spectra associated with MAPI layers which achieved PCEs above 10 % in solar cells [33, 40, 110–112]. However, the solar cells prepared during this work do not reach such efficiencies, likely, in part, due to the presence of defects, as will be discussed below. In addition to surface roughness and defects, other physical reasons like an anti-Stokes shift caused by the formation of polarons from photoexcited charge carriers could be considered as contribution to the difference of the band gaps determined with UV/VIS and PL spectroscopy [101, 157]. Since the band gaps derived from the PL measurements are also smaller than the energetic difference between E_F and the VBM of MAPI_{PbI2} and of MAPI_{PbCl2}, the use of those band gaps instead of the ones derived from UV/VIS measurements would not lead to any major change for the interpretation of the band energy diagrams of MAPI in figures 5.5, 5.24 and 5.41.

Comparing the PL spectra of MAPI_{PbI2} and MAPI_{PbCl2}, the qualitative dependence of the PL intensity on the substrate temperature and the determined band gaps are similar. However, the PL spectra of MAPI_{PbI2} show a shoulder at higher photon energies compared to the main emission, which is not present in the spectra taken from MAPI_{PbCl2}. A shoulder on the high binding energy side of the main emission directly rules out explanations like defects in the band gap or relaxation effects known from organic semiconductors. Also,

none of the crystallographic modifications of MAPI shows a band gap corresponding to the energetic position of the shoulder [103]. Moreover, the band gap of MAPI is reported to be rather invariant towards stoichiometric variations [128]. Imaginable causes for the shoulder might be surface effects caused by the large surface fraction of the free standing flakes or even an accelerated degradation of the MAPI flakes to a non-MAPI phase, compared to the dense layer.

5.4.2 Solar cells incorporating MAPI derived from lead iodide

To test the performance of the fabricated MAPI layers as solar cell absorbers, they were implemented into planar solar cells. Thereby, a simple stack consisting of FTO/c-TiO₂/MAPI/Spiro-MeOTAD/Au was used. For the solar cell fabrication the focus was set on MAPI fabricated from PbI₂ layers. Figure 5.58 shows the time stabilized values for the open circuit voltages V_{oc} , the short circuit current densities (J_{sc}), the fill factors (FF) and the efficiencies (η) of planar solar cells incorporating the 2step CSS MAPI layers. In figure 5.58, the effect of a C₆₀ layer between the TiO₂ layer and the MAPI layer and of an additional heat treatment of the MAPI layers can be observed. The C₆₀ layer and the heat treatment in air are intended to improve the performance of the fabricated solar cells by a reduction of the defect density and a modification of the TiO₂/MAPI interface [21, 111, 129, 155, 158–163]. In figure 5.58, the solar cells without a C₆₀ layer or a heat treatment show poor performance. Still, the IV curves of the solar cells show a clear diode behavior. The incorporation of a C₆₀ layer improves the V_{oc} , the J_{sc} and the efficiency of the solar cells presented in figure 5.58. Nevertheless, other solar cells fabricated from PbI₂ on FTO/c-TiO₂ substrates with the 2step CSS process show that also cells without a C₆₀ layer can match the performance of the cells with a C₆₀ layer and even excel them. However, without the C₆₀ layer, the solar cells on different substrates show a broad variation in their performance. Therefore, it appears that the parameters with the broadest variation are the photocurrent and, less pronounced, the open circuit voltage. In section 5.2.4 it was proposed that an interface phase (Pb(IO₃)₂) is likely to form between the O₂⁻ adsorbates on the TiO₂ layer and the lead salts during the PVD fabrication step. The presence and the amount of such an interface phase will scale with the concentration of the O₂⁻ adsorbates on the TiO₂. Hence, a varying concentration of O₂⁻ adsorbates on the TiO₂ caused by unmonitored fluctuations during the spray pyrolysis and the plasma treatment could explain the observed variation of the performance of the solar cells without a C₆₀ layer. A varying O₂⁻ adsorbate concentration, with the corresponding surface band bending, on the spray pyrolyzed and plasma treated TiO₂ layers is further indicated by the varying PES results obtained from similar processed TiO₂ layers in section 5.1.1. Unfortunately, no information about the band gap and the position of the energy levels in Pb(IO₃)₂ is available. Nevertheless, insulating properties of the Pb(IO₃)₂ phase or a detrimental influence on the contact formation between TiO₂ and MAPI would hinder the extraction of electrons from the MAPI absorber into the ETL,

resulting in an increased series resistance and in a decreased photocurrent. Hence, the mayor role of the C_{60} layer is to prevent the formation of the $Pb(IO_3)_2$ interface phase. The prevention of the formation of an interface phase and the beneficial effect of the organic interface layer, due to reduced charge carrier recombination at the TiO_2 /MAPI interface, on the solar cell performance are in accordance with literature [21,129,158,159].

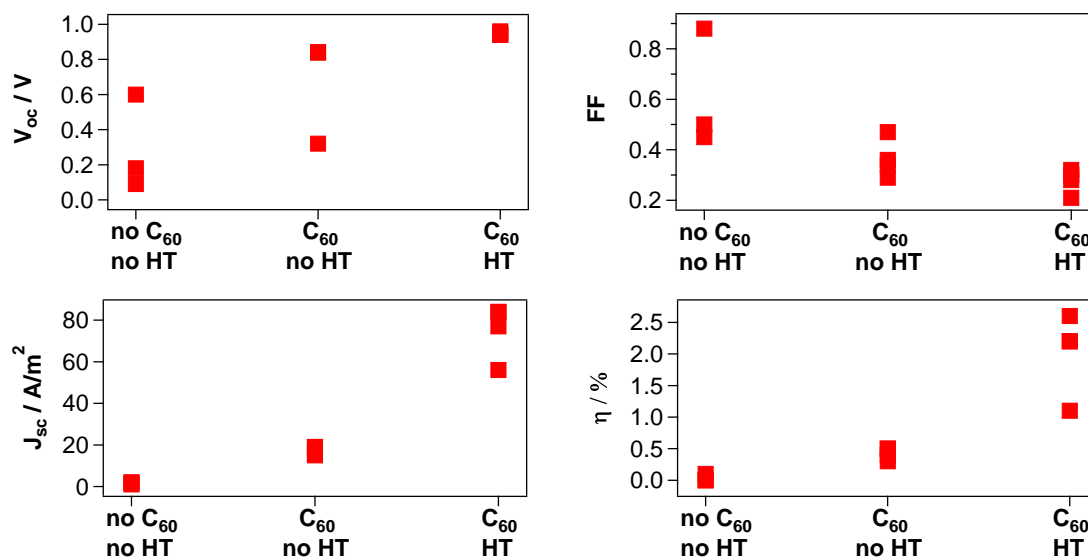


Figure 5.58.: Open circuit voltages (V_{oc}), short circuit current densities (J_{sc}), fill factors (FF) and efficiencies (η) of solar cells fabricated at $T_s=90^\circ C$ during the CSS process. Shown are solar cells without a C_{60} layer and without a heat treatment, with a C_{60} layer between TiO_2 and MAPI but without heat treatment and with a C_{60} layer and a heat treatment in air at $100^\circ C$ for 30 min. For every condition the time stabilized values of four solar cells on one substrate are shown, each solar cell with an area of $3.25\text{ mm} \times 10\text{ mm}$.

The heat treatment of the MAPI layers in air, prior to the Spiro-MeOTAD spin coating, yields a further increase of the PCE of the fabricated solar cells. Thereby, the most important effect of the heat treatment is a pronounced increase of the photocurrent. For the solar cells in figure 5.58, the photocurrent increase is accompanied by a small increase of the open circuit voltage. SEM and XRD experiments on CSS fabricated MAPI layers with and without a heat treatment in the tube furnace are presented in the master thesis of M.Sc. Christian Hoyer (see figures A.14 and A.15 in the appendix) [164]. The SEM images show that the morphological changes of the MAPI layers are limited to a reduction of the amount of the not recrystallized MAPI flakes (see also section 5.2.1 for comparison). The morphology and the grain size of the recrystallized grains is mainly unaffected. Furthermore, the heat treatment in the tube furnace appears to reduce the phase fraction of the cubic perovskite modification (see figure A.15) [164]. Besides the recrystallization of the flake like grains, other effects which are beneficial for the solar cell performance are reported for a heat treatment of the perovskite layer in literature. Especially J_{sc} , FF and η , but less pronounced also V_{oc} , are reported to profit from a reduction of the amount of trap states, recombination centers and grain boundaries during

a heat treatment [111, 155, 160, 162, 163]. In addition, results by Das et al. indicate that a heat treatment in air will improve the performance of the fabricated solar cells by the oxidation of metallic lead to lead oxide, in case metallic lead would form due to illumination during the vacuum fabrication steps [165]. It appears likely that a combination of all these effects can explain the beneficial effect of the heat treatment on the performance of the solar cells examined in this work.

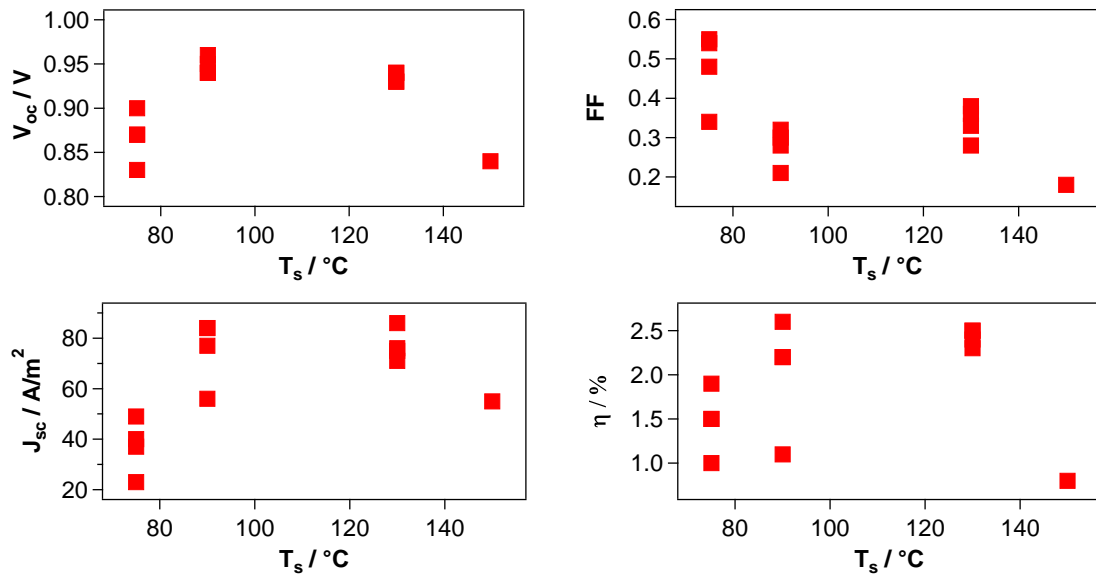


Figure 5.59.: Open circuit voltages (V_{oc}), short circuit current densities (J_{sc}), fill factors (FF) and efficiencies (η) of solar cells fabricated at substrate temperatures of 75 °C, 90 °C, 130 °C and 150 °C during the CSS process. The solar cells possess a C_{60} layer between the TiO_2 and the MAPI layer and were heat treated in air for 30 min at 100 °C. Plotted are the time stabilized values of four solar cells (only one for $T_s=150$ °C) on one substrate, each cell with an area of 3.25 mm x 10 mm.

The properties of the fabricated solar cells incorporating the 2step CSS MAPI absorber appear to be relatively invariant towards the substrate temperature during the CSS process, as figure 5.59 shows. However, the open circuit voltages, short circuit current densities and efficiencies of the solar cells incorporating the MAPI layers fabricated at substrate temperatures of 90 °C and 130 °C during the CSS process are slightly improved compared to the 75 °C and 150 °C samples, supporting the optimum substrate temperature window for the 2step CSS process estimated from the comparison of the SEM images in figure 5.14. The achieved efficiencies in the range of 1-3 % are low compared to solar cells incorporating MAPI as absorber which is produced by evaporation under vacuum conditions or ambient pressure CVD with varying contact materials [13, 21, 33, 37, 38, 40]. But, the combination of a cell area of 3.25 mm x 10 mm and the observed narrow efficiency distribution, especially for the $T_s=130$ °C substrate, shows that also square centimeter cells with that efficiency could be produced, indicating the potential of the CSS process to fabricate homogenous large area thin films. The IV characteristics of a solar cell incorporating a MAPI layer fabricated at $T_s=130$ °C are shown in figure 5.60.

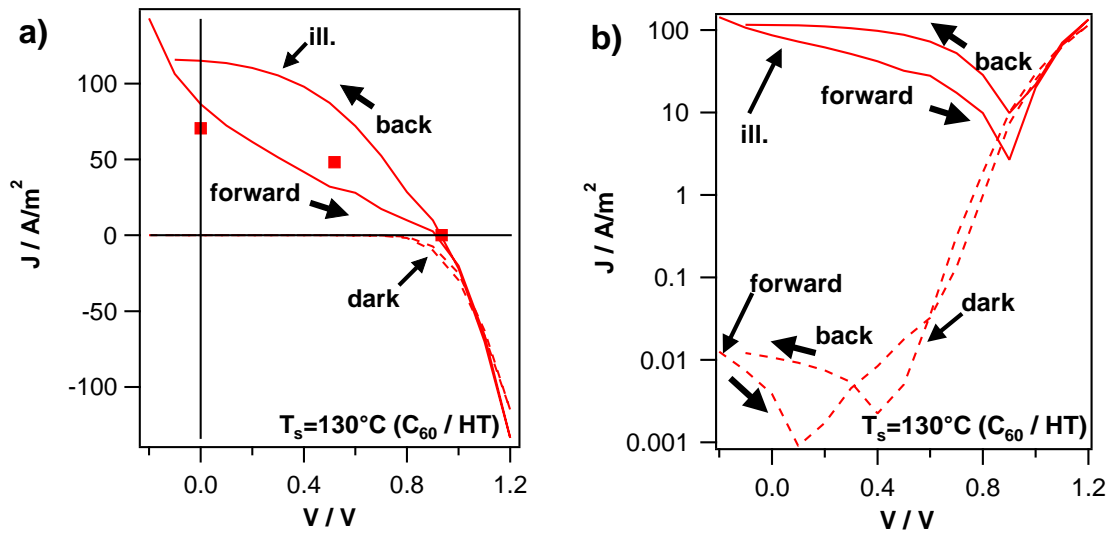


Figure 5.60.: IV characteristics in linear (a) and semilogarithmic (b) scale of a planar solar cell fabricated at a substrate temperature of 130 °C during the CSS process with a C₆₀ layer between the TiO₂ and the MAPI layer and a heat treatment in air for 30 min at 100 °C. The dashed curves denote the IV measurements in the dark, the solid lines the measurements under illumination. The red squares in a) denote the time stabilized values of J_{sc} , V_{oc} and the maximum power point.

The hysteresis, shown by the IV curves in figure 5.60, can be caused by several effects or by a combination of those [121, 156, 159, 166]. In general, the origin of hysteresis for perovskite solar cells is still topic to lively discussion in the research community [121, 156, 159, 166]. Based on current literature, it appears that the observed hysteresis is caused by the redistribution of ions [121, 156, 159, 166]. Thereby, iodine interstitials (I_i^-) appear to be the most likely candidates for the ion movement [121, 156]. But, also the movement of other ions like MA^+ is topic to current discussion [121]. Besides the ion migration, other effects can influence the hysteresis observed during IV measurements of perovskite solar cells [121, 159, 166]. To name a few, the interfaces between MAPI and the charge transport layers, the IV history of the solar cell, preconditioning of the solar cell and the measurement conditions have been found to have a pronounced influence on the hysteresis [121, 159, 166]. To exclude the effect of the hysteresis on the determination of the V_{oc} , J_{sc} and the maximum power point (MPP), their measures were determined as time stabilized values and can be considered as independent on the hysteresis. The experimental chapter gives detailed information about the respective measurement procedures.

Another interesting observation is that in figure 5.58 and in figure 5.59 the fill factor evolves in the opposite direction as the open circuit voltage, the short circuit current density and the efficiency. A possible explanation is indicated in figure 5.61, exemplarily for the solar cell also shown in figure 5.60.

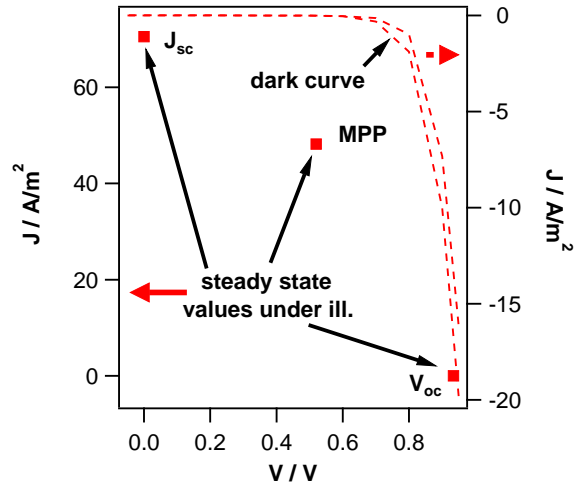


Figure 5.61.: Comparison of the shape of the dark IV curve and the curve of the time stabilized values (V_{oc} , J_{sc} , MPP) of a solar cell incorporating MAPI fabricated at $T_s=130\text{ }^\circ\text{C}$ during the CSS process step. The solar cell possesses a C_{60} layer between the TiO_2 and the MAPI layer and was heat treated in air for 30 min at $100\text{ }^\circ\text{C}$. Shown are both curves in the voltage range from -0.05 V to 0.95 volt . The right axis belongs to the dark curve, the left axis to the time stabilized values.

Figure 5.61 shows that for the examined solar cells the superposition approximation of dark- and photocurrent is not valid, meaning that the IV curve measured under illumination, denoted by the time stabilized values for V_{oc} , J_{sc} and the MPP in figure 5.61, has not the same shape as the dark IV curve [167]. Such a behavior can be caused by a voltage dependent photocurrent [54, 167]. The voltage dependence of the photocurrent may have different origins which strongly depend on the type of examined solar cell. Unfortunately, the exact determination of the origin of the voltage dependence of the photocurrent of the solar cells examined in this work is not possible. But, at least an attempt for an explanation will be given. Usually MAPI is reported to show rather long life times for both, electrons and holes [168]. However, the reduced charge screening in the orthorhombic MAPI modification is reported to reduce the life times of photoexcited charge carriers [101, 102]. In addition, the PL measurements presented in figure 5.57 indicate an increased non-radiative recombination in the 2step CSS MAPI layers. With that, the velocity with which the photogenerated charge carriers reach the charge selective contacts becomes more important to ensure an effective separation of photogenerated charges. Since the photocurrent is a voltage dependent current, the probability with which the charge carriers reach the electrodes depends on the potential difference between the electrodes, in case of a p/i/n-solar cell or on the band bending in the SCR in case of a p/n-solar cell. Either way, a potential applied in forward direction of the diode will reduce the potential difference responsible for the separation of photogenerated charge carriers and therefore slow down the charge carriers leading to an increased recombination and hence a reduced photocurrent with increasing voltage in forward direction. The observation that the FF evolves in the opposite direction compared to V_{oc} , J_{sc} and η in figures 5.58 and 5.59 can now also be explained. With an increasing pho-

to current, its influence on the shape of the IV characteristics becomes more relevant. In addition, the voltage dependence of the photocurrent causes a deviation of the measured IV characteristics from ideal diode IV characteristics. Hence, while V_{oc} , J_{sc} and η benefit from an increased photocurrent, the fill factor of the solar cells examined in this work decreases with increasing photocurrent due to an increasing deviation of the measured IV characteristics from ideal diode IV characteristics caused by the voltage dependence of the photocurrent.

As described above, the solar cell efficiencies achieved with the 2step CSS MAPI layers are lower than the efficiencies reported for MAPI solar cells fabricated with other methods. Literature values for MAPI solar cells (different layer stacks and fabrication methods) are around 1 V for the open circuit voltage, for the short circuit current density around $200 \pm 20 \text{ A/m}^2$ and around 70 % for the fill factor [13,21,33,36–38,40,112,131,147,169–171]. The comparison of the literature values with the time stabilized V_{oc} and J_{sc} values of 0.93 V and 70.5 A/m^2 and a fill factor of 38 % for the solar cell in figure 5.60 shows that all three parameters are smaller than the literature values for the 2step CSS solar cells. However, the open circuit voltage is in the range of the literature values. The main efficiency loss is caused by the low current density and the low fill factor. The low current density and the low fill factor can be caused by different effects. Losses of the fill factor can, for example, be due to the voltage dependence of the photocurrent caused by recombination of photogenerated charge carriers described above. Furthermore, a pronounced recombination of photogenerated charge carriers via defect states can also explain the observed low current densities. Hence, the defect density in the 2step CSS MAPI layers needs to be discussed at this point. The overall defect density in the bulk should be reduced by the heat treatment [111,160–163]. The role of grain boundaries in perovskite solar cells is still topic to scientific discussion [155,156,172]. Considering the grain boundary phase which was proposed as possible explanation for the crack formation during SEM measurements, the grain boundaries could appear as possible origin for defect states. However, the formation of cracks at grain boundaries is also reported for solar cells with active areas in the square centimeter range and efficiencies overcoming 15 % [91]. Hence, independent on the reason for the cracks, which only occur under intensive electron beam irradiation, they do not explain the observed PCEs. Furthermore, a dense morphology of the MAPI layers, like the one shown by the SEM images in figure 5.14 for $\text{MAPI}_{\text{PbI}_2}$ and in figure 5.43 for $\text{MAPI}_{\text{PbCl}_2}$, is reported to reduce the amount of defects caused by grain boundaries and hence the influence of the grain boundaries on the solar cell performance [155,156,173]. However, especially for solar cells showing low efficiencies, generally, the recombination of photogenerated charge carriers via grain boundary defects needs to be considered [155]. The recombination via defects at the ETL and HTL interfaces should be reduced due to the use of the C_{60} interlayer at the ETL side and Spiro-MeOTAD as (organic) HTL [159]. In conclusion, even though the grain boundaries do not appear to cause an exceptional high defect density in the 2step CSS MAPI layers and measures were taken to reduce the defect density in the bulk of the layers and at

the interfaces to the charge transport layers, it appears that the recombination via defects is still an important performance limitation for solar cells incorporating 2step CSS MAPI layers. An explanation which could add to this observation would be that the time of the heat treatment was chosen too short and the beneficial effect of a reduction of the defect density due to the heat treatment was not fully developed. Furthermore, as mentioned in the PL section of this chapter, the limited ability of the MA^+ cations to rotate and the respective reduced screening of charged species might enhance the recombination of the photogenerated charge carriers, via defects and band to band, in the orthorhombic MAPI modification compared to tetragonal or cubic MAPI [101–103]. The observation that the fabricated solar cells show rather low efficiencies for all examined substrate temperatures is in accordance with the assumption, made above when discussing the PL spectra, that the defect densities are independent on the substrate temperature during the CSS process. Besides the influence of defect states and recombination, another effect appears to limit performance of the solar cells prepared during this work. Since MAPI layers fabricated at all examined substrate temperatures possess a dense and homogenous morphology, at least beneath the flake like grains, it can be assumed that the influence of short circuits and weak diodes through the absorber layers on the IV characteristics is sufficiently small. The observation that the discrepancy between the measured solar cell parameters and the literature values is larger for J_{sc} and FF than for V_{oc} indicates that a high serial resistance might be part of the explanation of the measured solar cell characteristics (see also section 3.2.3). The reason for this is that the open circuit voltage is the only parameter which is not directly influenced by the serial resistance because it is obtained when the measurement circuit is current free [47]. Section 3.2.3 in the basics chapter gives a more detailed description of the equivalent circuit of a solar cell with the layer sequence used in this work. After the identification of the series resistance as probable cause of the low photocurrent, the possible causes of the series resistance will be discussed in the following. An insulating interface layer caused by a reaction of the O_2^- adsorbates on the TiO_2 and PbI_2 during the PVD step can be ruled out as reason for the high series resistance due to the use of the C_{60} layer. It rather appears that the most plausible cause of the high serial resistance is a thin layer of remnant PbI_2 between the FTO/ TiO_2 ETL and the MAPI absorber. Concerning the role of remnant PbI_2 in perovskite solar cells and its impact on their performance, different opinions are reported in literature [112, 114, 174–177]. As discussed in section 5.2.3 and shown in figures 5.24 and 5.25, it is likely that a potential barrier for electrons exists at the PbI_2 /MAPI contact. In addition, PbI_2 shows a poor conductivity [141]. Hence, if the PbI_2 remnants, indicated by the XRD measurements in figure 5.15, would be present as dense layers, they can hinder the electron transfer between the MAPI absorber and the FTO/ TiO_2 electrode and explain an increased serial resistance which limits the solar cell performance. The assumption that the remnant PbI_2 is present at the MAPI/ TiO_2 interface is plausible considering that the MAI inward diffusion front will emerge from the layer surface towards the TiO_2 during the transformation of PbI_2 to MAPI (see section 5.3.3 for comparison). Accordingly, flat PbI_2 grains located

directly at the interface will be transformed last and are the most likely candidates for unreacted PbI_2 . That the remnant PbI_2 is not distributed randomly is in agreement with the stoichiometric surface composition measured with PES. The stoichiometric surface composition further indicates that no MAI capping layer is present on the examined MAPI layers. Nevertheless, the influence of surplus MAI on top of the MAPI absorber layer needs to be considered. Figure 5.24 shows that the ΔE_{VBM} between MAPI and MAI is 0.32 eV. The valence band maximum offset will not cause problems in case a sufficient contact between the MAPI layer and the Spiro-MeOTAD HTL is given. As thin, dense layer however, the presence of MAI may hinder the extraction of holes from MAPI into the Spiro-MeOTAD electrode. In conclusion, since dense layers of both, PbI_2 and MAI, will hinder the charge transport from the MAPI absorber into the electrodes, it is crucial in a sequential fabrication process that the Pb-salt layers are completely reacted (no remnant PbI_2 interlayer) and the formation of a MAI capping layer is avoided at the same time. Only then the serial resistance is sufficiently low to provide a good charge extraction which is crucial for a well working solar cell. Furthermore, the observation of the high serial resistances due to thin interface layers supports the assumption made above that the observed low PL intensities are not caused by a pronounced charge transport from the MAPI into the FTO/ TiO_2 electrode but by non-radiative recombination. However, since no C_{60} interlayer was used for the PL samples a quenching of the PL intensity via recombination at interface defects needs to be considered in addition to the non-radiative recombination in the MAPI layers. In summary, the cause of the low PCEs of the fabricated solar cells is probably a hindered charge carrier extraction caused by a thin PbI_2 layer between the TiO_2 layer and the MAPI layer in combination with the recombination of photogenerated charge carriers, mainly via defects and possibly enhanced by a reduced charge screening in the orthorhombic perovskite modification.

Interestingly, while the PL measurements indicated a correlation of the PL intensity with the presence of the cubic MAPI modification, the IV measurements show no such dependence. Different reasons can explain this observation. On one hand, the XRD results from the work of Hoyer, shown in figure A.15 in the appendix, indicate a reduction of the amount of the cubic MAPI modification during the heat treatment. Thus it is not certain, that the (heat treated) MAPI layers used for the solar cell fabrication still possess MAPI in its cubic modification. On the other hand, assuming that the cubic modification is still present in the MAPI layers after the heat treatment, the cubic phase would be embedded into the orthorhombic matrix. Hence, the charge carriers would have to travel through the orthorhombic matrix, independent on whether they are generated in the cubic or in the orthorhombic phase fraction. Thus, the assumed higher yield of photoexcited charge carriers in the cubic perovskite modification compared to the orthorhombic perovskite modification would be quenched by the recombination of the photoexcited charge carriers during their travel through the orthorhombic phase.

The best performing solar cells, incorporating a 2step CSS fabricated MAPI layer derived from PbI_2 , were fabricated by M.Sc. C. Hoyer in 2015 and were built without a C_{60} layer. Solar cells incorporating a MAPI layer which was heat treated prior to the spin coating of the Spiro-MeOTAD layer, reached efficiencies up to 4.6 % [164]. But, also without the heat treatment, efficiencies in the range of 4.5 % were occasionally reached [164]. In addition to the solar cells incorporating MAPI layers derived from PbI_2 , solar cells incorporating MAPI layers derived from PbCl_2 were fabricated. All of those solar cells were fabricated without a C_{60} layer between the TiO_2 ETL and the MAPI absorber. Still, a solar cell with an efficiency of 4.2 % could be fabricated and is considered as proof of principle that the 2step CSS approach is suited to fabricate working solar cells from PbI_2 and from PbCl_2 base layers. However, independent on the used lead salt, efficiencies above 3 % could only be achieved rarely and not be intentionally reproduced.

5.4.3 Most important facts

- Solar cells with PCEs larger than 4 % could be fabricated incorporating $\text{MAPI}_{\text{PbI}_2}$ and $\text{MAPI}_{\text{PbCl}_2}$, serving as a proof of principle for the 2step CSS as fabrication route for perovskite solar cell absorbers.
- For most of the fabricated solar cells, the overall PCE is in the range of 2-3 %, independent on the substrate temperature. The reason for this is probably the combination of a thin PbI_2 interface layer between the TiO_2 layer and the MAPI layer with the recombination of photoexcited charge carriers, mainly via defects, in the MAPI layer. The recombination is possibly enhanced due to a reduced screening of charged species, caused by the limited ability of the MA^+ cations to reorientate in the orthorhombic MAPI modification.
- The use of a C_{60} layer between the TiO_2 and the MAPI layer enhances the reproducibility of the solar cells due to interface passivation. The interface passivation avoids the formation of unwanted interface phases like $\text{Pb}(\text{IO}_3)_2$ which would otherwise be detrimental for the solar cell performance.
- A heat treatment of the 2step CSS fabricated MAPI layers increases the efficiency, probably due to a reduction of the defect density
- The relatively large area and the narrow efficiency distribution of the solar cells on one substrate incorporating $\text{MAPI}_{\text{PbI}_2}$, especially for $T_s=90^\circ\text{C}$ and $T_s=130^\circ\text{C}$, indicate the potential of the 2step CSS process to fabricate solar cells with active areas in the cm^2 regime.



6 Summary and Conclusions

In the past chapters, the theoretical background, the experimental procedure and the results obtained during this work were presented. In this chapter, the most important results will be summarized in form of a summary and conclusion.

During the work presented in this thesis, the fabrication of methylammonium lead iodide, under application of a sequential closed space sublimation setup was evaluated. CSS was used as deposition technology because of it providing large area deposition perspectives as proven for CdTe. In addition, CSS is a technique which may be preferential for substituted halide perovskite absorbers e.g. with Sn substituting Pb. The fabricated MAPI layers, as well as the used base materials were examined by means of SEM, XRD, UV/VIS and PL spectroscopy and in vacuo PES. The characterization results were determined in dependence on the substrate temperature during the CSS process step and on the used lead salt, PbI_2 or PbCl_2 . PbCl_2 was used as base layer lead salt in addition to PbI_2 since it is reported to improve the optoelectronic properties of the fabricated perovskite layers and the efficiency of solar cells using these layers [43, 147, 148]. In addition, the use of different lead salts allows to assess to which extent the properties of the fabricated perovskite layers depend on the base material and under which conditions the perovskite properties become independent on the used lead salt. MAPI derived from PbI_2 and MAPI derived from PbCl_2 could be fabricated with high phase purity, independent on the substrate temperature. The MAPI layers derived from PbI_2 and PbCl_2 show very similar properties in XRD, PES, UV/VIS spectroscopy and PL spectroscopy experiments and differ only in their morphology. Besides the characterization of the properties of the finished MAPI layers, the interface between the glass/FTO/ TiO_2 substrate and PbI_2 was examined by an interface experiment. Furthermore, mechanisms for the transformation of PbI_2 and PbCl_2 to MAPI were proposed based on in vacuo PES results obtained during stepwise transformation of the lead salt layers to MAPI. Finally, the fabricated MAPI layers were implemented in solar cells in planar configuration, without a mesoporous TiO_2 scaffold, and their IV characteristics were recorded. The proof of principle for working solar cells, for all examined substrate temperatures and both lead salts could be achieved. Nevertheless, challenges and distinctive features of a MAPI solar cell fabrication route incorporating a CSS step became apparent. From those results, criteria and requirements for the implementation of the closed space sublimation into the production of MAPI layers can be derived. The potential of the 2step closed space sublimation as fabrication process for MAPI layers becomes most apparent considering the wide range of accessible substrate temperatures and the respective broad spectrum of morphologies, which even can be independent on the morphology of the used lead salt. The large observed process temperature window of

the CSS process, up to substrate temperatures of 150 °C, needs to be highlighted since, for the fabrication of MAPI layers, the combination of a high vacuum environment and substrate temperatures above 100 °C is a unique feature of the CSS process. Such substrate temperatures are only possible in an environment with high partial pressures of the MAI sublimation species [42]. A corresponding environment is provided in the CSS crucible. Additionally, the small volume of the CSS crucible, compared to the volume of a vacuum chamber, reduces the amount of MAI required to establish a certain pressure.

It could be shown that the evolution of the MAPI layer morphology can be separated in three processes, the transformation of the lead salt to MAPI by incorporation of MAI into the lead salt layers, a recrystallization of the MAPI grains, which is associated with a change in the shape of the grains, and finally an Ostwald ripening like grain growth process of the recrystallized grains. All three processes take place simultaneously during the transformation of PbI_2 and of PbCl_2 to MAPI. Their process velocity appears to increase with increasing substrate temperature. Since the layer morphologies of PbI_2 and PbCl_2 differ significantly and the morphology of PbCl_2 is more similar to the morphology of recrystallized MAPI, the morphological changes are more pronounced for the transformation of PbI_2 to MAPI than for the transformation of PbCl_2 to MAPI. Concerning their crystal structure, the MAPI layers fabricated with the 2step CSS were found to be dominated by the orthorhombic MAPI modification of the space group *Pnma*, independent on the used lead salt.

The optoelectronic properties of the fabricated MAPI layers, derived from PES, UV/VIS spectroscopy and PL spectroscopy experiments, correspond to literature values. The band gap of the examined MAPI layers is determined to be about 1.58 eV by UV/VIS spectroscopy, in accordance with PL experiments. Thereby, even though the presence of defects in the fabricated MAPI layers is likely to affect the UV/VIS spectra, their influence is superimposed by the influence of the surface roughness of the MAPI layers and by the absorption of the glass/FTO/ TiO_2 substrate. However, the examination of the PL spectra indicates the presence of defects inside the MAPI layers and for the respective non-radiative recombination. An interesting observation concerning the crystal structure and the photoactivity of the fabricated MAPI layers is the appearance and the properties of the cubic perovskite modification in the MAPI layers at low substrate temperatures. The PL measurements indicate that the cubic modification might be more photoactive than the orthorhombic modification, in accordance with the assumption of an enhanced recombination of photogenerated charge carriers in the orthorhombic perovskite modification [101–103].

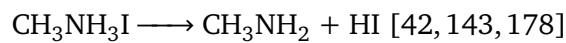
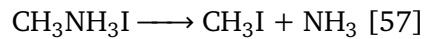
The PE spectra obtained from the MAPI layers are independent on the substrate temperature and are well in accordance with literature values for MAPI prepared with different wet chemical and gas phase techniques. The observation of a shoulder on the C1s emission indicates that a second organic cation is present in the MAPI layers in addition to CH_3NH_3^+ . Since carbon is the only element where the shoulder could be observed, it is assumed that the additional cation only contains carbon. A possible candidate would be

C_2H_6^+ . A respective formation mechanism, based on the assumption of surplus CH_3I in the perovskite layers, is proposed in section 5.2.3. Furthermore, based on stepwise transformation experiments, lead iodide could be identified as intermediate phase between PbCl_2 and MAPI. After the transformation of PbCl_2 to MAPI, neither a Cl emission nor a doping effect due to Cl ions could be determined in PES experiments on $\text{MAPI}_{\text{PbCl}_2}$ layers. In spite of the promising analytical results, the PCE of the fabricated solar cells remained limited to 2 to 3%, with few solar cells exceeding 4%. Thereby, the current density and the fill factor show the most pronounced discrepancy to literature values while V_{oc} is smaller but at least in the range of the values reported for MAPI absorbers fabricated with wet chemical and gas phase techniques, with varying electrode materials. As reason for the efficiency limitation a thin PbI_2 layer between the MAPI absorber and the $\text{FTO}/\text{TiO}_2/\text{C}_{60}$ ETL in combination with defect mediated recombination of photogenerated charge carriers is proposed. Thereby, the orthorhombic crystal structure and the respective reduced charge screening due to the reduced ability of the MA^+ cations to reorientate may increase the recombination of photogenerated charge carriers.

Due to the significant effect of a thin layer of remnant PbI_2 on the electron extraction on one hand and the similar effect a MAI capping layer would have on the hole extraction on the other hand, it has to be avoided that either too few or too much MAI is deposited during the CSS process step. This condition requires a precise control over the amount of MAI used for the transformation of a PbI_2 layer, for example by deposition rate control or by partial pressure control [1]. Such process control would also help to compensate fluctuations in the MAI sublimation behavior. Among other reasons, these fluctuations can be due to morphological changes of the MAI in the CSS crucible, for example a sintering of the MAI powder¹. Unfortunately, with the setup in use, such control mechanisms are not applicable. The amount of MAI is controllable only indirectly via the crucible temperature and the transformation time, making transformations in this closed environment susceptible to the formation of unwanted PbI_2 , and possibly PbCl_2 in case of $\text{MAPI}_{\text{PbCl}_2}$, or MAI layers [1]. An alternative to the precise control over the amount of MAI used during the transformation process step would be an intentional overreaction, resulting in a MAI capping layer, and the consecutive removal of the excess MAI by annealing processes or by rinsing the fabricated layers with isopropanol (see also section 4.2.3). However, keeping the aim of a fully vacuum processed perovskite solar cell in mind, the need of a wet chemical removal of excess MAI is not desirable. The removal of excess MAI via an annealing step under vacuum conditions requires to keep the MAPI layers at high temperatures for several minutes and bears the risk of a degradation of the perovskite layer. In addition, the removal of excess MAI did not lead to a pronounced increase of the solar cell performance in test experiments. Thus, the precise control of the MAI partial pressure remains the best option to fabricate perovskite layers without residual lead salt or surplus MAI with the 2step CSS process.

¹ Occasionally but not always, the observation was made, when the CSS crucible was refilled, that the MAI powder remaining in the CSS crucible was partly or completely sintered together.

Methylammonium lead iodide is one of the most described photoactive perovskites and is therefore well suited as model system for the assessment of fabrication techniques for perovskite thin films [7, 43–45]. Yet, while the need to control the amount of the used material is a general requirement of a 2step CSS process, the application of MAI in the CSS for the transformation of lead salts to MAPI causes some specific difficulties. As discussed in section 5.2.3, it is likely that MAI will decompose during the sublimation in the pressure/temperature regime preferential for the CSS process step [34, 42, 57, 143, 178]. Possible decomposition reactions are:



As discussed in section 5.2.3, the decomposition of MAI into CH_3I and NH_3 is considered as more applicable for the description of the experiments in this work. However, the co-existence of both dissociation product sets in the gas phase, with the respective different transformation mechanisms, has to be considered for the crucible temperatures below 160°C [42]. Due to the different molecular weights of the dissociation products, their potentially different sublimation pressures and sticking coefficients and their different inward diffusion rates, an overproportional loss of the more volatile species is likely to lead to a nonstoichiometric gas phase in the CSS crucible. This nonstoichiometric gas phase might even be an origin of defect states in the fabricated MAPI layers contributing to the defect mediated recombination of photogenerated charge carriers identified in chapter 5.4 as one of the limitations of the performance of the fabricated solar cells. Hence, there is a need to keep the reaction chamber tight. Therefore, an improved CSS setup must be realized which on one hand allows control over the amount of MAI used for the transformation of a lead salt layer to MAPI. On the other hand, the setup must provide a constant chemical activity of the reactants. Alternatively, the problem of the MAI dissociation could be solved by the use of reaction couples which are stable for the needed reaction conditions, e.g. CsI or CsBr , as precursors instead of MAI [1]. With those precursor materials inorganic perovskites like CsPbI_3 or CsPbIsBr could be fabricated. Considering those possible process modifications and the fact that working solar cells with an relatively large active area of $3.25\text{ mm} \times 10\text{ mm}$ and a narrow efficiency distribution (especially in the substrate temperature window between 90°C and 130°C) could be fabricated from PbI_2 and PbCl_2 layers in this work, the potential of the CSS as upscalable fabrication process for perovskite absorber layers is still apparent.

7 Outlook

In the conclusion chapter, the most important results and arguments of this work were presented and the potential and the advantages of the implementation of a closed space sublimation step into a processing route for perovskite absorber layers was pointed out. On the other hand, the challenges observed during this work were discussed. Some of these challenges are related to the CSS process itself while others concern the use of MAI in the CSS. Based on the presented results, possible routes to extend the research concerning the fabrication of MAPI layers, using a closed space sublimation setup will be presented in this outlook chapter.

Firstly, some direct modifications of the presented route for the fabrication of solar cells incorporating MAPI as absorber material will be discussed. In this work, solar cells incorporating the C_{60} passivation layer were only fabricated with $MAPI_{PbI_2}$ as absorber layer. Since the proof of principle of working solar cells could also be achieved for MAPI absorbers derived from $PbCl_2$, those absorbers should be tested in a solar cell stack incorporating C_{60} as well. Furthermore, at the time the wet chemical removal of excess MAI, caused by an intentional overreaction during the CSS process to avoid residual PbI_2 , was evaluated, no C_{60} layer was used between the TiO_2 and the MAPI layer in the fabricated solar cells. Therefore, even though the combination of the slight overreaction in the CSS process with the removal of excess MAI did not improve the solar cell efficiency when this process modification was evaluated, the combination of the C_{60} passivation layer and the intentional overreaction with consecutive MAI removal remains to be tested.

Since a heat treatment is reported to reduce the density of defects in MAPI, a further improvement of the PCE of the solar cells fabricated from 2step CSS MAPI layers could possibly be achieved by an optimization of the heat treatment conditions of the MAPI layers [111, 155, 160, 162, 163]. Furthermore, in case a tightly closed reaction chamber is realized in an improved CSS setup, it would allow to establish a suited atmosphere and pressure for the heat treatment of the 2step CSS MAPI layers. In that case, the heat treatment could be moved from the tube furnace to the reaction chamber, which would constitute a further step towards fully vacuum fabricated perovskite solar cells.

The passivation of the TiO_2 /MAPI interface by a C_{60} layer turned out to be necessary to achieve reproducible solar cell efficiencies. Considering that the C_{60} layer itself will be hole blocking [131], an additional TiO_2 layer appears not to be necessary for working solar cells. This assumption is in accordance with literature, where highly efficient solar cells using all organic ETL have been presented [13, 21, 33]. Thus, the testing of an organic ETL which can be deposited via sublimation under high vacuum conditions would be a step further to the in line fabrication of all vacuum manufactured solar cells. In ad-

dition, if a compact TiO₂ layer is omitted, the spray pyrolysis process, including the high temperature sintering step, can be avoided and a broader substrate range is accessible, including flexible substrates and other solar cells [13, 17, 18, 21]. However, considering the rough morphology of the used FTO substrates, the use of a thin C₆₀ layer without TiO₂ layer might result in strong deviations of the MAPI layer thickness and hence in a spatially inhomogeneous solar cells performance. ITO is smoother compared to FTO and could solve the problem. Nevertheless, PbI₂ forms a dense layer on ITO (see figure A.16 in the appendix), compared to the open, flake like structure on FTO, with low inward diffusion coefficients of the MAI sublimation species during the CSS process step. Hence, all process steps would need to be optimized again if glass/ITO substrates were used. A faster approach for the fabrication of TiO₂ free solar cells could be the use of PbCl₂ instead of PbI₂. PbCl₂ forms dense layers on FTO. Accordingly, the parameters for the transformation of a PbCl₂ layer to a MAPI layer are already adjusted for the transformation of a dense layer, possibly reducing the effort needed for the optimization of the transformation of a PbCl₂ layer on ITO.

No distinct influence of defect states in the MAPI layers on the optical absorption spectra of the MAPI layers fabricated during this work could be determined due the superposition of this influence by the influence of the surface roughness of the MAPI layers and the absorption of the glass/FTO/TiO₂ substrate. UV/VIS measurements on MAPI samples on glass substrates or on fine ground MAPI powder could therefore be suited to evaluate the influence of defect states on the UV/VIS spectra of MAPI more clearly and aid to identify the nature of those defect states.

The dissociative sublimation of MAI combined with the overproportional leakage rate of the smaller molecule out of the CSS crucible and the resulting nonstoichiometric gas phase might lead to defect states in the MAPI layers and hence be problematic for the examined CSS process. TGA results presented by Petrov et al. indicate that formamidinium iodide (FAI) will most likely show a similarly dissociative sublimation as MAI, even in a similar temperature regime [179]. Thus, using FAI in a CSS process step will result in the same problems observed for MAI and is hence not recommended. A similar behavior is assumed for other FA derived materials like FABr. Accordingly, the CSS process step appears to be best suited for the sublimation of inorganic precursor materials which sublime in a stoichiometric manner. Based on that requirement two research directions appear to be promising: The modification of, for example co-evaporated, organic-inorganic hybrid perovskites and the research on fully inorganic perovskites. The partial replacement of the organic cation or the halide ion of an organic-inorganic hybrid perovskite will be favored by the high substrate temperature available during a CSS process and the corresponding increased inward diffusion of the replacing ions into the hybrid perovskite. An example for such a process would be the fabrication of Cs_{0.15}FA_{0.85}Pb(I_{0.3}Br_{0.7})₃ under vacuum conditions, which is reported as wide band gap perovskite ($E_g \approx 2$ eV) tandem partner for MAPI in all perovskite solar cells as well as for silicon solar cells [21, 24]. In the publication of Forgacs et al. all layers of the perovskite/perovskite tandem solar

cell are fabricated by vacuum deposition techniques, only the $\text{Cs}_{0.15}\text{FA}_{0.85}\text{Pb}(\text{I}_{0.3}\text{Br}_{0.7})_3$ perovskite has been solution processed [21]. Also, in the publication by McMeekin, the $\text{Cs}_{0.15}\text{FA}_{0.85}\text{Pb}(\text{I}_{0.3}\text{Br}_{0.7})_3$ layer has been solution processed as tandem partner for a silicon solar cell [24]. Accordingly, to find a route, to fabricate complicated perovskites like $\text{Cs}_{0.15}\text{FA}_{0.85}\text{Pb}(\text{I}_{0.3}\text{Br}_{0.7})_3$ in a CSS process would ease the way towards industrial scale all vacuum processed tandem solar cells incorporating perovskite layers. A possible way for the fabrication of $\text{Cs}_{0.15}\text{FA}_{0.85}\text{Pb}(\text{I}_{0.3}\text{Br}_{0.7})_3$ under high vacuum conditions might be the transformation of FAPbBr_3 , deposited by co-evaporation, by exposure to CsI vapor in a CSS process. However, the applicable substrate temperatures will be limited by the degeneration or re-sublimation of the hybrid perovskite base layer. Hence, whether the substrate temperatures needed for a sufficient inward diffusion can be achieved and whether the stoichiometry of the resulting perovskite can be adjusted with sufficient accuracy remains to be determined with specifically adjusted experiments.

Besides the stoichiometric modification of predeposited hybrid perovskites, the fabrication of fully inorganic perovskites is a second promising field of research where the advantages of the CSS process could be used. In literature, reports of solar cells incorporating several purely inorganic perovskites can be found with PCEs up to 10% [180–183]. Moreover, with a broad range of accessible band gaps, for example 1.73 eV for CsPbI_3 , 1.9 eV for BiOI and 1.92 eV for CsPbI_2Br , inorganic perovskites can also be considered as wide band gap tandem partners [180,181,184]. In addition, the thermal stability of inorganic perovskites is reported to be enhanced compared to MAPI [25]. The stability towards moisture of inorganic perovskites is reported to be good, Li et al. report it to be improved compared to pure MAPI [180,185]. The mechanism of moisture affecting perovskite absorbers is reported to be based on the inward diffusion of water molecules into the perovskite layers and consecutive interactions of the water molecules and the organic perovskite cation, resulting in the outdiffusion and the loss of the organic cation and the respective degradation of the perovskite [25]. The interactions are reported to scale with the polarity of the cation [25]. Accordingly, the symmetrical charge distribution of inorganic cations should yield an improved stability compared to the polar organic cations [25]. On the other hand, the best moisture stability is not shown by purely inorganic perovskites but by FA-Cs mixed cation perovskites [25,182]. Therefore, the stability against moisture of the inorganic perovskites, for example CsPbI_3 and CsPbI_2Br , suffers mostly from the facts that their photoactive modifications are often thermodynamically not stable at room temperature and that the phase transition from their photoactive to their non-photoactive modification appears to be enhanced by moisture [25,182]. Thus, even though the field of fully inorganic perovskites offers several opportunities, also challenges like the stabilization of their photoactive modification under ambient conditions have to be overcome. For this, the CSS allows to perform experiments in a broad temperature window which can enhance the interdiffusion of the involved species and provides a broad window of achievable morphologies. Furthermore, a base salt layer morphology can be used which is favorable for interdiffusion but not for solar cells (porous morphology) with a consecutive

recrystallization during the CSS process to a dense morphology, well suited for solar cells. Finally, also for inorganic perovskites, some of the precursors, like CsBr, are environmentally sensitive. For the use of those materials, the high vacuum setup of the 2step CSS posses the further advantage of an oxygen and water free process environment.

In addition to the “standard” photovoltaic perovskites with a monovalent halide ion, metal chalcogenide perovskites like BaZrS₃, CaZrS₃ or SrTiS₃ begin to shift into the focus of the research community [186]. The chalcogenide perovskites are lead free, are expected to show suitable band gaps for mono-junction solar cells and good environmental stability [186]. However, up to date, they can not be solution processed but have to be fabricated via solid state reactions, requiring high temperatures [186]. Considering those challenges with respect to the fabrication, the CSS, providing the combination of high processing temperatures and a high vacuum environment, appears to be exceptionally suited as fabrication techniques for these emerging purely inorganic metal chalcogenide perovskite solar cell absorber materials.

A requirement, which appears to be crucial for every two step CSS process is that the amount of material used for the transformation reaction can be defined. This requirement can be fulfilled either by a self limiting process or by a strictly reproducible dependence between crucible temperature, deposition time and the amount of material implemented into the base layer. If those conditions are not given, as for the examined sublimation of MAI in the CSS, a mechanism to control the amount of material used during the transformation is needed. The technical implementation of such a control mechanism is not trivial. One possibility would be to combine the shutter with a quartz crystal deposition rate control. With calibration measurements, tooling and z-factors can be determined, relating the integral thickness deposited on the quartz crystal with the material amount implemented into the base layers. A sufficient control of the deposition rate via a quartz crystal is not possible for the sublimation of MAI [42]. However, for lead salts the rate control is quite reproducible. Hence, it might well be suited for a closed space sublimation of inorganic materials. Thereby, it appears to be more practical to use the transformation time as control parameter than the crucible temperature. Although, the power of the heating lamps can be adjusted quite fast, the crucible temperature will need some time to adjust and the crucible pressure to equilibrate. On the other hand, it is possible to automatize the shutter to close, when a certain amount of material is deposited during a CSS process. If needed, further in vacuo annealing steps can be applied to ensure a complete transformation. A similar control mechanism for the deposition time would be possible based on the measurement of the crucible pressure. Here, a constant pressure for a defined transformation time should correlate with a certain amount of material deposited or implemented into the base layer. However, since the deposition rate is significantly easier to measure compared to the exact pressure in the crucible, the deposition control using a quartz crystal appears to be the most promising one.

When discussing approaches for future research on perovskite thin films using CSS, the one step CSS should not be excluded. For the fabrication of MAPI a one step approach is not very promising considering the strong difference in the sublimation temperatures comparing lead salts and MAI. As a guide to assess the sublimation temperatures under high vacuum conditions, the boiling points at ambient pressure of the most relevant materials are given in table 7.1. Of course, since the boiling points are determined for ambient pressure and not for high vacuum they can only serve as a qualitative measure to compare the different materials. In addition, MAI, PbI_2 and PbCl_2 were found to sublime under high vacuum in this work and not to evaporate. A similar behavior is expected for the other materials in table 7.1.

Table 7.1.: Boiling temperatures T_b of selected inorganic compounds in °C at ambient pressure, taken from [142]. PbI_2 is reported to decompose during the evaporation, denoted by (dec). The approximate temperature in °C of the begin of the mass loss during TGA experiments on MAI at ambient pressure are given as comparison and are taken from [57]. Since MAI is also subliming dissociatively, it is also denoted with dec.

compound	$T_b / ^\circ\text{C}$
MAI	≈ 230 (dec)
PbI_2	872 (dec)
PbBr_2	892
PbCl_2	951
CsI	1280
CsCl	1297
CsBr	≈ 1300

The cesium containing compounds, CsI, CsCl and CsBr, have significantly higher sublimation temperatures compared to the lead salts PbI_2 , PbCl_2 and PbBr_2 . Thus, it is again not certain if a one step CSS would be applicable. However, the differences in the sublimation temperatures could possibly be compensated by the stoichiometry of the precursor material for the one step CSS.

In summary, the implementation of a closed space sublimation step into the fabrication route of perovskite absorber layers for solar cells is not at its end but at its beginning. For precursor materials which sublime dissociatively, especially organic precursors, the CSS is not suited. However, in the emerging fields of mixed cation, mixed halide perovskites and, even more, purely inorganic perovskites, the prospects are promising for further research projects, explicitly benefiting from the combination of the broad temperature processing window of the CSS and the high vacuum environment.



8 Acknowledgments

Das Schreiben einer Doktorarbeit ist ein Langzeitprojekt. Am Ende einer Thesis hat man sich nicht nur fachlich weiterentwickelt, sondern auch persönlich. Auf meinem Weg durch die Promotion habe ich viele Menschen getroffen, die mich unterstützt haben, mit denen ich gelacht und mit denen ich schöne Erinnerungen gesammelt habe. Diesen Menschen möchte ich im Folgenden danken.

Zuerst möchte ich Herrn Prof. Dr. Jägermann für die Möglichkeit zur Anfertigung meiner Promotion, für die Betreuung, die Diskussionen und die Ratschläge während meiner Zeit als Doktorand und das Korrekturlesen meiner Arbeit danken.

Da meine Promotion im Rahmen des BMBF Projektes Perosol (03SF0483A) stattfand, möchte ich auch dem Bundesministerium für Bildung und Forschung für die Finanzierung meiner Forschungsarbeit danken.

Meinem Gruppenleiter Dr. Thomas Mayer möchte ich für die Betreuung während der Promotion, die wissenschaftlichen und die lunchtime Diskussionen sowie für das Korrekturlesen meiner Dissertation danken.

Prof. Dr. Oliver Clemens danke ich dafür dass er das Zweitgutachten meiner Dissertation übernommen hat. Außerdem danke ich ihm für die Rietveldverfeinerungen sowie für seinen Rat und seine Unterstützung beim Auswerten der XRD Daten und bei der Erstellung meiner Publikation.

Prof. Dr. Ensinger und Prof. Dr. Hess danke ich dafür, dass sie sich als Prüfer für meine Disputation zur Verfügung gestellt haben.

Meinen Master- bzw. Bachelorstudenten Christian Hoyer und Serge Christian Enyegue Ondobo danke ich für die gemeinsame Zeit und die von ihnen geleistete Arbeit, welche zur Erweiterung unseres Wissens um die Herstellung und die Modifikation der CSS-Perowskitschichten beigetragen hat.

Kerstin Lakus-Wollny danke ich für die REM Aufnahmen, die gemeinsame Arbeit im DAISY-SOL und Antworten auf tausend Fragen.

Furthermore, I would like to thank Dr. Christoph Loho, Dr. Alexander Beneš, M.Sc. Kerstin Wissel, and M.Sc. Mohammad Ali Nowroozi for the XRD measurements and Dr. Chittaranjan Das for the deposition of the C₆₀ layers used for the solar cell fabrication.

Auch möchte ich der Feinmechanikwerkstatt des Fachbereichs Materialwissenschaft und Michael Weber für die schnelle und unkomplizierte Unterstützung beim Bauen und Reparieren unseres Laborequipments danken.

Another thanks goes to the surface science group for the support, the interesting discussions, the seminar travels to La Clusaz, and for the fun moments we had together.

A special thanks is due to the perovskite group guys for the collaboration, our discussions and for learning from and helping each other. Since the Perosol project started in 2014, I think we did a pretty good job. In particular, I want to thank M.Sc. Michael Wußler for the projects we worked on together, for our office discussions and for occasional joint *“rage against the machine”*: shared XPS trouble is half XPS trouble.

In addition to work, the fun should not be forgotten. Hence, I also want to thank the perovskite group guys for the joint conference travels and the evening group building events.

In nunmehr knapp über 10 Jahren in Darmstadt habe ich hier einige gute Freunde gefunden, deren Bekanntschaft ich nicht missen und bei denen ich mich hier für gemeinsame Zeit bedanken möchte: Christian, Christoph, Hans, Renè, Sandra, Laszlo, Silke, Tanju, Judith, die Rugby Abteilung der TG 1875 Darmstadt und alle die ich hier vielleicht vergessen habe, deren Bekanntschaft und Freundschaft ich jedoch nicht minder schätze.

Mein besonderer Dank gilt meinen Eltern, Bernhard und Beate Dachauer, meiner Familie und meinen Schul- und Jugendfreunden, die mir nicht nur während der Promotion sondern auch auf dem Weg dahin immer den Rücken gestärkt haben.

9 List of Figures

3.1. Schematic depiction of the band edge region of a metal, a semiconductor and an insulator.	18
3.2. Schematic depiction of the electron affinity χ , the work function ϕ , the ionization potential I_p , the band gap E_g and the Fermi level E_F of a semiconductor (a). Fermi-Dirac distribution for $T=0\text{ K}$ and $T>0\text{ K}$ (b).	19
3.3. Schematic illustration of a thin film solar cell consisting of a transparent front contact an electron transport layer, an absorber, a hole transport layer and a metallic back contact.	20
3.4. Schematic depiction of the charge density (a), the electric field (b), the potential distribution (c) and the band energy diagram (d) of an abrupt p/n-homo junction.	22
3.5. Schematic depiction of the band energy diagram and the charge carrier densities for a p/n-homo junction under forward (left) and reverse bias (right).	23
3.6. Schematic IV characteristic of an ideal p/n-diode in linear (a) and semilogarithmic scale (b)	24
3.7. Schematic IV characteristic of a real p/n-diode in semilogarithmic scale.	25
3.8. Schematic drawing of an anisotype p/n-junction before (a) and after (b) the thermal equilibrium is established.	26
3.9. Schematic drawing of an isotype n/n-junction before (a) and after (b) the thermal equilibrium is established.	27
3.10. Schematic layer stack of the solar solar cells used in this work (a) and equivalent circuits for a solar cell in the dark (b) and (c).	29
3.11. Equivalent circuits for a solar cell in the dark (a) and operated under illumination (b).	30
3.12. Equivalent circuits for a solar cell operated under short circuit (left) and open circuit (right) conditions.	31
3.13. Schematic IV curve of a solar cell in linear and semilogarithmic scale.	32
3.14. Solar spectrum just outside the earth's atmosphere (AM0) and at the surface for an angle of incidence around 48° (AM1.5).	33
3.15. Theoretical maximum efficiency of a single junction solar cell in dependence on the absorber band gap according to the Shockley-Queisser limit under AM1.5G illumination.	34
3.16. Schematic illustration of the potential energy E_{pot} in dependence on the distance z from the samples surface for physisorption a), non-dissociative chemisorption b) and dissociative chemisorption c).	36
3.17. Schematic arrangement of a PES measurement setup.	41
3.18. (a) Schematic representation of the X-ray diffraction on parallel lattice planes according to Bragg's law. (b) Schematic representation of a Bragg-Brentano setup.	45
3.19. Schematic depiction of a scanning electron microscope (a), the excitation volumina of the different excited species (b) and a magnified depiction of the tilted sample position used for the cross section experiments (c).	48

3.20. Schematic depiction of the setup used for the UV/VIS measurements in this work.	49
3.21. Schematic depiction of the setup used for the PL measurements in this work.	51
4.1. Flowchart of the sample preparation and characterization in this work. . . .	53
4.2. Schematic depiction of the used substrates: as purchased, after the FTO etching and after the TiO ₂ spray pyrolysis.	54
4.3. Schematic depiction of the spray pyrolysis setup used for the deposition of the compact TiO ₂ layers in this work (left). Layout of the substrate arrangement during the spray pyrolysis (right).	55
4.4. Schematic sketch of the DAISY-SOL.	57
4.5. Photograph of the different parts of a sample holder used for the vacuum deposition steps in the DAISY-SOL (a). A mounted sample holder with a sample is shown in (b).	57
4.6. Schematic depiction of the PVD chamber used to deposit PbI ₂ and PbCl ₂ layers.	58
4.7. Schematic illustration of the CSS chamber used for the transformation of PbCl ₂ or PbI ₂ to MAPI by exposure to MAI vapor.	60
4.8. Schematic cut (left top), top view (left bottom) and a typical photograph (right) of the used solar cell structure.	62
4.9. Exemplarily depiction of the background correction according to a Shirley function used in this work.	65
4.10. Graphical determination of the Fermi level, the valence band maximum energy position and the work function.	66
5.1. SEM images in SE contrast of a glass/FTO/TiO ₂ substrate in top view (left) and tilted 75° with respect to the horizontal (right).	71
5.2. Survey XP spectra of 30-50 nm TiO ₂ on a glass/FTO substrate measured with XPS, “as is” (bottom) and after an oxygen plasma treatment (top). . .	72
5.3. O1s and Ti2p core line XP spectra of 30-50 nm TiO ₂ on a glass/FTO substrate measured with XPS, “as is” (bottom) and after an oxygen plasma treatment (top).	73
5.4. Valence band spectra measured with XPS (a) and UP spectra (b) of 30-50 nm TiO ₂ on a glass/FTO substrate, “as is” (bottom) and after an oxygen plasma treatment (top).	74
5.5. Anderson alignment of MAPI and TiO ₂ “as is” (a) and after an oxygen plasma treatment (b).	76
5.6. Comparison of the valence band spectra of the plasma treated sample from figure 5.4 (bottom) and a similar fabricated plasma treated sample (top). .	77
5.7. XRD patterns of MAPI fabricated from PbCl ₂ layers on glass/FTO/TiO ₂ substrates with close (left) and closed (right) space sublimation.	80
5.8. Optimization of the crucible temperature T_c for defined substrate temperatures T_s during the CSS step of the fabrication of MAPI layers from PbI ₂ and PbCl ₂	81
5.9. Optimization of the transformation times for the best T_c/T_s pairs found in figure 5.8 (same samples in both graphs).	82
5.10. Degradation of a MAPI layer due to electron beam irradiation (before zooming (a), zoomed image (b) and after the zooming (c)).	85
5.11. Sample holder used to evaluate the influence of light on the PES experiments of a MAPI layer on a glass/FTO/c-TiO ₂ /m-TiO ₂ substrate.	86

5.12. XP spectra of a wet chemically prepared MAPI layer on a glass/FTO/c-TiO ₂ /m-TiO ₂ substrate under different illumination intensities.	87
5.13. SEM images in SE contrast of a PbI ₂ layer deposited by PVD on a glass/FTO/TiO ₂ substrate in top view (left) and tilted 75° with respect to the horizontal (right).	89
5.14. SEM images in SE contrast of MAPI layers fabricated at a T _s of 75 °C (t _t = 120 min), 90 °C (t _t = 80 min), 130 °C (t _t = 20 min, t _a = 20 min) and 150 °C (t _t = 18 min, t _a = 12 min) during the CSS process from PVD deposited PbI ₂ layers on glass/FTO/TiO ₂ substrates in top view (left) and cross section (tilted 75°) (right). (© 2019 WILEY-VCH Verlag GmbH & Co. KGaA, Weinheim, used with permission)	91
5.15. XRD patterns of MAPI layers fabricated from PbI ₂ on glass/FTO/TiO ₂ substrates at substrate temperatures of 75 °C, 90 °C, 130 °C and 150 °C during the CSS process.	92
5.16. XRD pattern and Rietveld refinement of a PbI ₂ layer deposited by PVD on a glass/FTO/TiO ₂ substrate.	93
5.17. Illustration of the crystal structure of PVD fabricated PbI ₂	94
5.18. XRD patterns and Rietveld refinements of MAPI layers fabricated from PVD deposited PbI ₂ on glass/FTO/TiO ₂ substrates at substrate temperatures of 75 °C (a) and 130 °C (b) during the CSS process.	95
5.19. Detailed XRD pattern of a MAPI layer fabricated from PbI ₂ on a glass/FTO/TiO ₂ substrate at T _s = 130 °C during the CSS process with Rietveld refinements for cubic and orthorhombic perovskite crystal structures (a). Detailed XRD patterns of MAPI layers fabricated at substrate temperatures of 75 °C, 90 °C, 130 °C and 150 °C during the CSS process (b).	95
5.20. Illustration of the crystal structure of MAPI.	97
5.21. Absorption coefficient α _{hv} of PbI ₂ and MAPI fabricated from PbI ₂ plotted against the photon energy E _{ph}	98
5.22. Survey spectra of MAPI (red), PbI ₂ (dark blue) and MAI (green) measured with XPS.	100
5.23. Valence band (XPS and UPS) and survey UP spectra of MAPI (red), PbI ₂ (dark blue) and MAI (green).	102
5.24. Band energy diagrams of PbI ₂ , MAPI and MAI derived from the PES data presented in table 5.5 and UV/VIS data from figure 5.21.	104
5.25. Schematic depiction of the band bending at PbI ₂ /MAPI junction in the dark.	105
5.26. I3d and Pb4f detail spectra of MAPI (red), PbI ₂ (dark blue) and MAI (green) measured with XPS.	106
5.27. N1s and C1s detail spectra of MAPI (red) and MAI (green) measured with XPS.	106
5.28. XP survey spectra measured on the bare glass/FTO/TiO ₂ substrate and between consecutive PbI ₂ depositions.	110
5.29. Sn3d XP detail spectra measured on the bare glass/FTO/TiO ₂ substrate and between consecutive PbI ₂ depositions.	111
5.30. I3d and Pb4f XP detail spectra for the bare glass/FTO/TiO ₂ substrate and after cumulative PbI ₂ deposition times of 1 s, 5 s and 15 s.	112
5.31. Ti2p and Pb4f XP detail spectra measured on the bare glass/FTO/TiO ₂ substrate and between consecutive PbI ₂ depositions.	113
5.32. (a) Shift of the valence band maximum positions of Ti, O, I and Pb with cumulative PbI ₂ deposition time. b) Shift of the Pb4f ^{7/2} (red) and Ti2p ^{3/2} (blue) core lines with respect to their position after a PbI ₂ deposition time of 3060 s for Pb4f ^{7/2} and 360 s for Ti2p ^{3/2}	114

5.33. Schematic band energy diagram of the TiO ₂ /PbI ₂ interface.	116
5.34. Survey spectra of MAPI fabricated from PbCl ₂ (red), MAPI fabricated from PbI ₂ (red) and PbCl ₂ (turquoise) measured with XPS.	118
5.35. XP detail spectra of the I3d and Cl2p emissions of MAPI fabricated from PbCl ₂ (red), MAPI fabricated from PbI ₂ (red) and of PbCl ₂ (turquoise).	119
5.36. XP detail spectra of the Pb4f emissions of MAPI fabricated from PbCl ₂ (red), MAPI fabricated from PbI ₂ (red) and of PbCl ₂ (turquoise).	119
5.37. XP detail spectra of the N1s and C1s emissions of MAPI fabricated from PbCl ₂ (red), MAPI fabricated from PbI ₂ (red) and of PbCl ₂ (turquoise).	120
5.38. Valence band spectra measured with XPS of MAPI fabricated from PbCl ₂ (red), MAPI fabricated from PbI ₂ (red) and of PbCl ₂ (turquoise).	121
5.39. Comparison of the absorption coefficients $\alpha_{h\nu}$ (offset 50000 cm ⁻¹) (left) and the directed reflection $R_{h\nu}$ and the transmission $T_{h\nu}$ (right) of MAPI fabricated from PbCl ₂ (red) and from PbI ₂ (dark blue) at a T_s of 90 °C during the CSS process step on glass/FTO/TiO ₂ substrates.	121
5.40. Absorption coefficient $\alpha_{h\nu}$ plotted against the photon energy for PbCl ₂ and MAPI fabricated from PbCl ₂ at CSS substrate temperatures of 75 °C, 90 °C, 130 °C and 150 °C on glass/FTO/TiO ₂ substrates.	122
5.41. Band energy diagrams of PbCl ₂ and MAPI _{PbCl2} derived from the PES data presented in figure 5.38 and table 5.7 and the UV/VIS data presented in figure 5.40.	123
5.42. SEM images in SE contrast of an about 110 nm thick PbCl ₂ layer deposited by PVD onto a glass/FTO/TiO ₂ substrate. Top view (left) and cross section (tilted 75°) (right).	124
5.43. SEM images in SE contrast of MAPI layers fabricated from PbCl ₂ on glass/FTO/TiO ₂ substrates at substrate temperatures of 75 °C, 90 °C, 130 °C and 150 °C during the CSS process. Top view (left) and cross section (tilted 75°) (right).	125
5.44. XRD patterns of MAPI layers fabricated from PbCl ₂ on glass/FTO/TiO ₂ substrates at substrate temperatures of 75 °C, 90 °C, 130 °C and 150 °C during the CSS process.	127
5.45. a) Detailed XRD patterns of MAPI layers fabricated from PbCl ₂ on glass/FTO/TiO ₂ substrates at substrate temperatures of 90 °C and 150 °C during the CSS process. b) Detailed XRD pattern and Rietveld refinement of a MAPI layer fabricated from PbCl ₂ at a substrate temperature of 150 °C during the CSS process.	128
5.46. Visualization of the crystal structures of PVD fabricated PbCl ₂ (a) PbI ₂ (b).	128
5.47. Temperature profile of the stepwise transformation of PbCl ₂ to MAPI using the CSS.	130
5.48. XP survey spectra measured on a freshly prepared PbCl ₂ layer and during the stepwise transformation of the PbCl ₂ layer to MAPI.	131
5.49. XP detail spectra of the I3d and Cl2p emissions measured on a freshly prepared PbCl ₂ layer and during the stepwise transformation of the PbCl ₂ layer to MAPI.	132
5.50. XP detail spectra of the N1s and C1s emissions measured on a freshly prepared PbCl ₂ layer and during the stepwise transformation of the PbCl ₂ layer to MAPI.	132

5.51. XP detail spectra of the Pb4f emissions measured on a freshly prepared PbCl ₂ layer and during the stepwise transformation of the PbCl ₂ layer to MAPI. Both Pb4f emissions (left) and higher magnification on Pb4f ^{7/2} emission (right).	134
5.52. Valence band spectra measured with XPS (a) and UPS (b) on a freshly prepared PbCl ₂ layer and during the stepwise transformation of the PbCl ₂ layer to MAPI.	136
5.53. Fitted valence band spectra measured with XPS on a freshly prepared PbCl ₂ layer and during the stepwise transformation of the PbCl ₂ layer to MAPI.	137
5.54. Superposition of the Pb4f ^{7/2} emissions measured on a freshly prepared PbCl ₂ layer and during the stepwise transformation of the PbCl ₂ layer to MAPI.	138
5.55. X-ray diffraction pattern measured after the stepwise transformation of a PbCl ₂ layer to MAPI (cumulative transformation time 5400 s).	140
5.56. Comparison of the PL spectra of MAPI layers fabricated from PbI ₂ on glass/FTO/TiO ₂ substrates by 2step CSS and by co-evaporation.	143
5.57. Photoluminescence spectra of MAPI _{PbI₂} samples, (a) and (c), and MAPI _{PbCl₂} samples, (b) and (d), prepared on glass/FTO/TiO ₂ substrates at substrate temperatures of 75 °C, 90 °C, 130 °C and 150 °C during the CSS process.	144
5.58. Open circuit voltages (V_{oc}), short circuit current densities (J_{sc}), fill factors (FF) and efficiencies (η) of solar cells fabricated at $T_s=90^\circ\text{C}$ during the CSS process. Shown are solar cells without a C ₆₀ layer and without a heat treatment, with a C ₆₀ layer between TiO ₂ and MAPI but without heat treatment and with a C ₆₀ layer and a heat treatment in air at 100 °C for 30 min.	148
5.59. Open circuit voltages (V_{oc}), short circuit current densities (J_{sc}), fill factors (FF) and efficiencies (η) of solar cells fabricated at substrate temperatures of 75 °C, 90 °C, 130 °C and 150 °C during the CSS process.	149
5.60. IV characteristics in linear (a) and semilogarithmic (b) scale of a planar solar cell fabricated at a substrate temperature of 130 °C during the CSS process with a C ₆₀ layer between the TiO ₂ and the MAPI layer and a heat treatment in air for 30 min at 100 °C.	150
5.61. Comparison of the shape of the dark IV curve and the curve of the time stabilized values (V_{oc} , J_{sc} , MPP) of a solar cell incorporating MAPI fabricated at $T_s=130^\circ\text{C}$ during the CSS process step. The solar cell possesses a C ₆₀ layer between the TiO ₂ and the MAPI layer and was heat treated in air for 30 min at 100 °C.	151
A.1. Calibration curve for the substrate temperature of the PVD chamber.	193
A.2. Calibration curve for the substrate temperature of the CSS chamber.	193
A.3. SEM image in SE contrast (top view) of a MAI layer deposited onto a glass/FTO/TiO ₂ substrate by CSS.	194
A.4. Detailed XRD patterns of MAPI layers fabricated from PbI ₂ on glass/FTO/TiO ₂ substrates at substrate temperatures of 75 °C, 90 °C, 150 °C during the CSS process with Rietveld refinements for cubic and orthorhombic perovskite crystal structures.	194
A.5. XP spectra of MAPI fabricated from PbI ₂ on glass/FTO/TiO ₂ substrates at substrate temperatures of 75 °C, 90 °C, 130 °C and 150 °C during the CSS process.	195

A.6. XP spectra of MAPI fabricated from PbI_2 on glass/FTO/ TiO_2 substrates at substrate temperatures of 75 °C, 90 °C, 130 °C and 150 °C during the CSS process.	196
A.7. XP detail spectra of N1s and C1s emissions of a freshly prepared PbI_2 layer and during the stepwise transformation of the PbI_2 layer to MAPI.	196
A.8. XP spectra measured during the stepwise deposition of PbI_2 on top of a glass/FTO/ TiO_2 substrate.	197
A.9. XP spectra of MAPI fabricated from PbCl_2 on glass/FTO/ TiO_2 substrates at substrate temperatures of 75 °C, 90 °C, 130 °C and 150 °C during the CSS process.	198
A.10. XP and UP spectra of MAPI fabricated from PbCl_2 on glass/FTO/ TiO_2 substrates at substrate temperatures of 75 °C, 90 °C, 130 °C and 150 °C during the CSS process.	199
A.11. Valence band and survey UP spectra of MAPI fabricated from PbCl_2 (red), MAPI fabricated from PbI_2 (red) and of PbCl_2 (turquoise).	200
A.12. UPS spectra measured on a freshly prepared PbCl_2 layer and during the stepwise transformation of the PbCl_2 layer to MAPI.	200
A.13. SEM images in SE contrast taken after the stepwise transformation of a PbCl_2 layer to MAPI (cumulative transformation time 5400 s). Top view (left) and cross section (tilted 75°) (right).	200
A.14. SEM images in SE contrast of MAPI layers fabricated from PbI_2 on glass/FTO/ TiO_2 substrates without (left) and with (right) a heat treatment at 120 °C for 30 min in air.	201
A.15. XRD patterns of MAPI layers fabricated from PbI_2 on glass/FTO/ TiO_2 substrates without and with a heat treatment at 120 °C for 30 min in air.	201
A.16. SEM images in SE contrast of a PbI_2 layer deposited by PVD on a glass/ITO/ TiO_2 substrate. Top view (left) and cross section (tilted 75°) (right).	202

10 List of Tables

5.1. Core line and valence band maximum positions, work functions ϕ and electron affinities χ of several glass/FTO/TiO ₂ substrates measured “as is” and after an oxygen plasma treatment.	73
5.2. Distances in eV between the core lines and the valence band maximum (all measured with XPS) of several glass/FTO/TiO ₂ substrates measured “as is” and after an oxygen plasma treatment.	78
5.3. Transformation parameters and Pb-salt layer thicknesses (calculated from the deposition rates) for all samples used in the optimization experiments presented in figures 5.8 and 5.9.	83
5.4. Unit cell dimensions of MAPI fabricated from PbI ₂ on glass/FTO/TiO ₂ substrates at substrate temperatures during the CSS process of 75 °C, 90 °C, 130 °C and 150 °C.	97
5.5. Core level positions, valence band maximum positions and work functions for PbI ₂ , MAI and MAPI fabricated from PbI ₂ at T_s of 75 °C, 90 °C, 130 °C and 150 °C during the CSS process.	101
5.6. Element ratios at the sample surface of MAPI derived from PbI ₂ , of PbI ₂ and of MAI samples obtained from XPS measurements with Scofield ionization cross sections.	101
5.7. Core emission line binding energy positions, valence band maximum positions and work functions of MAPI fabricated from PbCl ₂ , MAPI fabricated from PbI ₂ ($T_s=90$ °C) and of PbCl ₂	118
5.8. Element ratios at the sample surface of MAPI derived from PbCl ₂ , of MAPI derived from PbI ₂ ($T_s=90$ °C) and of PbCl ₂ samples obtained from XPS measurements with Scofield ionization cross sections.	118
5.9. Unit cell dimensions of MAPI fabricated from PbCl ₂ on glass/FTO/TiO ₂ substrates at substrate temperatures during the CSS process of 75 °C, 90 °C, 130 °C and 150 °C.	129
5.10. Core emission line binding energy positions, valence band maximum positions and work functions measured on a freshly prepared PbCl ₂ layer and during the stepwise transformation of the PbCl ₂ layer to MAPI.	135
7.1. Boiling temperatures T_b of selected compounds in °C at ambient pressure. .	165



Bibliography

- [1] R. Dachauer, O. Clemens, K. Lakus-Wollny, T. Mayer, and W. Jaegermann, "Characterization of Methylammonium Lead Iodide Thin Films Fabricated by Exposure of Lead Iodide Layers to Methylammonium Iodide Vapor in a Closed Crucible Transformation Process," *physica status solidi (a)*, vol. 216, no. 11, p. 1800894, 2019.
- [2] "Hauptaussagen. In: 1,5 °C globale Erwärmung. Ein IPCC-Sonderbericht über die Folgen einer globalen Erwärmung um 1,5 °C gegenüber vorindustriellem Niveau und die damit verbundenen globalen Treibhausgasemissionspfade im Zusammenhang mit einer Stärkung der weltweiten Reaktion auf die Bedrohung durch den Klimawandel, nachhaltiger Entwicklung und Anstrengungen zur Beseitigung von Armut. Deutsche Übersetzung auf Basis der Version vom 8.10.2018 und unter Berücksichtigung von Korrekturmeldungen des IPCC bis zum 14.11.2018.," 2018.
- [3] G. der Arbeitsgruppe Erneuerbare Energien-Statistik (AGEE-Stat) am Umweltbundesamt Fachgebiet 2.5 Zentrum für Sonnenenergie- und Wasserstoff-Forschung Baden-Württemberg (ZSW), "Erneuerbare Energien in Deutschland Daten zur Entwicklung im Jahr 2017," 2018.
- [4] B. Burger and et al., "Fraunhofer ISE: Photovoltaics Report, updated: 27 August 2018 ," 2018.
- [5] J. Fritsche, A. Klein, and W. Jaegermann, "Thin Film Solar Cells: Materials Science at Interfaces," *Advanced Engineering Materials*, vol. 7, no. 10, pp. 914–920, 2005.
- [6] D. B. Mitzi, "Synthesis, Structure, and Properties of Organic-Inorganic Perovskites and Related Materials," *Progress in Inorganic Chemistry*, vol. 48, pp. 1–121, 1999.
- [7] A. Kojima, K. Teshima, Y. Shirai, and T. Miyasaka, "Organometal Halide Perovskites as Visible-Light Sensitizers for Photovoltaic Cells," *Journal of the American Chemical Society*, vol. 131, no. 17, pp. 6050–6051, 2009.
- [8] I. Mesquita, L. Andrade, and A. Mendes, "Perovskite solar cells: Materials, configurations and stability," *Renewable and Sustainable Energy Reviews*, vol. 82, no. September 2017, pp. 2471–2489, 2018.
- [9] H. S. Jung and N.-G. Park, "Perovskite Solar Cells: From Materials to Devices," *Small*, vol. 11, no. 1, pp. 10–25, 2015.
- [10] P. Docampo, S. Guldin, T. Leijtens, N. K. Noel, U. Steiner, and H. J. Snaith, "Lessons Learned: From Dye-Sensitized Solar Cells to All-Solid-State Hybrid Devices," *Advanced Materials*, vol. 26, no. 24, pp. 4013–4030, 2014.
- [11] W. S. Yang, B.-W. Park, E. H. Jung, N. J. Jeon, Y. C. Kim, D. U. Lee, S. S. Shin, J. Seo, E. K. Kim, J. H. Noh, and S. I. Seok, "Iodide management in formamidinium-lead-halide-based perovskite layers for efficient solar cells," *Science*, vol. 356, no. 6345, pp. 1376–1379, 2017.

-
- [12] J.-P. Correa-Baena, M. Saliba, T. Buonassisi, M. Grätzel, A. Abate, W. Tress, and A. Hagfeldt, "Promises and challenges of perovskite solar cells," *Science*, vol. 358, no. 6364, pp. 739–744, 2017.
- [13] C. Momblona, L. Gil-Escrig, E. Bandiello, E. M. Hutter, M. Sessolo, K. Lederer, J. Blochwitz-Nimoth, and H. J. Bolink, "Efficient vacuum deposited p-i-n and n-i-p perovskite solar cells employing doped charge transport layers," *Energy & Environmental Science*, vol. 9, no. 11, pp. 3456–3463, 2016.
- [14] M. A. Green, Y. Hishikawa, E. D. Dunlop, D. H. Levi, J. Hohl-Ebinger, and A. W. Ho-Baillie, "Solar cell efficiency tables (version 52)," *Progress in Photovoltaics: Research and Applications*, vol. 26, no. 7, pp. 427–436, 2018.
- [15] W. S. Yang, J. H. Noh, N. J. Jeon, Y. C. Kim, S. Ryu, J. Seo, and S. I. Seok, "High-performance photovoltaic perovskite layers fabricated through intramolecular exchange," *Science*, vol. 348, no. 6240, pp. 1234–1237, 2015.
- [16] Y. Li, K. R. Scheel, R. G. Clevenger, W. Shou, H. Pan, K. V. Kilway, and Z. Peng, "Highly Efficient and Stable Perovskite Solar Cells Using a Dopant-Free Inexpensive Small Molecule as the Hole-Transporting Material," *Advanced Energy Materials*, vol. 8, no. 23, p. 1801248, 2018.
- [17] Q. Luo, H. Ma, Q. Hou, Y. Li, J. Ren, X. Dai, Z. Yao, Y. Zhou, L. Xiang, H. Du, H. He, N. Wang, K. Jiang, H. Lin, H. Zhang, and Z. Guo, "All-Carbon-Electrode-Based Endurable Flexible Perovskite Solar Cells," *Advanced Functional Materials*, vol. 28, no. 11, p. 1706777, 2018.
- [18] J. You, Z. Hong, Y. M. Yang, Q. Chen, M. Cai, T.-B. Song, C.-C. Chen, S. Lu, Y. Liu, H. Zhou, and Y. Yang, "Low-Temperature Solution-Processed Perovskite Solar Cells with High Efficiency and Flexibility," *ACS Nano*, vol. 8, no. 2, pp. 1674–1680, 2014.
- [19] N. K. Kumawat, M. N. Tripathi, U. Waghmare, and D. Kabra, "Structural, Optical, and Electronic Properties of Wide Bandgap Perovskites: Experimental and Theoretical Investigations," *The Journal of Physical Chemistry A*, vol. 120, no. 22, pp. 3917–3923, 2016.
- [20] L. Dimesso, M. Wussler, T. Mayer, E. Mankel, and W. Jaegermann, "Inorganic alkali lead iodide semiconducting APbI₃ (A=Li, Na, K, Cs) and NH₄PbI₃ films prepared from solution: Structure, morphology, and electronic structure," *AIMS Materials Science*, vol. 3, no. 3, pp. 737–755, 2016.
- [21] D. Forgács, L. Gil-Escrig, D. Pérez-Del-Rey, C. Momblona, J. Werner, B. Niesen, C. Ballif, M. Sessolo, and H. J. Bolink, "Efficient Monolithic Perovskite/Perovskite Tandem Solar Cells," *Advanced Energy Materials*, vol. 7, no. 8, p. 1602121, 2017.
- [22] J.-W. Xiao, L. Liu, D. Zhang, N. De Marco, J.-W. Lee, O. Lin, Q. Chen, and Y. Yang, "The Emergence of the Mixed Perovskites and Their Applications as Solar Cells," *Advanced Energy Materials*, vol. 7, no. 20, p. 1700491, 2017.
- [23] J. Werner, B. Niesen, and C. Ballif, "Perovskite/Silicon Tandem Solar Cells: Marriage of Convenience or True Love Story? - An Overview," *Advanced Materials Interfaces*, vol. 5, no. 1, p. 1700731, 2018.

-
- [24] D. P. McMeekin, G. Sadoughi, W. Rehman, G. E. Eperon, M. Saliba, M. T. Horantner, A. Haghighirad, N. Sakai, L. Korte, B. Rech, M. B. Johnston, L. M. Herz, and H. J. Snaith, "A mixed-cation lead mixed-halide perovskite absorber for tandem solar cells," *Science*, vol. 351, no. 6269, pp. 151–155, 2016.
- [25] T. Leijtens, K. Bush, R. Cheacharoen, R. Beal, A. Bowring, and M. D. McGehee, "Towards enabling stable lead halide perovskite solar cells; interplay between structural, environmental, and thermal stability," *Journal of Materials Chemistry A*, vol. 5, no. 23, pp. 11483–11500, 2017.
- [26] F. Sani, S. Shafie, H. Lim, and A. Musa, "Advancement on Lead-Free Organic-Inorganic Halide Perovskite Solar Cells: A Review," *Materials*, vol. 11, no. 6, p. 1008, 2018.
- [27] S. Shao, J. Liu, G. Portale, H.-H. Fang, G. R. Blake, G. H. ten Brink, L. J. A. Koster, and M. A. Loi, "Highly Reproducible Sn-Based Hybrid Perovskite Solar Cells with 9% Efficiency," *Advanced Energy Materials*, vol. 8, no. 4, p. 1702019, 2018.
- [28] Z. Li, T. R. Klein, D. H. Kim, M. Yang, J. J. Berry, M. F. A. M. van Hest, and K. Zhu, "Scalable fabrication of perovskite solar cells," *Nature Reviews Materials*, vol. 3, no. 4, p. 18017, 2018.
- [29] M. Liu, M. B. Johnston, and H. J. Snaith, "Efficient planar heterojunction perovskite solar cells by vapour deposition," *Nature*, vol. 501, no. 7467, pp. 395–398, 2013.
- [30] C.-W. Chen, H.-W. Kang, S.-Y. Hsiao, P.-F. Yang, K.-M. Chiang, and H.-W. Lin, "Efficient and Uniform Planar-Type Perovskite Solar Cells by Simple Sequential Vacuum Deposition," *Advanced Materials*, vol. 26, no. 38, pp. 6647–6652, 2014.
- [31] L. K. Ono, S. Wang, Y. Kato, S. R. Raga, and Y. Qi, "Fabrication of semi-transparent perovskite films with centimeter-scale superior uniformity by the hybrid deposition method," *Energy & Environmental Science*, vol. 7, no. 12, pp. 3989–3993, 2014.
- [32] L. K. Ono, M. R. Leyden, S. Wang, and Y. Qi, "Organometal halide perovskite thin films and solar cells by vapor deposition," *Journal of Materials Chemistry A*, vol. 4, no. 18, pp. 6693–6713, 2016.
- [33] S.-Y. Hsiao, H.-L. Lin, W.-H. Lee, W.-L. Tsai, K.-M. Chiang, W.-Y. Liao, C.-Z. Ren-Wu, C.-Y. Chen, and H.-W. Lin, "Efficient All-Vacuum Deposited Perovskite Solar Cells by Controlling Reagent Partial Pressure in High Vacuum," *Advanced Materials*, vol. 28, no. 32, pp. 7013–7019, 2016.
- [34] J. Ávila, C. Momblona, P. P. Boix, M. Sessolo, and H. J. Bolink, "Vapor-Deposited Perovskites: The Route to High-Performance Solar Cell Production?," *Joule*, vol. 1, no. 3, pp. 431–442, 2017.
- [35] G. Liang, H. Lan, P. Fan, C. Lan, Z. Zheng, H. Peng, and J. Luo, "Highly Uniform Large-Area (100 cm²) Perovskite CH₃NH₃PbI₃ Thin-Films Prepared by Single-Source Thermal Evaporation," *Coatings*, vol. 8, no. 8, p. 256, 2018.
- [36] Y. Li, J. K. Cooper, R. Buonsanti, C. Giannini, Y. Liu, F. M. Toma, and I. D. Sharp, "Fabrication of Planar Heterojunction Perovskite Solar Cells by Controlled Low-Pressure Vapor Annealing," *The Journal of Physical Chemistry Letters*, vol. 6, no. 3, pp. 493–499, 2015.

-
- [37] P. Luo, S. Zhou, W. Xia, J. Cheng, C. Xu, and Y. Lu, "Chemical Vapor Deposition of Perovskites for Photovoltaic Application," *Advanced Materials Interfaces*, vol. 4, no. 8, p. 1600970, 2017.
- [38] W.-H. Lee, C.-Y. Chen, C.-S. Li, S.-Y. Hsiao, W.-L. Tsai, M.-J. Huang, C.-H. Cheng, C.-I. Wu, and H.-W. Lin, "Boosting thin-film perovskite solar cell efficiency through vacuum-deposited sub-nanometer small-molecule electron interfacial layers," *Nano Energy*, vol. 38, no. April, pp. 66–71, 2017.
- [39] C.-Y. Chen, H.-Y. Lin, K.-M. Chiang, W.-L. Tsai, Y.-C. Huang, C.-S. Tsao, and H.-W. Lin, "All-Vacuum-Deposited Stoichiometrically Balanced Inorganic Cesium Lead Halide Perovskite Solar Cells with Stabilized Efficiency Exceeding 11%," *Advanced Materials*, vol. 29, no. 12, p. 1605290, 2017.
- [40] Q. Guo, C. Li, W. Qiao, S. Ma, F. Wang, B. Zhang, L. Hu, S. Dai, and Z. Tan, "The growth of a CH₃NH₃PbI₃ thin film using simplified close space sublimation for efficient and large dimensional perovskite solar cells," *Energy & Environmental Science*, vol. 9, no. 4, pp. 1486–1494, 2016.
- [41] S. G. Kumar and K. S. R. K. Rao, "Physics and chemistry of CdTe/CdS thin film heterojunction photovoltaic devices: fundamental and critical aspects," *Energy & Environmental Science*, vol. 7, no. 1, pp. 45–102, 2014.
- [42] M. J. Bækbo, O. Hansen, I. Chorkendorff, and P. C. K. Vesborg, "Deposition of methylammonium iodide via evaporation – combined kinetic and mass spectrometric study," *RSC Advances*, vol. 8, no. 52, pp. 29899–29908, 2018.
- [43] M. A. Green, A. Ho-Baillie, and H. J. Snaith, "The emergence of perovskite solar cells," *Nature Photonics*, vol. 8, no. 7, pp. 506–514, 2014.
- [44] D. H. Cao, C. C. Stoumpos, C. D. Malliakas, M. J. Katz, O. K. Farha, J. T. Hupp, and M. G. Kanatzidis, "Remnant PbI₂, an unforeseen necessity in high-efficiency hybrid perovskite-based solar cells?," *APL Materials*, vol. 2, no. 9, p. 091101, 2014.
- [45] P. K. Nayak, D. T. Moore, B. Wenger, S. Nayak, A. A. Haghighirad, A. Fineberg, N. K. Noel, O. G. Reid, G. Rumbles, P. Kukura, K. A. Vincent, and H. J. Snaith, "Mechanism for rapid growth of organic–inorganic halide perovskite crystals," *Nature Communications*, vol. 7, no. 1, p. 13303, 2016.
- [46] S. Hunklinger, *Festkörperphysik*. München: Oldenbourg Wissenschaftsverlag, 2 ed., 2009.
- [47] S. Sze and K. K. Ng, *Physics of Semiconductor Devices*. Hoboken, New Jersey, USA: John Wiley & Sons, Inc., 2006.
- [48] W. Shockley and H. J. Queisser, "Detailed Balance Limit of Efficiency of p-n Junction Solar Cells," *Journal of Applied Physics*, vol. 32, no. 3, pp. 510–519, 1961.
- [49] T. Hellmann, M. Wussler, C. Das, R. Dachauer, I. El-Helaly, C. Mortan, T. Mayer, and W. Jaegermann, "The difference in electronic structure of MAPI and MASI perovskites and its effect on the interface alignment to the HTMs spiro-MeOTAD and CuI," *Journal of Materials Chemistry C*, vol. 7, no. 18, pp. 5324–5332, 2019.
- [50] Z. Hawash, L. K. Ono, and Y. Qi, "Recent Advances in Spiro-MeOTAD Hole Transport Material and Its Applications in Organic-Inorganic Halide Perovskite Solar Cells," *Advanced Materials Interfaces*, vol. 5, no. 1, p. 1700623, 2018.

-
- [51] P. Würfel and U. Würfel, *Physics of Solar Cells*. Weinheim, Germany: Wiley-VCH Verlag GmbH & Co. KGaA, 2 ed., 2009.
- [52] S. Siol, “Kupfer-Chalkogenide für photovoltaische Anwendungen,” dissertation, 2014.
- [53] “IEC EN 60904-3:1993. Photovoltaische Einrichtungen - Teil 3: Messgrundsätze für terrestrische photovoltaische (PV) Einrichtungen mit Angaben über die spektrale Strahlungsverteilung,” 1993.
- [54] D. Abou-Ras, T. Kirchartz, and U. Rau, eds., *Advanced Characterization Techniques for Thin Film Solar Cells*, vol. 1. Weinheim, Germany: Wiley-VCH Verlag GmbH & Co. KGaA, 2 ed., 2016.
- [55] H. Lüth, *Solid Surfaces, Interfaces and Thin Films*. Graduate Texts in Physics, Berlin, Heidelberg: Springer Berlin Heidelberg, 2010.
- [56] P. W. Atkins and J. de Paula, *Physikalische Chemie*. Weinheim, Germany: Wiley-VCH Verlag GmbH & Co. KGaA, 4 ed., 2006.
- [57] E. J. Juarez-Perez, Z. Hawash, S. R. Raga, L. K. Ono, and Y. Qi, “Thermal degradation of CH₃NH₃PbI₃ perovskite into NH₃ and CH₃I gases observed by coupled thermogravimetry–mass spectrometry analysis,” *Energy & Environmental Science*, vol. 9, no. 11, pp. 3406–3410, 2016.
- [58] W. D. Callister Jr. and D. G. Rethwisch, *Materials Science and Engineering*. Hoboken, New Jersey, USA: John Wiley & Sons, Inc., 8 ed., 2011.
- [59] M. Weidner, “Fermi Level Determination in Tin Oxide by Photoelectron Spectroscopy,” dissertation, 2016.
- [60] Thermo ELECTRON CORPORATION, *ESCALAB 250 System Manual*, 2003.
- [61] S. Tougaard and P. Sigmund, “Influence of elastic and inelastic scattering on energy spectra of electrons emitted from solids,” *Physical Review B*, vol. 25, no. 7, pp. 4452–4466, 1982.
- [62] A. Klein, T. Mayer, A. Thissen, and W. Jaegermann, “Photoelectron Spectroscopy in Materials Science and Physical Chemistry:,” *Bunsen-Magazin*, vol. 10, no. 4, pp. 124–139, 2008.
- [63] D. A. Shirley, “High-Resolution X-Ray Photoemission Spectrum of the Valence Bands of Gold,” *Physical Review B*, vol. 5, no. 12, pp. 4709–4714, 1972.
- [64] C. D. Wagner, L. E. Davis, M. V. Zeller, J. A. Taylor, R. H. Raymond, and L. H. Gale, “Empirical atomic sensitivity factors for quantitative analysis by electron spectroscopy for chemical analysis,” *Surface and Interface Analysis*, vol. 3, no. 5, pp. 211–225, 1981.
- [65] J. Scofield, “Hartree-Slater subshell photoionization cross-sections at 1254 and 1487 eV,” *Journal of Electron Spectroscopy and Related Phenomena*, vol. 8, no. 2, pp. 129–137, 1976.
- [66] A. G. Shard, “Detection limits in XPS for more than 6000 binary systems using Al and Mg K α X-rays,” *Surface and Interface Analysis*, vol. 46, no. 3, pp. 175–185, 2014.

-
- [67] L. Spieß, G. Teichert, R. Schwarzer, H. Behnken, and C. Genzel, *Moderne Röntgenbeugung*. Wiesbaden: Vieweg+Teubner, 2009.
- [68] W. Borchardt-Ott and H. Sowa, *Kristallographie*. Springer-Lehrbuch, Berlin, Heidelberg: Springer Berlin Heidelberg, 2013.
- [69] W. Q. Hong, “Extraction of extinction coefficient of weak absorbing thin films from special absorption,” *Journal of Physics D: Applied Physics*, vol. 22, no. 9, pp. 1384–1385, 1989.
- [70] D. K. Schroder, *Semiconductor Material and Device Characterization*. Hoboken, New Jersey, USA: John Wiley & Sons, Inc., 3 ed., 2006.
- [71] T. Hellmann, “Construction and optimization of an automatic spray pyrolysis system to deposit TiO₂ films for the use in perovskite solar cells,” Advanced Research Lab report, 2016.
- [72] Bruker AXS, *Topas V5, General profile and structure analysis software for powder diffraction data, User’s Manual*. Karlsruhe, Germany, 2014.
- [73] V. Pfeifer, “Grenzflächeneigenschaften von Anatas und Rutil,” diploma thesis, 2013.
- [74] D. Guerin and S. I. Shah, “Reactive-sputtering of titanium oxide thin films,” *Journal of Vacuum Science & Technology A: Vacuum, Surfaces, and Films*, vol. 15, no. 3, pp. 712–715, 1997.
- [75] J.-c. Dupin, D. Gonbeau, P. Vinatier, and A. Levasseur, “Systematic XPS studies of metal oxides, hydroxides and peroxides,” *Physical Chemistry Chemical Physics*, vol. 2, no. 6, pp. 1319–1324, 2000.
- [76] G. Liu, W. Jaegermann, J. He, V. Sundström, and L. Sun, “XPS and UPS Characterization of the TiO₂/ZnPcGly Heterointerface: Alignment of Energy Levels,” *The Journal of Physical Chemistry B*, vol. 106, no. 23, pp. 5814–5819, 2002.
- [77] K. Shen, K. Wu, and D. Wang, “Band alignment of ultra-thin hetero-structure ZnO/TiO₂ junction,” *Materials Research Bulletin*, vol. 51, pp. 141–144, 2014.
- [78] S. Kashiwaya, T. Toupance, A. Klein, and W. Jaegermann, “Fermi Level Positions and Induced Band Bending at Single Crystalline Anatase (101) and (001) Surfaces: Origin of the Enhanced Photocatalytic Activity of Facet Engineered Crystals,” *Advanced Energy Materials*, vol. 8, no. 33, p. 1802195, 2018.
- [79] P. Reckers, “Electronic properties of titania (and AZO) and its interface to organic acceptor materials,” dissertation, 2017.
- [80] S. Porsgaard, P. Jiang, F. Borondics, S. Wendt, Z. Liu, H. Bluhm, F. Besenbacher, and M. Salmeron, “Charge State of Gold Nanoparticles Supported on Titania under Oxygen Pressure,” *Angewandte Chemie International Edition*, vol. 50, no. 10, pp. 2266–2269, 2011.
- [81] A. Borodin and M. Reichling, “Characterizing TiO₂(110) surface states by their work function,” *Physical Chemistry Chemical Physics*, vol. 13, no. 34, pp. 15442–15447, 2011.
- [82] H. P. Marques, A. R. Canário, A. M. C. Moutinho, and O. M. N. D. Teodoro, “Tracking hydroxyl adsorption on TiO₂ (110) through secondary emission changes,” *Applied Surface Science*, vol. 255, no. 16, pp. 7389–7393, 2009.

-
- [83] A. L. Linsebigler, G. Lu, and J. T. Yates, "Photocatalysis on TiO₂ Surfaces: Principles, Mechanisms, and Selected Results," *Chemical Reviews*, vol. 95, no. 3, pp. 735–758, 1995.
- [84] W. Hebenstreit, N. Ruzycski, G. S. Herman, Y. Gao, and U. Diebold, "Scanning tunneling microscopy investigation of the TiO₂ anatase (101) surface," *Physical Review B*, vol. 62, no. 24, pp. R16334–R16336, 2000.
- [85] J. Blomquist, L. E. Walle, P. Uvdal, A. Borg, and A. Sandell, "Water Dissociation on Single Crystalline Anatase TiO₂ (001) Studied by Photoelectron Spectroscopy," *The Journal of Physical Chemistry C*, vol. 112, no. 42, pp. 16616–16621, 2008.
- [86] L. E. Walle, A. Borg, E. M. J. Johansson, S. Plogmaker, H. Rensmo, P. Uvdal, and A. Sandell, "Mixed Dissociative and Molecular Water Adsorption on Anatase TiO₂ (101)," *The Journal of Physical Chemistry C*, vol. 115, no. 19, pp. 9545–9550, 2011.
- [87] J. F. Moulder, W. F. Stickle, P. E. Sobol, and K. D. Bomben, *Handbook of X-ray Photoelectron Spectroscopy*. Eden Prairie, MN, USA: Physical Electronics, Inc., 1992.
- [88] M. A. Henderson, W. S. Epling, C. L. Perkins, C. H. F. Peden, and U. Diebold, "Interaction of Molecular Oxygen with the Vacuum-Annealed TiO₂ (110) Surface: Molecular and Dissociative Channels," *The Journal of Physical Chemistry B*, vol. 103, no. 25, pp. 5328–5337, 1999.
- [89] M. Stöhr, "Deposition and Characterisation of CH₃NH₃PbI₃ Perovskite for Thin Film Solar Cells," master thesis, 2018.
- [90] V. Pfeifer, P. Erhart, S. Li, K. Rachut, J. Morasch, J. Brötz, P. Reckers, T. Mayer, S. Rühle, A. Zaban, I. Mora Seró, J. Bisquert, W. Jaegermann, and A. Klein, "Energy Band Alignment between Anatase and Rutile TiO₂," *The Journal of Physical Chemistry Letters*, vol. 4, no. 23, pp. 4182–4187, 2013.
- [91] M. Yang, Y. Zhou, Y. Zeng, C.-S. Jiang, N. P. Padture, and K. Zhu, "Square-Centimeter Solution-Processed Planar CH₃NH₃PbI₃ Perovskite Solar Cells with Efficiency Exceeding 15%," *Advanced Materials*, vol. 27, no. 41, pp. 6363–6370, 2015.
- [92] T. Baikie, Y. Fang, J. M. Kadro, M. Schreyer, F. Wei, S. G. Mhaisalkar, M. Graetzel, and T. J. White, "Synthesis and crystal chemistry of the hybrid perovskite (CH₃NH₃)PbI₃ for solid-state sensitised solar cell applications," *Journal of Materials Chemistry A*, vol. 1, no. 18, p. 5628, 2013.
- [93] A. Pisoni, J. Jaćimović, O. S. Barišić, M. Spina, R. Gaál, L. Forró, and E. Horváth, "Ultra-Low Thermal Conductivity in Organic–Inorganic Hybrid Perovskite CH₃NH₃PbI₃," *The Journal of Physical Chemistry Letters*, vol. 5, no. 14, pp. 2488–2492, 2014.
- [94] A. Kovalsky, L. Wang, G. T. Marek, C. Burda, and J. S. Dyck, "Thermal Conductivity of CH₃NH₃PbI₃ and CsPbI₃ : Measuring the Effect of the Methylammonium Ion on Phonon Scattering," *The Journal of Physical Chemistry C*, vol. 121, no. 6, pp. 3228–3233, 2017.
- [95] C. Xiao, Z. Li, H. Guthrey, J. Moseley, Y. Yang, S. Wozny, H. Moutinho, B. To, J. J. Berry, B. Gorman, Y. Yan, K. Zhu, and M. Al-Jassim, "Mechanisms of Electron-Beam-Induced Damage in Perovskite Thin Films Revealed by Cathodoluminescence

-
- [107] I. Deretzis, A. Alberti, G. Pellegrino, E. Smecca, F. Giannazzo, N. Sakai, T. Miyasaka, and A. La Magna, "Atomistic origins of CH₃NH₃PbI₃ degradation to PbI₂ in vacuum," *Applied Physics Letters*, vol. 106, no. 13, p. 131904, 2015.
- [108] R. Wasylishen, O. Knop, and J. Macdonald, "Cation rotation in methylammonium lead halides," *Solid State Communications*, vol. 56, no. 7, pp. 581–582, 1985.
- [109] J. C. S. Costa, J. Azevedo, L. M. N. B. F. Santos, and A. Mendes, "On the Deposition of Lead Halide Perovskite Precursors by Physical Vapor Method," *The Journal of Physical Chemistry C*, vol. 121, no. 4, pp. 2080–2087, 2017.
- [110] P.-S. Shen, J.-S. Chen, Y.-H. Chiang, M.-H. Li, T.-F. Guo, and P. Chen, "Low-Pressure Hybrid Chemical Vapor Growth for Efficient Perovskite Solar Cells and Large-Area Module," *Advanced Materials Interfaces*, vol. 3, no. 8, p. 1500849, 2016.
- [111] J. J. van Franeker, K. H. Hendriks, B. J. Bruijnaers, M. W. G. M. Verhoeven, M. M. Wienk, and R. A. J. Janssen, "Monitoring Thermal Annealing of Perovskite Solar Cells with In Situ Photoluminescence," *Advanced Energy Materials*, vol. 7, no. 7, p. 1601822, 2017.
- [112] L. Wang, W.-C. Lin, C. McCleese, A. Kovalsky, Y. Zhao, and C. Burda, "Complete Conversion of PbI₂ to Methyl Ammonium PbI₃ Improves Perovskite Solar Cell Efficiency," *ChemPhysChem*, vol. 18, no. 1, pp. 47–50, 2017.
- [113] Y. Zou, Q. Meng, H. Mao, and D. Zhu, "Substrate effect on the interfacial electronic structure of thermally-evaporated CH₃NH₃PbI₃ perovskite layer," *Organic Electronics*, vol. 41, pp. 307–314, 2017.
- [114] T. P. Gujar, T. Unger, A. Schönleber, M. Fried, F. Panzer, S. van Smaalen, A. Köhler, and M. Thelakkat, "The role of PbI₂ in CH₃NH₃PbI₃ perovskite stability, solar cell parameters and device degradation," *Physical Chemistry Chemical Physics*, vol. 20, no. 1, pp. 605–614, 2018.
- [115] B. Gebremichael, G. Alemu, and G. Tessema Mola, "Conductivity of CH₃NH₃PbI₃ thin film perovskite stored in ambient atmosphere," *Physica B: Condensed Matter*, vol. 514, no. March, pp. 85–88, 2017.
- [116] P. Schulz, E. Edri, S. Kirmayer, G. Hodes, D. Cahen, and A. Kahn, "Interface energetics in organo-metal halide perovskite-based photovoltaic cells," *Energy & Environmental Science*, vol. 7, no. 4, pp. 1377–1381, 2014.
- [117] X. Liu, C. Wang, L. Lyu, C. Wang, Z. Xiao, C. Bi, J. Huang, and Y. Gao, "Electronic structures at the interface between Au and CH₃NH₃PbI₃," *Physical Chemistry Chemical Physics*, vol. 17, no. 2, pp. 896–902, 2015.
- [118] C. Wang, X. Liu, C. Wang, Z. Xiao, C. Bi, Y. Shao, J. Huang, and Y. Gao, "Surface analytical investigation on organometal triiodide perovskite," *Journal of Vacuum Science & Technology B, Nanotechnology and Microelectronics: Materials, Processing, Measurement, and Phenomena*, vol. 33, no. 3, p. 032401, 2015.
- [119] M. Shirayama, H. Kadowaki, T. Miyadera, T. Sugita, M. Tamakoshi, M. Kato, T. Fujiseki, D. Murata, S. Hara, T. N. Murakami, S. Fujimoto, M. Chikamatsu, and H. Fujiwara, "Optical Transitions in Hybrid Perovskite Solar Cells: Ellipsometry, Density Functional Theory, and Quantum Efficiency Analyses for CH₃NH₃PbI₃," *Physical Review Applied*, vol. 5, no. 1, p. 014012, 2016.

-
- [120] W.-J. Yin, T. Shi, and Y. Yan, "Unusual defect physics in CH₃NH₃PbI₃ perovskite solar cell absorber," *Applied Physics Letters*, vol. 104, no. 6, p. 063903, 2014.
- [121] P. Lopez-Varo, J. A. Jiménez-Tejada, M. García-Rosell, S. Ravishankar, G. Garcia-Belmonte, J. Bisquert, and O. Almora, "Device Physics of Hybrid Perovskite Solar cells: Theory and Experiment," *Advanced Energy Materials*, vol. 8, no. 14, p. 1702772, 2018.
- [122] M. L. Petrus, J. Schlipf, C. Li, T. P. Gujar, N. Giesbrecht, P. Müller-Buschbaum, M. Thelakkat, T. Bein, S. Hüttner, and P. Docampo, "Capturing the Sun: A Review of the Challenges and Perspectives of Perovskite Solar Cells," *Advanced Energy Materials*, vol. 7, no. 16, p. 1700264, 2017.
- [123] M. Weiss, J. Horn, C. Richter, and D. Schlettwein, "Preparation and characterization of methylammonium tin iodide layers as photovoltaic absorbers," *physica status solidi (a)*, vol. 213, no. 4, pp. 975–981, 2016.
- [124] R. Lindblad, D. Bi, B.-w. Park, J. Oscarsson, M. Gorgoi, H. Siegbahn, M. Odelius, E. M. J. Johansson, and H. Rensmo, "Electronic Structure of TiO₂ /CH₃NH₃PbI₃ Perovskite Solar Cell Interfaces," *The Journal of Physical Chemistry Letters*, vol. 5, no. 4, pp. 648–653, 2014.
- [125] Z. Hawash, S. R. Raga, D.-Y. Son, L. K. Ono, N.-G. Park, and Y. Qi, "Interfacial Modification of Perovskite Solar Cells Using an Ultrathin MAI Layer Leads to Enhanced Energy Level Alignment, Efficiencies, and Reproducibility," *The Journal of Physical Chemistry Letters*, vol. 8, no. 17, pp. 3947–3953, 2017.
- [126] L. Liu, J. A. McLeod, R. Wang, P. Shen, and S. Duhm, "Tracking the formation of methylammonium lead triiodide perovskite," *Applied Physics Letters*, vol. 107, no. 6, p. 061904, 2015.
- [127] S. Chen, T. W. Goh, D. Sabba, J. Chua, N. Mathews, C. H. A. Huan, and T. C. Sum, "Energy level alignment at the methylammonium lead iodide/copper phthalocyanine interface," *APL Materials*, vol. 2, no. 8, p. 081512, 2014.
- [128] J. Emara, T. Schnier, N. Pourdavoud, T. Riedl, K. Meerholz, and S. Olthof, "Impact of Film Stoichiometry on the Ionization Energy and Electronic Structure of CH₃NH₃PbI₃ Perovskites," *Advanced Materials*, vol. 28, no. 3, pp. 553–559, 2016.
- [129] S. Olthof and K. Meerholz, "Substrate-dependent electronic structure and film formation of MAPbI₃ perovskites," *Scientific Reports*, vol. 7, no. December 2016, p. 40267, 2017.
- [130] L. Li, S. Tong, Y. Zhao, C. Wang, S. Wang, L. Lyu, Y. Huang, H. Huang, J. Yang, D. Niu, X. Liu, and Y. Gao, "Interfacial Electronic Structures of Photodetectors Based on C₈BTBT/Perovskite," *ACS Applied Materials & Interfaces*, vol. 10, no. 24, pp. 20959–20967, 2018.
- [131] C. M. Wolff, F. Zu, A. Paulke, L. P. Toro, N. Koch, and D. Neher, "Reduced Interface-Mediated Recombination for High Open-Circuit Voltages in CH₃NH₃PbI₃ Solar Cells," *Advanced Materials*, vol. 29, no. 28, p. 1700159, 2017.
- [132] Q. Wang, Y. Shao, H. Xie, L. Lyu, X. Liu, Y. Gao, and J. Huang, "Qualifying composition dependent p and n self-doping in CH₃NH₃PbI₃," *Applied Physics Letters*, vol. 105, no. 16, p. 163508, 2014.

-
- [133] O. E. Semonin, G. A. Elbaz, D. B. Straus, T. D. Hull, D. W. Paley, A. M. van der Zande, J. C. Hone, I. Kyymissis, C. R. Kagan, X. Roy, and J. S. Owen, "Limits of Carrier Diffusion in n-Type and p-Type CH₃NH₃PbI₃ Perovskite Single Crystals," *The Journal of Physical Chemistry Letters*, vol. 7, no. 17, pp. 3510–3518, 2016.
- [134] D. Song, P. Cui, T. Wang, D. Wei, M. Li, F. Cao, X. Yue, P. Fu, Y. Li, Y. He, B. Jiang, and M. Trevor, "Managing Carrier Lifetime and Doping Property of Lead Halide Perovskite by Postannealing Processes for Highly Efficient Perovskite Solar Cells," *The Journal of Physical Chemistry C*, vol. 119, no. 40, pp. 22812–22819, 2015.
- [135] A. Zohar, I. Levine, S. Gupta, O. Davidson, D. Azulay, O. Millo, I. Balberg, G. Hodes, and D. Cahen, "What Is the Mechanism of MAPbI₃ p-Doping by I₂? Insights from Optoelectronic Properties," *ACS Energy Letters*, vol. 2, no. 10, pp. 2408–2414, 2017.
- [136] J. Shi, H. Zhang, Y. Li, J. J. Jasieniak, Y. Li, H. Wu, Y. Luo, D. Li, and Q. Meng, "Identification of high-temperature exciton states and their phase-dependent trapping behaviour in lead halide perovskites," *Energy & Environmental Science*, vol. 11, no. 6, pp. 1460–1469, 2018.
- [137] S. A. Veldhuis, P. P. Boix, N. Yantara, M. Li, T. C. Sum, N. Mathews, and S. G. Mhaisalkar, "Perovskite Materials for Light-Emitting Diodes and Lasers," *Advanced Materials*, vol. 28, no. 32, pp. 6804–6834, 2016.
- [138] Q. Lin, A. Armin, P. L. Burn, and P. Meredith, "Organohalide Perovskites for Solar Energy Conversion," *Accounts of Chemical Research*, vol. 49, no. 3, pp. 545–553, 2016.
- [139] C. Wehrenfennig, M. Liu, H. J. Snaith, M. B. Johnston, and L. M. Herz, "Charge-carrier dynamics in vapour-deposited films of the organolead halide perovskite CH₃NH₃PbI_{3-x}Cl_x," *Energy & Environmental Science*, vol. 7, no. 7, pp. 2269–2275, 2014.
- [140] M. E. Ziffer, J. C. Mohammed, and D. S. Ginger, "Electroabsorption Spectroscopy Measurements of the Exciton Binding Energy, Electron–Hole Reduced Effective Mass, and Band Gap in the Perovskite CH₃NH₃PbI₃," *ACS Photonics*, vol. 3, no. 6, pp. 1060–1068, 2016.
- [141] M. Shkir, H. Abbas, Siddhartha, and Z. R. Khan, "Effect of thickness on the structural, optical and electrical properties of thermally evaporated PbI₂ thin films," *Journal of Physics and Chemistry of Solids*, vol. 73, no. 11, pp. 1309–1313, 2012.
- [142] D. R. Lide, ed., *CRC Handbook of Chemistry and Physics, Internet Version 2005*. Boca Raton, FL, USA: CRC Press, 2004.
- [143] D. P. Nenon, J. A. Christians, L. M. Wheeler, J. L. Blackburn, E. M. Sanehira, B. Dou, M. L. Olsen, K. Zhu, J. J. Berry, and J. M. Luther, "Structural and chemical evolution of methylammonium lead halide perovskites during thermal processing from solution," *Energy & Environmental Science*, vol. 9, no. 6, pp. 2072–2082, 2016.
- [144] P. Umari, E. Mosconi, and F. De Angelis, "Relativistic GW calculations on CH₃NH₃PbI₃ and CH₃NH₃SnI₃ Perovskites for Solar Cell Applications," *Scientific Reports*, vol. 4, no. 1, p. 4467, 2015.
- [145] "<https://srdata.nist.gov/xps>."

-
- [146] “<https://www.sigmaaldrich.com>.”
- [147] P. Docampo, F. C. Hanusch, S. D. Stranks, M. Döblinger, J. M. Feckl, M. Ehrensperger, N. K. Minar, M. B. Johnston, H. J. Snaith, and T. Bein, “Solution Deposition-Conversion for Planar Heterojunction Mixed Halide Perovskite Solar Cells,” *Advanced Energy Materials*, vol. 4, no. 14, p. 1400355, 2014.
- [148] R. Wang, C. Wu, Y. Hu, J. Li, P. Shen, Q. Wang, L. Liao, L. Liu, and S. Duhm, “CH₃NH₃PbI_{3-x}Cl_x under Different Fabrication Strategies: Electronic Structures and Energy-Level Alignment with an Organic Hole Transport Material,” *ACS Applied Materials & Interfaces*, vol. 9, no. 8, pp. 7859–7865, 2017.
- [149] Y. Peng, G. Jing, and T. Cui, “High-performance perovskite solar cells fabricated by vapor deposition with optimized PbI₂ precursor films,” *RSC Advances*, vol. 5, no. 116, pp. 95847–95853, 2015.
- [150] V. V. Sobolev, A. I. Kalugin, I. V. Vostrikov, and V. V. Sobolev, “Electronic structure and optical properties of lead chloride,” *Journal of Surface Investigation. X-ray, Synchrotron and Neutron Techniques*, vol. 3, no. 1, pp. 48–57, 2009.
- [151] R. L. Sass, E. B. Brackett, and T. E. Brackett, “THE CRYSTAL STRUCTURE OF LEAD CHLORIDE,” *The Journal of Physical Chemistry*, vol. 67, no. 12, pp. 2863–2864, 1963.
- [152] R. W. G. Wyckoff, *Crystal Structures, second edition*, vol. 1. NY, USA: Interscience Publishers New York, 1963.
- [153] A. Wakamiya, M. Endo, T. Sasamori, N. Tokitoh, Y. Ogomi, S. Hayase, and Y. Murata, “Reproducible Fabrication of Efficient Perovskite-based Solar Cells: X-ray Crystallographic Studies on the Formation of CH₃NH₃PbI₃ Layers,” *Chemistry Letters*, vol. 43, no. 5, pp. 711–713, 2014.
- [154] S. Wang, L. K. Ono, M. R. Leyden, Y. Kato, S. R. Raga, M. V. Lee, and Y. Qi, “Smooth perovskite thin films and efficient perovskite solar cells prepared by the hybrid deposition method,” *Journal of Materials Chemistry A*, vol. 3, no. 28, pp. 14631–14641, 2015.
- [155] W. Tress, M. Yavari, K. Domanski, P. Yadav, B. Niesen, J. P. Correa Baena, A. Hagfeldt, and M. Graetzel, “Interpretation and evolution of open-circuit voltage, recombination, ideality factor and subgap defect states during reversible light-soaking and irreversible degradation of perovskite solar cells,” *Energy & Environmental Science*, vol. 11, no. 1, pp. 151–165, 2018.
- [156] T. S. Sherkar, C. Momblona, L. Gil-Escrig, J. Ávila, M. Sessolo, H. J. Bolink, and L. J. A. Koster, “Recombination in Perovskite Solar Cells: Significance of Grain Boundaries, Interface Traps, and Defect Ions,” *ACS Energy Letters*, vol. 2, no. 5, pp. 1214–1222, 2017.
- [157] Y. Kanemitsu, “Luminescence spectroscopy of lead-halide perovskites: materials properties and application as photovoltaic devices,” *Journal of Materials Chemistry C*, vol. 5, no. 14, pp. 3427–3437, 2017.
- [158] W. Ke, D. Zhao, C. R. Grice, A. J. Cimaroli, J. Ge, H. Tao, H. Lei, G. Fang, and Y. Yan, “Efficient planar perovskite solar cells using room-temperature vacuum-processed C60 electron selective layers,” *Journal of Materials Chemistry A*, vol. 3, no. 35, pp. 17971–17976, 2015.

-
- [159] J. B. Patel, J. Wong-Leung, S. Van Reenen, N. Sakai, J. T. W. Wang, E. S. Parrott, M. Liu, H. J. Snaith, L. M. Herz, and M. B. Johnston, "Influence of Interface Morphology on Hysteresis in Vapor-Deposited Perovskite Solar Cells," *Advanced Electronic Materials*, vol. 3, no. 2, p. 1600470, 2017.
- [160] S. R. Raga, M.-C. Jung, M. V. Lee, M. R. Leyden, Y. Kato, and Y. Qi, "Influence of Air Annealing on High Efficiency Planar Structure Perovskite Solar Cells," *Chemistry of Materials*, vol. 27, no. 5, pp. 1597–1603, 2015.
- [161] A. Dualeh, N. Tétreault, T. Moehl, P. Gao, M. K. Nazeeruddin, and M. Grätzel, "Effect of Annealing Temperature on Film Morphology of Organic-Inorganic Hybrid Perovskite Solid-State Solar Cells," *Advanced Functional Materials*, vol. 24, no. 21, pp. 3250–3258, 2014.
- [162] Y.-Z. Zheng, X.-S. Lai, Y. Luo, E.-F. Zhao, F.-L. Meng, X.-F. Zhang, and X. Tao, "Effects of precursor concentration and annealing temperature on CH₃NH₃PbI₃ film crystallization and photovoltaic performance," *Journal of Physics and Chemistry of Solids*, vol. 107, no. February, pp. 55–61, 2017.
- [163] P. Luo, Z. Liu, W. Xia, C. Yuan, J. Cheng, and Y. Lu, "Uniform, Stable, and Efficient Planar-Heterojunction Perovskite Solar Cells by Facile Low-Pressure Chemical Vapor Deposition under Fully Open-Air Conditions," *ACS Applied Materials & Interfaces*, vol. 7, no. 4, pp. 2708–2714, 2015.
- [164] C. Hoyer, "Optimierung von vakuum-prozessierten CH₃NH₃PbI₃ Perovskit-Schichten für Photovoltaik-Anwendungen," master thesis, 2015.
- [165] C. Das, M. Wussler, T. Hellmann, T. Mayer, and W. Jaegermann, "In situ XPS study of the surface chemistry of MAPI solar cells under operating conditions in vacuum," *Physical Chemistry Chemical Physics*, vol. 20, no. 25, 2018.
- [166] E. L. Unger, E. T. Hoke, C. D. Bailie, W. H. Nguyen, a. R. Bowring, T. Heumüller, M. G. Christoforo, and M. D. McGehee, "Hysteresis and transient behavior in current–voltage measurements of hybrid-perovskite absorber solar cells," *Energy & Environmental Science*, vol. 7, no. 11, pp. 3690–3698, 2014.
- [167] R. Scheer and H.-W. Schock, *Chalcogenide Photovoltaics*. Weinheim, Germany: Wiley-VCH Verlag GmbH & Co. KGaA, 2011.
- [168] T. Wang, B. Daiber, J. M. Frost, S. A. Mann, E. C. Garnett, A. Walsh, and B. Ehrler, "Indirect to direct bandgap transition in methylammonium lead halide perovskite," *Energy & Environmental Science*, vol. 10, no. 2, pp. 509–515, 2017.
- [169] J. H. Heo, D. H. Song, H. J. Han, S. Y. Kim, J. H. Kim, D. Kim, H. W. Shin, T. K. Ahn, C. Wolf, T.-W. Lee, and S. H. Im, "Planar CH₃NH₃PbI₃ Perovskite Solar Cells with Constant 17.2% Average Power Conversion Efficiency Irrespective of the Scan Rate," *Advanced Materials*, vol. 27, no. 22, pp. 3424–3430, 2015.
- [170] Q. Chen, H. Zhou, Z. Hong, S. Luo, H.-S. Duan, H.-H. Wang, Y. Liu, G. Li, and Y. Yang, "Planar Heterojunction Perovskite Solar Cells via Vapor-Assisted Solution Process," *Journal of the American Chemical Society*, vol. 136, no. 2, pp. 622–625, 2014.

-
- [171] H.-S. Ko, J.-W. Lee, and N.-G. Park, "15.76% efficiency perovskite solar cells prepared under high relative humidity: importance of PbI₂ morphology in two-step deposition of CH₃NH₃PbI₃," *Journal of Materials Chemistry A*, vol. 3, no. 16, pp. 8808–8815, 2015.
- [172] Z. Chu, M. Yang, P. Schulz, D. Wu, X. Ma, E. Seifert, L. Sun, X. Li, K. Zhu, and K. Lai, "Impact of grain boundaries on efficiency and stability of organic-inorganic trihalide perovskites," *Nature Communications*, vol. 8, no. 1, p. 2230, 2017.
- [173] S. Shao, M. Abdu-Aguye, T. S. Sherkar, H.-H. Fang, S. Adjokatse, G. ten Brink, B. J. Kooi, L. J. A. Koster, and M. A. Loi, "The Effect of the Microstructure on Trap-Assisted Recombination and Light Soaking Phenomenon in Hybrid Perovskite Solar Cells," *Advanced Functional Materials*, vol. 26, no. 44, pp. 8094–8102, 2016.
- [174] Q. Jiang, Z. Chu, P. Wang, X. Yang, H. Liu, Y. Wang, Z. Yin, J. Wu, X. Zhang, and J. You, "Planar-Structure Perovskite Solar Cells with Efficiency beyond 21%," *Advanced Materials*, vol. 29, no. 46, p. 1703852, 2017.
- [175] Z. Li, C. Zhang, Z. Shao, Y. Fan, R. Liu, L. Wang, and S. Pang, "Controlled surface decomposition derived passivation and energy-level alignment behaviors for high performance perovskite solar cells," *Journal of Materials Chemistry A*, vol. 6, no. 20, pp. 9397–9401, 2018.
- [176] B. Shi, X. Yao, F. Hou, S. Guo, Y. Li, C. Wei, Y. Ding, Y. Li, Y. Zhao, and X. Zhang, "Unraveling the Passivation Process of PbI₂ to Enhance the Efficiency of Planar Perovskite Solar Cells," *The Journal of Physical Chemistry C*, vol. 122, no. 37, pp. 21269–21276, 2018.
- [177] T. Meier, T. P. Gujar, A. Schönleber, S. Olthof, K. Meerholz, S. van Smaalen, F. Panzer, M. Thelakkat, and A. Köhler, "Impact of excess PbI₂ on the structure and the temperature dependent optical properties of methylammonium lead iodide perovskites," *Journal of Materials Chemistry C*, vol. 6, no. 28, pp. 7512–7519, 2018.
- [178] A. Dualeh, P. Gao, S. I. Seok, M. K. Nazeeruddin, and M. Grätzel, "Thermal Behavior of Methylammonium Lead-Trihalide Perovskite Photovoltaic Light Harvesters," *Chemistry of Materials*, vol. 26, no. 21, pp. 6160–6164, 2014.
- [179] A. A. Petrov, E. A. Goodilin, A. B. Tarasov, V. A. Lazarenko, P. V. Dorovatovskii, and V. N. Khrustalev, "Formamidinium iodide: crystal structure and phase transitions," *Acta Crystallographica Section E Crystallographic Communications*, vol. 73, no. 4, pp. 569–572, 2017.
- [180] B. Li, Y. Zhang, L. Fu, T. Yu, S. Zhou, L. Zhang, and L. Yin, "Surface passivation engineering strategy to fully-inorganic cubic CsPbI₃ perovskites for high-performance solar cells," *Nature Communications*, vol. 9, no. 1, p. 1076, 2018.
- [181] C. Liu, W. Li, C. Zhang, Y. Ma, J. Fan, and Y. Mai, "All-Inorganic CsPbI₂Br Perovskite Solar Cells with High Efficiency Exceeding 13%," *Journal of the American Chemical Society*, vol. 140, no. 11, pp. 3825–3828, 2018.
- [182] J. K. Nam, S. U. Chai, W. Cha, Y. J. Choi, W. Kim, M. S. Jung, J. Kwon, D. Kim, and J. H. Park, "Potassium Incorporation for Enhanced Performance and Stability of Fully Inorganic Cesium Lead Halide Perovskite Solar Cells," *Nano Letters*, vol. 17, no. 3, pp. 2028–2033, 2017.

-
- [183] Q. Zeng, X. Zhang, X. Feng, S. Lu, Z. Chen, X. Yong, S. A. T. Redfern, H. Wei, H. Wang, H. Shen, W. Zhang, W. Zheng, H. Zhang, J. S. Tse, and B. Yang, "Polymer-Passivated Inorganic Cesium Lead Mixed-Halide Perovskites for Stable and Efficient Solar Cells with High Open-Circuit Voltage over 1.3 V," *Advanced Materials*, vol. 30, no. 9, p. 1705393, 2018.
- [184] R. L. Z. Hoyer, L. C. Lee, R. C. Kurchin, T. N. Huq, K. H. L. Zhang, M. Sponser, L. Nienhaus, R. E. Brandt, J. Jean, J. A. Polizzotti, A. Kursumović, M. G. Bawendi, V. Bulović, V. Stevanović, T. Buonassisi, and J. L. MacManus-Driscoll, "Strongly Enhanced Photovoltaic Performance and Defect Physics of Air-Stable Bismuth Oxide (BiOI)," *Advanced Materials*, vol. 29, no. 36, p. 1702176, 2017.
- [185] J. Duan, Y. Zhao, B. He, and Q. Tang, "Simplified Perovskite Solar Cell with 4.1% Efficiency Employing Inorganic CsPbBr₃ as Light Absorber," *Small*, vol. 14, no. 20, p. 1704443, 2018.
- [186] A. Jodłowski, D. Rodríguez-Padrón, R. Luque, and G. de Miguel, "Alternative Perovskites for Photovoltaics," *Advanced Energy Materials*, vol. 8, no. 21, p. 1703120, 2018.



A Appendix

Experimental - Synthesis

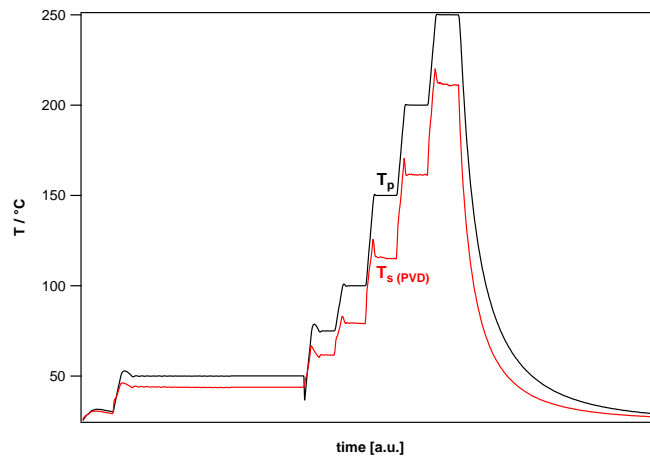


Figure A.1.: Calibration curve for the substrate temperature of the PVD chamber. The temperature of the FTO/TiO₂ side of the substrate is plotted in red, the temperature of the sample holder plate in black.

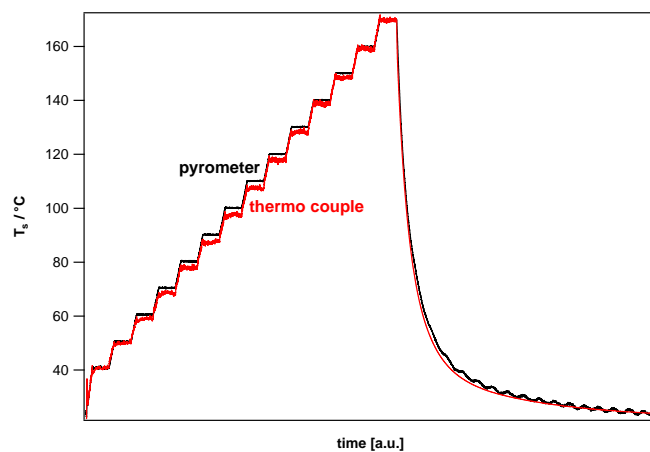


Figure A.2.: Calibration curve for the substrate temperature of the CSS chamber. The temperature of the glass backside of the substrate measured with a thermo couple is plotted in red, the temperature measured with the chamber pyrometer in black.

MAPI fabricated from lead iodide

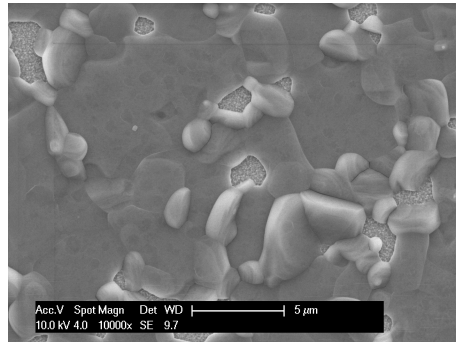


Figure A.3.: SEM image in SE contrast (top view) of a MAPI layer deposited onto a glass/FTO/TiO₂ substrate by CSS. Through the holes in the MAPI layer, the fine grained substrate is visible.

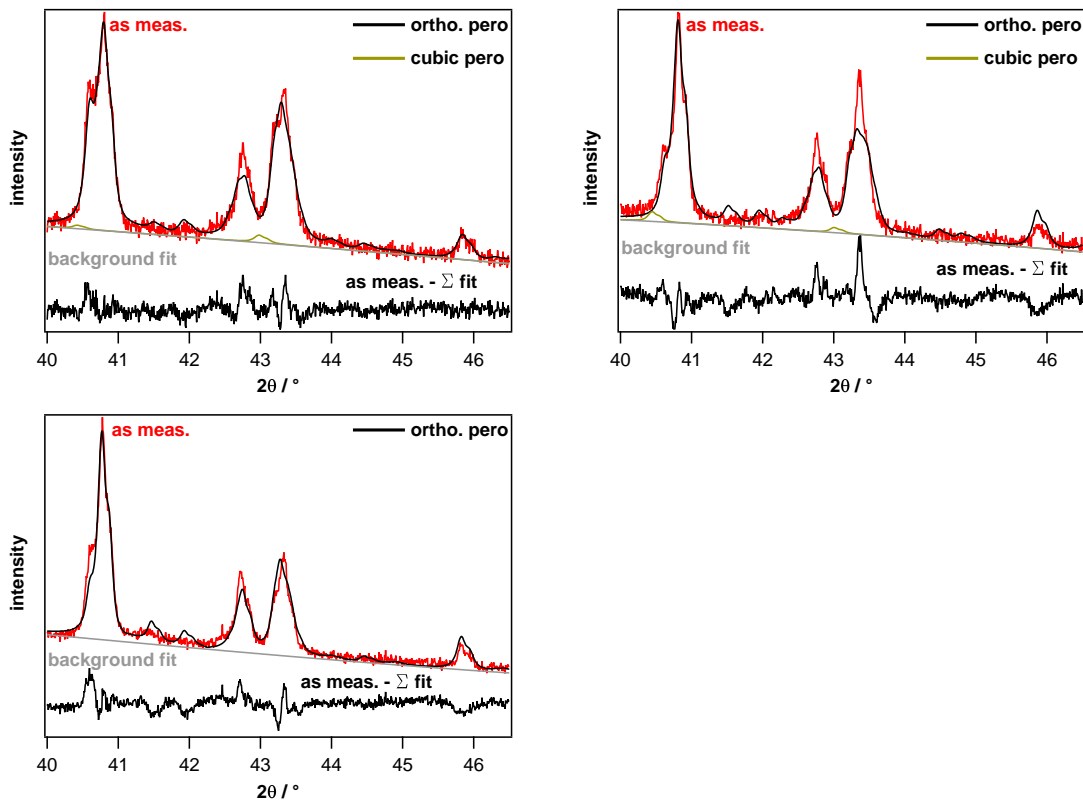


Figure A.4.: Detailed XRD patterns of MAPI layers fabricated from PbI₂ on glass/FTO/TiO₂ substrates at substrate temperatures of 75 °C, 90 °C, 150 °C during the CSS process (red curves). The background is denoted in light gray. In addition, Rietveld refinements of the perovskite phases are given: black for the orthorhombic and green for the cubic phase. The difference between the measured curves and the superposition of the perovskite refinements and the background is denoted in black with “as meas. - Σ fit”.

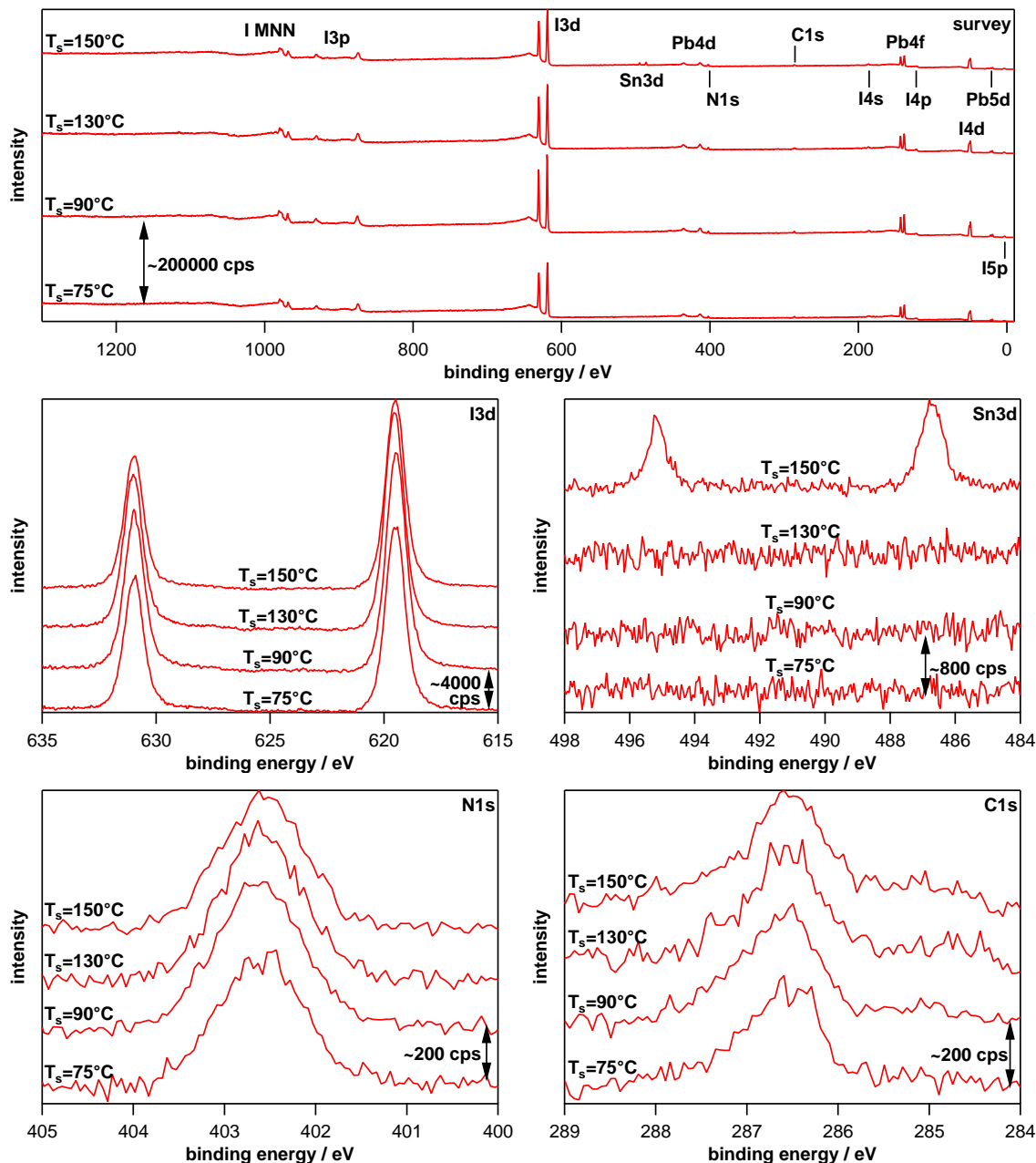


Figure A.5.: XPS spectra of MAPI fabricated from PbI_2 on glass/FTO/ TiO_2 substrates at substrate temperatures of 75 °C, 90 °C, 130 °C and 150 °C during the CSS process. The spectra were measured directly after the layer fabrication, without breaking the vacuum conditions. The offset between the two bottom curves is given as a guide to the eye for the intensity. In the survey spectrum, only the most prominent lines are labeled.

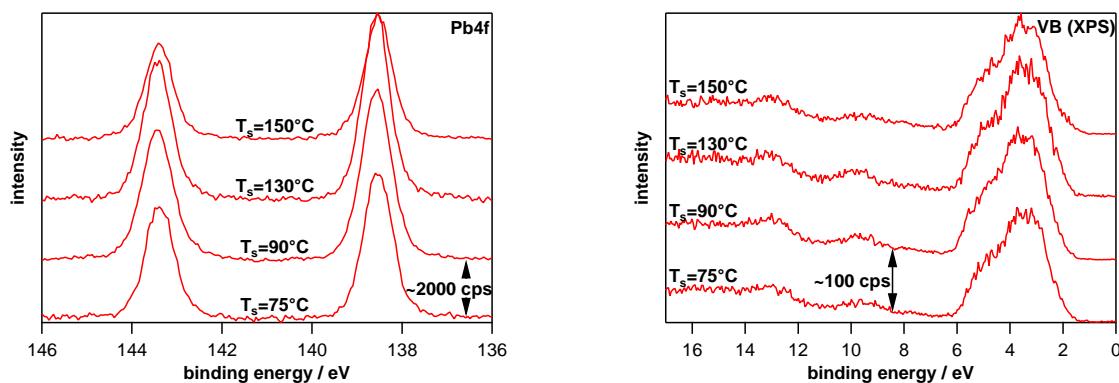


Figure A.6.: XP spectra of MAPI fabricated from PbI_2 on glass/FTO/ TiO_2 substrates at substrate temperatures of 75 °C, 90 °C, 130 °C and 150 °C during the CSS process. The spectra were measured directly after the layer fabrication, without breaking the vacuum conditions. The offset between the two bottom curves is given as a guide to the eye for the intensity.

Evolution of MAPI from lead iodide

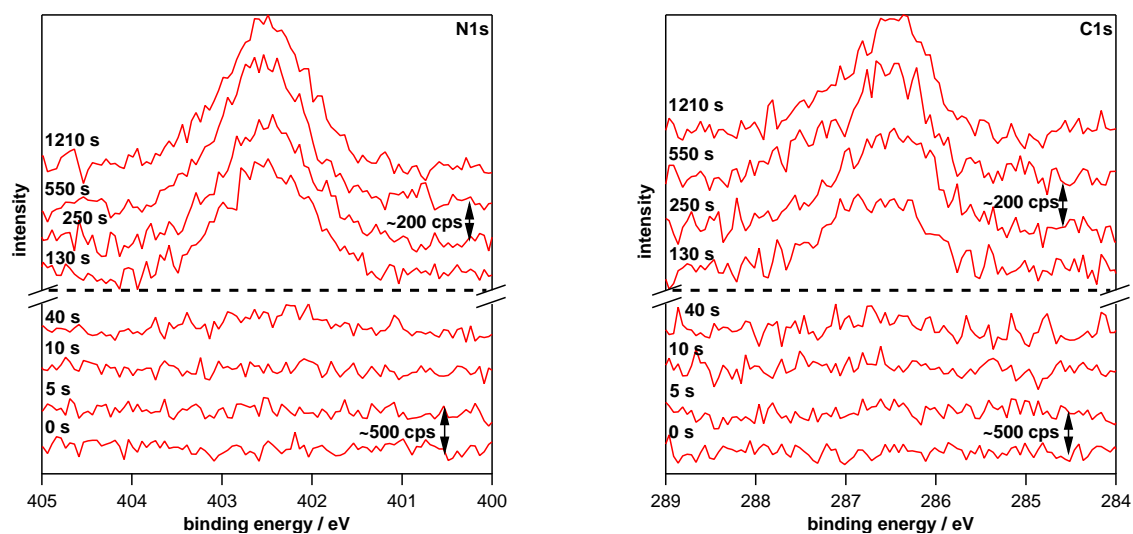


Figure A.7.: XP detail spectra of N1s and C1s emissions measured on a freshly prepared PbI_2 layer and during the stepwise transformation of the PbI_2 layer to MAPI, without breaking the vacuum conditions. To carry out the transformation experiment, a PbI_2 layer was deposited onto a glass/FTO/ TiO_2 substrate by PVD. Afterward, the PbI_2 layer was transformed to MAPI in the CSS with a crucible temperature of 90 °C. The substrate was not heated during the transformation. In addition to the measurements on the bare substrate, PES measurements were carried out after each transformation step. The transformation times shown in the figures are cumulative transformation times. The offsets are given as a guide to the eye to access the intensity.

The titanium dioxide/lead iodide interface

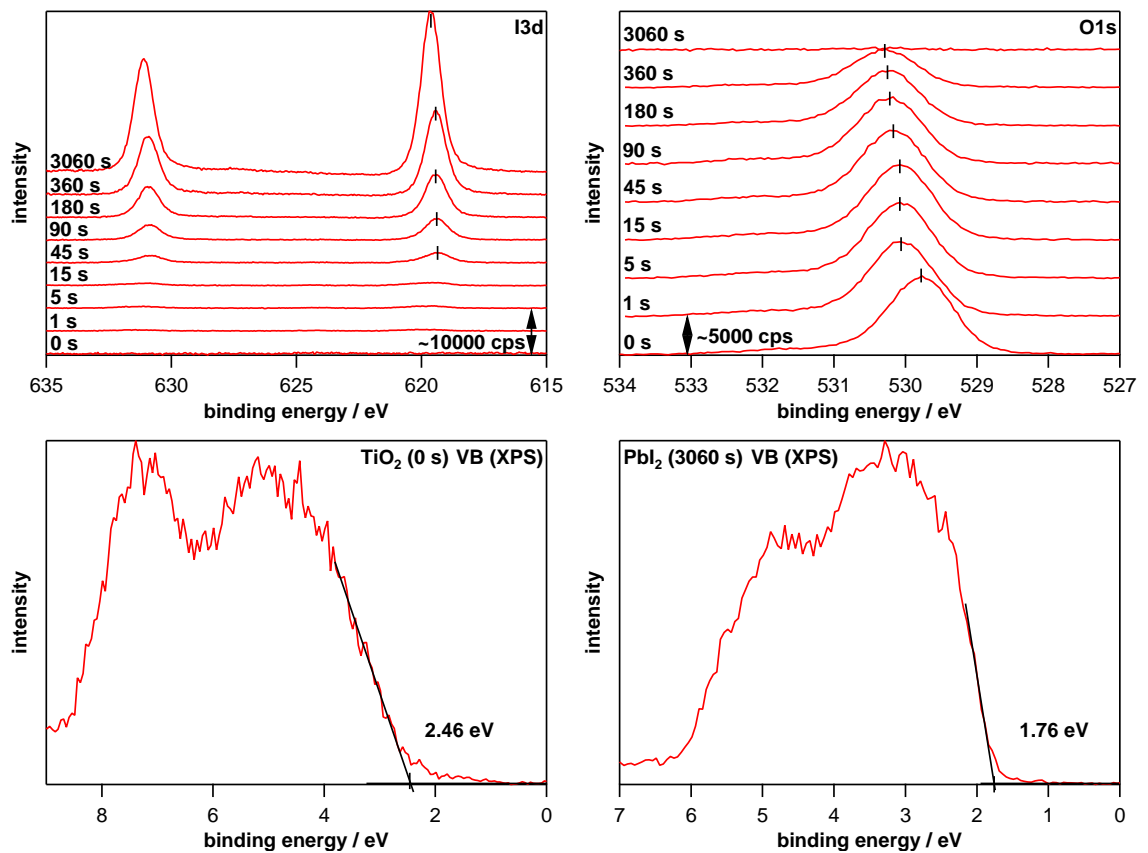


Figure A.8: XP spectra measured on the bare glass/FTO/TiO₂ substrate and between consecutive PbI₂ depositions without breaking the vacuum conditions. The I3d and O1s emissions as well as the valence band spectra of the bare TiO₂ substrate (0 s) and the finished PbI₂ layer (3060 s) are shown. The shown deposition times are cumulative deposition times. The offset between the two bottom curves is given as a guide to the eye for the intensity.

MAPI fabricated from lead chloride

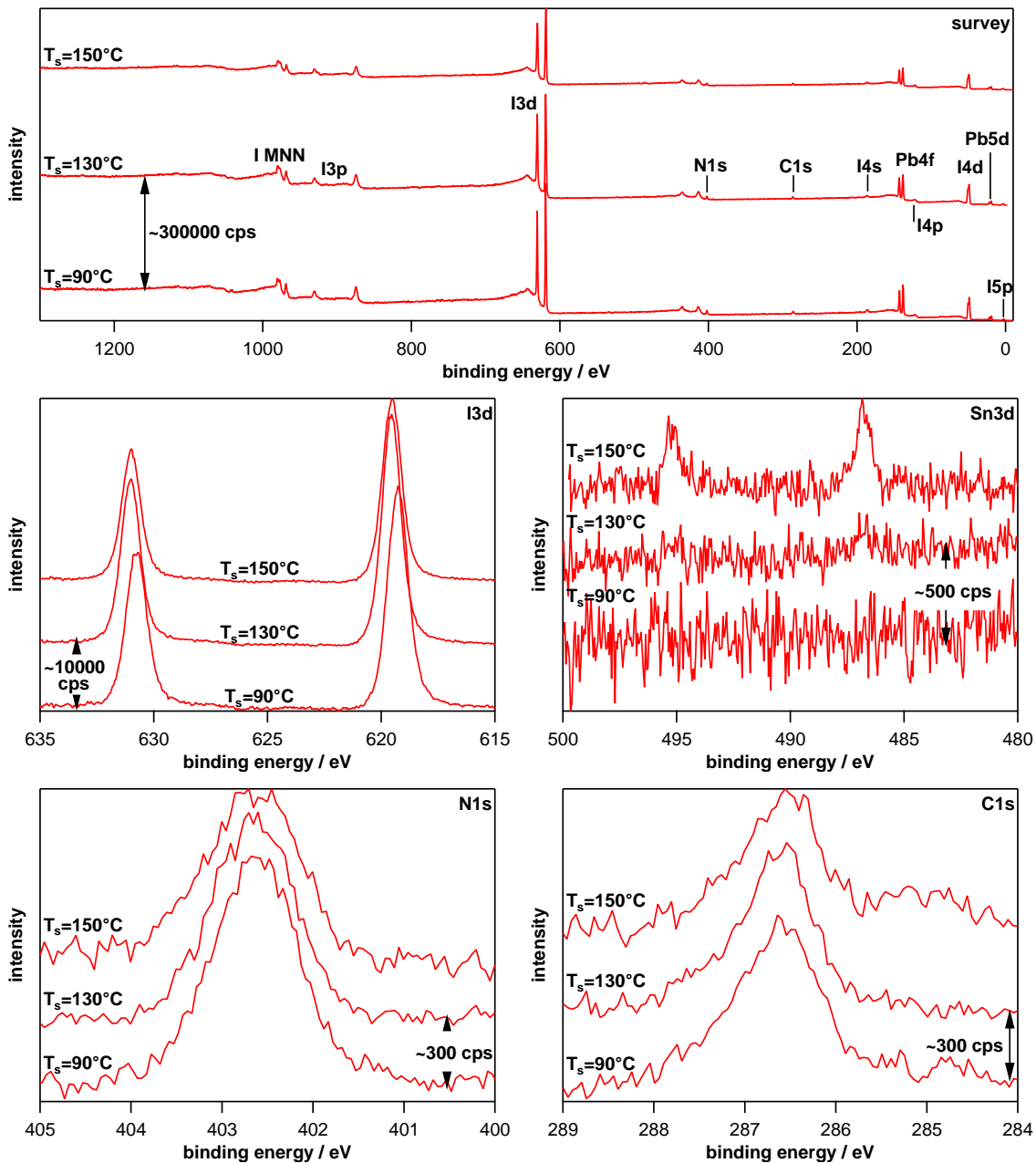


Figure A.9.: XPS spectra of MAPI fabricated from PbCl_2 on glass/FTO/ TiO_2 substrates at substrate temperatures of 75 °C, 90 °C, 130 °C and 150 °C during the CSS process. The spectra were measured directly after the layer fabrication, without breaking the vacuum conditions. The offset between the two bottom curves is given as a guide to the eye for the intensity. In the survey spectrum, only the most prominent lines are labeled.

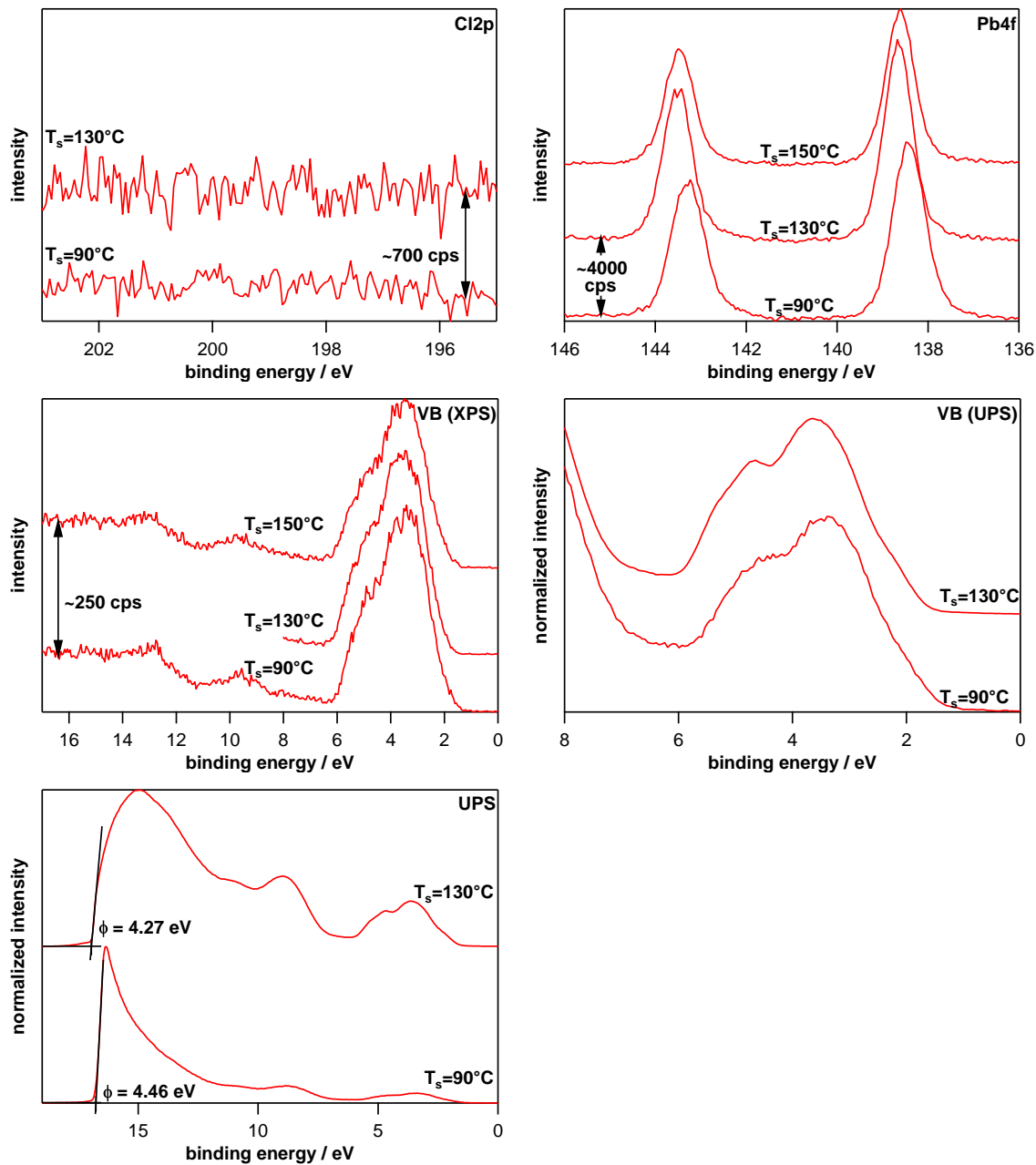


Figure A.10.: XP and UP spectra of MAPI fabricated from PbCl_2 on glass/FTO/ TiO_2 substrates at substrate temperatures of 75 °C, 90 °C, 130 °C and 150 °C during the CSS process. The spectra were measured directly after the layer fabrication, without breaking the vacuum conditions. The UP spectra are normalized in intensity scale. In the XP spectra, the offset between the two bottom curves is given as a guide to the eye for the intensity.

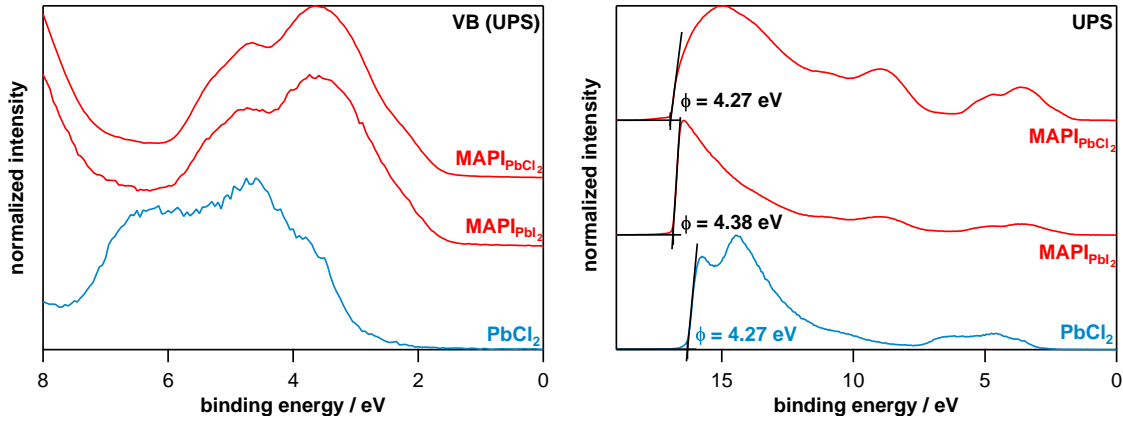


Figure A.11.: Valence band and survey UP spectra of MAPI fabricated from PbCl_2 (red), MAPI fabricated from PbI_2 (red) and of PbCl_2 (turquoise). The spectra are measured directly after the layer fabrication, without breaking the vacuum conditions. The spectra are normalized in intensity scale.

Evolution of MAPI from lead chloride

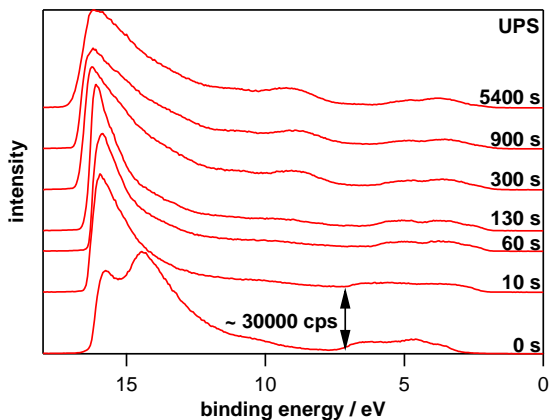


Figure A.12.: UPS spectra measured on a freshly prepared PbCl_2 layer and during the stepwise transformation of the PbCl_2 layer to MAPI. The shown transformation times are cumulative transformation times. The offset between the two bottom curves is given as a guide to the eye for the intensity.

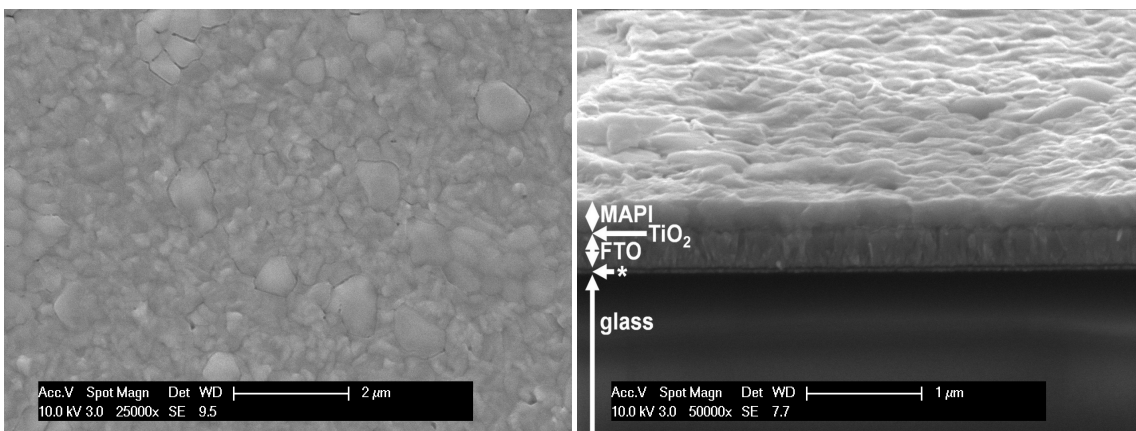


Figure A.13.: SEM images in SE contrast taken after the stepwise transformation of a PbCl_2 layer to MAPI (cumulative transformation time 5400 s). Top view (left) and cross section (tilted 75°) (right).

Influence of a heat treatment, in a tube furnace in air, on the morphology and the crystal structure of MAPI layers

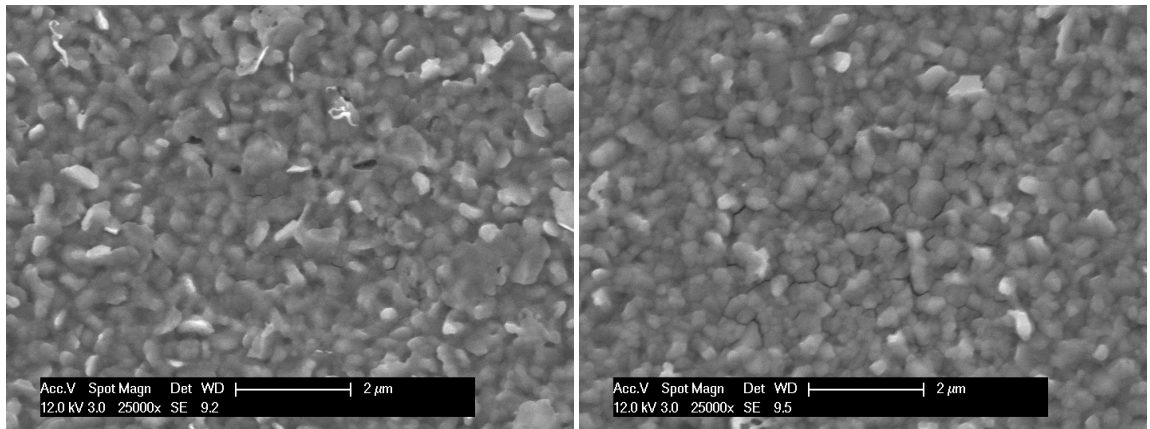


Figure A.14.: SEM images in SE contrast of MAPI layers fabricated from PbI_2 on glass/FTO/ TiO_2 substrates without (left) and with (right) a heat treatment at 120 °C for 30 min in air. The presented images are part of the master thesis of M.Sc. Christian Hoyer [164]. The parameters of the CSS process step were $T_c=120$ °C, $T_s=75$ °C and $t_t=30$ min.

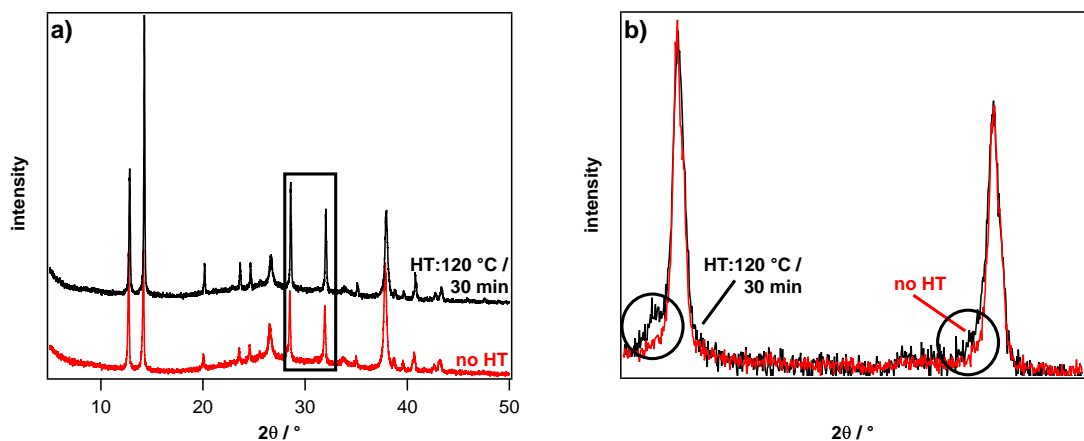


Figure A.15.: XRD patterns of MAPI layers fabricated from PbI_2 on glass/FTO/ TiO_2 substrates without and with a heat treatment at 120 °C for 30 min in air. In (a), the patterns are shown as measured. In (b), the reflections, showing the presence of the cubic modification of MAPI (black frame in a) are highlighted. To do so, the patterns are aligned in 2θ scale and normalized in intensity scale. The presented XRD patterns are part of the master thesis of M.Sc. Christian Hoyer [164]. The parameters of the CSS process step were $T_c=120$ °C, $T_s=75$ °C and $t_t=30$ min.

Lead iodide on ITO

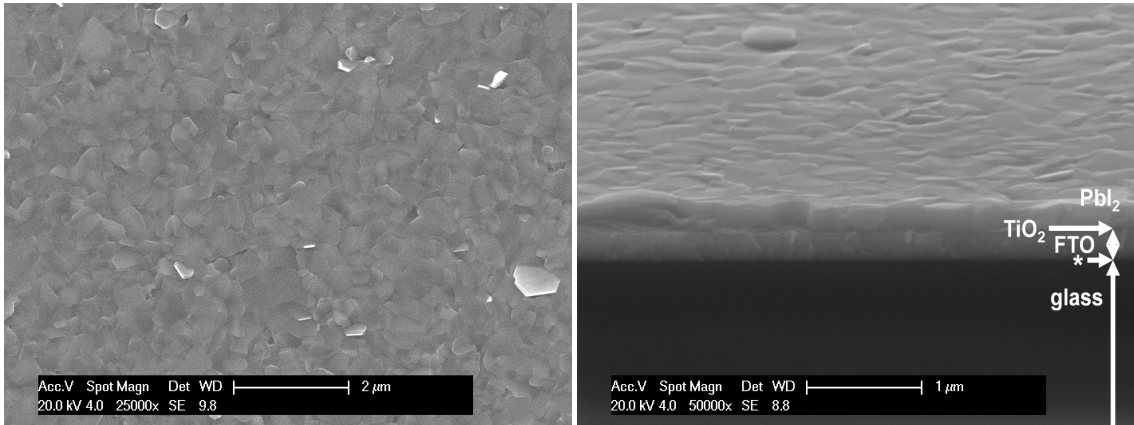


Figure A.16.: SEM images in SE contrast of a PbI₂ layer deposited by PVD on a glass/ITO/TiO₂ substrate. Top view (left) and cross section (tilted 75°) (right). The PbI₂ layer was deposited with a rate of approximately 0.5 Å/s while the substrate was kept at a substrate temperature of about 50 °C. The deposition parameters match those of the PbI₂ layer shown in figure 5.13 on a glass/FTO/TiO₂ substrate.

B Publications, conference contributions and student theses

Publications

- **Characterization of Methylammonium Lead Iodide Thin Films Fabricated by Exposure of Lead Iodide Layers to Methylammonium Iodide Vapor in a Closed Crucible Transformation Process**
R. Dachauer, O. Clemens, K. Lakus-Wollny, T. Mayer, W. Jaegermann, *physica status solidi (a)*, vol. 216, no. 11 p.1800894, 2019
- **The difference in electronic structure of MAPI and MASI perovskites and its effect on the interface alignment to the HTMs spiro-MeOTAD and CuI**
T. Hellmann, M. Wussler, C. Das, R. Dachauer, I. El-Helaly, C. Mortan, T. Mayer and W. Jaegermann, *Journal of Materials Chemistry C*, vol. 7, no. 18, pp. 5324-5332, 2019

Conference contributions

- **Closed Space Sublimation for lead and tin perovskites**
R. Dachauer, I. Elhelaly, C. Wittich, H. Köbler, M. Wußler, K. Lakus-Wollny, T. Hellmann, C. Mortan, A. Beneš, C. Loho, M. A. Nowroozi, E. Mankel, Th. Mayer, O. Clemens, W. Jaegermann, *Perovskite Thin Film Photovoltaics (ABXPV) 2017, Valencia, Spain (poster presentation)*
- **XPS studies on $\text{CH}_3\text{NH}_3\text{PbI}_3$ (MAPI) fabricated under UHV conditions**
R. Dachauer, C. Ondobo, M. Wußler, C. Wittich, O. Clemens, A. Beneš, C. Loho, K. Lakus-Wollny, E. Mankel, T. Mayer, W. Jaegermann, *BMBF Workshop Perovskites October 2016, Würzburg, Germany (poster presentation)*
- **Comparison of perovskites formed through Closed Space Sublimation from PbI_2 and PbCl_2 layers**
R. Dachauer, C. Hoyer, M. Wußler, O. Clemens, A. Beneš, C. Loho, K. Lakus-Wollny, E. Mankel, T. Mayer, W. Jaegermann, *International Conference on Hybrid and Organic Photovoltaics (HOPV) 2016, Swansea, Great Britain (poster presentation)*
- **A modified physical vapor deposition technique for the fabrication of perovskite solar cells**
R. Dachauer, M. Wußler, O. Clemens, A. Beneš, C. Loho, K. Lakus-Wollny, P. Reckers, J. Türck, C. Wittich, L. Dimesso, E. Mankel, T. Mayer, W. Jaegermann, *Spring Meeting of the European Materials Research Society (E-MRS) 2015, Lille, France (poster presentation)*

Summer schools

- **International Summer School on Photovoltaics and New Concepts of Quantum Solar Energy Conversion (Quantsol) 2015**
Hirschegg, Austria

Supervised student theses

- **Optimierung von vakuum-prozessierten $\text{CH}_3\text{NH}_3\text{PbI}_3$ Perowskit-Schichten für Photovoltaik-Anwendungen**
C. Hoyer, Masterthesis, 2015

C Résumé

Professional experience

09/2014- **Research associate / PhD student**
02/2018 TU Darmstadt, Surface Science division

Semester abroad

08/2013- **Chalmers University of Technology, Gothenburg, Sweden**
12/2013 Awardee of the “Dr. Jürgen Ulderup-Stipendium”

Academic education

10/2011- **Materials Science (in English language)**
09/2014 TU Darmstadt

- Degree: Master of Science (mark 1.07 - Award for the best final degree of the master program materials science in winter semester 2013/2014)
- Master thesis with the title “Influence of oxygen on the performance of small molecular and polymeric thiophene-based organic field effect transistors” (mark 1.0)

10/2008- **Materialwissenschaft (materials science)**
09/2011 TU Darmstadt

- Degree: Bachelor of Science (mark 1.6)
- Bachelor thesis with the title “Mechanisches Legieren und Untersuchen der Oxidationseigenschaften von Eisenaluminiden, mit bis zu 5 at% Titan” (“Mechanical alloying and examination of the oxidation properties of iron aluminides which contain up to 5 at% titanium”)(mark 1.3)
- Stipendiary of “Studienstiftung des deutschen Volkes” from 11/2008 till 12/2013

Alternative to compulsory military service

08/2007- **Assistant to nursing staff**
04/2008 Cardiologic unit of the Kerckhoff Klinik, Bad Nauheim

School education

08/2004- **Burrgymnasium, Friedberg**
06/2007 General qualification for university entrance (Abitur)(mark 1.1)

09/1998- **Adolf-Reichwein-Schule, Friedberg**
07/2004 Secondary school certificate (Realschulabschluss)

08/1994- **Geschwister-Scholl-Schule, Niddatal**
07/1998